Bangor University

DOCTOR OF PHILOSOPHY

Design, Implementation and Analysis of a 5.8 GHz Radar for Insect and Micro-Target Monitoring

Aldabashi, Nawaf

Award date:
2023

Awarding institution:
Bangor University

[Link to publication](#)

Bangor University

DOCTOR OF PHILOSOPHY

Design, Implementation and Analysis of a 5.8 GHz Radar for Insect and Micro-Target Monitoring

Aldabashi, Nawaf

Award date:
2023

Awarding institution:
Bangor University

[Link to publication](#)

PRIFYSGOL
BANGOR
UNIVERSITY

DESIGN, IMPLEMENTATION AND ANALYSIS

OF A 5.8 GHz RADAR FOR INSECT AND

MICRO-TARGET MONITORING

Written by

Nawaf Aldabashi

School of Computer Science and Electronic Engineering

2022/23

A thesis submitted in partial fulfilment for the degree of

Doctor of Philosophy

(68) "And your Lord inspired to the bee, "Take for yourself (homes/nests) among the mountains, houses, and among the trees and [in] that which they (humans) construct."

(69) "Then eat (addressed to female bee) from all the fruits and follow (addressed to female bee) the ways of your Lord laid down [for you]. There emerges from her bellies (referring to a single female bee) a drink, varying in colours, in which there is healing for people. Indeed, in that is a sign for those who contemplate."

– The Holy Quran – Chapter 16 – The Bee

(68) "A'th Arglwydd a ysbrydolodd i'r wenynen, "Cymer i ti dy hun (cartrefi/nythod) ymhlith y mynyddoedd, y tai, ac ymhlith y coed ac [yn] yr hyn y maent hwy (bodau dynol) yn ei adeiladu."

(69) "Yna bwyta (wedi'i gyfeirio at wenynen fenywaidd) o'r holl ffrwythau, a dilyn (cyfeiriad at wenynen fenywaidd) ffyrdd dy Arglwydd a osodwyd [i ti]. Daw diod o'i boliau (gan gyfeirio at wenynen sengl) ddiod yn amrywio o ran lliwiau, lle mae iachâd i bobl. Yn wir, mae hynny'n arwydd i'r rhai sy'n myfyrio."

- Y Quran Sanctaidd - Pennod 16 - Y Wenynen

Declaration and Consent

I hereby declare that this thesis is the results of my own investigations, except where otherwise stated. All other sources are acknowledged by bibliographic references. This work has not previously been accepted in substance for any degree and is not being concurrently submitted in candidature for any degree unless, as agreed by the University, for approved dual awards.

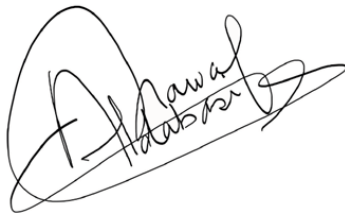Yr wyf drwy hyn yn datgan mai canlyniad fy ymchwil fy hun yw'r thesis hwn, ac eithrio lle nodir yn wahanol. Caiff ffynonellau eraill eu cydnabod gan droednodiadau yn rhoi cyfeiriadau eglur. Nid yw sylwedd y gwaith hwn wedi cael ei dderbyn o'r blaen ar gyfer unrhyw radd, ac nid yw'n cael ei gyflwyno ar yr un pryd mewn ymgeisiaeth am unrhyw radd oni bai ei fod, fel y cytunwyd gan y Brifysgol, am gymwysterau deuol cymeradwy.

Statement of Originality

The work presented in this thesis is entirely from the studies of the individual student, except where otherwise stated. Where derivations are presented and the origin of the work is either wholly or in part from other sources, then full reference is given to the original author. This work has not been presented previously for any degree, not is it at present under consideration by any other degree awarding body.

Signed:
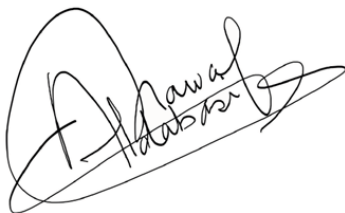
Statement of Availability

I hereby acknowledge the availability of any part of this thesis for viewing, photocopying or incorporation into future studies, providing that full reference is given to the origins of any information contained herein. I further give permission for a copy of this work to be deposited with the Bangor University Institutional Digital Repository, the British Library ETHOS system, and/or in any other repository authorised for use by Bangor University when the approved bar on access has been lifted. I acknowledge that Bangor University may make the title and a summary of this thesis/dissertation freely available.

Signed:

Abstract

The work presented in this thesis contributes to researching honeybee monitoring applications, with the aim of providing an unobtrusive monitoring solution to extend our understanding of bee behaviour and help preserve the globally threatened honeybee population.

This study presents the design and assembly of a 5.8 GHz continuous wave (CW) radar used for unobtrusive insect monitoring from a 2 to 3-meter distance. The system was designed based on matching the radar cross section (RCS) of a 4 mm steel sphere to that of a honeybee model, which estimated the RCS of the bee using a full-wave electromagnetic (EM) simulator. A honeybee hive was monitored, resulting in readouts containing accurate Doppler shifts of flying honeybees. These were used to extract the RCS of 164 free-flying honeybees and was found to be within the range of -55 to -60 dBsm ± 3 dBsm, which was within the RCS EM simulations.

The radar was integrated on a cost-effective 45 mm × 40 4-layer PCB and was further developed for in-phase and quadrature output, supporting the identification of positive and negative Doppler shifts. It allowed the extraction of micro-Doppler signatures and provided readouts of honeybee and bumblebee wing beats that matched their expected wing beat frequency, demonstrating the capability of operating as a radar-based insect classification system.

The radar was integrated with machine learning (ML) to allow automatic classification of bee behaviour. The first ML model classified a hive's outgoing and incoming bees with an accuracy of 87.83%. The second ML model added hovering bees as a third classification group, which achieved a classification accuracy of 93.37%, thereby demonstrating the performance of the radar.

Finally, a feasibility study of a coated honeybee was performed, where the upper part of the thorax and abdomen were identified as ideal coating locations. The study estimated a maximum detection range enhancement of 4.2 metres from the original 2.4 metres through the application of 100 μm Silver coating.

This work led to several publications and demonstrated the ability of unobtrusive insect monitoring using widely available 5.8 GHz components. It addressed a research gap in honeybee RCS at 5.8 GHz and the feasibility of increased radar range monitoring using coating that will pave the way for further insect monitoring studies.

Acknowledgements

have been a great family friend and I appreciate the top-tier memories we have shared and continue to share. Dr. Amira Eltokhy thank you for being a great colleague and for becoming a precious family friend. Further, Dr. Noel, Dr. Helder Anizelli, Dr. Tudor Dr. Bing Yan, thank you for you're the lovely memories and the fun discussions we shared during our tea breaks. I would also like to thank Dr. Jake Shearwood and Dr. James Monks for their contributions, especially during the early months of the PhD and their continued friendship. Finally, I would like to thank Sam Williams for his contributions towards the project with his machine learning contributions and his continued assistance with coding, testing and data collection.

A special gratitude goes towards my dear family. My two younger brothers whom both encouraged me and always expressed how proud they were. Fahad who has been working hard daily trying to help our household with no time off. Thank you for this and know that you are appreciated. Mishal who has been handling two jobs with barely enough time to sleep and juggling his medical conditions along the way to look out for our household. Know that you too are appreciated. It always made me smile how they pretended to understand what I was doing and occasionally even received impractical technical suggestions. My dear mother who always encouraged me and supported me on a daily basis. Despite her personal turbulences, she was always there to support me. I would like to also thank my father, who tirelessly demonstrated the example of hard work. I would also like to express my gratitude to my friend and brother Saad Al-khattaf and his beloved family for their initial mental and financial support that allowed me to start my educational journey.

I would like to thank my wife, who has demonstrated unbelievable patience, incredible source of care, provided me with a loving home after each work day and encouraged me every step throughout in my life. I will take this opportunity to express my unending gratitude, as without her, I would have never come this far. Thanks to her loving persistence, I maintained a healthier work-life relationship than I normally would. Thank you for being so supportive, thank you for being my best friend and wife. All words combined, in every language I know, would not be enough to express my gratitude. Additionally, I would like to thank my in-laws (Tonnie, Anita, Jeroen and Wouter) for their kindness and warm wishes.

Finally, I would like to say thank you to my little baby boy Saleh (the righteous one), who's contributions towards my PhD were immense joy, immeasurable love and many sleepless nights. I dedicate this PhD to you.

Last but not least, I would like to thank all my friends, Abdulla Almahous, Moath, Ali Alshouli, Ahmed Langawi, Mohammad Albadr, Mohammad Almansour, Abdulwahab Alkandari and everyone else that supported me throughout this time.

Contributions

Journal Publications

2022   A Machine Learning Integrated 5.8 GHz Continuous Wave Radar for Honeybee Monitoring and Behaviour Classification

N. Aldabashi, S. M. Williams, A. Eltokhy, E. Palmer, P. Cross and C. Palego, "A Machine Learning Integrated 5.8-GHz Continuous-Wave Radar for Honeybee Monitoring and Behavior Classification," in IEEE Transactions on Microwave Theory and Techniques, doi: 10.1109/TMTT.2023.3248785

2021   Early prediction of bumblebee flight task using machine learning

S.M. Williams, N. Aldabashi, C. Palego, J.L. Woodgate, J.C. Makinson, P. Cross, Computers and Electronics in Agriculture, Volume 184, 2021, 106065, ISSN 0168-1699, https://doi.org/10.1016/j.compag.2021.106065.

2020   C-Band Telemetry of Insect Pollinators Using a Miniature Transmitter and a Self-Piloted Drone

Shearwood, J., Aldabashi, N., Eltokhy, A., Franklin, E.L., Raine, N.E., Zhang, C., Palmer, E., Cross, P. and Palego, C, in IEEE Transactions on Microwave Theory and Techniques, vol. 69, no. 1, pp. 938-946, Jan. 2021, doi: 10.1109/TMTT.2020.3034323.

Conference Papers

2021   A Printed Circuit Board Continuous Wave Doppler Radar for Machine Learning-Enhanced Biometrics

N. Aldabashi, S. M. Williams, P. Cross and C. Palego, "A Printed Circuit Board Continuous Wave Doppler Radar for Machine Learning-Enhanced Biometrics," 2021 IEEE MTT-S International Microwave and RF Conference (IMARC), KANPUR, India, 2021, pp. 1-4, doi: 10.1109/IMaRC49196.2021.9714590.

2021   Integration of 5.8GHz Doppler Radar and Machine Learning for Automated Honeybee Hive Surveillance and Logging

N. Aldabashi, S. Williams, A. Eltokhy, E. Palmer, P. Cross and C. Palego, 2021 IEEE MTT-S International Microwave Symposium (IMS), Atlanta, GA, USA, 2021, pp. 625-628, doi: 10.1109/IMS19712.2021.9574826.

2020   Localization and tracking bees using a battery-less transmitter and an autonomous unmanned aerial vehicle

Shearwood, J., Williams, S., Aldabashi, N., Cross, P., Freitas, B.M., Zhang, C. and Palego, C, 2020 IEEE/MTT-S International Microwave Symposium (IMS), Los Angeles, CA, USA, 2020, pp. 1263-1266, doi: 10.1109/IMS30576.2020.9223950.

LIST OF CONTENTS

List of Contents

List of Figures

List of Tables

List of Acronyms

Acronym	Full form
AC	Alternating Current
ADC	Analog-To-Digital Converter
AI	Artificial Intelligence
AM	Amplitude Modulation
ATS	Advanced Telemetry Systems
BCEL	Binary Cross Entropy Loss
BPM	Beats Per Minute
CAD	Computer-Aided Design
CBCPW	Conductor Backed Coplanar Waveguide
CPD	Critical Point Drying
CPW	Coplanar Waveguide
CST	Computer Simulation Technology
CW	Continuous Wave
DBSM	Decibel over a Square Metre
DC	Direct Current
DDT	Dichlorodiphenyltrichloroethane
DIY	Do-It-Yourself
DJI	Da-Jiang Innovations
DVAV	Dorso-Ventral Abdominal Vibration
E-FIELD	Electric Field
EIRP	Effective Isotropic Radiated Power
EM	Electromagnetic

EPC	Electronic Product Code
FD	Freeze Drying
FFT	Fast Fourier Transform
FMCW	Frequency-Modulated Continuous Wave
GHZ	Gigahertz
GNSS	Global Navigation Satellite System
HDMS	Hexamethyldisilazane
HF	High Frequency
H-FIELD	Magnetic Field
HMC	Hittite Microwave Corporation
HMM	Hidden Markov Model
HP	Hewlett Packard
HZ	Hertz
I/Q	In-Phase and Quadrature
ID	Identification
IEEE	Institute Of Electrical and Electronics Engineers
IF	Intermediate Frequency
IOT	Internet Of Things
KESS	Knowledge Economy Skills Scholarships
KHz	Kilohertz
LED	Light-Emitting Diode
LF	Low Frequency Band
LFM	Linear Frequency Modulation
LNA	Low-Noise Amplifier
LO	Local Oscillator

LoS	Line Of Sight
LP	Linear Prediction
LPF	Low Pass Filter
LSF	Line Spectral Frequencies
LVR	Linear Voltage Regulation
MAXIM	Maxim Integrated
MCP	Microchip Technology
MDS	Minimum Detectable Signal
MEMS	Micro-Electro-Mechanical Systems
MHz	Megahertz
MIT	Massachusetts Institute of Technology
ML	Machine Learning
ms	Millisecond
mAh	Milli-Ampere Per Hour
NF	Noise Figure
NI	National Instruments
NM	Nanometre
NN	Neural Networks
ODE	Ordinary Differential Equation
OP	Operational Amplifier
OPA	Operational Amplifier
PCB	Printed Circuit Board
PEC	Perfect Electric Conductor
RCS	Radar Cross Section
RF	Radio Frequency

RFID	Radio Frequency Identification
RMS	Root Mean Square
RSSI	Received Signal Strength Indicator
Rx	Receiving Antenna
SAR	Synthetic Aperture Radar
SEM	Scanning Electron Microscope
SMA	Sub-Miniature Coaxial Cable Connector
SMPS	Switched Mode Power Supply
SNR	Signal To Noise Ratio
STFT	Short-Time Fourier Transform
SVM	Support Vector Machines
Tx	Transmitting Antenna
UAV	Unmanned Aerial Vehicle
UK	United Kingdom
USA	United States of America
USB	Universal Serial Bus
USDA	United States Department of Agriculture
UWB	Ultra-Wideband
VCO	Voltage-Controlled Oscillator
VHF	Very High Frequency
VNA	Vector Network Analyzer
μm	Micrometre

Chapter 1. Literature Review

1.1 Motivation

Insect biomass has been undergoing dramatic decreases over the past years, due to loss of natural insect habitats, increased pollution, synthetic pesticides, climate change and biological factors [1], [2]. Insect biomass loss may have reached a tipping point, with the potential of driving 40% of the world's insect species to extinction over the coming decades [1]. Insect decline is threatening global insect biodiversity, including species which help maintain crucial ecosystem functions [1]. In an experiment conducted over a 27 year period in German nature reserves total flying insect biomass suffered a 75% decline [3]. This has an undeniable impact on essential ecosystem functions, such as pollination [3], [4], detrivory functions [5], [6], herbivory functions [7], cycling of nutrients and acting as a food source for wide classes of animals [4], [6].

A global threat facing bee populations is agricultural intensification causing habitat loss and fragmentation [8]–[10]. For instance, 85% of Iowa was once a grassland, providing a good bee habitat, while less than 0.1% of this grassland now remains [11]. Bumblebee (*Bombus terrestris*) foraging plants in the UK have undergone disproportionate decline, where out of 97 foraging species, 76% declined in abundance over the past 90 years and 71% suffered range restrictions [12]. A continuous succession of flowers is needed from April to August, to allow bee colonies to thrive, and crops alone are unlikely to provide this continuous succession [13]. This can cause colonies to starve and die, which causes less plants to seed due to lack of pollination, leading to less foraging for bees in subsequent years [14].

The combination of flower-rich habitat loss with pressing bee mortality threats due to insecticides such as Neonicotinoids have been strongly implicated as main drivers to pollinator decline. Neonicotinoids, an insecticide that protects all part of the crop — by travelling through the plant's tissue — to provide effective pest control, while generally being toxic to insects in minute quantities. For instance, the ingestion dose of clothianidin and imidacloprid (both belong to the N-nitroguanidines class of neonicotinoids) capable of killing 50% of individuals (LD_{50}) in honeybees (*Apis mellifera*) is 4 ng and 5 ng respectively, which is $1/10,000^{th}$ the LD_{50} for dichlorodiphenyltrichloroethane (DDT) [15]. According to Professor D. Goulson, one teaspoon of neonicotinoids is sufficient to kill 1.25 billion honeybees [16].

Neonicotinoids are used more than other classes of insecticides [17], with imidacloprid being the 2nd most widely used agrochemical globally [18], [19]. Seed dressing is commonly mentioned to have an accurate targeting of crop [18], where 80-98% is not absorbed by the crop and a small proportion (<2%) becomes lost as dust during sowing [20], which is enough to cause direct mortality in flying honeybees nearby [20], [21]. With neonicotinoids used for crops (e.g., sunflower, oilseed rape, raspberries) that are forage sources for managed and wild bees [13], [17], [22], negative effects such as reduction of learning, foraging, navigation abilities, homing capabilities, cognitive functions and memory are evident in both honeybees and bumblebees [23]–[27]. It is still poorly understood how these adverse effects interact with other stressors such as different pesticides, diseases and food stress, which undoubtably have an impact on bee health [13], [28]. The UK government supported restrictions on using neonicotinoids in 2018 and granted an emergency authorisation in 2021 to apply thiamethoxam to treat sugar beet seed, where the final decision revoked its use [29]. This demonstrates that the application of neonicotinoids can still be employed in the future.

This study reports the design and development of a highly sensitive, low cost 5.8 GHz radar that allows unobtrusive monitoring of insects. The system has a wide variety of potential applications that would allow tag-less insect observation and insect behavioural study. Finally, the study also investigated the potential ability to increase the monitoring range up to ~4 metres using a metallic nanomaterial coating, which can be added to the thorax of the insect.

1.2 Global decline of Entomofauna

There is growing concern about the global decline in biodiversity. Significant declines have occurred for pollinators, which provide crucial ecosystem services, such as pollination, to both humans and the broader environment. For example, pollinators contribute 75% of global imported crop's quality and yield estimated to be worth $57 billion annually in the USA alone [30] and between $235 to $557 billion globally [31].

According to recent studies, the biosphere has entered the sixth mass extinction (Anthropocene), driven by human activity [32]. Sánchez-Bayo *et al*., reviewed seventy-three peer-reviewed studies on insect decline and estimated that at current rates 40% of insect species could be driven to extinction over the coming decades [1]. These rates of decline are unprecedented and it is feared that such a decline could lead to multiple

extinction events [33]. Thus, immediate action is required to understand insect behaviour and introduce ways of mitigating insect losses.

1.3 Apidea and their decline

Bees (*Apidea*) — recognised as the most important pollinating insects — which include the European honeybee and the Buff-tailed bumblebee [34], are facing significant challenges. Particularly, the European honeybee, to which 80% of global pollination services are attributed [35]. Honeybees are responsible for 35% of global crop production [34], [36]. In addition to the pollination of nearly $20 billion worth of crops in the US, wild bees are responsible for an additional $4 billion according to the American Beekeeping Federation and the United States Department of Agriculture (USDA) [37]. Theoretically, crops can be pollinated by farmers manually, at an annual cost of $1.5 billion [38], while pollinators provide the service for free.

The Buff-tailed bumblebee, is also known to pollinate a large number of wild plants [39], [40]. Memmot *et. al.,* studied the impact of insect species absence on plant decline rates. Upon inspecting the absence of bumblebee pollination in the simulation, the result showed the highest plant species decline rate when compared to simulations where other pollinators were removed [41]. As a result, bumblebees have seen an increase in commercial domestication for agricultural pollination services [42].

1.3.1 Main drivers behind decline

The decline of bees is believed to be a combined effect of harsh climate changes, interactions between toxins, pesticides, parasites, pathogens and other stressors [1], [43]–[45]. This section provides a brief overview of the main drivers for the decline of insect biomass.

Habitat loss is believed to be the reason behind global mammal and bird decline [46], which is caused by human activities. Habitats are transformed into building grounds for different purposes, causing insects to retreat from their ecosystem [47],[48]. It is important to encourage governments to introduce benefits and subsidiaries to motivate agricultural intensification. An example can be drawn from the Dutch government's incentive to encourage crop diversification on farmlands to encourage biodiversity through subsidies for the use of 5% of their farmland [49].

Pollution is the second main driver, which includes fertilisers and synthetic pesticides. Modern agriculture controls crop pests (using pesticides), fungal infections (fungicides) and weeds (herbicides), where both pesticides and fungicides can be toxic to insects [50]. Although herbicides do not impose a toxic impact on insects, they cause vegetation biodiversity decline [51]. Pesticides such as fipronil and neonicotinoids can have significant impacts on pollinators. These pesticides impose sub-lethal effects that are known to impair the immune system of bees, making them susceptible to infections caused by Varroa mites [52]. Varroa mites are globally spread, parasitic mites that feed on honeybees with an infectious rate of 95-100% within the infection spread radius [43]. In addition to the reduction of bee foraging behaviour [53]–[55], fipronil and neonicotinoids impair the reproduction system of both the queen and the drones, reducing their longevity and compromising colonies long-term viability [56], [57]. In addition to weather, the combination of the aforementioned reasons are the main drivers to insect decline. This urges the need to develop an insect monitoring system that can assess insects to better understand how they use the environment and space. Different tracking technologies are reviewed in the next sections of this chapter.

1.4 Radio Frequency Identification (RFID)

RFID systems are comprised of RFID tags (transponders), that are queried by the RFID interrogator (reader) to transmit their unique identification via an encoded short-range radio frequency signal when the tags are in close contact with the RFID interrogator [58]. An example of an RFID system is shown in Figure 1.1. RFID tags can be either self powered (active RFID tags) or powered by the incoming signal (passive RFID tags). Self powered tags contribute towards the tag's weight and size, making them larger and heavier than passive tags [59]. Such heavier tags can be carried by larger insects and can be detected by the reader over a thirty-metre distance. As there is no battery equipped on a passive RFID tag, the tag is cheaper to develop, not limited to a battery life and thus operates longer. RFID tags have been designed and employed to operate in frequency ranges between 100 KHz to 10 GHz and have been available commercially since 1980 [60]. RFID tags have a history of wide use cases such as product management, product tracking, access management and electronic travel documents. RFID is considered a standardised and matured technology, operating mainly within the low frequency band (LF), high frequency band (HF) and very-high frequency band (VHF), which represent the 3 KHz to 300 KHz, 3 MHz to 30 MHz and 30 MHz to 300 MHz frequency bands respectively [59].
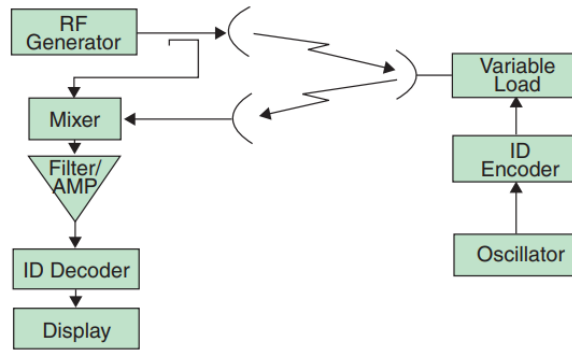
Figure 1.1: RFID system schematic diagram [60].

For more than a decade, RFID tags have been used to monitor insects, operating under different frequency bands, which alternatively dictate the detection range [61]. The detection range is typically sub-1 meter to 5 meter, where other tags have been reported to be limited to 4 mm in detection range [61]–[63]. Due to the effectiveness of RFID tags, the system has been widely developed as a monitoring and tracking solution for a wide range of animals, including and not limited to birds, fish, wasps and ants [64]–[67].

Passive RFID systems, have two different architectures, where the tag is either read/activated by a laser beam or via a radio signal. When using laser activated RFIDs, the laser beam is detected by the tag's photocell and provides the antenna with the power needed to transmit a radio signal, broadcasting unique information that allows the tag to be read and identified. When using radio signal based passive RFID tags, the emitted radio signal is intercepted by the passive RFID tag if both the transmitter and RFID tag operate at the same resonant frequency. Upon activation of the passive RFID tag, it backscatters a radio signal containing the unique information of the tag, allowing it to be identified.

A low cost monitoring solution was developed by De Souza *et al.,* that combined the design and development of a RFID monitoring system [68]. The system used a patch antenna with a coaxial feed, which was designed, simulated and optimised using CST Microwave Studio to achieve a resonant frequency of 875 MHz. The design incorporated a thicker substrate to increase the antenna's bandwidth, whilst choosing a high permittivity to reduce the antenna's size.
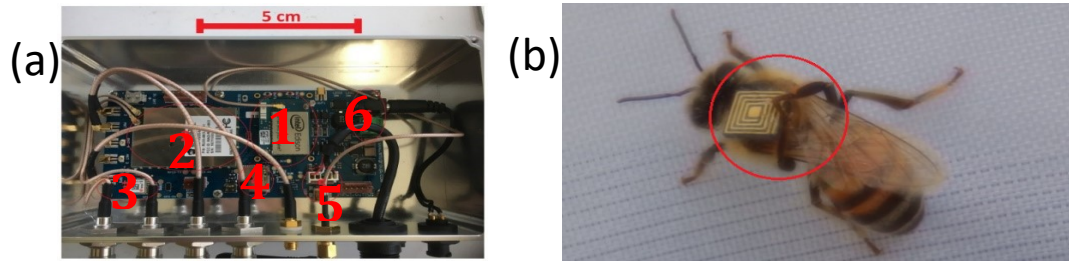
Figure 1.2: (a) Printed circuit board showing the main components: (1) IoT module; (2) HP-SiP module; (3) GNSS receiver; (4) micro-SD card; (5) micro-USB I/O; and (6) power regulator [68]. (b) Hitachi Chemicals RFID tag placed on the bee's thorax. Clearly illustrating the bee trying to remove the RFID [68].

The RFID tags used, Figure 1.2(b) are manufactured by Hitachi Chemical and are 2.5 mm × 2.5 mm × 0.4 mm in size, weighing 5.4 mg and operating at both 860 MHz and 920 MHz. Each tag has a 128-bit Electronic Product Code (EPC), which is used to store the tag's unique hexadecimal ID and the bee's metadata. The metadata contains information such as the bee's species, tagging platform, type information, country, site and bee number. The hardware is shown in Figure 1.2(a), which combines the printed circuit board (PCB), Global Navigation Satellite System (GNSS) receiver, Micro-SD card, Internet of Things (IoT) module (dual-core microprocessor), HP-SiP module (HI-Power System in Package – RFID reader), power regulator and micro-USB for the device's input and output. The HP-SiP module, provides power levels up to 31.5 dBm, supports up to 4 antennas and can read hundreds of tags per second. The study was able to identify individual bee activities, which were listed as a series of events starting from 8:10 AM by leaving the hive, registering various other events (e.g., entering and leaving hive) throughout the day and logging the bee's return to the hive for the night.

The main limitation with the use of RFID tags is the range of detection and the need of readers to increase the detection range. The readers would require the insect to move within their narrow detection, which are commonly custom designed to fit both the bee and the RFID tag. This forces the insects to manoeuvre through narrow and restricted hive entrances, which has the tendency to disturb bee behaviour, especially during warm days, where both temperatures and moisture tend to be high. Furthermore, RFID tags that are read by laser beams, suffer from detection success, detection failures and errors as the tag can easily be misaligned with the narrow laser beamwidth. Finally, RFID tags are electronic components, which have a variable operational lifespan that can be decreased if the RFID tag is damaged, continuously disrupted (through flight and through hive tunnel access) and operated at higher temperatures. To be able to support longer distances, the readers would have to be positioned at different checkpoints, which increases the

complexity and supporting electronics. RFID transponders and their supporting electronics can be costly, which is considered another limitation for an RFID solution. Moreover, RFID solutions require power, which can limit their application in remote areas or areas with no fixed power solutions. A solar panel powered RFID solution, would increase the potential of RFID applications.

1.5 Radio Telemetry

In 1959 LeMunyan *et al.*, were the first to use radio telemetry based tracking for studying the movement behaviour of vertebrates due to the small size (7.5 cm × 4 cm × 1.4 cm) and weight (122.5 grams) of the transmitter and power supply [69]. The first radio telemetric based study investigated the cottontail rabbits (*Sylvilagus floridanus*). Since then, radio telemetry has been involved in various animal studies that involved animal tracking. An early example of such studies involved the giant tortoise (*Geochelone*), which was examined for a week, using a 1 cm diameter spherical frequency modulated radio transmitter [70]. The transmitter, covered in plastic and silicon rubber was ingested by the turtle, as it was embedded into a banana. Every 1-4 hours, the group observed the signal from the radio receiver, indicating the turtle's body temperature [70]. Early methods of tag attachment were incision, feeding and using adhesive, where the latter method is still used. Radio telemetric systems, shown in Figure 1.3, comprise three main components [71]:

1. Battery powered transmitter (active tag): Fitted on the target to emit radio frequency signals. The emitted radio signals are commonly in the (VHF), which ranges from 30-300 MHz.

2. Antenna system: Utilised to extend the receiving range of the system.

3. Radio receiver: Receives and processes the tag's emitted radio signal.
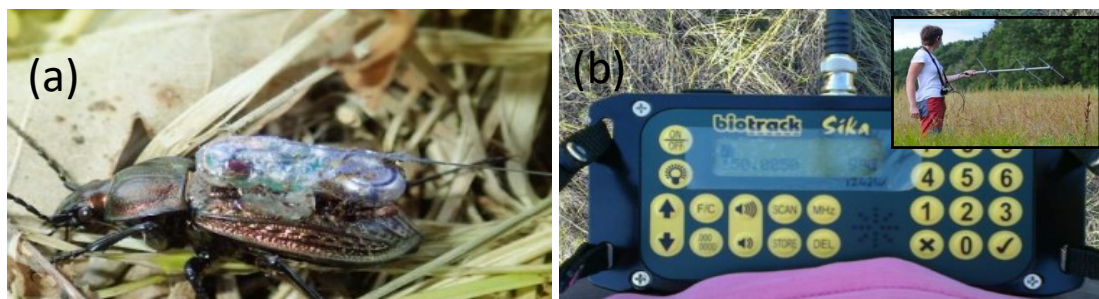
Figure 1.3: (a)Battery-powered radio signal transmitter (active tag, mainly consists of a transmitter, power source and an emitting antenna). (b) Receiver unit. Inset shows hand-held Yagi receiving antenna, mainly designed to receive the tag's resonant frequency and designed to have a high gain [72].

With radio telemetry, it is possible to tag a target and obtain accurate data on the target's movements and location [71]. Radio telemetry is capable of tracking individual insects, as each tag emits a unique frequency, with a high resolution that can reach up to several centimetres. Yet again, the weight of the tags are considered one of the main limitations in radio telemetry tracking of insects [71].

1.5.1 Battery Powered Radio Telemetry

The first radio telemetric study performed on insects, was in 1988 by Hayashi *et. al.*, performed on the dobsonfly larvae (*Protohermes grandis*). Since then, there has been a substantial increase in radio telemetric research. Different studies were performed on various insect taxa, including butterflies [73], dragonflies [74]–[76], orthopterans [77], [78], beetles [79], [80] and hymenopterans [71], [81], [82].

Radio telemetric tags operate using batteries to extend their detection range. Literature reports various detection ranges with an average distance of 0.5 km to a maximum of 1.5 km [75]. The first bee related radio telemetric study was conducted on carpenter bees (*Xylocopa flavorufa*), which revealed valuable data regarding carpenter bee foraging [81]. The study showed that carpenter bee cowpea pollination was conducted at a distance of 6 km from the bee's nest, whereas shorter range flights (100 m) would be during poor weather conditions. The foraging trips were reported to be lower than the bee's maximum flight range, which may be correlated to the presence of the tag, restricting the bee's natural flight range and behaviour. The study used a 350 mg LB-2N transmitter, with a 14 cm long antenna that was four times longer than the bee itself, as shown in Figure 1.4(b). Due to the limited size of the hive's entrance — being the same size of the bee — the transmitter would be forced off of the bee upon the bee's entry.

Hence, transmitters were lost during the study, and recovered by manually moving to the tag's location. The study also mentioned that bees learned how to dispose their transmitter during flight or by returning to their nests, which caused the group to record several incomplete flights [81]. An early example of radio telemetry adaptation on bees was demonstrated with the Orchid bee (*Euglossini*), since orchid bees are known to be strong flyers, they demonstrated their capability of carrying 300 mg tags with little difficulty. The tags were fitted on male orchid bees (*Exaerete frontalis*), where radio telemetry was able to identify a radio signal 5 km away. The study tagged 16 bees, with the 300 mg Fisher IL transmitter from Sparrow systems.
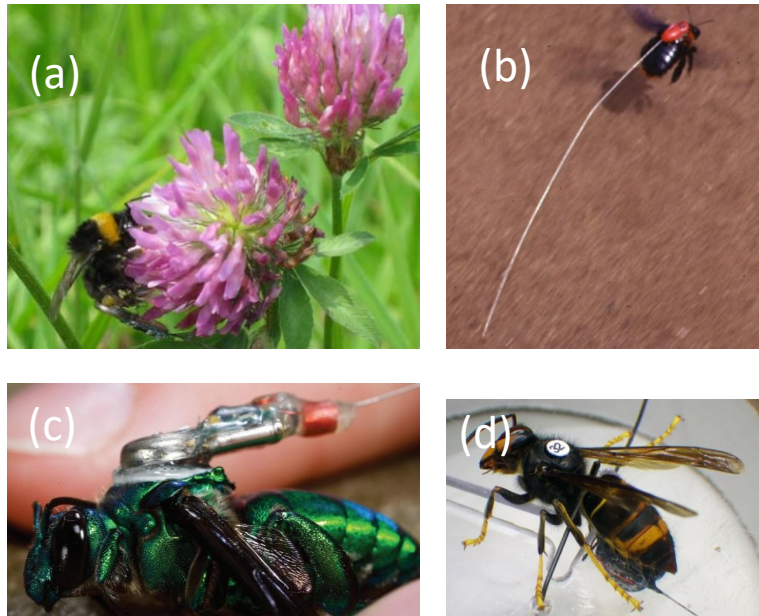
Figure 1.4: Different radio telemetry tags (a) Bumblebee (*Bombus terrestris*) with a tagged 200 mg transmitter [82]. (b) Carpenter bee (*Xylocopa flavorufa*) flying with an attached 350mg tag with a 14 cm antenna [82]. (c) Orchid bee (*Exaerete frontalis*) with an attached 300 mg transmitter [71]. (d) Asian hornet worker attached with 280 mg PicoPip transmitter [83].

Out of the 16 tagged bees, 4 bees including tags were lost. Other bees were observed for 5 days and thus gathered 3 to 13 independent locations per tagged bee. Three different movement patterns were discussed in the study, which were hypothesised to have different implications for pollination related services [84].

Another insect that has attracted research focus is the Asian hornet (*Vespa velutina*). Studies involving monitoring and the localisation of this insect are increasing due to the insect's direct threat to the bee's ecosystem. The most effective method of preventing their long term damage, is the early detection and destruction of their nest [85].

In an attempt to introduce new ways of localising their nests — as these are difficult to detect and locate —Kennedy *et. al.*, utilised radio telemetry [83]. An Asian hornet was caught and fitted with the Pip19 and PicoPip tags from a British company known as ATS (formerly known as Biotrack, Ltd), weighing 220 and 280 mg respectively. The Pip19 and PicoPip had a life expectancy of 4 and 12 days respectively [83]. The authors were able to track 5 previously undiscovered nests, located about 1.3 km from the hornet's location of release, where the average time needed to find a nest was 92 ± 37 minutes. The study indicated the use of radio telemetric tags to be a valuable asset to tracking the hornets to their nest.

Though finding the 5 nests, the authors also mentioned that not all hornets were able to fly, unless the tag to hornet weight ratio was capped at 0.8. The group also mentioned, the loss of two hornets when using the light Pip19/Ag190 tags as they rapidly flew away after being released and consequently lost their radio signal soon after they were no longer visually discernible [83].

The price of a radio telemetric tag depends on different factors, such as size, life span and the range it can support. The common price for an active tag ranges from £130 to £250 [86], [87]. An example is the 150 mg, 3 mm × 12 mm LOTEK nanotags, which costs £207 each, which causes the system's costs to be its main limitation. An example of such costs can be seen based on a government contract that requested 120 Nanotags [88]. To use the tags, the Nanotag Infrared Activator and Adaptor are required, costing £115 and £32 respectively. To receive the signal from the transmitter, the LOTEK SRX800-M2 receiver needs to be purchased as well, along with a three element Yagi antenna (£2110 and £123 respectively). For an entire system of 120 Nanotags the total cost was £27,461 [88]. Another drawback of active tags is their limited operational lifespan.

For instance, in a study by Wikelski *et al.*, the battery life of the Fisher 300 mg transmitter from Sparrow Systems lasted 10 days [84]. Another example is the A2405 tag produced by ATS, which is limited to seven days [82], [86]. However, newer transmitters use a pulsing mechanism to extend the tag's battery life, which allows tags to operate up to 3 to 4 weeks [87]. The Lotek Nanopin, is one of the lightest tags, weighing 130 mg, and pulses every 3 seconds for an operational lifetime of 12 days, but can be adjusted to pulse slower for an extended operational lifetime of up to 29 days respectively [87].

1.5.2 Battery-less Radio Telemetry

Early designs of a battery-less transmitter were developed in 2009 by Chang *et al.,* where energy was extracted from a Hawkmoth (*Manduca sexta*) [89]. The energy harvester delivered 1 mW of electrical power at 1 V DC. The group enhanced the mechanical resonator by tuning it to the moth's wingbeat frequency. The energy harvesting was conducted in two steps, the first step was a linear AC poly-phase permanent-magnet synchronous generator, which was for the reciprocating energy convertor, which is a linear AC poly-phase permanent magnet synchronous generator. It enhances the moth wing flapping vibrations. Whereas the second step was the collection of electronics responsible for the rectification and conditioning of the generator's output weight (showed in Figure 1.5(a)), allowing general usage of the output power.
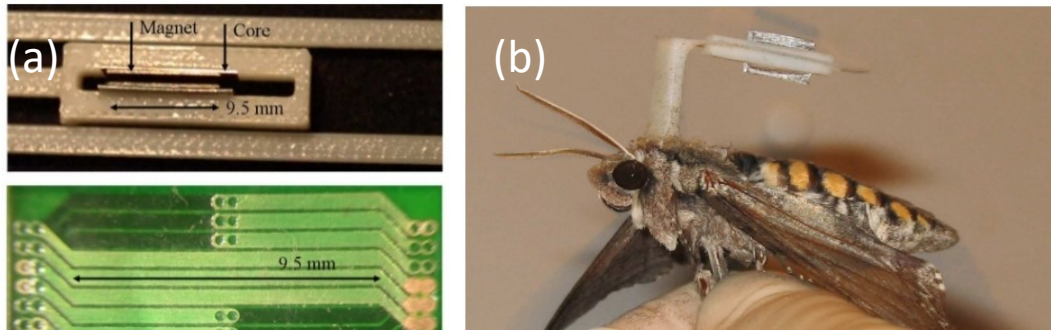
Figure 1.5: (a) Fabrication details of the generator design (b) Attached energy harvesting device to a Hawkmoth [89].

The tag's total weight shown in Figure 1.5(b), was 669 mg and since hawkmoths are known as strong flyers with a payload capacity of nearly 1 gram, the tag's weight seemed reasonable. The study concluded with the need of reducing the tag's mass, eliminating wire losses, increasing harvesting efficiency and improving the power electronics [89].

A similar approach was followed by Reissman *et al.,* in 2011 [90]. The group designed and developed a miniature energy harvesting device, weighing a total of 492 mg, which was fitted on a Hawkmoth. The harvester, shown in Figure 1.5(b), comprised a piezoelectric transducer that converted the vibrational movement induced by the insect into electrical power (up to 59 μW_{RMS}). The device was equipped with a power management unit and an LED, which allowed the accumulation of the generated power and pulsing an LED. Though the device demonstrated functionality, the tag itself was still heavy (nearly 500 mg) considering much lighter tags weighing 150 mg still present potentially behaviour altering effects on insects [71], [82]. The proof of concept developed by this group helped understand the potential of insect-based energy harvesting tag approaches. A group demonstrated the capability of eliminating all three aforementioned problems related to radio telemetry by introducing an energy harvesting transmitter that can be autonomously tracked by a UAV. Shearwood *et al.*, [91] demonstrated a compact, battery-less and lightweight (90 mg) 5.8 GHz transmitter (suitable for both honeybees and bumblebees) coupled with a phased array antenna to extract angle of arrival and target localisation. The tag' circuit is shown in Figure 1.6(a), while the tag placed on a bumblebee is shown in Figure 1.6(b). The receiver was fitted on a UAV and the angle of arrival was estimated using the received signal strength indicator (RSSI). The system, shown in Figure 1.6(c), was built using a voltage detector with a wide dynamic bandwidth (up to 70 dB), making it ideal for sensitive targets.
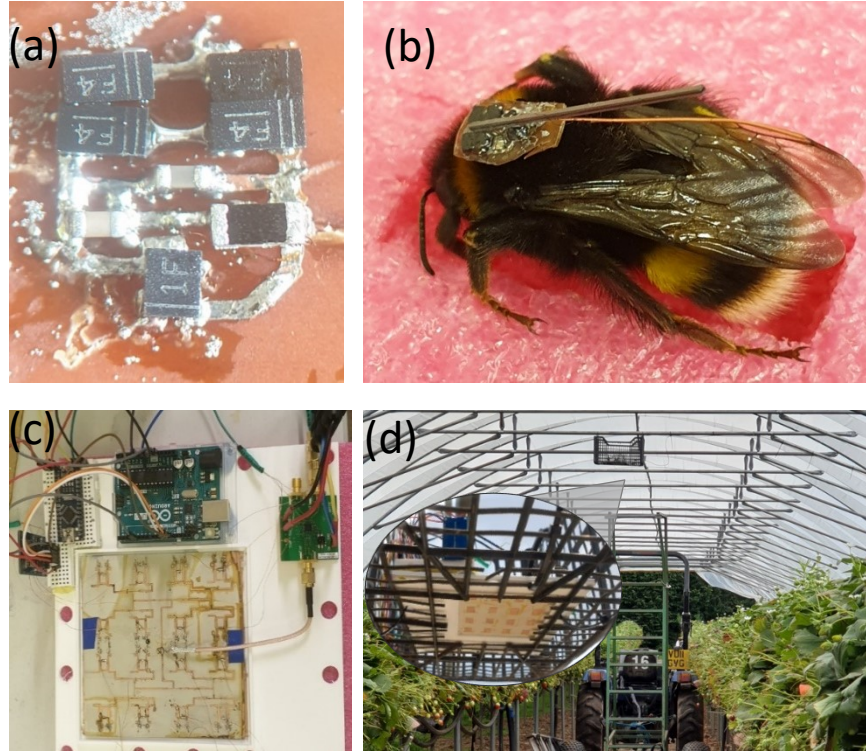
Figure 1.6: (a) Magnified image of the transmitter's circuitry, showing both the rectifier circuit and the pulsing circuit. (b) Bumblebee during tag attachment while positioned gently in a sponge. (c) Stationary monitoring system with Arduino, log detector, SD card adapter, STM32F407VGTx microcontroller and phased array antenna. (d) Deployed monitoring system in a polytunnel. Inset of (d) shows a close up view of the stationary monitoring system showing the 4×4 patch array of the phased antenna. Photos: Nawaf Aldabashi.

At the heart of the system was the microcontroller, which computed the angle of arrival. The transmitter had two versions, a flexible substrate-based transmitter with a total weight of 30 mg, and an older version built on non-flexible substrate, weighing 80 mg. The transmitter was able to harvest energy from the bee's flight during vibration, through a piezoelectric beam, which generated a pulse of 1.5 V per second and transmitted the signal via a monopole antenna.

The receiver system was mounted on a DJI M200 drone and was able to operate automatically at a distance of 20 metres. The tracking system also supported stationary use, where it monitored tagged bees around their hive. This is shown in Figure 1.6(d), as the system was placed in a polytunnel. Field results demonstrated the device's capability to autonomously track a 5.8 GHz VCO transmitting a continuous signal up to a distance of 50 metres. The system provided a valuable proof of concept indicating the possibility to a) achieve lighter weight tags by the elimination of the battery, b) significant tag cost reductions and c) demonstrating autonomous tracking of insects, whilst eliminating the need of triangulation methods.

1.6 Harmonic Radar

The idea of a harmonic radar came from the intentions of removing clutter observed in a traditional radar. The transponder would detect the radar's transmission and respond by sending a different frequency. To achieve this, the signal received by the tag is fed into a non-linear element (e.g. Schottky diode), which allows the re-radiation of the harmonics of the resonant frequency [92], [93]. Hence, the naming convention of harmonic radar.

In return, the harmonic radar receiver is tuned to receive the different returning (harmonic) frequency. The transponder is incorporated into a tag which is then attached to the insect, which causes the signal reflected from the insect to stand out from the surrounding static objects (clutter) [94]. Since the tag requires no battery, significant miniaturisation is possible [95].

In 2016, Woodgate *et al.*, used a harmonic radar to study 4 bumblebee workers' natural foraging behaviour, recording every flight made during their entire life cycle [96]. The study identified two different flight methods, exploration and exploitation, looked into the difference of the flights, their occurrences and how it changed throughout the bee's lifecycle. The bumblebees were tracked using 32 mm wavelength harmonic radar, shown in Figure 1.7(a), which rotates every 3 seconds. The bees were tagged on their thorax with a transponder which consisted of a 16 mm vertical dipole (weighing 15 mg), which would return the original radar's transmitted signal at double the frequency and half the original wavelength. The harmonic tag is shown in Figure 1.7(b). The harmonic radar was equipped with a parabolic dish, for receiving only the returning signal from the transponder. As long as the bee remained in the radar's approximate 800 metres line of sight (LoS), the radar provided the azimuth and elevation coordinates of the bee's direction and distance at an interval of 3 seconds. The coordinates were converted to GPS coordinates via MATLAB [96]. It was mentioned that bees on the ground or flying at a low altitude (<2.5 meter), were seldom detected by the harmonic radar as it would not be within the radar's LoS. The study showed that exploitation flights do not only occur at early stages of the bee's life, but can occur throughout the bee's life. The study further showed that bees demonstrated variation in exploring their environment, their rate of exploration and exploitation, durations of foraging and their foraging frequency [96].
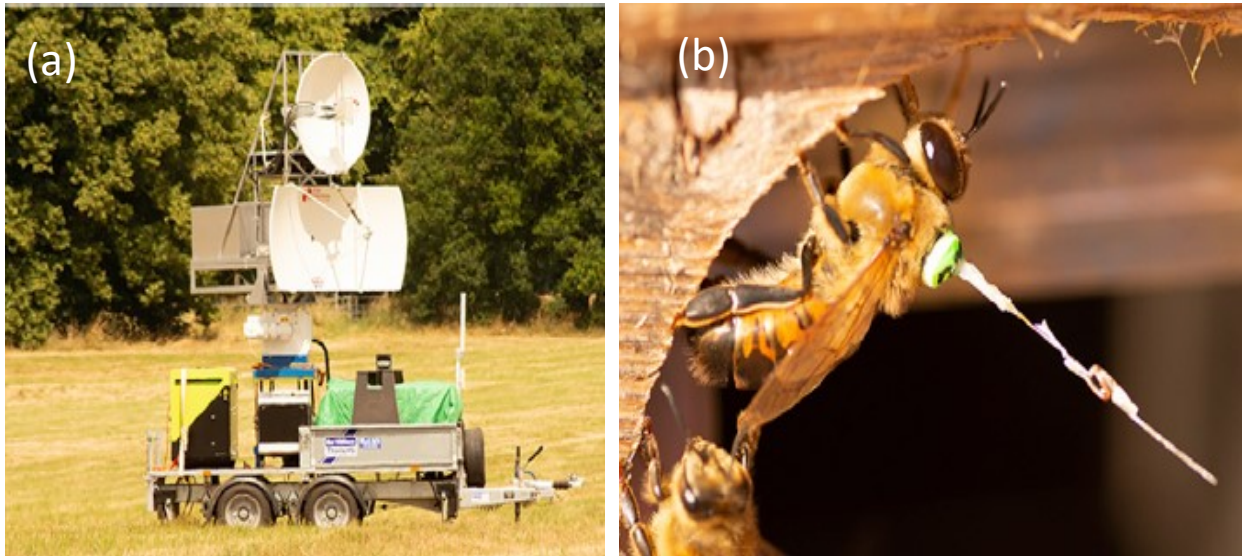
Figure 1.7: (a) 9.3 GHz harmonic radar used in Rothamsted (b) Honeybee with attached harmonic tag [97].

Woodgate *et. al.*, continued to use the harmonic radar for further studies in ecology, where one of the latest studies was related to honeybees and their mating congregation areas [97]. The study revealed a switch between straight periods of flight to an often-repeating looping pattern. This indicated a collective honeybee behaviour. Honeybees were tracked from three hives, where 648 flight segments were recorded over a period of two years in Rothamsted. The harmonic radar used for the study was similar to the abovementioned study and is shown below in Figure 1.7(a). Harmonic radars are either stationary, allowing no mobility or handheld systems allowing mobility. Stationary harmonic radars, provide high power output of tens of kilowatts [93], [96]–[99].

Conversely handheld harmonic radars provide more flexibility, but at a shorter range and a lower transmitted power. The limitation of a stationary harmonic radar is that the system is only capable of being used on flat terrain, while the target remains in the radar's beamwidth [100]. A harmonic radar needs consistent LoS between the antennas and the tagged target, which explains why the aforementioned studies were unable to detect bees flying below 2.5 meters [93], [96]–[99]. The technological expertise required to design, build and maintain a harmonic radar are challenging, in addition to their high costs [94]. A passive harmonic radar tag does not allow identification of different targets. It supports multiple targets, but does not support individual target identification, as opposed to active tags, which have a unique signal [94]. Finally, the tracking range of stationary harmonic radars is limited to less than 1 km [101].

1.7 Tag impacts on insects and the environment

It is important to consider the impact of tags on the insect, the wildlife and the environment. Insect tagging guidelines exist that ensure the tag's weight does not exceed the maximum nectar and pollen load of the tagged insect, which for a bumblebees should be <12% of its body weight [82]. Bumblebees are known to be able to withstand heavy nectar and pollen loads that may reach 100% of their body mass, yet it was pointed out that this is likely to affect their natural energy consumption [102].

Tag weight variations were also reported to cause beyond-natural energy consumption and significant physical hindrance, in addition to affecting the insect's metabolism [71], [82]. In another example of insect metabolism loss, a Scarabid beetle (*Osmoderma eremita*) was tagged and monitoring to quantify its body mass variations from the insect's tagging until its death. The insect was found to have lost 13% of its body mass, which was believed to be correlated to the increased energy consumption inflicted by the additional weight of the tag [103]. Hence, there has been growing concern that tagging insects may affect behaviour negatively, even when stricter 5% guidelines are used [104]. As for honeybees, adopted guidelines for tagging are that the tag's weight does not exceed the maximum nectar and pollen load, which typically accounts for 35% and 20% of the body's weight respectively, but can reach a maximum of 80% [105][105]. Hence, placing tags that weigh as low as 30% of their body weight can impact their behaviour. In addition to the tag's weight, other parameters such as its balance, size, drag and even the glue used for attachment may affect an insects' take-off ability and overall behaviour [82], [106].

In a systematic review, 94 species were studied in a total of 173 reviewed tag-related publications [107]. A total of 69 papers (39.9%) did not mention any possible impacts of the tags, where 84 papers (48%) only mentioned the qualitative impact on the results, which were in the lines of the tag not hindering normal behaviour. Another tag related drawback, is the potential loss of the tag and its impact on both the environment and wildlife. Wikelski *et al.,* mentioned how 5 tagged orchid bees lost their transmitter, and later 3 dead bees were found on the ground and one in a spider hole, which shows how lost tags can have a risk on other wildlife. Since insects are a valuable food source for various animals, the tags could be consumed by larger insect-preying animals which may impose adverse effects on the animal [84].

Another study mentioned that tagged bees displayed longer rest periods of up to 45 minutes, indicating increased energy use due to the additional tag's weight and further found a lower flower visitation rest. This impacts the natural behaviour of the insect, and allows them to be an easy target for insect-eating animals, which was the case with the tagged bee in the spider hole [82],[84]. An example of bumblebees losing their tags can be seen in Figure 1.8(a), where a bumblebee managed to remove its tag, while still kept in a container prior to field experiments and the other bee (Figure 1.8(b)) was found post experiments crawling with no sight of the attached tag.

The hairiness (pilosity) on a pollinator is an important trait, associated with their pollination effectiveness [108]. It establishes an insulation layer that mitigates the loss of heat, thus playing an important role in thermoregulation and the mortality of the insect [109]. It was evident from field experiments, that bees did not hesitate to inflict self-harm to remove the attached tags, which causes them to lose important sensing, pollinating and thermoregulating capabilities.

Throughout the review conducted by Batsleer *et al.,* only 21 papers (12.1%) discussed the impact on the tagged insect's movement, survival and primary behaviour [107]. Additionally, 108 papers (62.4% of the total papers investigated) did not mention whether the used tags were recovered, which insinuates the question of whether these were left out in the wild [107]. The paper illustrated a histogram showing the mass to body ratio for RFID, harmonic radar and radio telemetry in Figure 1.9.
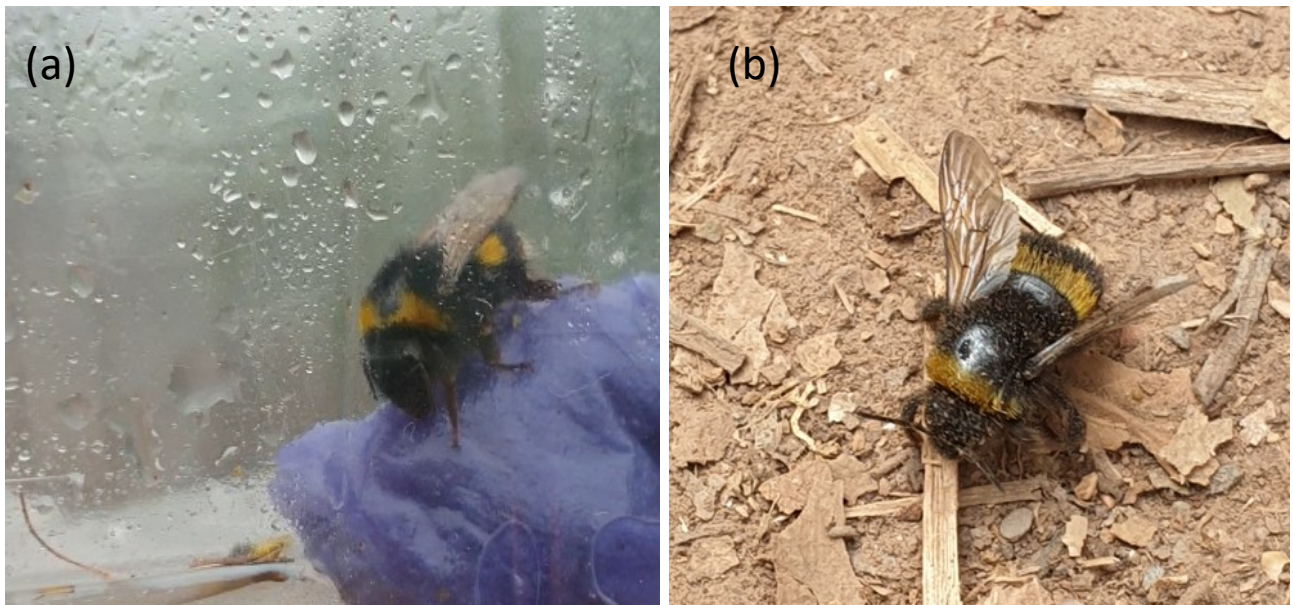
Figure 1.8: (a) A contained bumblebee that forced the piezoelectric tag off its body, exposing a patch without hair pre-field experiments (b) Another post-experiment bumblebee found crawling without a tag, with no sign of the tag. Photos: Nawaf Aldabashi.
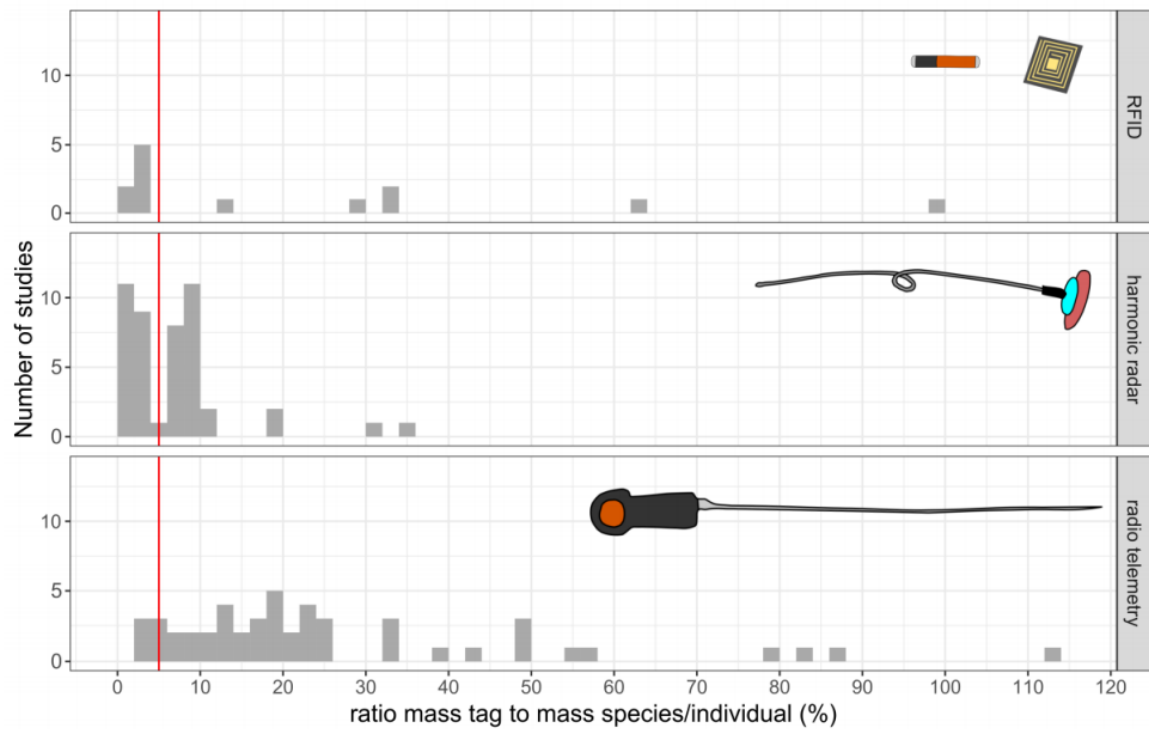
Figure 1.9: Ratio mass to body mass histogram for RFID, harmonic radar and radio telemetry, indicating the 5% threshold (red line) [107].

The review finally concluded that only 40% of the papers provided bare minimal justification on their chosen tagging and tracking method or fully ignored the tag's potential side effects [107].

When studying potential impacts of tagging approaches, it is important to understand that even simpler Capture-Mark-Recapture techniques utilising simple paint marks to identify individuals, also reported to influence changes in foraging behaviour, aggression and grooming [107]. This suggests that the application of more visible identification/tracking methods could influence similar or even worse behaviour. Thus, urging the need for a tag-free approach.

1.8 Entomological Radar

Radar technology is significantly used in studies that involve the monitoring and observation of a wide range of animals. Radar allowed researchers to study speed, wingbeats frequency, migration altitudes of birds, bats and insects [110]. The idea of using this technology to study animal migration came to existence after identifying phantom signals on screens during the second world war as migrating birds [111].

Radar biology summarises different radar-based animal monitoring disciplines, such as radar ornithology which is used to monitor the flight and migration of birds. Radar

entomology is the utilisation of radar technology to study insects, their behaviour and their movement [112]. There have been various developments towards entomological radar that provided means of recording various information about insects.

Throughout the development of this technology and as higher frequency microwave wavelengths were utilised in the late 1940s and 1950s, insect echo observations were noticed as warm-weather echoes [112]. Radar meteorologists were puzzled when observing such echoes with no clouds in the perimeter [112]. The earliest reliable insect echoes were reported in 1949, which demonstrated the potential of using this technology for insect scanning [113]. This was followed by Rainey's radar detection of a locusts swam in 1954 [114]. Rainey' hypothesis was that raindrops did not exceed 6 mm in diameter, and that rarely 10 of such drops would be present per cubic meter during the heaviest recorded rainfall [114]. Rainey took into account that most of the locust's weight was water, and when considering this fact alone, a swarm of 10 flying locusts would expect to deliver an echo at least 1 order of magnitude greater than heavy precipitation. Their first locust radar sighting was recorded in 1954 in between Bushire and Kuwait using a naval radar 2 hours past sunset [114]. This early finding was interesting as it demonstrated flight after dark by insects known for their day travelling behaviour, which emphasises the advantage of a radar system for monitoring purposes as it can provide monitoring even when no visuals can be obtained.

1.8.1 Doppler radar

The Doppler shift is a phenomenon that allows the extraction of the target's speed, and as a result, Doppler radars have been used to monitor insects without the need of a tag. These devices send a high frequency signal and receive the echo that is reflected back from the moving target. The echo is analysed against the original signal that was sent out, which then allows the extraction of the target's speed based on the indicated Doppler shift.

The ability to measure vibration is a useful trait when inspecting in-hive behaviour. Since sound is energy that is generated through vibrations caused by moving particles [115], sound is also a form of vibration. The frequency of sound is given by the number of vibrations (cycles) per second, which causes the pitch of the sound to increase (higher frequency) or decrease (lower frequency) [115]. This can be measured using a microphone, but since sound is a collection of vibrations (rapid movements) a radar could detect these movements as well.

A study by H. Aumann demonstrated the use of a 5.8 GHz radar to measure vibrational amplitude, where the output was recorded as audio files allowing data collection and processing techniques to be applied [116]. Their device demonstrated a suitable frequency response below 500 Hz, deeming it fit to be applied as a microphone to record in-hive vibrational metrics. Both the radar and a microphone were used to record bee signals at a distance of 15 cm as shown in Figure 1.10(a).

It is important to note that during the experiment, a 7 mm thick plywood panel was removed to allow the signals to be picked up, which normally would remain present. The device was able to measure sounds produced by a queen bee, and it was interesting to observe that the hive had two queen bees, which if not controlled could reduce the survivability rate of the hive. This is evident in Figure 1.10(d), which shows the two signals obtained from queen honeybees. Figure 1.10 also illustrates a visual comparison between the radar acting as a microphone and an acoustic microphone in (b) and (c) respectively. The radar microphone was considered to outperform the acoustic microphone as the acoustic microphone seemed to observe the harmonic frequencies as the fundamental frequencies, whereas the radar microphone distinguished the fundamental frequency from the harmonic frequencies clearly.
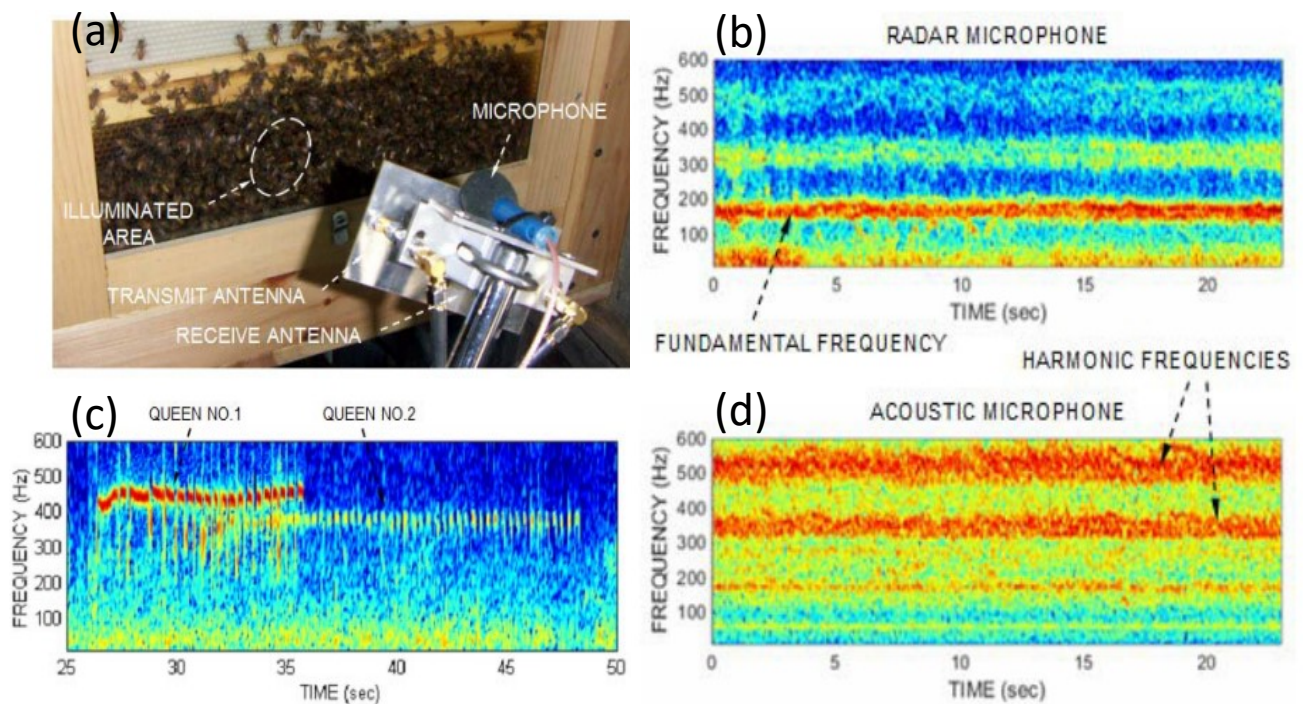
Figure 1.10: (a) Radar microphone at a 15 cm distance from the hive (b) Radar microphone readings (c) Acoustic microphone readings (d) Two queens tooting and quacking [116].

Although the use of a radar to record internal vibrations is interesting, it is important to point out that the necessity of the panel removal and the 15 cm recording distance, indicated a lack of sensitivity and usability of the device. Radars have been employed from frequency ranges of 5.8 GHz to 24 GHz for tag-less monitoring of honeybees [117]–[120]. Incoming and outgoing bees at the hive entrance generate a Doppler shift whose magnitude and duration can be correlated to insect motion and activity. The setup of such Doppler radars, shown in Figure 1.11, is usually placed at the entrance of the hive, facing outwards or at a distance from the hive facing inwards, which allows the radar waves to intercept incoming and outgoing bees.
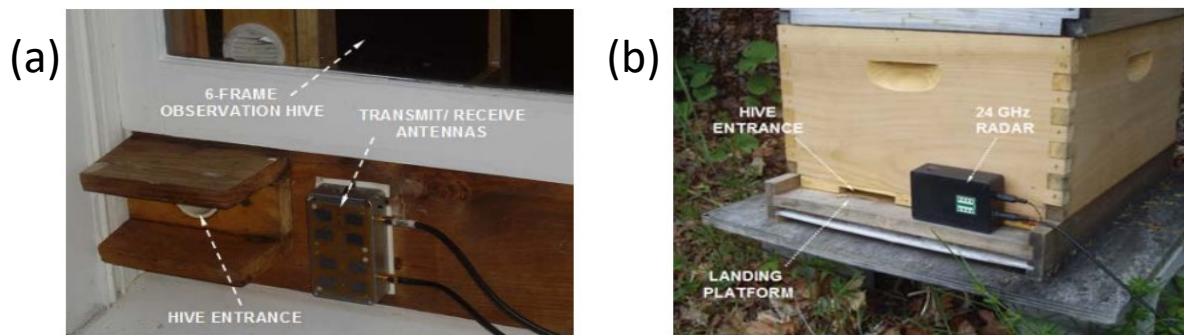
Figure 1. 11: (a) 5.8 GHz radar setup at the hive's entrance (b) 24 GHz radar at hive's entrance [117], [120].

The results obtained can be interpreted to extract useful metrics. An example of such results is shown in Figure 1.12, which shows incoming and outgoing honeybees. The bees' results shown here, portray the non-invasiveness of the radar approach. There are several advantages of using radars for insect monitoring. Since there is no evidence in literature suggesting insects' ability to perceive radar waves — although investigating their perception of radar waves would make a compelling study — it is safe to say that insects have no perception of radar waves. Additionally, radars provide the benefit of diurnal and nocturnal monitoring. Moreover, radars can also identify wingbeat signatures and abdominal pumping associated with respiration, where the breathing was observed in the 1-2.5 Hz power spectra by Schaefer [121], [122]. Furthermore, radar observations provide tag-less monitoring of insects, which prevents restricting the insect's movement and maintains the insect's natural behaviour.
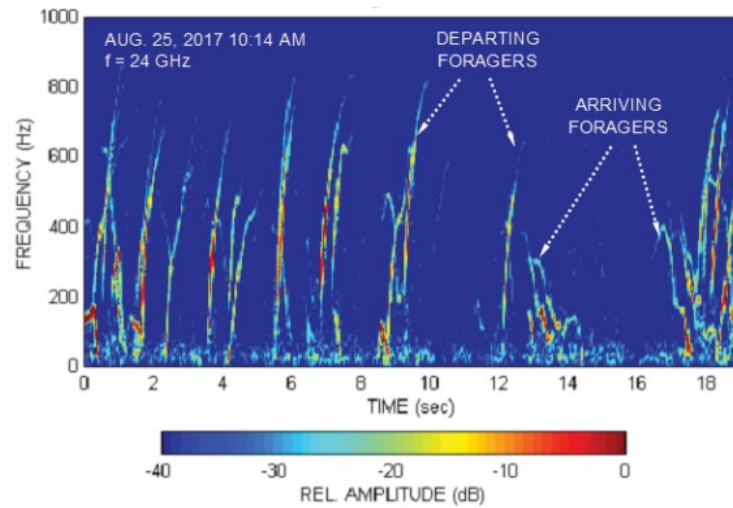
Figure 1.12: Doppler time intensity of departing and arriving honeybees [120].

The removal of tags provides benefits to the insect itself and its surroundings. Additionally, radars are able to measure multiple signals including the required target, while allowing the extraction of useful metrics such as the speed of the target. Such signals could include other insects or surrounding movement including vibration, which can be vital to a hive's overall wellbeing.

Honeybees communicate using vibration [123], [124], commonly referred to as 'tooting,' 'quacking' and 'whooping' are among such known communication terms [125], [126]. Among the many different vibrational signals bees use to communicate, a simple signal that lasts for a couple of seconds is to hold on to the recipient with the front limbs while vibrating the body, known as the dorso-ventral abdominal vibration (DVAV) [127]. This rapid movement, ranging from 10 to 22 Hz signals "prepare for greater activity" [127]. Yet again, such vibrations can theoretically be measured using a radar.

This was attempted by H. Aumann *et.al.,* using their device named Janus, shown in Figure 1.13(b). The Janus combined a 24 GHz commercial radar enclosed with a piezoelectric transducer that monitored bee flying activity whilst measuring incidental vibrations emitted by the bees inside the hive [128]. Upon investigating the signals the authors found a high correlation between radar signatures and vibrational measurements during two unusual and unwanted hive related events known as robbing and swarming [128], [129]. Swarming is a honeybee's natural reproduction where a bee colony splits into two or more separate colonies [130], [131]. The measurements recorded by the Janus sensor were then sent via a wireless link to a laptop for processing. To achieve this, the Janus sensor was connected to a remote bee activity sensor.

Figure 1.13: (a) Janus sensor showing the RF side and the piezoelectric side (b) The commercial components used which include the 24 GHz radar [128].
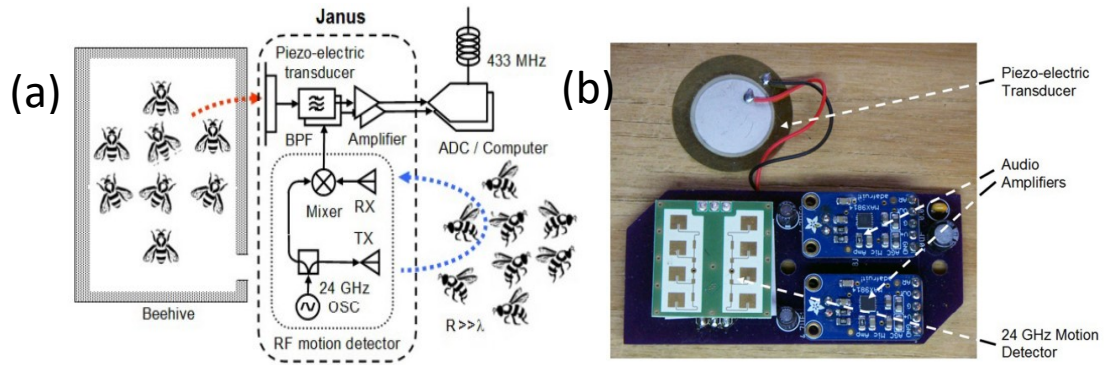
The sensor connected to a Janus sensor was equipped with a 433 MHz transmitter, a solar flux sensor, microprocessor, a timer, and a 5 V booster regulator which allows wireless data transmission and the measurement of environmental metrics around the hive. The device provided daily measurements for three beehives from July 2020 to October 2020. The study showed swarming and robbing events (Figure 1.14(c) and (d)). Despite the results indicating a high correlation between vibration and radar measurements, it is important to point out that the radar measurements shown in Figure 1.14(e) provide a real signal only which makes discriminations between incoming and outgoing bees very difficult when bee activity is high.

Figure 1.14: (a) hive with the Janus sensor (b) Janus sensor (c) Robbing event (d) Swarming event (e) Bee flights (f) Vibrations recorded [128].
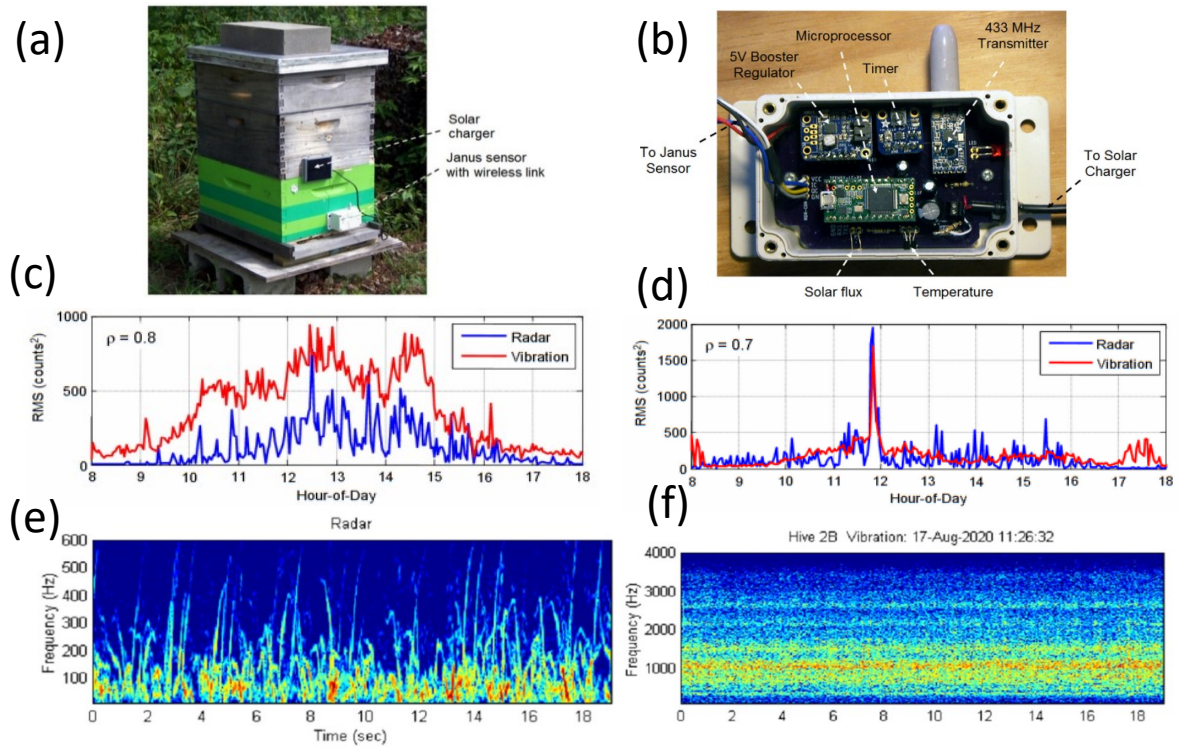
Conversely, radar technology is relatively complex which potentially requires microwave engineering expertise and or costly set-ups. Though the information that can be extracted from the use of a Doppler radar is useful, it lacks cardinal direction, which is difficult to implement and increases the complexity of the radar. Additionally, there are a small number of studies that claim a potential negative impact of exposing insects to high frequency radiation (6 GHz and above).

For instance Thielens *et al.,* mentioned an increase in RF absorption $\geq$ 6 GHz upon simulating the impact on realistic insect models obtained from real Micro-CT imaged insects [132]. Whilst literature that reviewed the studies investigating the impact of high frequency on insects indicated a minor to no effects on bee behaviour, many of the studies suffered from a lack of statistical measurements [133].

1.9 Alternative methods

There are other methods that are worthy of consideration, such as acoustic tracking, theoretical models, light detection and ranging, homing experiments and microsatellite approaches. Radioactive isotope paint was used in 1979 by Baars *et al.*, to track beetles by painting them with radioactive material [134]. The radioactive paint emitted considerable amounts of gamma rays that were detectable using scintillation detection at several metre distance. A significant issue was that though insects are less sensitive to radiation compared to vertebrates, the insects died within weeks due to radiation [134].

Another approach is precision apicultural, where such systems have demonstrated their potential and have become a widespread solution to monitoring and managing various hives [135], [136]. Precision apiculture applications vary based on the different data collection method used, which can be either a singular or a multitude of individual bee data, entire colony's data and regional data. Individual bee data comprises individual bee behaviour, such as the bee's entrance and departure from the hives. Entire colony data, involves various intra-hive data such as humidity, gas level, weight, vibration, sound and temperature [135]–[137].

Another approach is recording insect sounds utilising micro-electro-mechanical systems (MEMS) and processing the recorded sound using signal processing methods. Such methods have been put into place to track bumblebees arriving and departing from their hives with high accuracy. Additionally hive-related acoustics can indicate important

events as pointed our earlier such as swarming and robbing events [128], [129], which can be detected using low cost microphones. The following acoustic approach was able to distinguish between departing and arriving bumblebees with a 96.2% achieved accuracy in classifying the events. Samples of the recorded waveforms are shown in Figure 1.15, along with their envelopes [138]. The microphones placement, though mentioned to have minimal disturbance, required a hole to be drilled in the hive, with the microphone placed through the hole at a distance of 8 cm from the entrance. The samples show a broad waveform in Figure 1.15(a), which represents an arriving bumblebee. This is due to the bumblebee decelerating as it approaches the hive to land. Figure 1.15(b) displays the respective arrival envelope of the bumblebee. Whereas Figure 1.15(c) shows a short pulse, which indicates a departing bumblebee. The envelop of Figure 1.15(c) is shown in Figure 1.15(d), which shows a short peak in the signal. The difference observed in these two types of signals is of capital importance to chapter 3 and chapter 4.

Other methods have demonstrated monitoring capabilities as well, such as LIDAR. This method has been implemented to monitor the movement of honeybees at a distance of 90 metres [139]. Though this method demonstrated a high range monitoring capability, it is not able to identify multiple targets, which is a major disadvantage. The use of microsatellites was also explored for the quantification of foraging activity in terms of foraging range and forager nest density , while deploying small coloured opalith tags for insect identification[140]. This method enabled visual insect monitoring and tracking within the foraging site, but is known to be time consuming and difficult. Hence, it is not the ideal method to provide entomologist for on the spot insect monitoring [141].
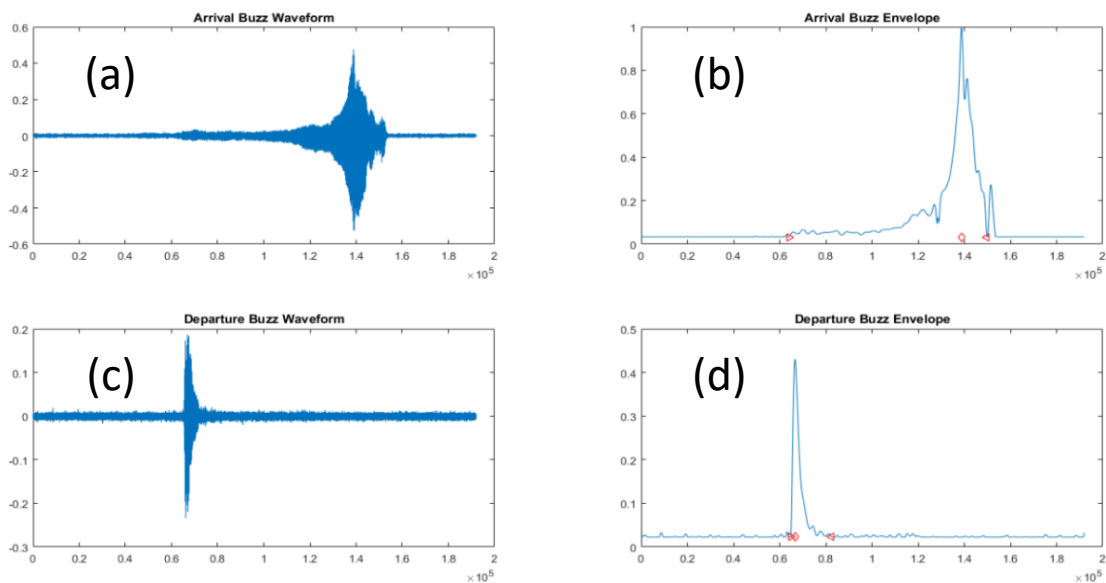
Figure 1.15: (a) Sound recording of an arriving bumblebee (b) Arrival buzz envelop (c) Sound recording of a departing bumblebee (d) Departure buzz envelope [138].

Maximum foraging range algorithms have also been widely implemented to obtain maximum foraging range approximations through the correlation of insect body size and flight range [142]. Another way of implementing a similar theoretical model is by considering the insect's energy budget to analyse the optimal foraging theory in order to estimate the maximum range of foraging [143]. Moreover, additional maximum foraging range is also approximated utilising homing experiments. These kind of studies have been implemented on a wide range of insects that are capable of returning with resources to their nest, such as bumblebees, honeybees and solitary bees [144]. These insects' ability to return home was investigated by exposing the insects to unknown environments, whilst conducting visual observations on their returning abilities [144].

1.10 Aims and objectives

The project aimed to design a non-contact monitoring device for insects. This was based on the design and development of a 5.8 GHz Continuous Wave (CW) radar utilising the 5.8 GHz for autonomous insect monitoring and the study of potential range increase through the use of Silver nanoparticles. The project's objectives are listed below.

- Feasibility investigation of a radar system design for targets as small as insects, to obtain a clear signal, whilst maintaining a convenient monitoring range.
- Build a suitable radar system able to monitor insects.
- Ensure the radar is portable and provides on the spot monitoring.
- Investigate the feasibility of nanoparticle coating to increase target detection range.
- Demonstrate the capabilities of the radar-based insect monitoring system by monitoring beehives and analysing the extracted data.
- Investigate the suitability of the radar data for machine learning applications.
  - o The binary classification of incoming and outgoing honeybees from a hive.
  - o The ternary classification of incoming, outgoing and hovering honeybees.

1.11 Main contributions

- Feasibility study of a radar system design for insect detection and monitoring.
- Simulated various radar cross sections of targets including metal calibration spheres and a honeybee.
- Honeybee radar cross section extraction which was in close approximation to simulated values.

- Maintained the design constraints that allowed a suitable monitoring range, whilst developing a portable proof of concept radar solution.

- Developed three main versions of the radar system: prototype radar (v1), PCB CW radar (v2) and PCB in-phase quadrature radar (v3), which demonstrated effective insect monitoring and the radar's size was continuously decreased while various performance metrics were enhanced.

- Studied the feasibility of nanoparticle coating to increase target detection range and quantified its impact.

- Studied various insect wing beats in a simulation setting and experimentally using the designed radar system, where different insects were used for wing beat measurements

- Demonstrated the suitability of machine learning for radar applications.

- Expanded upon the usability of the radar by demonstrating its feasibility for medical applications.

1.12 Applications

Designing and developing a radar system sensitive enough to monitor flying bees, has countless potential applications, from an ecological, agricultural and commercial standpoint. Several applications are listed below.

- Tag-less monitoring to extract valuable metrics based on their natural behaviour.

- Monitor in-hive metrics (vibration) to evaluate internal activity of the hive as early indicators of swarming and robbing events

- Autonomous beehive activity logging, which can be extended to also support specific flower/fruit patches activity logging, individual polytunnel entrances activity logging

- Monitoring fruit strains to identify strains that encourage/discourage bee activity

- Pesticide-inflicted behaviour assessment via radar monitoring

- Monitoring insect wing beat frequency using the radar to alarm the hive owner of a potential threat (e.g., Asian hornet).

- Machine learning assisted prediction of a robbing or swarming event

- Machine learning assisted hive performance prediction

- Machine learning assisted polytunnel performance prediction

- Machine learning assisted flower/fruit patches performance prediction.

- Biomedical applications to monitor a patient's heart rate, respiration, and cough.

- Full medical/elderly patient non-invasive health monitoring

  o The combination of several applications provides a full medical/elderly patient monitoring solution that inspects breathing, heartbeat, sleep apnea/disorders, motion and detect falls within the patient's room.

1.13 Thesis layout

Chapter two introduces the concept of radar cross section (RCS) and demonstrates multiple RCS simulations on different targets. The chapter further discusses insects as radar targets, while presenting RCS simulations to aid in the theoretical estimation of honeybee RCS. This chapter performs a preliminary study on coating bees by answering questions related to the possibility of coating, coating location, coating thickness and potential impact of coating.

Chapter three reports on the design, simulation, assembly and initial testing of a 5.8 GHz radar. Three different radar designs are presented, starting with the prototype radar (v1), the PCB radar (v2) and finally concluding with a plug-and-play in-phase quadrature radar (v3).

A calibration method is also introduced in chapter three, which uses 4 mm steel spheres that were simulated in chapter two to extract the RCS of free flying honeybees. This chapter concludes with studying coated and non-coated wooden sphere in a pendulum setting to study its impact on the RCS and how coating could impact the RCS of a honeybee.

Chapter four demonstrates the correlation of bee signals and simulated signals using pendulum motion and controlled sphere motion simulations with respect to the radar. The simulation outputs are compared to different honeybee signals obtained from field experiments. Furthermore, the radar readouts' suitability for machine learning is demonstrated in chapter four, showing a Binary (two-class: incoming bees and outgoing bees) prediction and a Ternary (three-class: incoming, outgoing and hovering) prediction performed by the research group.

Finally, a honeybee based micro-Doppler simulation is presented, while showing experimental micro-Doppler signatures of honeybees and bumblebees. This chapter concludes with a demonstration of using the radar for biomedical purposes such as vital sign detection.

Chapter five concludes the study, outlining the key findings, the future work that can be implemented and presents several key applications that can be employed to further expand on the current study.

Chapter 2.   Insect Radar Cross Section Study

This chapter discusses the theory behind the insect radar cross section (RCS) at the radar's frequency of operation (5.8 GHz), which is essential for the radar's design and development. The theory involved, the literature supporting the computational simulations, the electromagnetic simulations (EM) performed and the results regarding the RCS are discussed herein.

2.1 The IEEE definition of the RCS

The RCS of the target, denoted as σ, is a measurement that defines how effective a target reflects or absorbs an incoming signal. It is a measurement of the power scattered when a target intercepts an incident wave [145]. The RCS is independent of distance as it is normalised to the power density of the incident wave [145]. It is used to define the target characteristics and not the effect of the receiver sensitivity and distance, transmitter's power nor the position of the transmitter [145].

A target's RCS is measured in m^2 or dBsm (decibel over a square metre). Backscattering is the term used for reflections that occur at 180° of the initial direction of the signal, which is the case for monostatic radars. The RCS is commonly mistaken for the size of the object, whereas in reality it is a collective parameter, taking into account different characteristics of the target. It can be perceived as the fraction of the intercepted power that the target object scatters back according to the target's characteristics [119]. Consider the radar's radiated power P.

$$P = \sigma W_i = \frac{Y_0 |E_i|^2}{2}$$

2.1

Where Y_0 is the admittance of free space (0.00265 S) and E_i is the strength of the incident electric field. An assumption is made that the scatterer exposed to the wave behaves similar to an antenna, as it extracts power of an effective area σ. Hence the extracted power is calculated as the product of the power density W_i and the captured area σ. It is assumed that the target scatters/radiates the captured power in all directions uniformly as an isotropic antenna [145]. If the radar's radiated power is P, the scattered power density W_S (watts per unit area) is equal to the transmitter power divided by the surface ($4\pi R^2$) area of an imaginary sphere with a radius R [146]. However, if the target is small in comparison with the distance R where the scattering takes place, then the

power density of the scattered power will decrease with R according to the following equation:

$$W_S = \frac{P}{4\pi R^2} = \frac{\sigma Y_0 |E_i|^2}{8\pi R^2} \qquad 2.2$$

The scattered power density can be expressed in terms of scattered electric field strength,

$$W_S = \frac{E_s H_s}{2} = \frac{Y_0 |E_s|^2}{2} \qquad 2.3$$

When using equation 2.2 and 2.3 to solve for the area σ,

$$\sigma = 4\pi R^2 \frac{|E_s|^2}{|E_i|^2} = 4\pi R^2 \frac{|H_s|^2}{|H_i|^2} \qquad 2.4$$

The capture area or σ is known as the RCS, where the first expression in equation 2.4 can be equally replaced with the second expression that relies on the scattering H_s and incident magnetic field H_i [145]. Using equation 2.4, the RCS can be measured when the distance R, the strength of the incident electric field (or power density) and the strength of scattered electric field (or power density) are known [145]. This leads to three main cases of scattering: backscatter (monostatic radars), bistatic scattering (bistatic radars) and forward scattering [145], as shown in Figure 2.1. The RCS definition was standardised to eliminate the undesirable influence of the RCS measurement being a function of the environment. Hence, the definition of the RCS was standardised to the formal definition of the RCS (also known as the IEEE definition of the RCS) by forcing the distance R to approach infinity [145], [146]:

$$\sigma = \lim_{R \to \infty} 4\pi R^2 \frac{|E_s|^2}{|E_i|^2} \qquad 2.5$$

The RCS is a function of the following [145]:

- Target material
- Target geometry
- Position of both the transmitter and receiver relative to the target
- Target's angular orientation
- Wavelength of the radar
- Transmitter polarisation
- Receiver polarisation
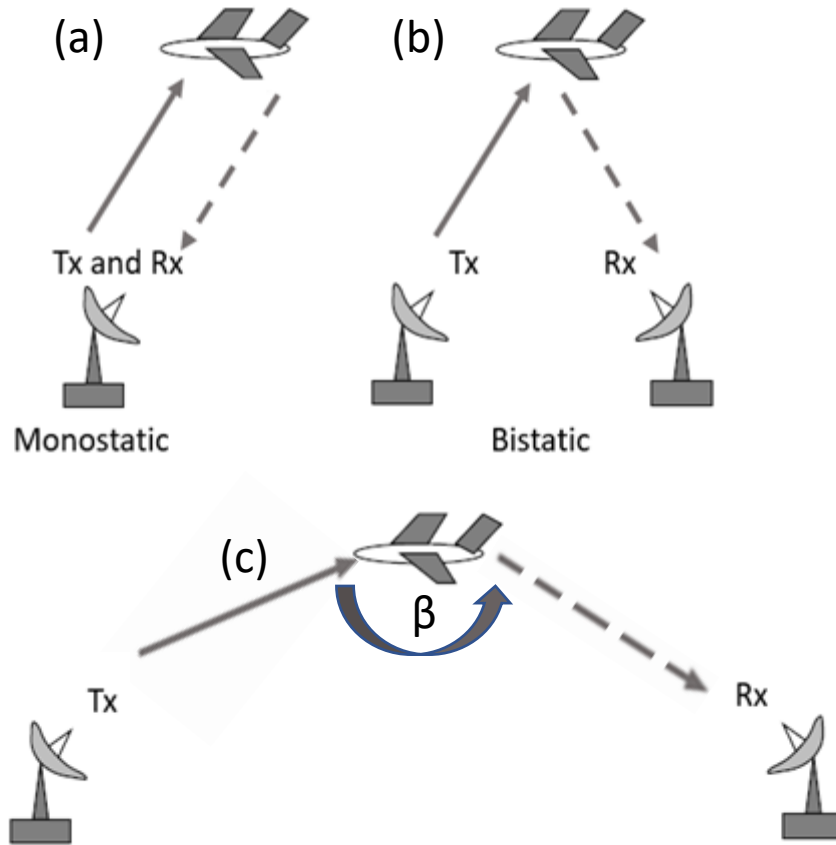
Figure 2.1: Illustration of a radar setup observing a target. (a) Monostatic radar setup (b) Bistatic radar setup (c) Forward scattering [147].

Note equation 2.5 indicates that RCS is dependent on distance R, although theoretically it is known to be independent of distance. In practice, changes in distance result in attenuation of the scattered EM wave's power as it propagates through space. Hence, the distance/range is taken into account to compensate for the scattered EM wave's power decrease/attenuation.

2.2 Insects as radar targets

Insects appearing in common radar sightings intended for weather or military applications are considered a nuisance. During the early 1960s, radar sightings contained multiple dots of unknown origin, which were named as "angels" or "ghosts" [146]. Further studies carried out demonstrated that the RCS of measured insects in the lower atmosphere was very likely the source of the unknown reflectors (angels) [118].

Since water behaves almost as metal as a reflector of radio waves and insects mainly consists of water/liquid, insects are capable of reflecting a radar signal [112], [148]–[150]. However, insects are still considered very small radar targets in comparison

to common targets. This is illustrated in Figure 2.2, which emphasises the low RCS of insects in comparison to other targets.

Radar targets deliver one of three general scattering properties; Rayleigh, Mie or optical scattering properties. This depends if the target's greatest circumference is approximately equal to (Mie/resonance region), or much smaller (Rayleigh) or much larger than the wavelength of the radar (Optical region) [146].
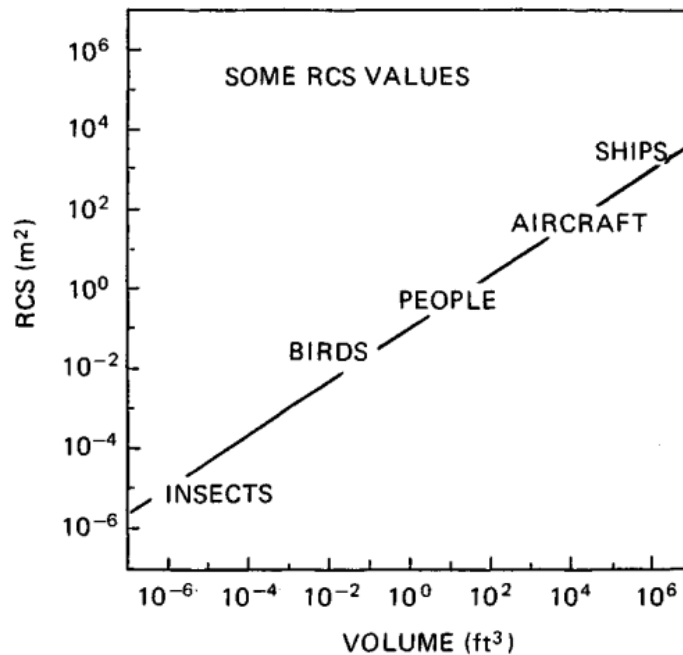
Figure 2.2: RCS summary of common radar targets. The locations of the targets on this graph is a general illustration [151].

2.3 Insect Radar Cross Section

The knowledge of an insect's RCS is a prerequisite to quantitative studies [152], [153]. Various papers have discussed the RCS of insects at a wide range of frequencies such as 9.4 GHz up to 34 GHz, where studies performed RCS experiments with captured insects and others performed free-flying experiments [118]–[120]. The outcomes of these experiments are summarised in Table 2.1 [118], [119].

Smaller insects' RCS and raindrops fall within the Rayleigh region, where the majority of the insects' RCS (weight<200 mg) resides [112], [148], except larger insects (weight>200 mg) such as dragonflies fall within the Mie region [112]. This makes insect detection difficult using a 3 cm wavelength radar for detection [148]. A target resides in the Rayleigh region, when the wavelength is larger compared to the target's dimensions.

Table 2.1: Insect RCS measurements collected from different studies [118]–[120].

Insect	L (mm)	W (mm)	RCS Lateral (cm^2)	RCS Transversal (cm^2)	λ (mm)	Polarisation	Ref.
Range crane fly *Timpula simplex*	13	1	0.30	0.02	31.89	-	[118]
Green bottle fly- *Lucilia caesar*	9	3	0.25	0.10	31.89	-	[118]
Honey bee (worker) *Apis mellifera*	13	6	1	0.30	31.89	-	[118]
Convergent lady beetle *Hippodamia convergens*	5	3	0.02	0.01	31.89	-	[118]
Blue winged locust *Trimeratropic dyanipennis*	20	4	9.60	0.96	31.89	-	[118]
Honey bee (worker) *Apis mellifera*	-	-	0.3	0.0011	37-24	Horizontal	[119]
Honey bee (worker) *Apis mellifera*	-	-	0.98	0.0058	37-24	Horizontal	[119]
Boll weevil *Anthonomus grandis*	-	-	0.0079	0.0010	37-24	Horizontal	[119]
Honey bee (worker) *Apis mellifera*	-	-	0.41	0.062	37-24	Vertical	[119]
Honey bee (worker) *Apis mellifera*	-	-	0.73	0.044	37-24	Vertical	[119]
Boll weevil *Anthonomus grandis*	-	-	0.025	0.0022	37-24	Vertical	[119]
Honey bee (worker) *Apis mellifera (free flying)*	-	-	0.1 (free flying)		12.5	-	[120]

However, in the Rayleigh region, the cross-section is proportional to the fourth power of the radar's wavelength, and is thus determined more by the volume of the target than by the target's shape [145], [154]. Hence, radar echoes of rain drops are commonly described by Rayleigh scattering. A method used to reduce rain clutter in radars is to operate at a lower frequency to significantly reduce rain backscatter. The use of an X band radar (at 9 GHz with λ=33 mm) would experience approximately 34 dB more backscatter caused by precipitation than an L band radar (at 1.3 GHz with λ=230 mm) [154].

Similarly, it can be concluded that when an increased backscatter is required from targets in the Rayleigh region, increasing the frequency will cause an increase in resulting backscatter [145], [154]. Since insects reside in the Rayleigh region, it indicates the increase in the effective size of smaller insects upon decreasing the radar wavelength. In other words, increasing the frequency of the radar (decreasing the wavelength) increases the effective RCS of the insect, making it a clearer radar target [145], [148], [154]. The main interest in this study is the RCS of honeybees and bumblebees. The RCS of a honeybee has been experimentally investigated at different frequency bands such as 9.4 GHz, 8-12 GHz and 24 GHz [118],[15], [120]. The first study conducted by Hajovsky in 1965, investigated the RCS at 9.4 GHz, where a thread was used to suspend the insect and the insect's RCS was then measured [118]. The RCS values reported for honeybees at 9.4 GHz ranged from –40 dBsm to – 45 dBsm.

Another study reported the RCS of multiple insects, including honeybees using horizontal and vertical polarization [119]. This study specifically meant to investigate the impact of the polarization and aspect angle (insect alignment to the impinging wave). These two terms are discussed in further detail in section 2.5.3 and 3.15. The author analysed the two datasets, where the RCS changes due to the changes in the primary axis of the target and the change in RCS due to the rotation of the polarisation plane about the LoS, while the insect was maintained at a fixed aspect angle. It is important to note that the RCS experiments conducted were in anesthetised insects, which meant that the RCS measurements were not affected by the insect's wingbeats and the insects varying positional movement. These two factors can affect the RCS measurements and their collective impact on RCS is known as temporal modulation [119]. Several RCS measurements of insects were mentioned and are included in Table 2.1. Among these RCS measurements were honeybee RCS measurements for two 11 mm sized honeybees, where the observed RCS of 1 honeybee drone is illustrated in Figure 2.3. The RCS results for both honeybees' horizontal front and side view were –69.5 dBsm, –45.2 dBsm for the first honeybee and –62.3 dBsm, –40 dBsm for the second honeybee respectively. Similarly, the RCS results for vertical front view and side view were –69.2 dBsm, –54.9 dBsm for the first honeybee and -53.8 dBsm, –48.2 dBsm for the second honeybee respectively [119].

Interestingly, the authors mentioned how the RCS of an insect can be approximated with the RCS of a water sphere of the same weight. Since water spheres are hard to control, the authors used steel spheres of 3.175 mm and 6.350 mm diameter to calibrate their radar, which provided an RCS of 0.012 and 0.537 cm^2 respectively.
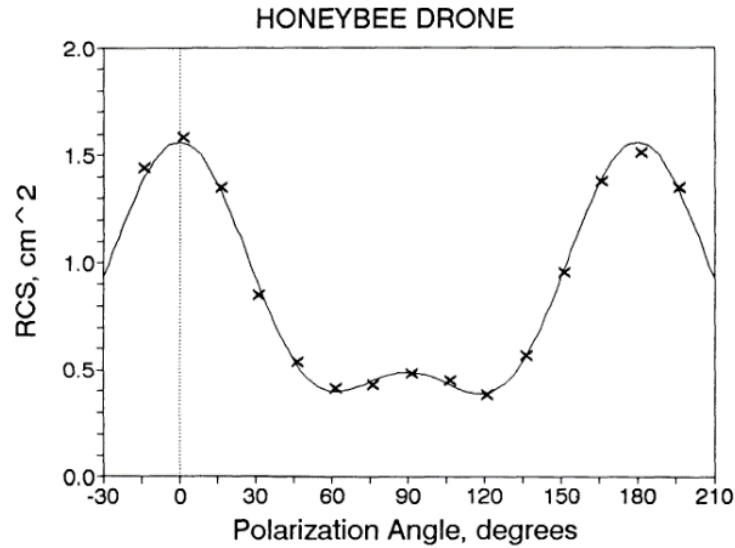
Figure 2.3: RCS of honeybee vs polarization angle, illustrating the RCS change with polarisation [119].

Riley performed X-band radar measurements of insect RCS as a function of insect body axis and the plane of polarisation. Riley demonstrated the change in RCS based on the insect's positioning with respect to the E-vector for anaesthetised insects. The main outcome of the study indicated that the insect's maximum RCS occurs when the insect's body axis is perpendicular to the E-vector. This occurs when the E-vector is at 90° to the insect's body axis, which is illustrated in Figure 2.4 [150].
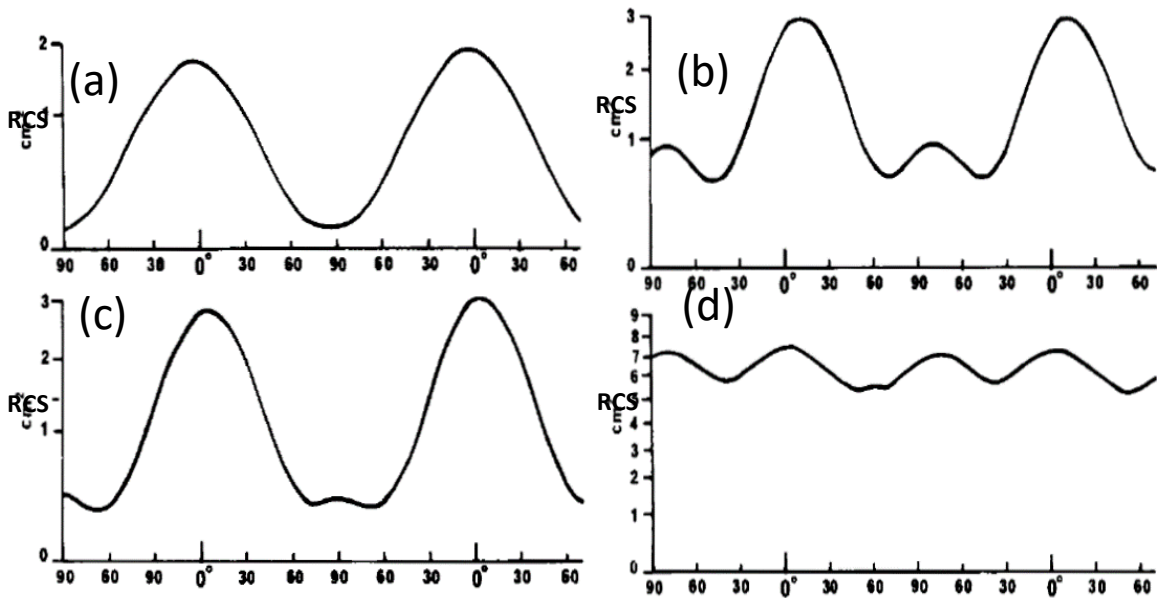
Figure 2.4: RCS variation as a function of insect's body axis and E-vector. The progression from (a) to (d) shows the maxima to correspond to the E-vector being 90° to the insect's body. (a) *Spodoptera littoralis*, (African cotton leafworm) 95 mg (b) *Melanoplus sanguinipes* (Migratory grasshopper) 320 mg, (c) *Spodoptera littoralis* (African cotton leafworm) 220 mg, (d) *Schistocerca gregaria* (Desert locust) 2590 mg [150].

It is important to note that free-flying insects will have a continuously changing position that will cause the RCS to vary as it flies. Riley combined insect RCS measurements from different sources and plotted the RCS of the insects as a function of their mass on a curve of a spherical water droplet obtained from Herman [155] to demonstrate insect RCS's comparability to spherical water droplets of the same mass [150]. This is shown in Figure 2.5, where honeybees are located at a transition region between the Rayleigh and Mie region.

A more recent study, investigated the RCS of free flying honeybees at 24 GHz [120]. The RCS was averaged at –50 dBsm for 11 honeybees [120]. The authors performed an EM simulation of a spherical water droplet at 10.5 GHz and 24 GHz, where the RCS obtained was found to be a few dB lower than that of a steel sphere. The authors concluded that once taking into account the frequency dependence of the dielectric constant of water at 24 GHz, the water droplet and the steel sphere were very close in terms of RCS [120].
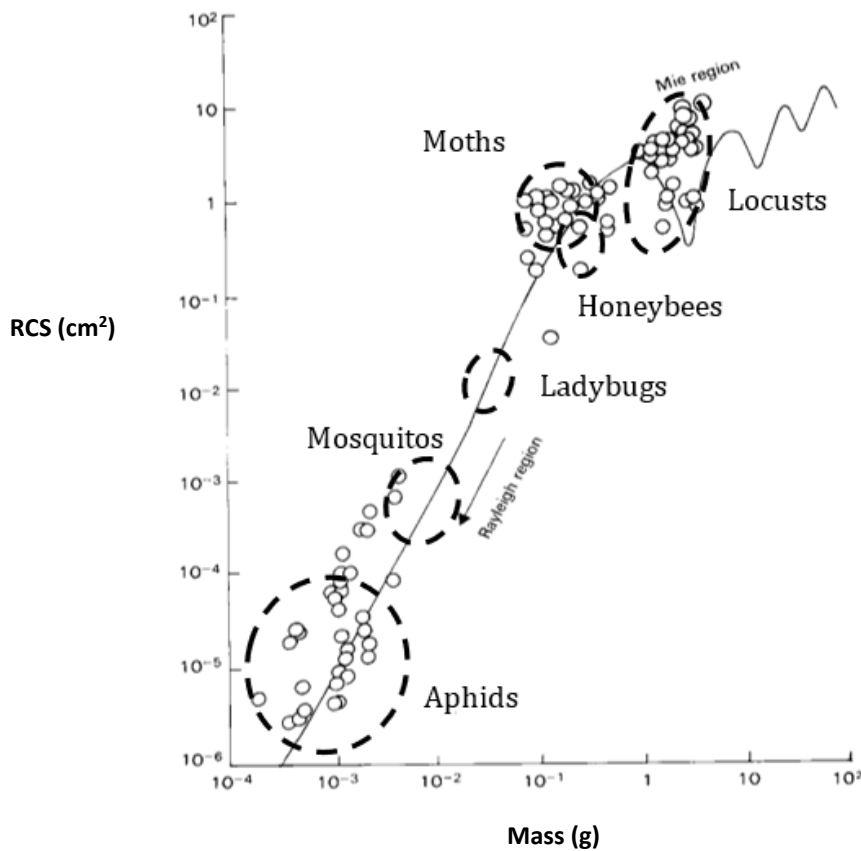
Figure 2.5: RCS measurements at a wavelength of 3.2 cm showing variation of different insects as a function of insect mass. This is plotted on the RCS plot of a spherical water droplet of increasing mass [148]. The shapes inserted in the Figure were reproduced from [151].

The authors indicated using this comparative simulation between the steel sphere and water sphere, that the steel sphere could be used to perform calibration on a radar instead of a water sphere which is difficult to control and use for calibration purposes [120].

2.4 Radar Cross Section Simulation

The studies mentioned emphasised the relation between the RCS of water and steel spheres at their frequencies of interest. The most analytical study was the study performed by Aumann, which investigated this at 24 GHz [120]. However, for the purpose of this study 5.8 GHz is the frequency of interest, which was a requirement for this project as 5.8 GHz supports integration with the research group's existing tracking technologies. Theoretically, a target's RCS can be solved by calculating Maxwell's equations with proper boundary conditions. However, this is only the case for objects with simple geometries, where the majority of targets are considered to have a complex RCS except simple geometrical targets used in calibration [145]. Among common radar calibration targets are flat plates, cylinders, corner reflectors and most importantly spheres [151], [156]–[158]. A good calibration result for flat plates would demonstrate a sharp peak with small sidelobes which would match the RCS pattern expected for the calibration target [145]. This is an important step prior to conducting radar-based experiments. To gain full understanding of previous RCS studies and support modelling of more complex structures, simulations of different objects were performed to compute their RCS.

2.4.1 Flat plate

As mentioned earlier, a target's RCS depends on various factors and is not directly related to the physical size of the target. An example of a target with an RCS much larger than its physical size is a conducting flat plate. The RCS of a conducting plate with an impinging wave at a normal direction with respect to the plate is given by [157], [159].

$$\sigma_{plate} = \frac{4\pi A}{\lambda^2} \times A = \frac{4\pi A^2}{\lambda^2} = \frac{4\pi w^2 l^2}{\lambda^2} \qquad 2.6$$

Where A is the area of the plate, λ is the wavelength used, w is the width and l is the length. When considering a wavelength of 1 cm and A= 1 m^2, the RCS would be equal to 12,560 m^2, which is much larger compared to the physical dimensions. An example below shows the theoretical calculation of the RCS of a 100 mm^2 steel plate.

Type	Bistatic Scattering
Approximation	enabled (kR >> 1)
Monitor	farfield (f=5.8) [pw]
Component	Abs
Output	RCS
Frequency	5.8 GHz
Total ACS	0.0000 m2
Total RCS	0.01966 m2
RCSmax	0.4552 m2
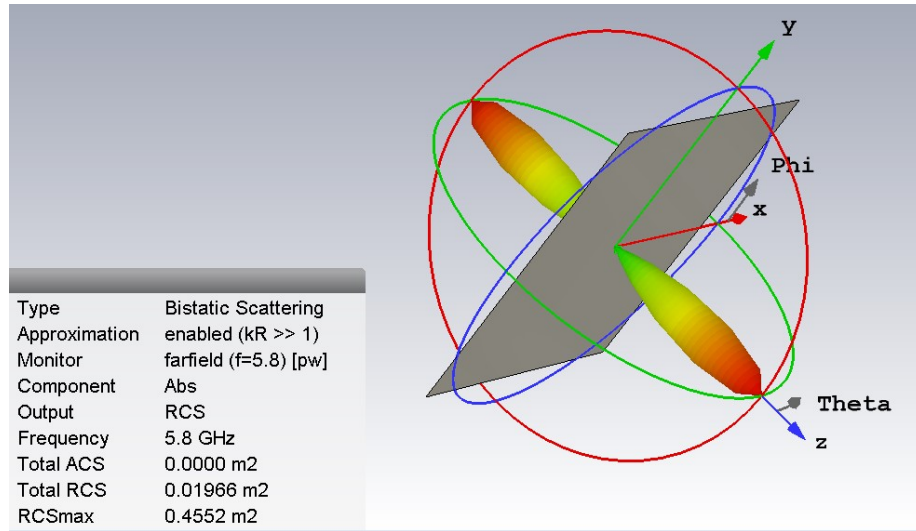
Figure 2.6: RCS simulation of a 100 m² flat plate at 5.8 GHz indicating an RCS of 0.4552 m²

Applying Equation 2.6 at 5.8 GHz frequency would indicate a λ of 51.69 mm, which would result in an RCS of 0.46 m². Complex targets cannot be theoretically calculated; hence the use of EM simulation tools can provide a valuable approximation if this is performed correctly. A simulation of a similar target using CST Microwave studio as an EM simulation tool resulted in an RCS of 0.455 m² which is in close approximation to the theoretical result. This is shown in Figure 2.6 below.

Alves and Rezende simulated the RCS of a flat plate with an area (A) of 1 m² using a software called CADRCS at the frequencies of 1 GHz and 10 GHz, while varying the aspect angle from $-20°$ to $20°$ of the simulated radar signal [160]. The flat plate RCS simulation was similarly attempted using CST Microwave Studio. The flat plate with an A= 1 m² was simulated with perfect electric conductor (PEC) as a material at the frequency of 1 GHz and 10 GHz, while varying the impinging radar signal's aspect angle from $-20°$ to $20°$ on the plate.

The simulated plate results are shown in Figure 2.7(a) and (b). The flat plate's RCS can be clearly seen to show a peak centred at both Figure 2.7(a) and (b), which represents the 0° and 180° azimuth aspect angle where the radar signal is perpendicular to the plate. This peak reflects the highest RCS measurement, while being surrounded by smaller sidelobes. However, the RCS of a flat plate is strongly dependent on the angle of incidence θ [161]. To calculate the RCS at angles other than the 0° (broadside) equation 2.7 is used

$$\sigma_{Plate(non-broadside)} = \frac{4\pi a^4}{\lambda^2}\left[\frac{\sin(ka\ \sin\theta)}{ka\ \sin\theta}\right]^2 \qquad 2.7$$

Where a is the side length of the plate, θ is the aspect angle, k is the wave number [161]. The sidelobes in Figure 2.7(a) and (c) indicate the plate's ability to scatter energy back at different efficiency in different angles. It can also be seen that the number of sidelobes increase while their width decreases in higher frequency. This is due to the modulating term $sin(ka\ sin\theta)$ in equation 2.7. Figure 2.7(a) and (b) shows the RCS simulation that was implemented as means to ensure RCS simulation functionality.

This simulation demonstrated the changes in RCS due to the different frequency and radar signal's aspect angle. The CST RCS simulation converges towards RCS results shown in [160]. Similarly, a steel flat plate was obtained, the dimensions were measured (l=32 cm w=5.2 cm, h=0.3 cm) and was modelled in CST Microwave studio as shown in Figure 2.7(b). The RCS of the flat plate was first simulated using CST Microwave studio and an additional simulation was performed using Altair FEKO EM Simulation software to obtain a verification on the simulated RCS. Figure 2.7(b) and (d) show a peak RCS of 14800 cm² at ±90° performed in CST and a peak RCS of ~15000 cm² at 90° performed in Altair FEKO. Although the simulations were conducted using different simulation software, the RCS results were remarkably close.
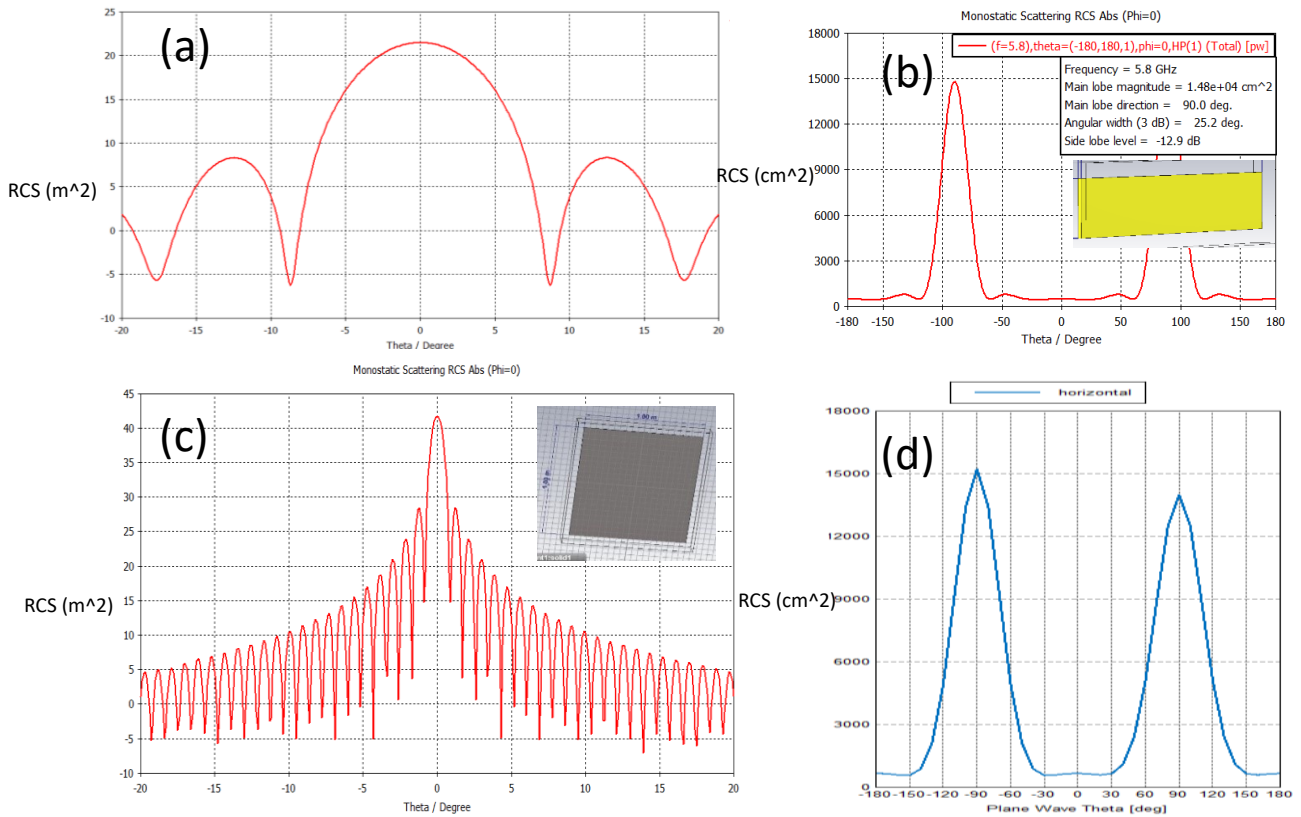
Figure 2.7: RCS simulation of a 1 m² flat plate at (a)1 GHz and (b) CST simulation illustrating a peak RCS of 14800 cm² at 90°. Inset shows simulated steel plate. (c) 10 GHz CST simulation. Inset shows the 1 m² flat plate (d) Altair FEKO simulation illustrating a peak RCS of ~15000 cm² at 90°.

2.4.2 Sphere

A conducting sphere is known to be the best example of radar calibration targets owing it to its scattering properties and symmetry [162]. The latter results in the incident radiation to scatter uniformly in all direction (isotropic scattering). This makes the sphere's RCS independent of the radar's aspect angle θ [161]. Additionally, large spheres that are much larger than the wavelength have an RCS which is independent of the frequency [161]. Figure 2.8, shows a simple conducting sphere's RCS, as function of the normalised circumference expressed in wavelengths (ka), if the sphere's radius r is much larger than the wavelength then the sphere's RSC is [159].

$$\sigma_{sphere} = \pi r^2 \qquad\qquad 2.8$$

In the Mie/resonance region the RCS of the target fluctuates/oscillates with the frequency. This region shows RCS changes that are due to waves that constructively and destructively interfere with one another. The constructive wave is due to the wave directly being reflected back from the sphere, whereas the destructive wave is known as creeping wave, that creeps around the back of the sphere to return to the radar and interfere with the reflection [146], [151]. This demonstrates the wavelength's impact on the RCS, as the wavelength dramatically affects the RCS due to their interaction with incident EM waves and their induced EM fields on the target [119].
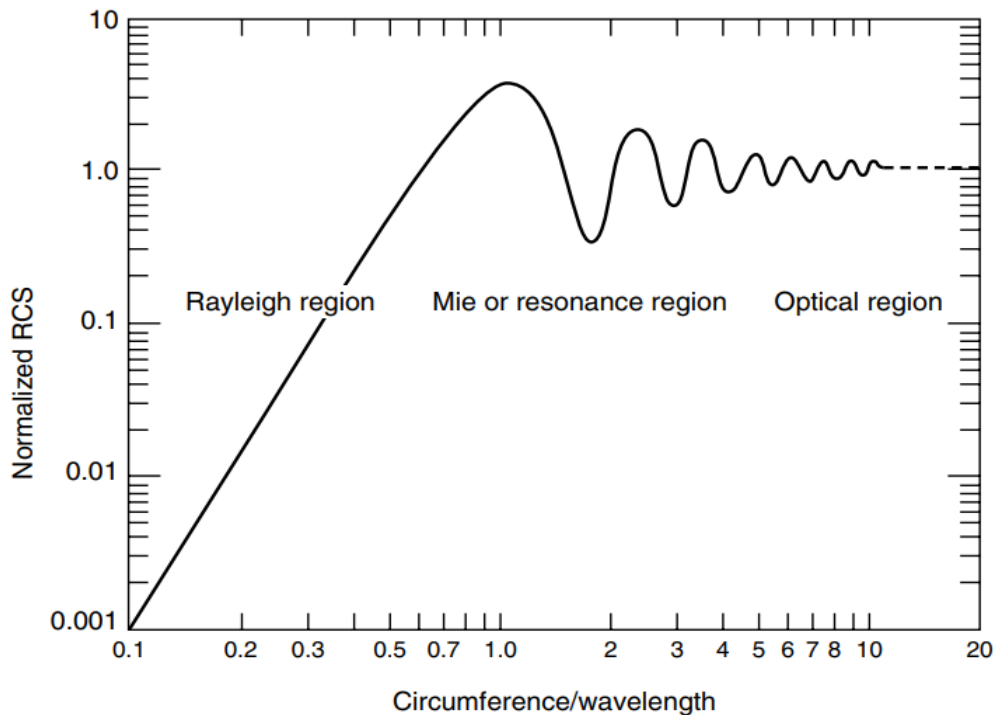
Figure 2. 8: The three different regions of a conducting sphere's RCS, the Rayleigh region, the Mie region and the Optical region [159].

In the optical region the sphere's RCS is independent of the frequency. In this region, the sphere's dimensions are larger than the wavelength, where the RCS of the target approaches the value of πa^2. The RCS of an object is affected more by the object's shape than by its area because scattering only takes place on the visible surface that faces the radar. An example of this is a camera's flash illuminating a target, where the area illuminated is only the area visible to the flash. Similarly the area that is directly illuminated by the radar would only be visible instead of the entire surface of the target [146], [151], [154]. In the optical regime the backscatter cross section of a conducting sphere is provided by the following formula

$$\sigma_{sphere} = \pi r^2, r \gg \lambda \qquad\qquad 2.9$$

As mentioned earlier, spheres are important in this study as they offer a close approximation to insects, which is why different spheres were extensively simulated and in chapter 3 and 4 experimented with. Different simulations were performed to evaluate the RCS of numerous sphere sizes and their approximation to the RCS of bees.

A study was performed to compare the RCS simulations with the theoretically calculated RCS of spheres. Calculating the RCS of a sphere can be performed by using equation 2.8. Assuming a radius of 2.5 cm, the RCS is calculated as $RCS_{sphere} = \pi r^2 = 0.00196 \ m^2$. Three spheres with a radius of 2.5 cm were simulated to measure their RCS. The three spheres were modelled as a PEC, wood (ε= 1.6) and water respectively. This was conducted to inspect the RCS at 5.8 GHz for similar targets using different materials. The sphere model with a radius of 2.5 cm is shown in Figure 2.9 as an inset.

The maximum simulated RCS values shown in Figure 2.9 were 0.0019782 m², 0.0017583 m² and 0.00010 m² for the PEC, water and wooden sphere respectively. Note that the closest value to the theoretical calculation was the PEC of 0.0019782 m², whereas the water model slightly deviated from the theoretical calculation due to the interaction of the EM waves with different dielectric constants of the water. The wooden sphere observed a significant reduction in RCS due to its low dielectric constant and conductivity.

Though most attention in this study was directed towards flat plates and spheres, there are other common targets used for radar calibration. Table 2.2 mentions important radar calibration targets along with their theoretical RCS equation [145], [157], [159]
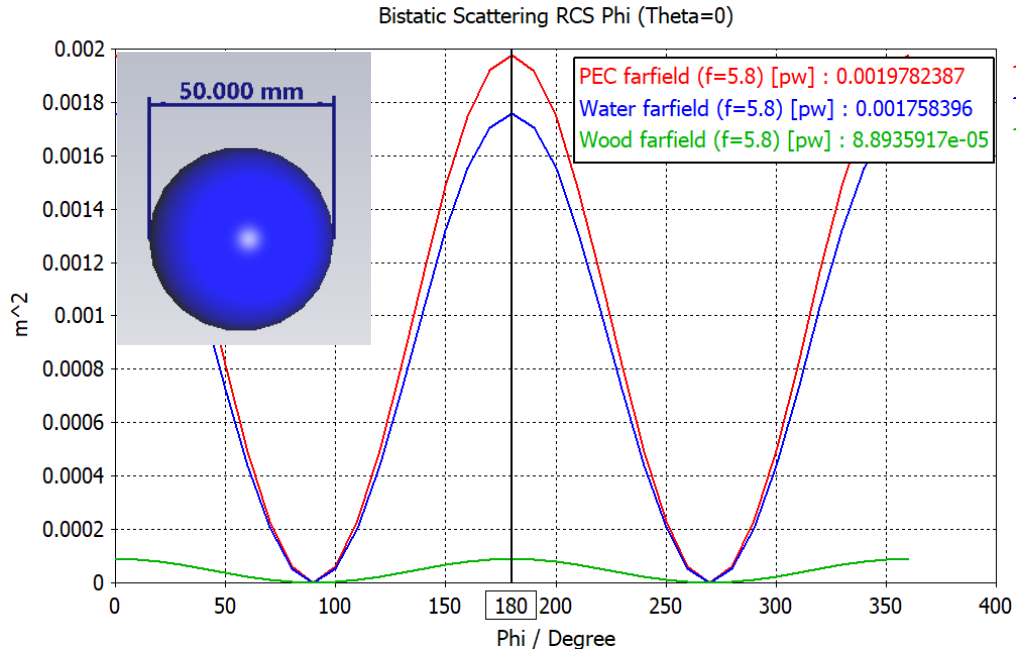
Figure 2.9: RCS simulation of three different material spheres of 2.5 cm radius. The materials were PEC, water and wood. Inset shows water sphere model in CST.

Table 2.2: List of equations for the calculation of theoretical RCS values of different shapes [145], [157], [159].

Target	Aspect angle	RCS equation	Symbol
Sphere	Any	πr^2	r = Radius
Cone	Axial	$\dfrac{\lambda^2}{16\pi}\tan^4\theta$	θ = Cone half angle
Cylinder	Normal to axis	$\dfrac{2\pi a L^2}{\lambda}$	a=Radius, L=Length
Dihedral	Maximum direction	$\dfrac{8\pi a^2 b^2}{\lambda^2}$	a, b = Length of side
Trihedral	Maximum direction	$\dfrac{4\pi a^4}{3\lambda^2}$	a = Edge length
Circular plate	Angle to normal	$\dfrac{\pi a^2}{\tan^2\theta}J_1^2(2ka\,\sin\theta)$	a= Radius of plate $J_1()$= 1st order Bessel function a,b= Length of side
Square plate	Angle to normal	$\dfrac{4\pi a^4}{\lambda^2}\left[\dfrac{\sin(ka\,\sin\theta)}{ka\,\sin\theta}\right]^2$	a = Length of side
flat plate	Normal to axis	$\dfrac{4\pi A^2}{\lambda^2}$	a = Plate area

2.4.3 Insect RCS approximation

The CST simulations performed up to this point provided a confident start on RCS simulations. Comparing RCS simulation with peer reviewed research and coupling the CST results with Altair FEKO provided additional assurance that the RCS simulations were reliable. Thus, the approach followed in [120] to simulate a steel sphere and a water sphere was implemented.

The assumption made by Riley and Wolf, assumed that the backscattering properties of an insect can be represented by a water droplet of the same mass [148], [150], [163] and can be utilised to reduce the complexity of the RCS approximation. Insect RCS approximation is complex due to the involvement of multiple shapes, layers and a variety of dielectric constants.

Though with modern techniques such as micro-computer tomography imaging, such as the one used by Thielens *et. al*, [132], exact insect models can be obtained from dead insects. These could perhaps be used in the future to provide more accurate RCS approximations, which to this point has not been implemented yet.

Nevertheless, the use of water droplets (further to be referred to as water spheres) to represent the backscattering properties of an insect, is supported by Riley and Wolf [148], [150], [163] for RCS approximation and is computationally efficient since spheres are a common radar calibration standard.

The simulation of water and steel spheres at frequencies of 24 GHz and 10 GHz were carried out by Aumann in [120]. The water model used in this study was the Debye model. The Debye model is a widely utilised EM model for simulating water and its interaction with EM waves. The Debye model describes frequency-dependant polarisation as a result of the motion of its electric dipoles in response to an external electric field. The water model is treated as a dielectric material, with a complex permittivity that is described by the Debye model and takes into account multiple parameters (shown in Table 2.3) that allow accurate simulation of water.

Table 2. 3 Parameters of water Debye model used in CST

Property	Value
ε∞	3.1
ε'	78.4
σ	1.59 S/m
ρ	1000 kg/m3
μ	1
Temperature	25 ° Celsius
Thermal Conductivity	0.6 W/m×k
Relaxation time	8.27e-12

In [120], a steel sphere and a water (Debye model) sphere were parametrically simulated, with incrementing diameters. This is shown in Figure 2.10(a). Note how the figure agrees with the trend shown in Figure 2.5. This is due to the water and steel sphere adhering to the RCS trend of a theoretically calculated sphere in [148].

The simulations were carried out at 10.5 GHz for both steel and water spheres, followed by 24 GHz. Both sphere diameters were incremented by steps of 1 mm starting from 1 mm to 10 mm. The simulation accuracy was set at medium, while the source type was chosen as a plane wave. To obtain RCS measurements, two Farfield/RCS field monitors were used at 10.5 GHz and 24 GHz. Monostatic RCS was simulated by sweeping both Phi and Theta angles from 0° to 180°. Since the frequency of interest is 5.8 GHz, the approach followed earlier was repeated.

The simulated water sphere predicted an RCS increase mirroring the size increase, as shown in Figure 2.11. The RCS range was between −104.58 to −33.71 dBsm between 1 mm and 15 mm respectively. Based on literature, an insect with approximately the same water volume as a 15 mm water sphere would have an RCS close to the 15 mm water sphere [141], [143], [156]. Nevertheless, the use of water spheres or droplets in real life is difficult, as it requires the control of a specific volume of water for experimentation and calibration purposes.

(a)

(b)

RCS EM Simulation water and steel sphere
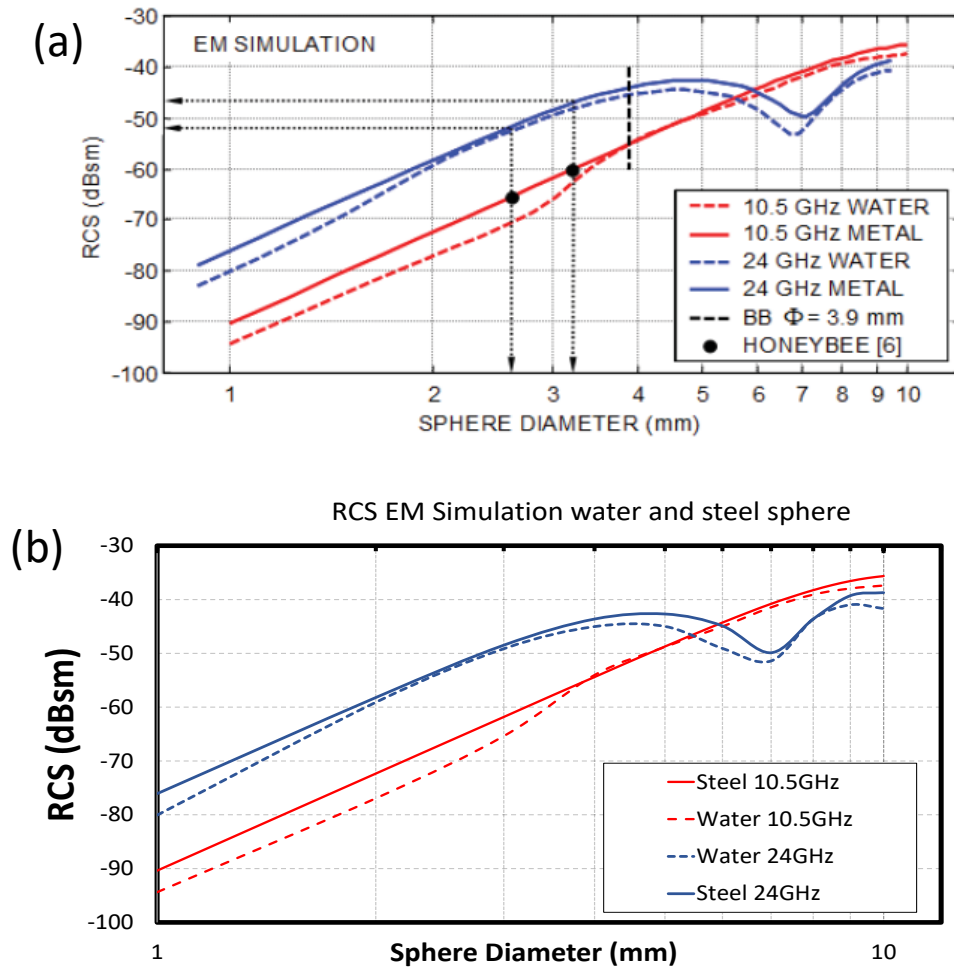
Figure 2.10: (a) Simulated RCS of a steel sphere and a water droplet [120] (b) RCS simulation replicated using CST Microwave Studio.

Thus, the inability to use water as a testing material and the inability to control water volume were two challenges that were faced. A work around would be to find a physical sphere that has approximately the same RCS as the water sphere.
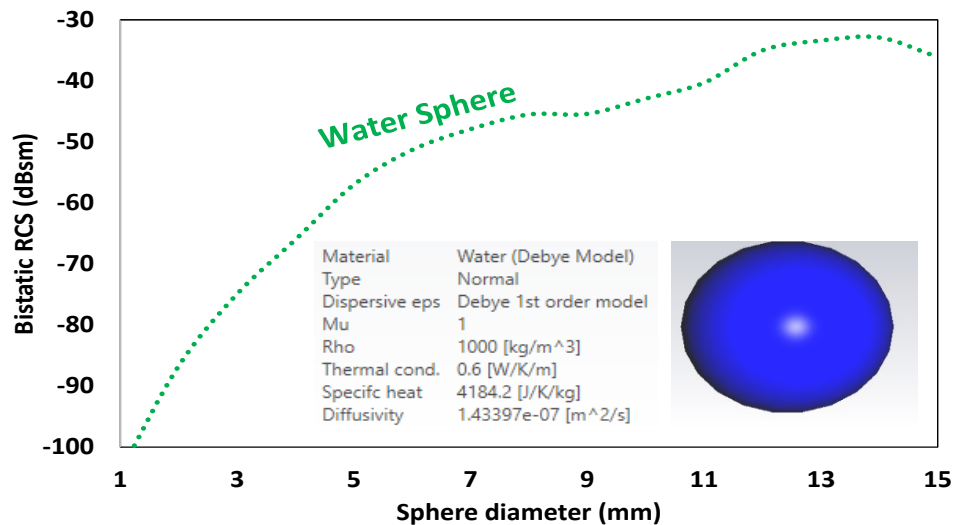
Figure 2.11: Simulated RCS of water sphere at 5.8 GHz. Inset shows the water sphere model used and the properties of the Debye model.

79

2.4.3.1 Hydrogel/Silica sphere

An early approach to address these challenges, involved the use of Silica gel spheres, also known as hydrogel spheres, shown in Figure 2.12(a). These hydrogel based products are made out of polymeric materials with a hydrophilic structure that allows them to absorb a large amount of water [164]. Such spheres are commonly used for their high moisture absorption. When placed in a container with water, hydrogel spheres absorb water content and thus grown in size. This allowed a somewhat controlled sphere with water content, simultaneously addressing the two challenges faced. The hydrogel beads were modelled in CST Microwave studio using the Integral Equation Solver. Since the hydrogel sphere absorbs water to grow in size, two spheres were modelled.

The inner sphere being the water content and the larger outer sphere being the silicon shell of the hydrogel. Once the sphere starts absorbing water, the inner sphere's water content would increase, causing it to expand in size. Figure 2.12(b) and (c) show a CST model of a 4 mm diameter hydrogel sphere where the silica thickness was chosen to be 0.175 mm thick. The water content in the hydrogel sphere was modelled using CST Debye model (DC ε'=78, σ=1.59 S/m). The accuracy was set at medium, while the source type was chosen as a plane wave. A single Farfield/RCS field monitor was used at 5.8 GHz and an RCS sweep was implemented to sweep both Phi and Theta angles from 0° to 180°.

The result of the silica gel sphere simulation is shown in Figure 2.13, which indicated an RCS range between −107.74 to −31.67 dBsm between 1 mm and 15 mm respectively. The simulation was expanded to cover a range of different silica gel spheres diameters ranging from 1mm to 15 mm.
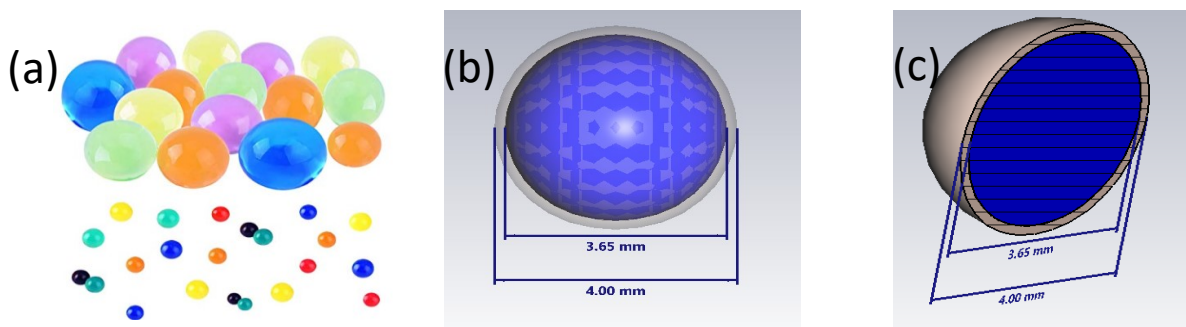
Figure 2.12: (a) Hydrogel spheres, when no water is absorbed and when water is absorbed (b) Hydrogel sphere showing internal water content (c) Cross section of Hydrogel sphere showing Silica layer and water content.
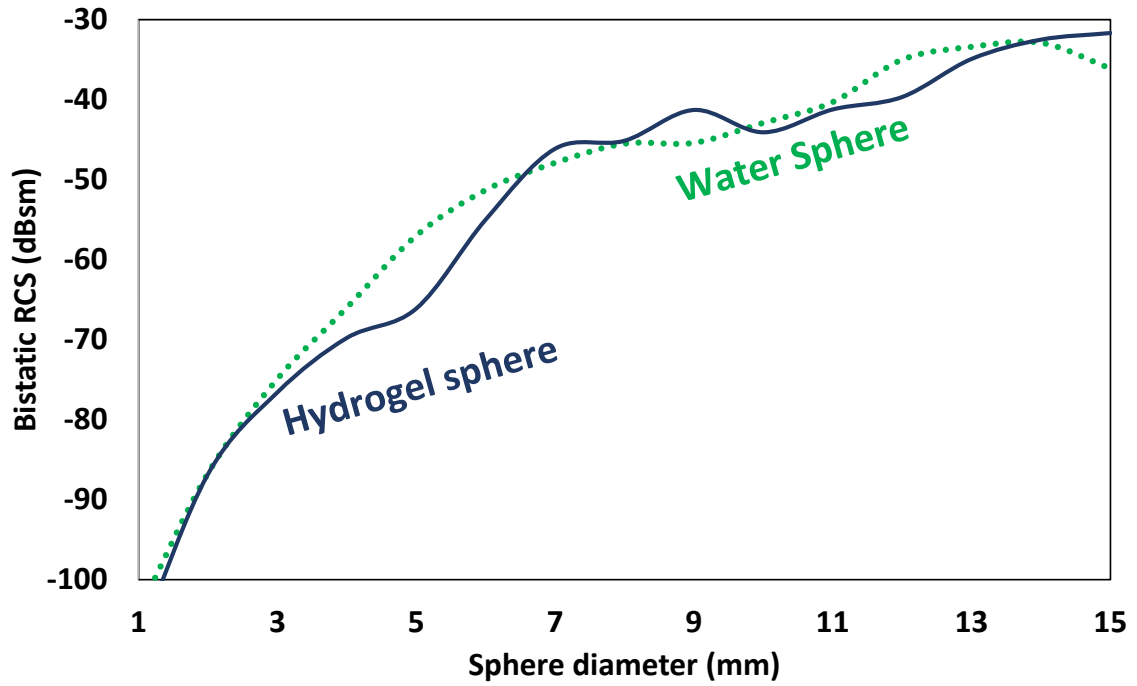
Figure 2.13: Hydrogel/Silica gel sphere model in CST Microwave studio with varying diameter.

The simulated RCS results of the hydrogel spheres were plotter to visualize the change in RCS as the diameter increases. Additionally, the hydrogel sphere RCS results were plotted with the water sphere RCS results to show the similarity in RCS. Though several hydrogel gel spheres were different in terms of RCS, it can be noticed that the RCS of hydrogel gel spheres with a diameter from 2 mm to 5 mm were closely matched to the RCS of water spheres with the same diameter. From 6 mm onwards, the hydrogel gel sphere starts to deviate from the water sphere. This indicates that the ideal hydrogel gel diameter for experimentation would be from 2 mm to 5 mm.

Multiple experiments with the hydrogel spheres, revealed that it was difficult to control hydrogel spheres maximum diameter and shape/size stability as they would deflate over time due to water content loss. This ruled out the use of hydrogel gel spheres for experimentation purposes or for calibration. As a result, an alternative target that could be correlated with water spheres' RCS was needed.

2.4.3.2 Steel sphere

Since steel spheres are a common RCS calibration practice and can be obtained in small diameters, a parametric simulation was carried out on steel spheres. The material chosen was steel (DC $\varepsilon'=1$, $\sigma=7.69\times 10^6$ S/m). The simulations were carried out similarly to the water sphere simulations at 5.8 GHz, while maintaining similar simulation parameters.
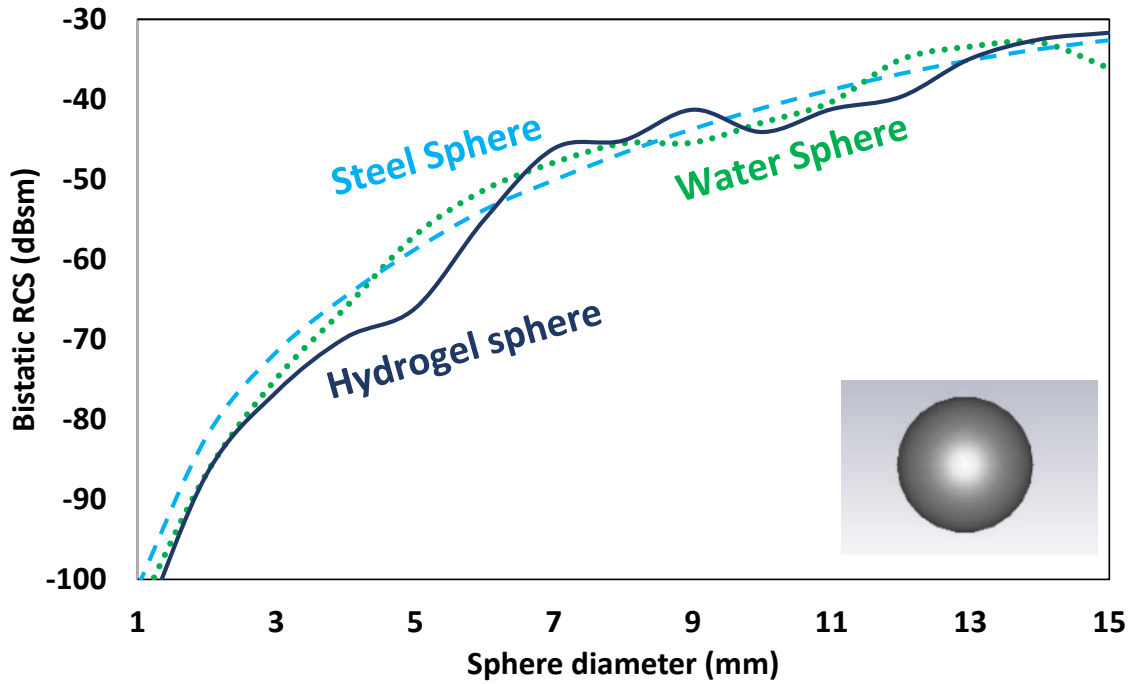
Figure 2.14: Simulated RCS of steel spheres, water spheres and hydrogel spheres with increasing diameter at 5.8 GHz.

Simulated RCS values of interest of 4 mm, 3 mm and 2 mm steel spheres were −64.6, −71.6 and −82.1 dBsm respectively. Upon combining the simulated RCS results of steel, water and hydrogel spheres, an interesting correlation was observed, which showed that the three different targets' RCS was in close approximation to one another. The combined simulated RCS plots are shown in Figure 2.14.

This is especially the case when looking at 3 to 5 mm simulated RCS of steel and water sphere, which were −71.6, −64.6, −58.76 (for steel) and −74.9, −66 and −57 dBsm (for water) respectively. The difference between these values was surprisingly small considering both the vastly different materials. The closest simulated RCS match obtained for steel and water spheres, was the 4 mm sphere where the difference was −1.4 dBsm This suggested that a 4 mm steel sphere was the closest to being equal to a 4 mm water sphere. Thus, the 4 mm steel sphere was the most suitable diameter of steel spheres for calibration purposes.

2.5 Honeybee RCS approximation

At this point, it is still unclear whether any of the steel and water simulated RCS values are related to honeybees in any way. Thus, it is important for this study to find a correlation between the simulated RCS targets in order to find their relationship with honeybee RCS simulation.

2.5.1 Ellipsoid

When simulating insects, several authors have attempted to use an ellipsoid filled with water, as it provides a simple shape that roughly resembles the body of an insect [165]–[168]. Since the majority of the insect's body is fluids, a water ellipsoid seemed feasible [168]. The RCS of an ellipsoid can be calculated by [162].

$$RCS_{Ellipsoid} = \frac{\pi a^2 b^2 c^2}{(a^2 (\sin\theta)^2 (\cos\varphi)^2 + \ b^2 (\sin\theta)^2 (\sin\varphi)^2 + c^2 (\cos\theta)^2)^2} \qquad 2.10$$

Where *a, b* and *c* represent the radius value held in *x* axis, *y* axis and *z* axis respectively as shown in Figure 2.15. When *a, b* and *c* are equal, the ellipsoid would become a sphere and thus the RCS would be equal to that of a sphere and can be found in table 2.2. When the radius of *a* is equal to that of radius *b*, the ellipsoid becomes a spheroid and equation 2.10 is reduced to [162],

$$RCS_{Spheroid} = \frac{\pi b^4 c^2}{(a^2 (\sin\theta)^2 + c^2 (\cos\theta)^2)^2} \qquad 2.11$$
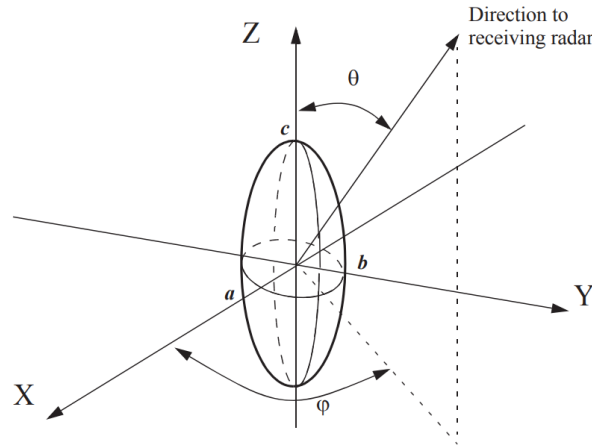
Figure 2.15: Ellipsoid and its 3 parameters (*a, b* and *c*) that define its length, width and height.

Using an ellipsoid, a simple insect model can be obtained, which was modelled and simulated using CST Microwave studio. Knowing that the length of a honeybee can reach up to 15 mm, the length of the ellipsoid was set to range from 1 mm to a maximum of 15 mm, with increments of 1 mm.

The height of the ellipsoid was set to 2 mm and the width was set to 3 mm, to approximate a honeybee. The ellipsoid used water (Debye model with ε'=78 and σ=1.59 S/m) as material and was simulated using the Integral Equation Solver. Figure 2.16 shows the CST model of the water ellipsoid as an inset, while showing the simulated RCS plot of the ellipsoid, using the same simulation properties (accuracy, plane wave and sweep).
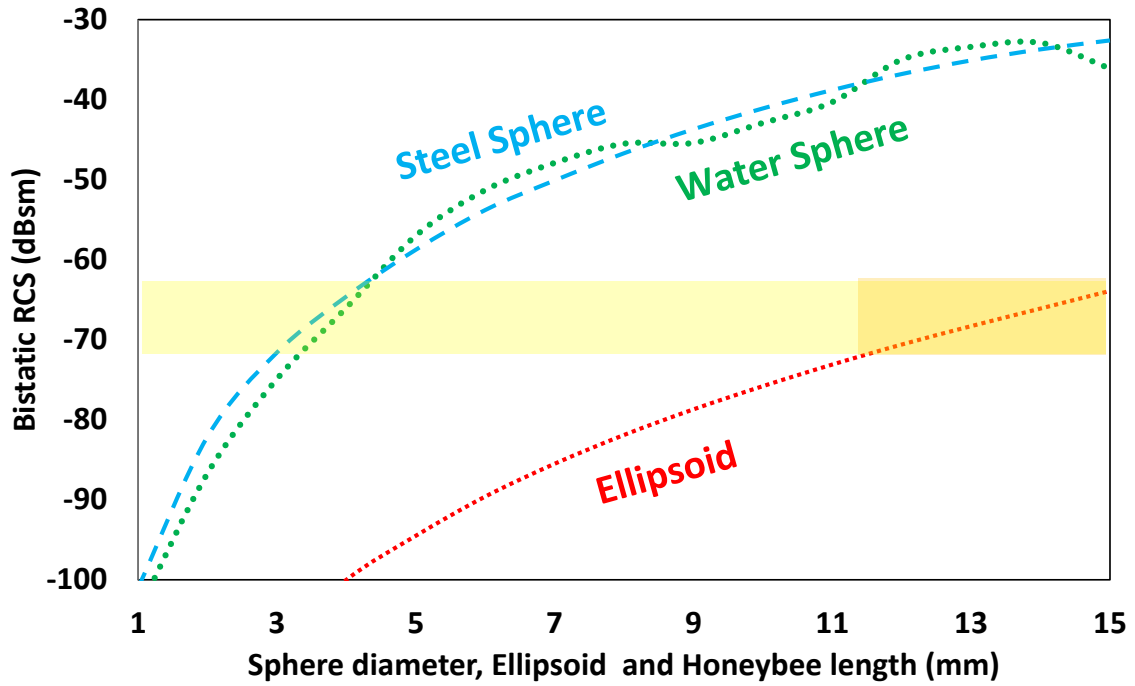
Figure 2.16: Simulated RCS of steel sphere, water sphere and ellipsoid showing an overlap in RCS of the 10 to 15 mm long ellipsoid and 3 to 4 mm water and steel spheres.

Though the use of an ellipsoid simplifies the RCS simulation by reducing the complexity of geometrical properties of a honeybee, the model is only valid in the range of 10 mm to 15 mm, as this is the approximated length range of a honeybee. As a result, RCS simulations of 1 to 9 mm length can be discarded, leaving only the (orange) highlighted area in Figure 2.16 to be of importance. The highlighted area from 10 to 15 mm resulted in an RCS simulation of -75.8 to -63.9 dBsm respectively.

Upon inspecting the combined plots, it can be concluded that the ellipsoid RCS simulation ranging from 10 to 15 mm overlaps with the steel sphere and water sphere simulated RCS for sphere diameters ranging from 3 mm to 4 mm. This is shown in the yellow highlight that emphasises the overlap. The overlap means that the ellipsoid representing a simplified honeybee model has a simulated RCS value that intersects with the simulated RCS values of both the 3 to 4 mm water and steel spheres. Critically, the difference between 4 mm diameter steel spheres and the 15 mm ellipsoid's RCS was a 0.7 dBsm difference. It can be noted that the slope of the spheres differs to that of the ellipsoid. This is believed to be due to the slower rate of change of the ellipsoid surface area as compared to that of the spheres.

2.5.2 Honeybee

The simulation results indicated a relatively close value of the water sphere and steel sphere RCS at 5.8GHz, which was found to coincide with the simulated RCS of a 10 to 15 mm long ellipsoid. The RCS simulation have provided a correlation between the water spheres, an ellipsoid (simplified honeybee model) and a steel sphere that is in close proximity to their simulated RCS. To further support the RCS simulations, a full bee model was simulated. Different models were attempted as shown in Figure 2.17. The final model of choice was based on the most realistic model among the models attempted. The simulation followed a similar approach to the previous RCS simulations. The honeybee was filled with water (Debye model with ε'=78 and σ=1.59 S/m) and the length of the honeybee was incremented from an initial starting length of 10 mm to 15 mm. Both the simulation parameters and simulation setup were kept the same to previous RCS simulations in order to prevent unwanted simulation deviations.
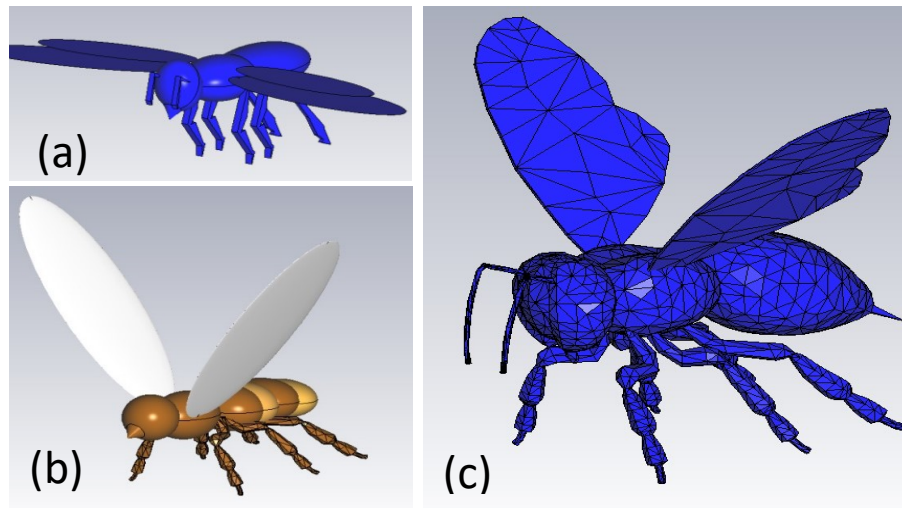
Figure 2.17: Three honeybee models that were attempted (a) 1st custom designed honeybee (b) 2nd Custom designed honeybee (c) Honeybee CAD model that was used for simulations [169].

The simulated honeybee RCS shown as the orange line within the yellow in Figure 2.18, approached the 4 mm steel sphere simulated RCS when considering honeybees of 13 mm and 14 mm long. Interestingly, the RCS of the honeybee model also coincides with the ellipsoid RCS simulation for an ellipsoid of 15 and 14 mm long. Given that the honeybee RCS simulation overlaps with the points of the ellipsoid, it gives the honeybee simulation a promising outcome. Nevertheless, it is important to refine the details of the simulation in order to obtain a theoretical outcome of higher accuracy and provide results that are as close to a realistic value as possible. Therefore, the parameters used for the simulation of the honeybee were further investigated.
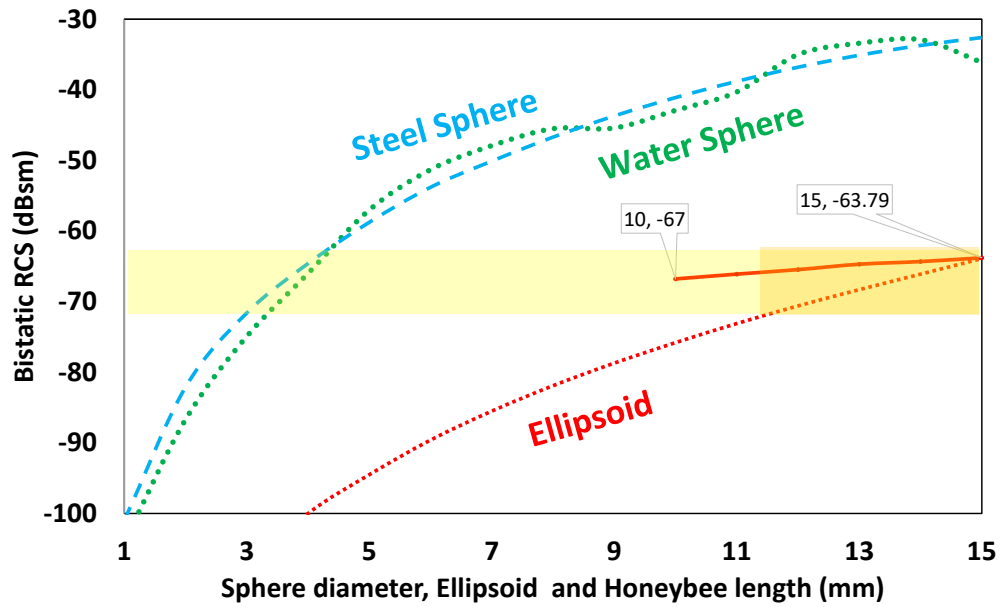
Figure 2.18: Simulated honeybee (Debye model with ε'=78 and σ=1.59 S/m) results added to the RCS simulations to show its overlap. Tick marks added to honeybee slope display minimum and maximum values.

A study in 2020, measured the dielectric constant and conductivity of Western honeybees and populated a table with results ranging from 0.6 GHz to 128 GHz [170]. According to the study, the dielectric constant and conductivity were with ε'=38 and σ=5.05 S/m at 6 GHz, while the values used in this study were based on a Debye model with ε'=78 and σ=1.59 S/m.

This showed a discrepancy in both key parameters used to those found in literature, which are crucial for accurate RCS simulation. Thus, the honeybee model was re-simulated using the dielectric constant and conductivity values extracted from [170] to support a more refined and realistic simulation. The refined honeybee simulation is shown in Figure 2.19. The simulation results of the refined honeybee ranging from 10 mm to 15 mm indicated a simulated RCS of −70.7 and −67.5 dBsm respectively. Upon inspecting the combined simulated RCS plots, a highlighted area was inserted in Figure 2.19, to indicate the RCS range of both the 10 mm to 15 mm ellipsoid and 10 mm to 15 mm honeybee. The highlights were extended to reach the water and steel sphere. This indicated an intersection range matching the simulated RCS of the honeybee and ellipsoid with the RCS of the water and steel sphere. The intersection range, showing an orange rectangular area in Figure 2.20, displayed a sphere diameter of approximately 3 mm to 4 mm. This meant that the simulated RCS range of the ellipsoid and honeybee combined are equal in terms of RCS with that of a steel sphere ranging from 3 mm to 4 mm.
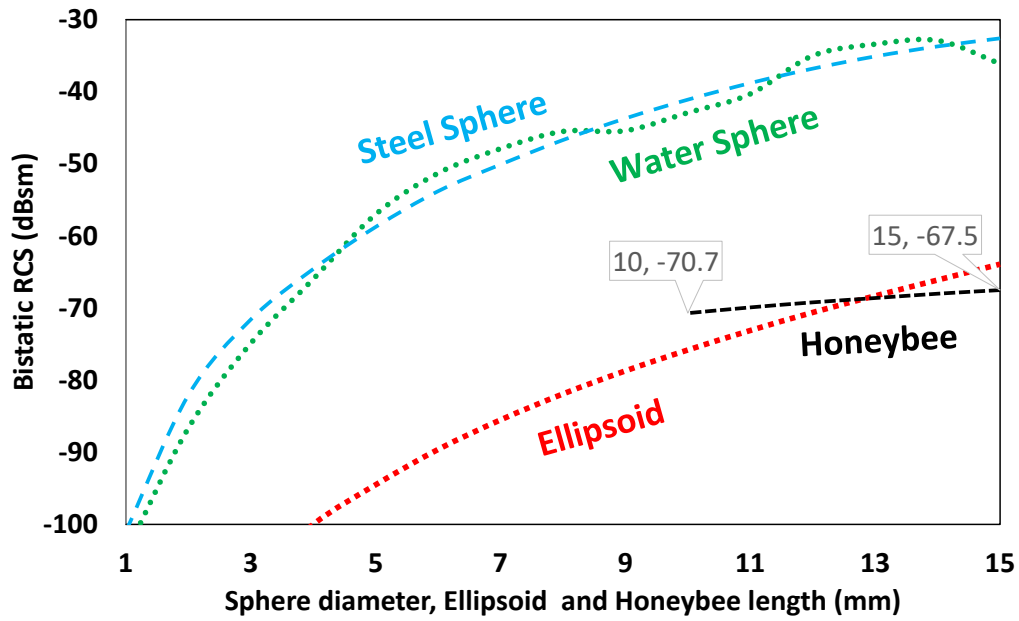
Figure 2.19: Simulated honeybee (Debye model with ε'=38 and σ=5.05 S/m) results added to the RCS simulations to show its overlap. Tick marks added to honeybee slope display minimum and maximum values.

Upon inspecting the honeybee simulation, it can be noted that this directly intersects only 3 to 4 mm steel sphere. The simulation results allowed an extraction of real-life targets that potentially match the RCS of a honeybee. Since the simulation results indicated a relatively close value of the water sphere and steel sphere RCS at 5.8 GHz and that the RCS of the 3 mm to 4 mm diameter steel spheres matched the 10 mm to 15 mm ellipsoid's RCS (-75.8 to -63.9dBsm respectively) with a 0.7 dBsm difference between the 4 mm steel sphere, it validates the use of a 4 mm steel sphere for calibration purposes.
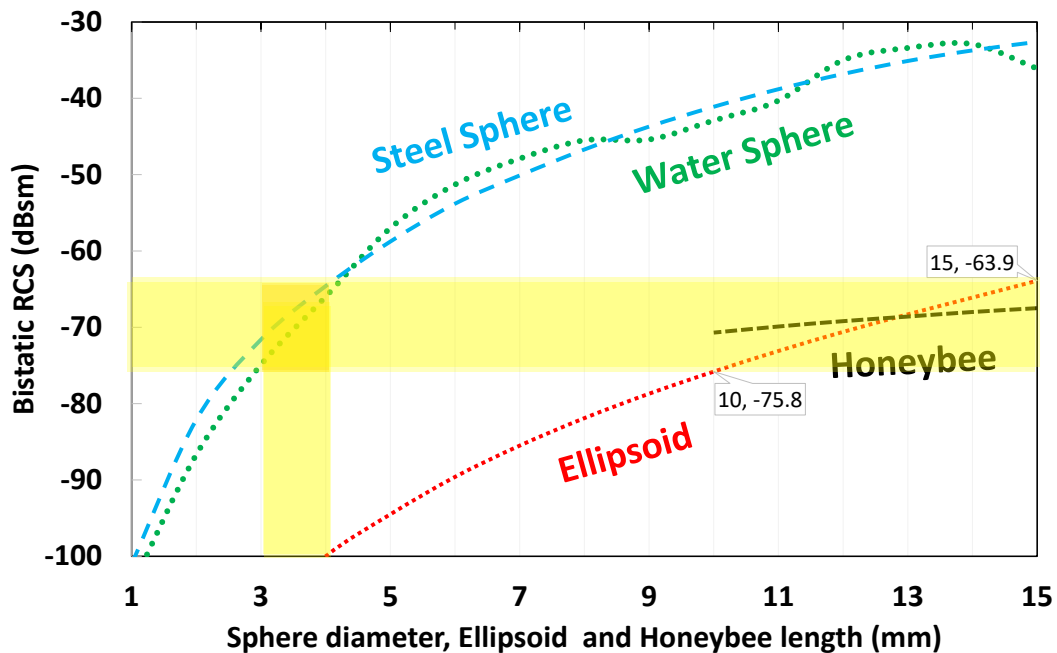
Figure 2.20: Simulated RCS of honeybee and ellipsoid intersects with that of a 3 mm to 4 mm steel sphere.

For further validation, the simulated honeybee RCS (ranging between −70.7 and −67.5 dBsm) for honeybee length of 10 mm to 15 mm overlaps with the ellipsoid and steel sphere RCS, hence further supporting the adoption of 4 mm steel sphere for calibration.

2.5.3 Honeybee simulation aspect angle

As mentioned earlier, when inspecting the RCS of spherical targets, the aspect angle does not have an impact due to the sphere's symmetrical geometry. However, with complex targets, the aspect angle becomes an important parameter in RCS. It is important from an experimental and a simulation standpoint to realise the impact of the EM wave's aspect angle on the bee. This is to understand the orientation that allows the maximum reflectivity and to support optimal placement of the radar. The radar can be placed at the entrance of the hive to face-out as illustrated in Figure 2.21(a) or to face the hive as shown in Figure 2.21(b). When facing out from the entrance, the radar closely observes events that occur at the entrance/exit, where the bees are closest to the radar.
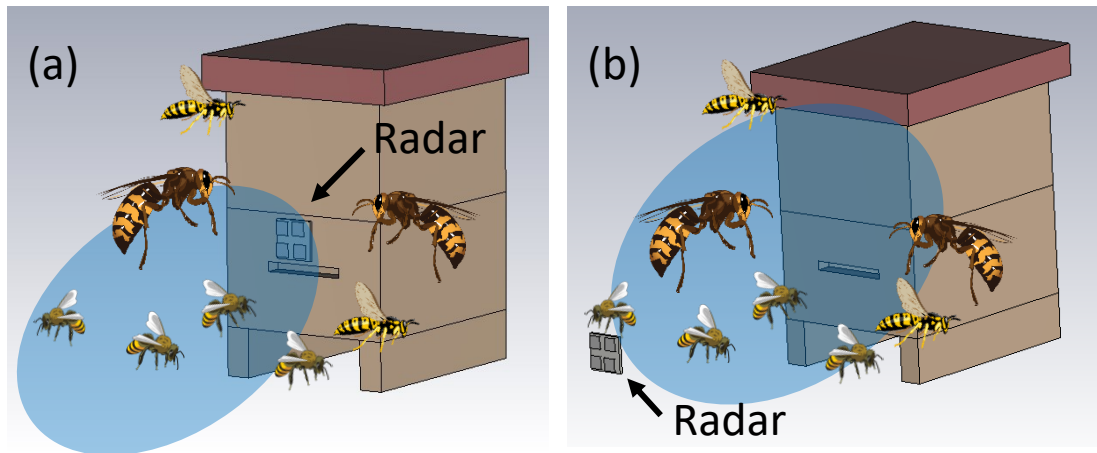
Figure 2.21: (a) Radar facing out of the hive (b) Radar facing the hive. Insets in both figures show a collection of honeybees, wasps and Asian hornets hovering around the hive

Due to this region being the most active of the hive, and the fact that bees come in close approximation to the radar, other signals in the background (e.g., hovering) are drowned (disappear behind the higher intensity of larger signals) in the activity of closer arriving/departing bees.

Additionally, though the majority of the transmitted EM waves would be facing out (depends on the antenna's gain), it is possible that signals from behind the radar (inside of hive) can be picked up. Since the inside of the hive can be busy with thousands

of buzzing bees, this can cause significant interference at lower frequencies. Further, this setup restricts monitoring range flexibility as the radar would only be able to detect bees up to its maximum distance, which limits having a variable monitoring distance. Nevertheless, this placement would be optimal for hive logging as incoming and outgoing bees come within very close approximation to the radar.

This maximises both the signal to noise ratio and the overall quality of the received signals for hive logging but suffers from lack of flexibility, lowers area of hive monitoring and causes less events to be captured efficiently. Upon using this placement for hive logging, it is important to shield the rear of the radar to reduce rear activity detection as radars can pick up signals behind the antennas. Considering the presence of a bee colony within a hive, it would be able to pick up their continuous movements and body vibrations.

The other radar setup is shown in Figure 2.21(b), where it is placed opposite the hive (facing the hive), does not restrict most of the radar's interaction with only the entrance/exit. Since the radar faces the hive, a larger range of hive-based activity can be observed, resulting in potentially much larger range of events that can be monitored. Bees approaching the hive and leaving the hive are equally monitored while increased activity at the entrance does not cause the signals to be drowned as the radar is position away from the busiest part of the hive. Further, this setup enables the radar to be moved closer or further from the hive based on the requirements of the experiments, providing an additional advantage of monitoring range and of signal to noise ratio flexibility.

The setup in Figure 2.21(a) would result in the majority of the bees having a heads-on (bee's rear upon departing) interaction with the radar's EM waves as these signals represent the highest magnitude recorded compared to lower magnitude activity (e.g., hovering bees). On the other hand, the setup in Figure 2.21(b) is placed away from the busy entrance of the hive, allowing other events to be recorded. EM waves in this setup, radiate on either side of the bee as it approaches from the sides of the hive (including hovering bees) and radiate heads-on as it flies towards the hive entrance.

To theoretically characterise the placement of the antenna for both facing out the hive and facing the hive CST Microwave studio was used. The radar's transmitted wave was simulated as a plane wave radiating outwards towards the hive. Since the radar would not be placed above honeybees and bees were not observed to fly under the radar, EM waves impinging the upper part of the thorax and abdomen were not studied. This

would also result in a large RCS dataset of less relevant RCS plots. Figure 2.22(a) illustrates the farfield plot with the antenna facing the hive and facing out the hive, while (b) illustrates the polar plot. Facing the hive, allowed the observation of bees hovering across the entrance with their sides towards the antenna. Here, the highest reflection was obtained when the insect's sides were towards the antenna, with lower intensity peaks at both the head and rear of the insect. This reflects the situation of hovering bees, which would be difficult to spot when the antenna is facing out the hive. The antenna was then moved to face the hive, where it would be imping heads-on with leaving bees and rear-on with entering bees. The only difference noted was that the reflected signal was a fraction smaller when placed at the entrance, while showing a uniform reflection around the bee. This explains why placing the antenna facing out of the hive is good for bee activity logging purposes, but not for monitoring as the increased activity at the entrance would drown that of the more distant hovering signals.
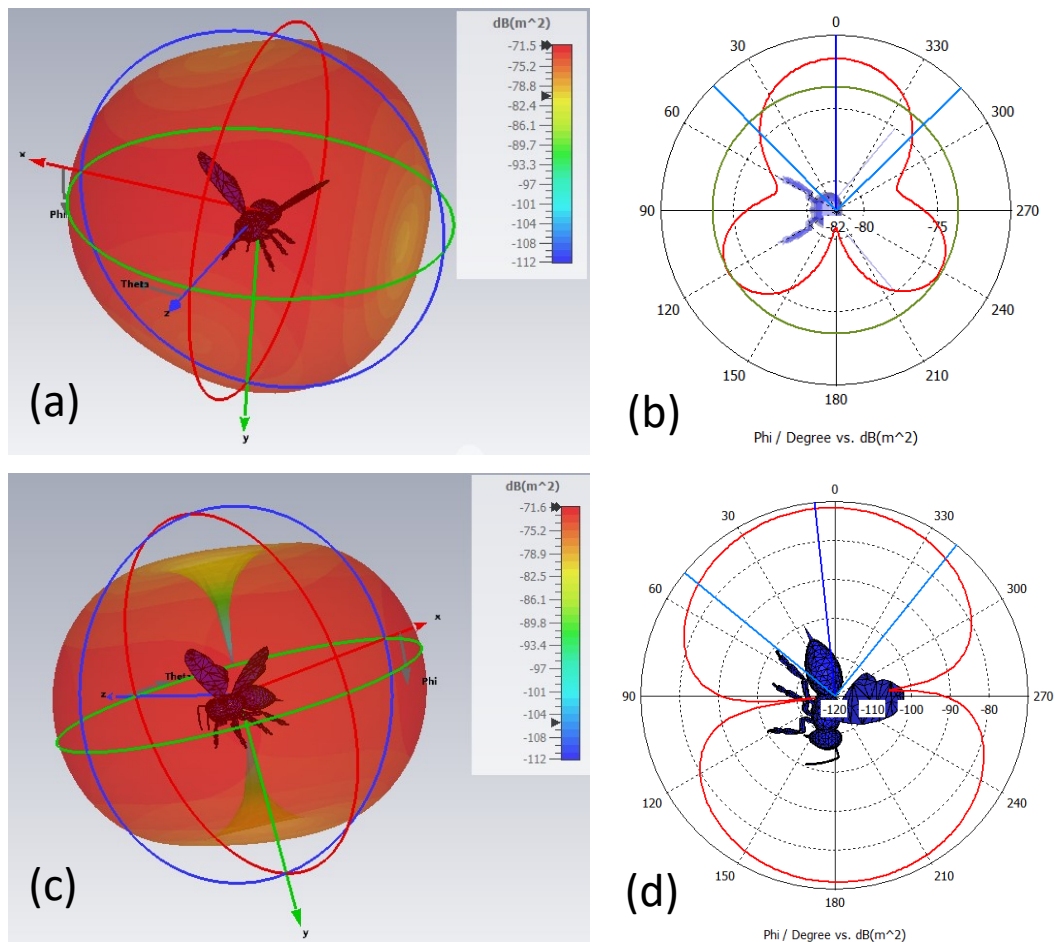
Figure 2.22: (a) EM wave radiating towards the left side of the bee and causing the highest reflection in the side of impingement. (b)The highest reflection can be noted at the side of impingement (c) EM wave radiating towards the rear side of the bee and causing the highest reflection in the rear and front of the bee (d) High reflection is noted on both the rear and front part of the bee, with a more uniform reflection pattern.

The simulation indicated that both placements are valid, and that both provided a reflection of ~ -71 dBsm. Thus, reflections obtained from an aspect angle from the side of the bee are almost equal to those obtained from the front/rear of a bee. However, to prevent focusing the radar's capabilities only to a fixed area (entrance/exit) which could drown other signals, to allow a wider range of observation, to enable a flexible range of radar placement, to monitor more events and capture other insects interacting with the hive, facing towards the hive is favoured. This provided an understanding of the insect's interaction with the EM waves, indicating regions of highest reflected signal strength to support a rationale for the systematic placement of the radar.

2.6 Radar Cross section simulation of coated targets

The previous simulations demonstrated theoretical RCS approximations of targets with either steel spheres or water material (water sphere, honeybee and ellipsoid). While there is a large focus of research towards reducing the RCS using coating material and metamaterial, there is little to no research dedicate to RCS increase using coating. Since the RCS of a target also depends on the target's material, it is interesting to investigate the impact of a coating layer on the targets to potentially enhance their RCS.

To study and demonstrate the impact of a metallic coating, a 4 mm wooden sphere was simulated in a similar manner as in the previous section. This was investigated as a target was needed that could be both simulated and practically examined while not being metallic in nature. Other than the hydrogel spheres, steel sphere and a large wooden sphere, no smaller non-metallic targets were previously simulated. Hence, a new target was obtained, which was a 4 mm wooden sphere. The wooden sphere is shown in Figure 2.23(a)-(c).
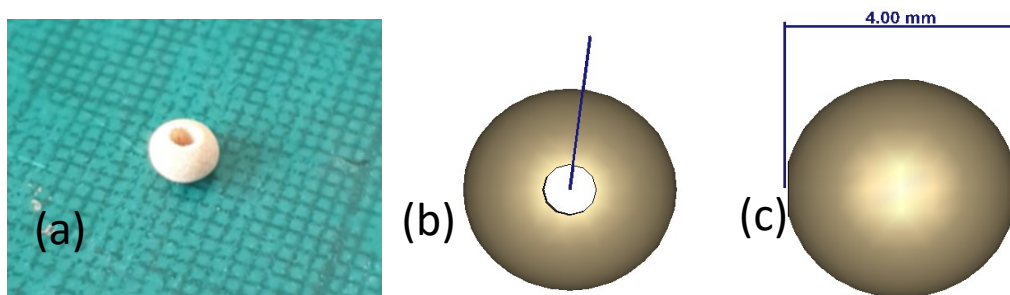
Figure 2.23: (a) Wooden sphere target purchased for testing (b) CST model of the wooden sphere target showing the centre hole (c) Side view of the wooden sphere.

Note that the wooden sphere had a hole in its centre, as it is commonly used for DIY accessories. The hole was measured and taken into account during the simulation. However, due to the impingement of the EM wave on the side of the sphere with no holes, the RCS plot remains similar to the steel and water sphere, deeming the hole to have no effect on the simulation.

The wooden sphere's simulated RCS value was -83.9 dBsm. Notably, this is lower than both the 4 mm steel sphere and 4 mm water sphere, which were -64.6 and -66 dBsm respectively. This was believed to be due to the low conductivity of wood when compared to steel and to the low dielectric constant when compared to water. Yet the trend of the wooden sphere is similar to that of the steel and water sphere due to their shared geometry. For a wooden sphere to reach the RCS values of a 4 mm steel sphere and water sphere it would have to be 8 mm in size (-65.7 dBsm). The simulated RCS values were collected and plotted in Figure 2.24.

Figure 2.24 showed a clear difference between the simulated RCS of a wooden sphere and that of both the steel and water sphere. The mean difference between the steel and wooden sphere was -17.394 dBsm and the mean difference between the water and wooden sphere is -15.72 dBsm. To further put this in perspective, if the radar designed had a minimum detectable RCS of -80 dBm, then the 4 mm steel and 4 mm water sphere (-71.6 and -74.9 dBsm respectively) would be detected, while the 4 mm wooden sphere (-91.4 dBsm) would be undetectable.
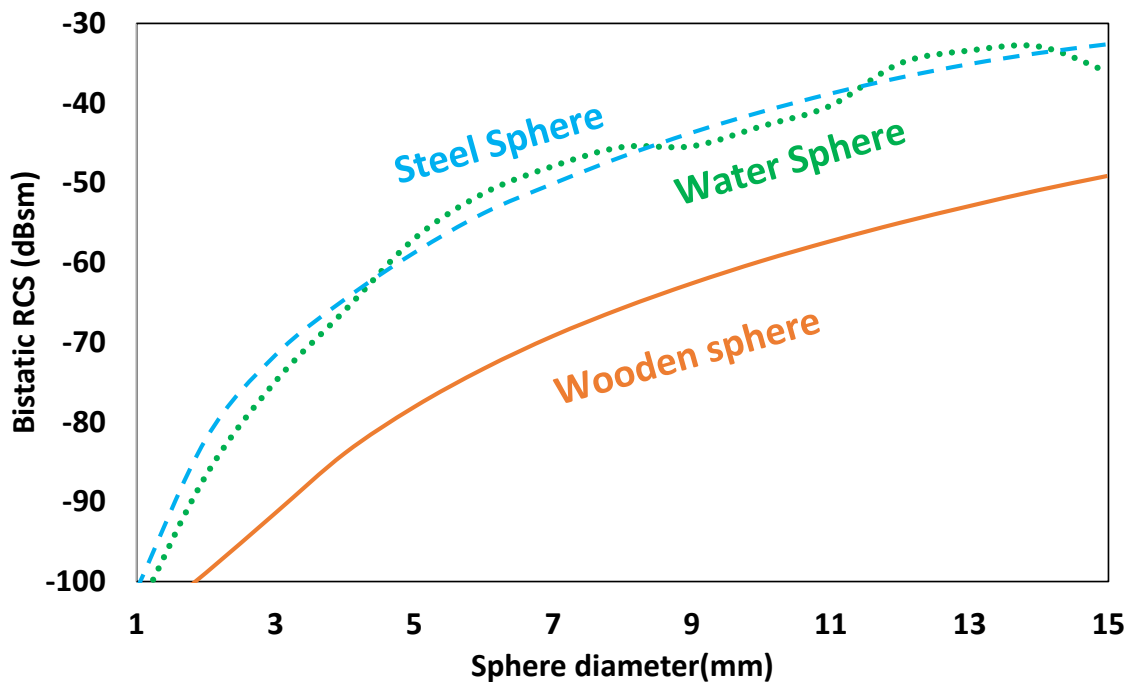
Figure 2.24: Simulated RCS of wooden sphere plotted alongside the steel sphere and water sphere.

To study the impact of coating, the same 4 mm wooden sphere target was coated with different coating layers. The coating layers ranged from 1 nanometre (nm) to 100 micrometres (μm), in intervals of 10 decades. The coated wooden sphere was simulated using the same parameters in the previous simulations, the only difference being the coating layer. Figure 2.25 shows the simulated RCS of the coated wooden sphere when the Silver coating is increased. It can be concluded that Silver coatings within the nm range has little to no impact on the RCS of the wooden sphere, even when a 100 nm coating was applied, the RCS increase was 0.02 dBsm. It was only at 100 μm, where a clear increase of 1.296 dBsm was observed. The 100 μm coating was considered to be applied as it clearly demonstrated its effectiveness in increasing the RCS of the wooden sphere.

A simulation was conducted to evaluate the performance of a 100 μm Silver coating on different diameters of wooden spheres using the same parameters in the previous simulations. Figure 2.26 shows a plot with of the simulated RCS of the coated wooden sphere, which illustrated the impact of the 100 μm Silver coating. This caused an RCS increase, which was evident from the dark brown line when compared to the dashed orange line in Figure 2.26. The RCS increase reached an average value of 11.77 dBsm, which is a significant increase in RCS considering the negligible coating thickness applied. As for the coated 4 mm woo den sphere's RCS, an increased coating thickness would further increase the RCS as concluded from Figure 2.25.
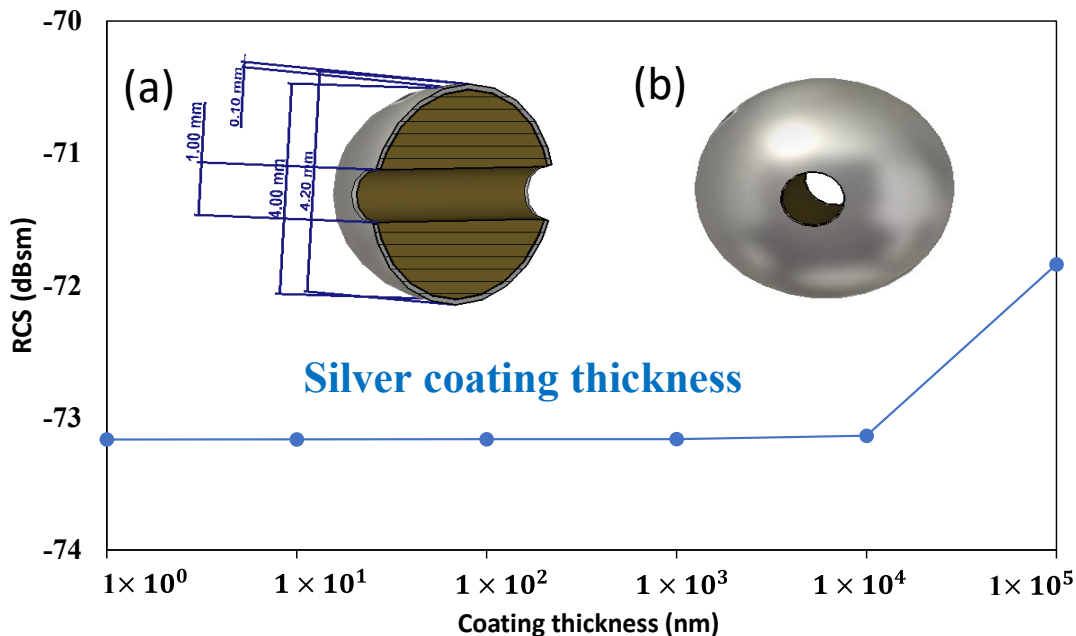
Figure 2.25: Wooden sphere RCS simulation to study the impact of different coating thicknesses, indicating a slight increase in RCS starting at 10 μm and significantly increases at 100 μm. Inset (a) Cross sectional view showing the inner wooden material of the coated sphere and showing the 100 μm coating. Inset (b) coated wooden sphere.
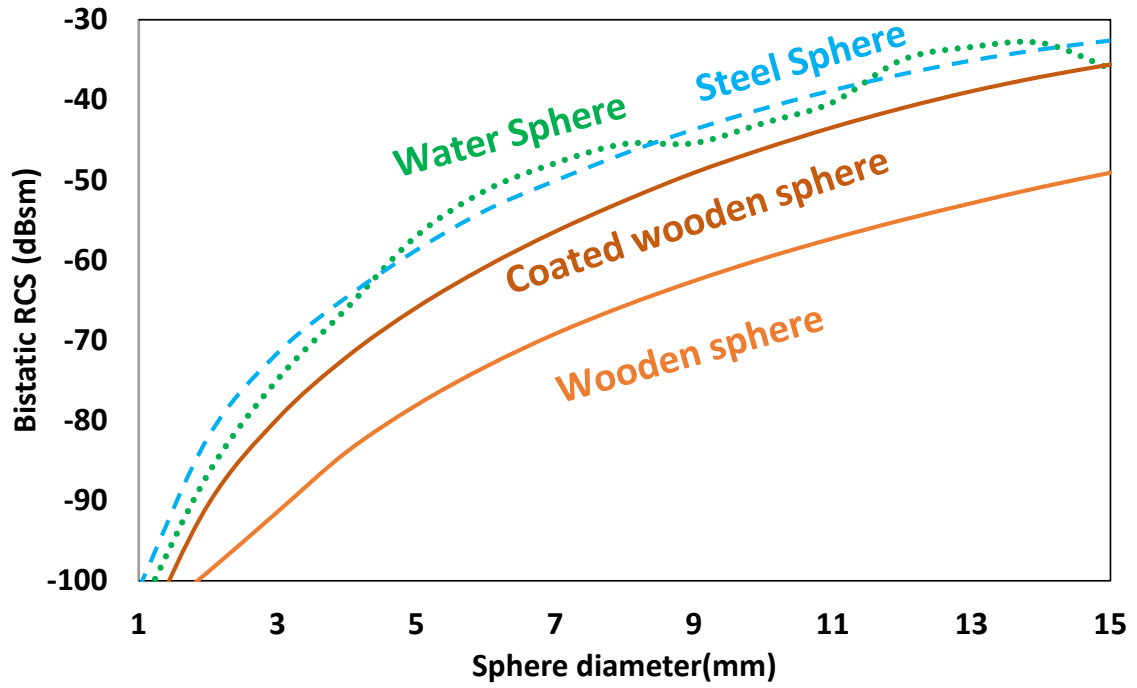
Figure 2.26: Simulated RCS of coated wooden sphere plotted alongside the uncoated wooden sphere, steel sphere and water sphere.

Considering the example of a minimum detectable signal of -80 dBm, if the wooden sphere were to still be detected, the radar would require hardware alteration to detect the wooden sphere's signal. This would cost expenses, time, effort and would require an expert. This is where target coating can be utilised to allow undetectable targets to become detectable. The increase in RCS corresponds to the target appearing 'larger' to the radar due to the target's increased reflectivity as part of the higher conductivity. This also translates to an increase in radar range based on the radar equation, which will be mentioned in more detail in the next chapter.

To illustrate the increase in detection range of the coated wooden sphere compared to the wooden sphere, the minimum detectable signal against range is plotted using equation 2.12.

$$Range = \sqrt[4]{\frac{P_t G^2 \lambda^2 \sigma}{P_r 4\pi^3}}$$

2.12

Where P_t is the transmitted power, G is the antenna gain, λ is the wavelength, σ is the RCS of the target and P_r is the received power. Plugging in the values with respect to a 1 watt 5.8 GHz radar, antenna gains of 12 dBi and the respective RCS of the two targets (uncoated and coated wooden sphere). This is plotted in Figure 2.27, illustrating the increment in range as a function of the target's RCS. The uncoated wooden sphere is

shown as the orange dashed line, the coated wooden sphere is represented by the solid brown line, both of a 4 mm in diameter. It can be seen that the solid brown line is higher than the orange dashed line, which translates to an increased range. To further demonstrate the increase in range between the coated and non-coated target, the red dotted line, representing the minimum detectable signal can be used as a reference.

Doing so, a data point directly before the minimum detectable signal (-80 dBm) was chosen. This data point corresponded to the maximum theoretical range to detect the target. Using this data point, the maximum range values can be extracted which are 0.6 metre and 1.2 metre for the uncoated wooden sphere and the coated wooden sphere respectively. This indicated that the coated wooden sphere achieved double the range of the uncoated wooden sphere, further emphasising the advantage of coating a target.
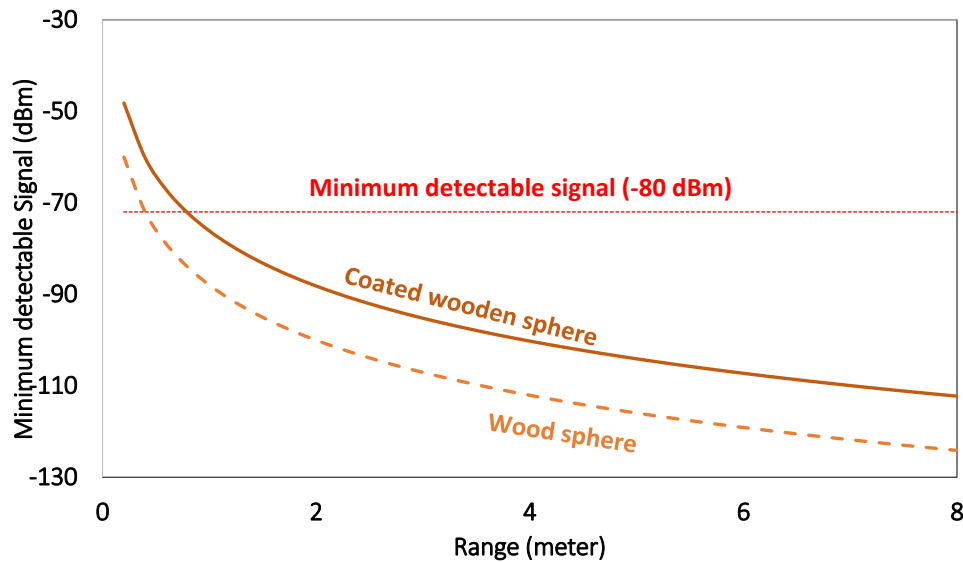
Figure 2.27: Minimum detectable signal plot vs range is plotted with respect to a 1 watt 5.8 GHz radar, antenna gains of 12 dBi and the respective RCS of a non-coated wooden sphere and a coated wooden sphere.

2.7 Coating methods

In order to deposit a 100 µm Silver coating, it would be important to assess different deposition techniques available. Different coating techniques shown in Figure 2.28 were investigated via profilometer readings, such as (a) spray coating, (b) brush strokes and (c) drop casting. Among these methods, a single brush stroke was found to be the most effective in providing an approximate thickness of 100 µm, whereas the other methods provided much thinner layers. Spray coating was used to coat a glass substrate with a thin layer of Silver (dispersed in water) from Sigma Aldrich. The coating was sprayed twice, which upon profilometer inspection achieved and an average surface thickness of 200 nm (approximately 100 nm per spray), as shown in Figure 2.28(a).
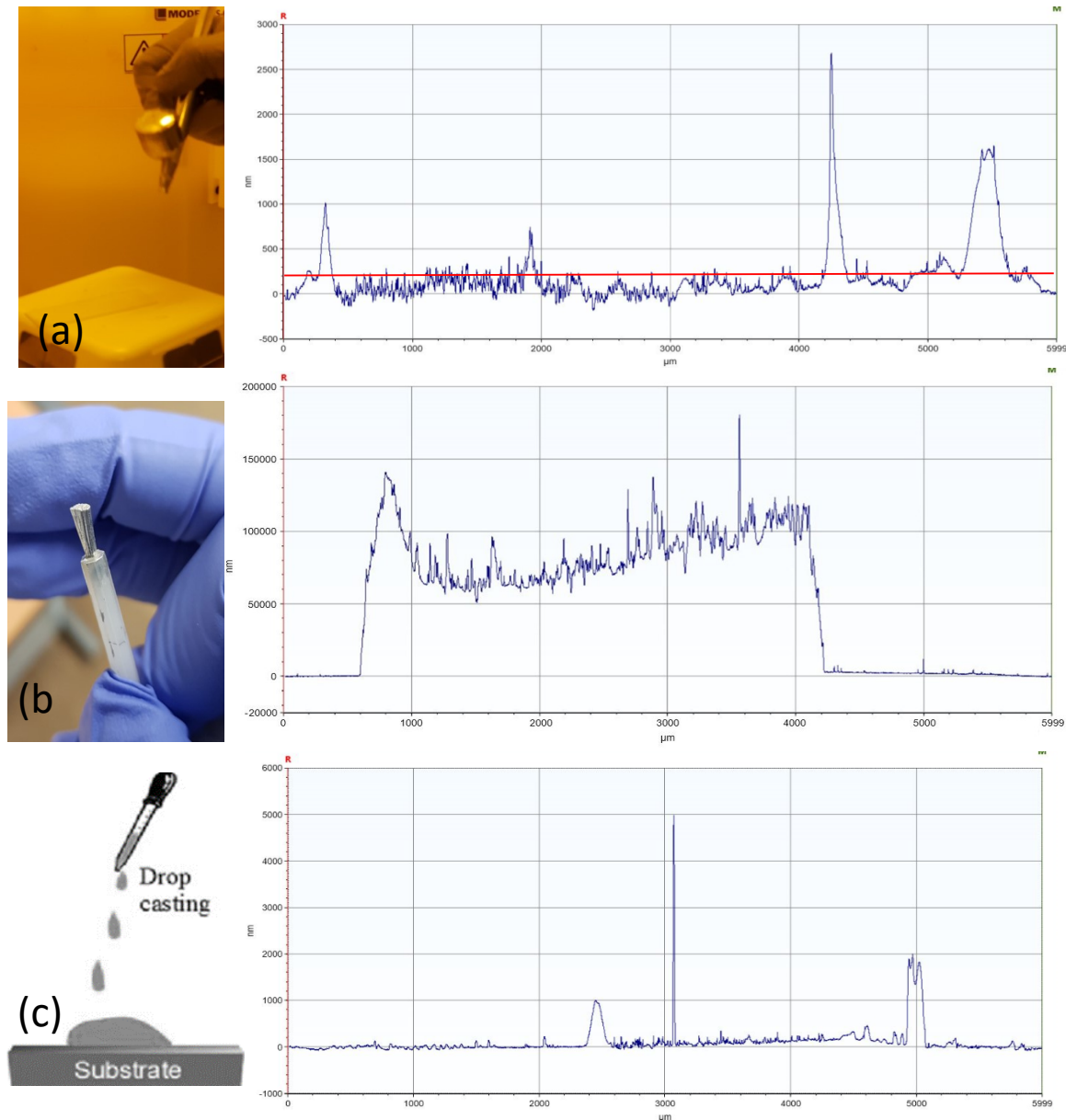
Figure 2.28: Samples that were investigated via profilometer readings. (a) Spray coating, (b) brush strokes and (c) drop casting.

It can be argued that the spray coating nozzle can be larger, allowing a larger spray area. The issue here would be that the sprayed coating would cover unwanted regions on the bee, as controlling the sprayed material would be very difficult. A method to counter nanomaterial sized coating to reach unwanted areas, would be to produce a mould that would only expose the back of the bee. This could solve the issue, but due to different bee sizes and future intentions to use different insects, this method would be limited. The spray coated substrate showed some high peaks in the profilometer scans, which are believed to be due to contaminations on the substrate's surface. This is a limitation of substrate cleanliness as to an immediate disadvantage of the spray coating method and can be observed on other coated samples as well.

Drop casting was also attempted for the same Silver dispersion, which provided an average surface thickness of 100 nm with evident drop casting "coffee rings" on the sides of the deposition (common artefact in drop casted samples). Substrate impurities can also be seen to cause large spikes in profilometer data. As a result, a single brush stroke would be the best solution to apply a layer of ~100 μm.

2.8 Preliminary study prior to coating bees

Before a bee could be considered for coating, several studies were conducted to answer crucial technical and ethical questions. Such questions are:

a) Does the bee's body support coating?

b) Is coating a bee dangerous for its health?

c) Where would the ideal coating region be?

d) How thick should the coating be?

e) Will coating bees have a positive outcome for its use in radar applications.

To answer the first question, it was important to inspect the insect's body surface, in order to characterise its suitability for potential coating. The body of the bee was inspected using two methods: optical inspection using an optical microscope and a surface topography using a Scanning Electron Microscope (SEM). The Eclipse ME600L optical Nikon microscope provided images of the insect's body, identifying potential locations for coating, shown in Figure 2.29. The microscope identified the abdomen, thorax and limbs suitable for coating, but failed to identify the approximate lengths of the observed hair and the morphological structure of the hair. This encouraged to have a closer view using the SEM. However, SEMs operate under high vacuum and require conductive targets. As a result, performing an SEM scan of a biological specimen faces two main challenges;

a) Biological specimens contain fluids which may outgas in a high vacuum, damaging the biological sample and the SEM system.

b) Biological specimens are not conductive enough for the focused electron beam. As a result, the bee's surface would first need to be coated with a metallic layer to increase the insect's conductivity to support electrons to reflect of the surface of the insect's body. Nonconductive targets would absorb the electrons and result in scanning faults. Hence, the insect needs to be fully coated.

Figure 2.29: A 12.3 mm long dead honeybee inspected using a Nikon microscope, showing different areas of interest.

In order to fully coat the insect with a metallic layer to support SEM scans, straightforward coating methods such as dip coating, drop casting, spray coating and spin coating would result in overcoating or insufficient coating. Hence, the most effective form of coating would be thermal evaporation or sputtering. Since our biological specimen (bee) does not withstand the heat of a thermal evaporator, the sputtering machine makes the most suitable approach. However, the sputtering system works under high vacuum as well, which can cause issues to the sample and the sputtering system. As a result, prior to coating, the sample requires to be dried (remove its internal liquid content).

2.8.1 Biological sample drying

This is an important prerequisite to exposing biological samples in any machine that operates under a vacuum (e.g., sputtering machine, thermal evaporator, plasma etcher, and SEM). There are different methods of sample drying, among such methods are; conventional air drying and chemical drying agents. Conventional air drying involves leaving the sample to dry over time. The issue with this method is that as fluids and air leave the gradually leave the insect's body, it causes associated surface tension to rise, which could result in 45% shrinkage of the insect, thus mis-forming the original shape and size in addition to distorting the insect's structural integrity [171]. To preserve these negative impacts, chemical drying agents are recommended. Chemical drying agents

allows drying of biological samples without crushing the insect's structure due to tension forces and without the need of significant investments on methods such as freeze drying (FD) or critical point drying (CPD).

The drying process was carried out in Bangor University's clean room, within the fume hoods to contain the toxic fumes. This is shown in the experimental setup illustrated in Figure 2.30(a).

The insect's dead body was placed in a vial filled with a 100% concentration of Ethanol for 20 minutes as shown in Figure 2.30(b). The sample would then be transferred to a new vial containing a solution of 2:1 Hexamethyldisilazane (HDMS) for 20 minutes. Caution needs to be practiced while working with HDMS as it is a highly toxic solution. The sample was then moved to a new vial containing 100% HDMS and was left loosely covered in the fume hood overnight, as shown in Figure 2.30(c). A day later, when inspecting the sample, the HDMS evaporated and the sample was dehydrated and ready for sputtering.
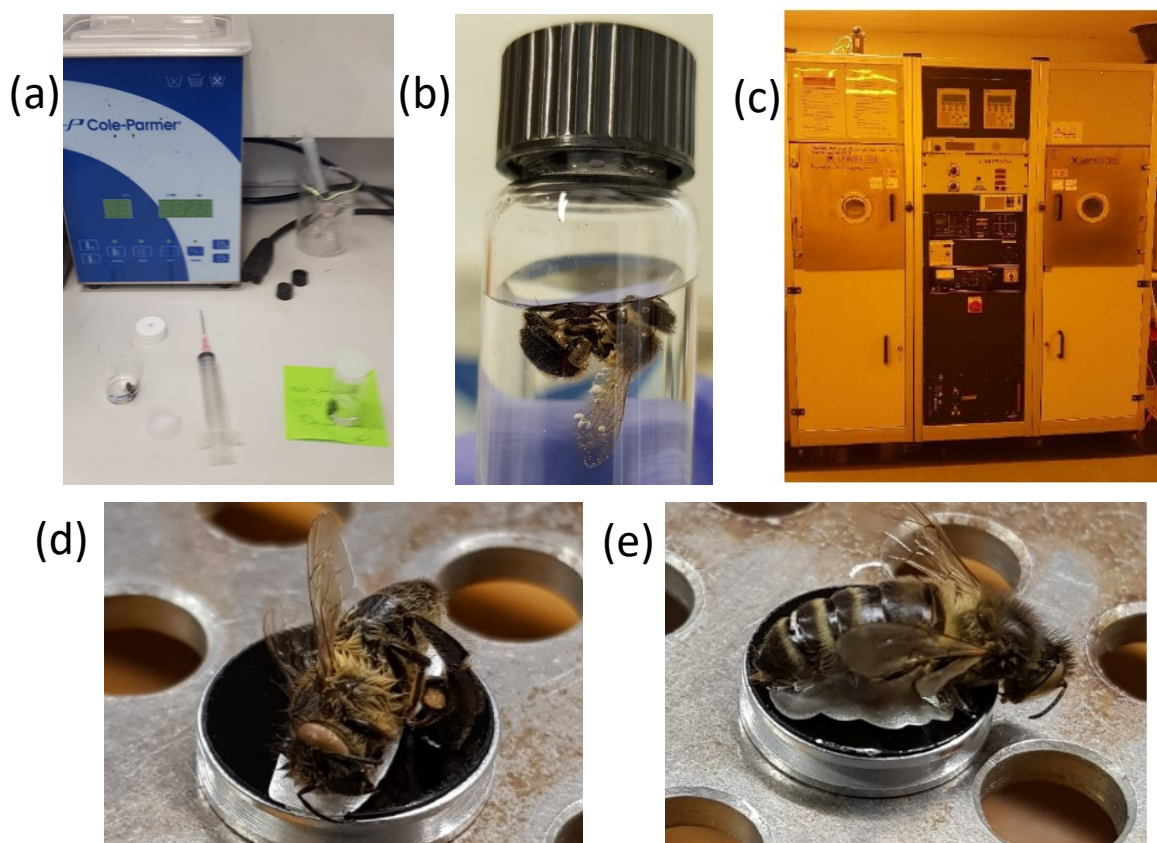
Figure 2.30: (a) Experimental setup for the chemical drying of the honeybees (b) Honeybee submerged in 100% ethanol solution(c) Leybold Univex 350 Sputtering Machine in the clean room [172] (d) Honeybee 1 fixed to sputtering machine chuck (e) Honeybee 2 fixed to sputtering machine chuck.

The chemically dried honeybees are visible in Figure 2.30(d) and (e). It can be observed that the external structure of the bees was preserved, the bee's morphology was maintained and it has not been crushed/squished together due to tension forces. This was achieved without the requirement of large investments for specialised equipment through a quicker method. It is important to emphasise the toxicity of HMDS for biological sample chemical drying process and the complete adherence to the University's safety regulations is highly recommended.

2.8.2 Sputter coating

The dehydrated bees were then prepared for the sputtering machine, by securing the bees on metal stubs as shown in Figure 2.30(d) and (e). Once the chuck containing the bees was loaded in the sputtering machine, chromium was loaded into the sputtering machine and 20 nm thickness of coating was chosen. The sputtering was performed in a Leybold Univex 350 Sputtering Machine shown in Figure 2.30(c).

Once completed the metallic coating of chromium was clearly visible as shown in Figure 2.31(a) and (b). The coated bees maintained their shape during the coating due to an effective chemical drying process and were not crushed during the sputtering process. The coated bees were removed and prepared for SEM scanning in the imaging laboratory.
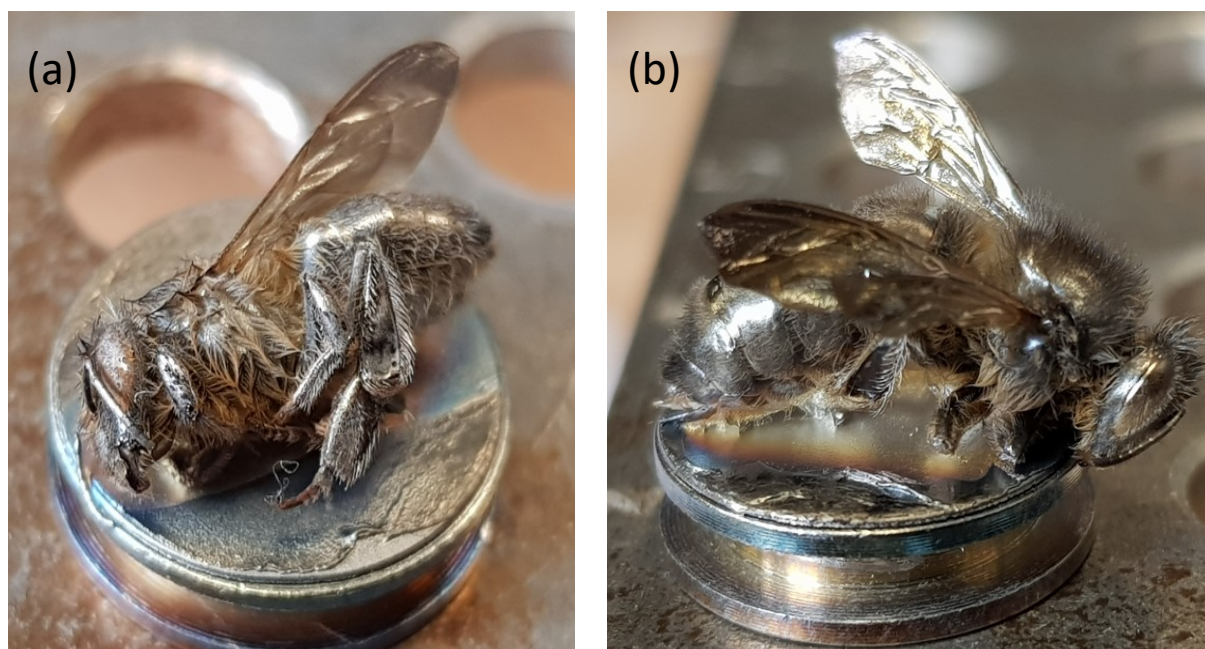
Figure 2.31: The 20 nm Chromium sputtered bees (a)Honeybee 1 (b) Honeybee 2.

2.8.3 Scanning Electron Microscope

Once the honeybees are dried and coated, the SEM supports the use of these samples and can thus provide accurate topographical scans. The SEM scans were performed using the Hitachi S-520SEM, located in the imaging lab in Bangor University. After the scan, the bees maintained their structural integrity, which is another indicator to the effectiveness of HMDS drying procedure. Several SEM scans were obtained of the bee, where the four most important ones are shown in Figure 2.32. The rest of the SEM scans can be found in Appendix A.
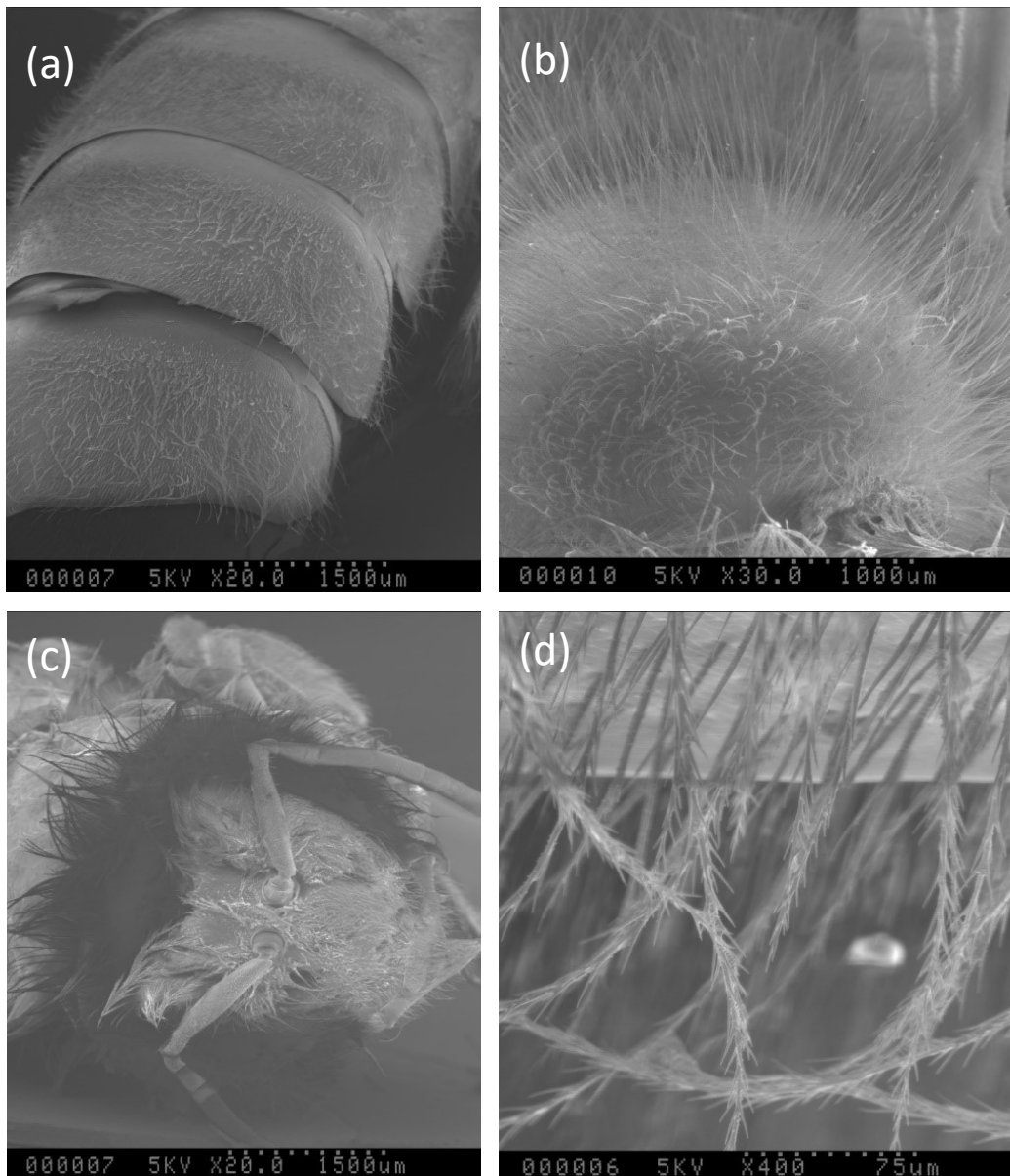
Figure 2.32: SEM scans of Chromium sputter coated honeybees indicating different morphological features of the bees which are not visible using an optical microscope (a) Abdomen of a coated honeybee (b) Thorax of a coated honeybee (c) Head of a coated honeybee showing the antennas and part of the abdomen as well (d) 400x image of the honeybee abdomen seta.

The SEM scans showed interesting close-up images of the bee's morphology, indicating several places that could be considered suitable for coating due to the hairy body of the insect. The two most interesting locations observed were the thorax and the abdomen of the insect. These areas displayed long hair, known as *seta.* The length of the seta was visually approximated based on the SEM's indicated scaling, which resulted in seta length ranging from 300 to a 1000 μm.

Other interesting areas that were suitable for coating were the lower parts of the abdomen, thorax and the limbs as these were also covered in long seta. In fact, the longest seta observed was around the limbs and thorax. Interestingly enough, these observations were in line with literature, where the longest hairs noted were also from the same region identified in this study [173]. The SEM scans provided visual evidence of suitable areas which seemed favourable for coating applications in terms of the available area for coating and the bee's seta. This answers the initial question of whether bee bodies morphologically support a coating layer.

2.8.4 Ideal coating location

It was concluded earlier that a 100 μm Silver coating would effectively increase the RCS of a wooden sphere. Applying the same methodology to a bee would provide an interesting study that may potentially increase the insect's RCS. This method seems feasible, since a 100 μm Silver coating is a very low thickness, has negligible weight and could cause no constraints on a honeybee if deposited on a honeybee's thorax and abdomen. A wide range of simulations took place to decide the optimal coating method for a honeybee, where at first it was expected to coat the entire thorax and abdomen.

The SEM scans provided a good overview of suitable locations for coating (abdomen, thorax and limbs). However, further investigations concluded that honeybees cannot have their abdomen, thorax and limbs fully coated. As for the limbs, these are used to gather pollen and coating them could potentially limit and obstruct their pollination capabilities. Furthermore, it was mentioned in [174] and illustrated in Figure 2.33 below, that honeybees have 10 small holes on each side of their body, two on their thorax and eight on their abdomen. These holes are known as spiracles and support the breathing of honeybees. Coating an entire bee, may block these spiracles, limiting their breathing capabilities.
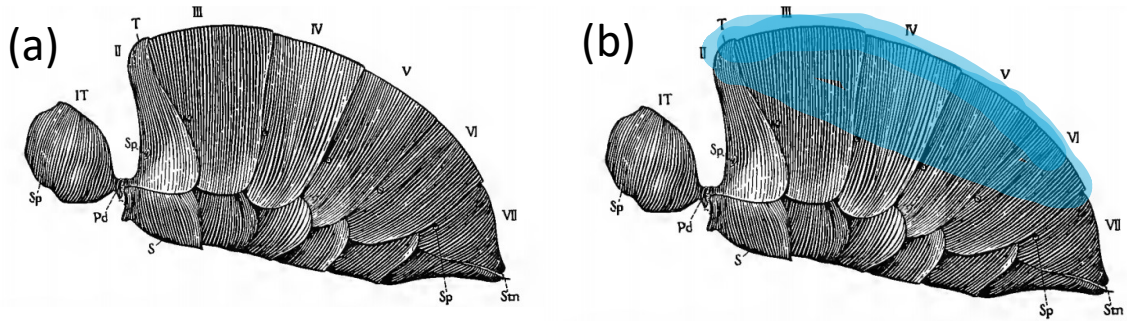
Figure 2.33: (a) A honeybee thorax illustrating the spiracles (b) Coated region shown on the top of the bee in blue [174].

In a study by White *et al.,* honeybee spiracles were blocked with wax. It was noticed that bees lost their power of flight, where White related the impact to be similar to that of a severe infestation of a mite called the *Acarapis woodi* [175]. As a result, it is important to take these spiracles into account and prevent blocking them via a full-body coating. Figure 2.33(a), shows the spiracles on the sides of the honeybee's body, which need to be avoided. An optimal location for coating is thus the upper part of the abdomen and thorax as indicated in Figure 2.33(b) in blue. This answers the question regarding the potential danger, negative impact associated with coating and how these dangers could be prevented by choosing an ideal coating region. The 100 μm coating of Silver was decided to be placed on the top of the honeybee The bee model that was used for the previous simulations was used again, whereas this time, a 100 μm Silver coating layer was applied to the bee as shown in Figure 2.34(b) below.
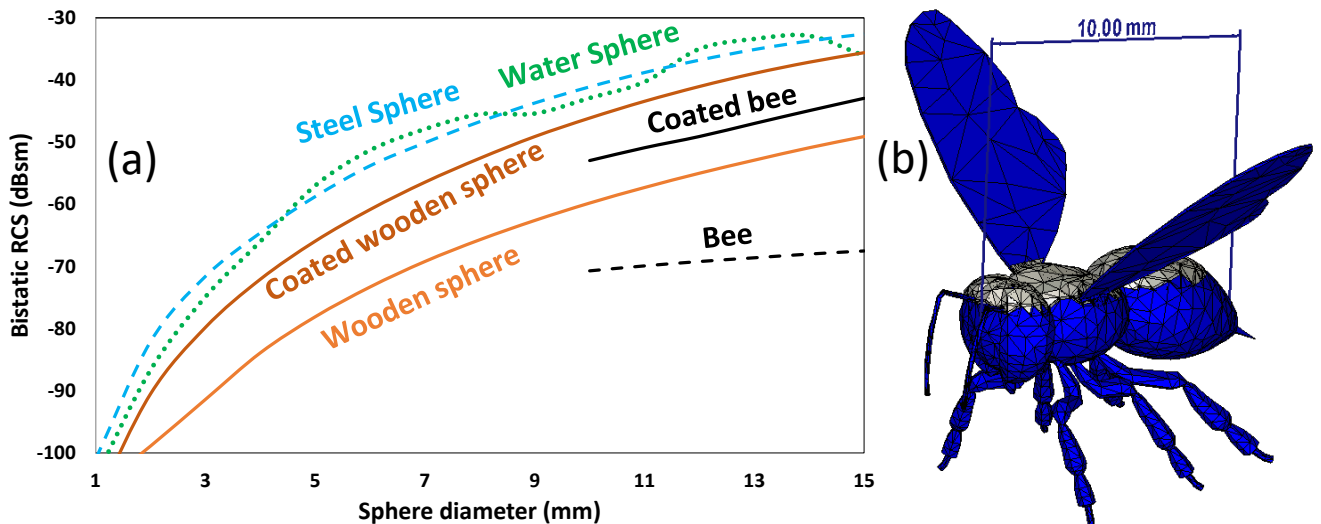
Figure 2.34: (a) Collective plot of RCS simulation showing the simulation of an uncoated honeybee (dashed black line) and a coated honeybee in a black line. (b) A honeybee model of approximately 10 mm long with a 100 μm of Silver coating on the upper layer of the bee in CST Microwave studio used for honeybee RCS simulation.

The coated honeybee was similarly simulated in CST Microwave studio using the same RCS simulation settings. The result of the RCS simulation is shown in Figure 2.34(a), which combined the previously shown RCS simulations, in order to provide a complete overview of the RCS simulation.

Figure 2.34(a) demonstrated the impact of the Silver coating on the honeybee. The average increase in RCS was observed to be $\sim$ 21 dBsm, which is a significant increase. To put this in perspective, an uncoated bee of 10 mm length had an RCS of -70.07 dBsm. This is nearly equal to a 3 mm steel sphere (simulated RCS of -70.08 dBsm), whereas a coated honeybee of same length has a simulated RCS of -52.97 dBsm, which is nearly equal to a 6 mm steel sphere (-52.8 dBsm).

Effectively, since the 10 mm uncoated bee is almost equal to a 3 mm steel sphere in terms of RCS, and the 10 mm coated bee is almost equal to the 6 mm steel sphere in terms of RCS. A conclusion can be made that the coating applied had the same impact of doubling the size of the steel sphere if the RCS of the steel sphere was target under investigation. In other words, if this RCS increase was studied explicitly for the steel sphere, an increase from -70.08 to -52.8 dBsm would indicate that the steel sphere has doubled in size. This clearly demonstrates the potential impact of coating an object to increase the target's RCS.

As shown earlier in Figure 2.27 using the radar range equation (2.12), the minimum detectable signal against the range of the non-coated wooden sphere and coated wooden sphere was plotted, a similar approach can be carried out for the uncoated honeybee and coated honeybee. This allowed finding the increased range due to the coating applied. Figure 2.35 was plotted while considering a 1 watt, 5.8 GHz radar, with 12 dBi antenna gain, a minimum detectable signal of -80 dBm, a 10 mm long uncoated bee's RCS of -70.07 dBsm and a coated bee's RCS of -52.97 dBsm.

Figure 2.35 shows a graph plotted as a function of RCS to study the maximum distance that the radar can support. Both the uncoated and coated bee converged towards the minimum detectable signal as the range increases. However, due to the difference in RCS values, the convergence occurs at different ranges. The uncoated bee (blue dashed line) reached a distance of 2.4 metres while the coated bee (blue solid line) reaches a distance of 3.8 metres. This is an increase of 0.6 metres, which demonstrates the feasibility of coating to increase the detection range. However, this is the case for a 10 mm long honeybee, being the approximated smallest length of a honeybee.
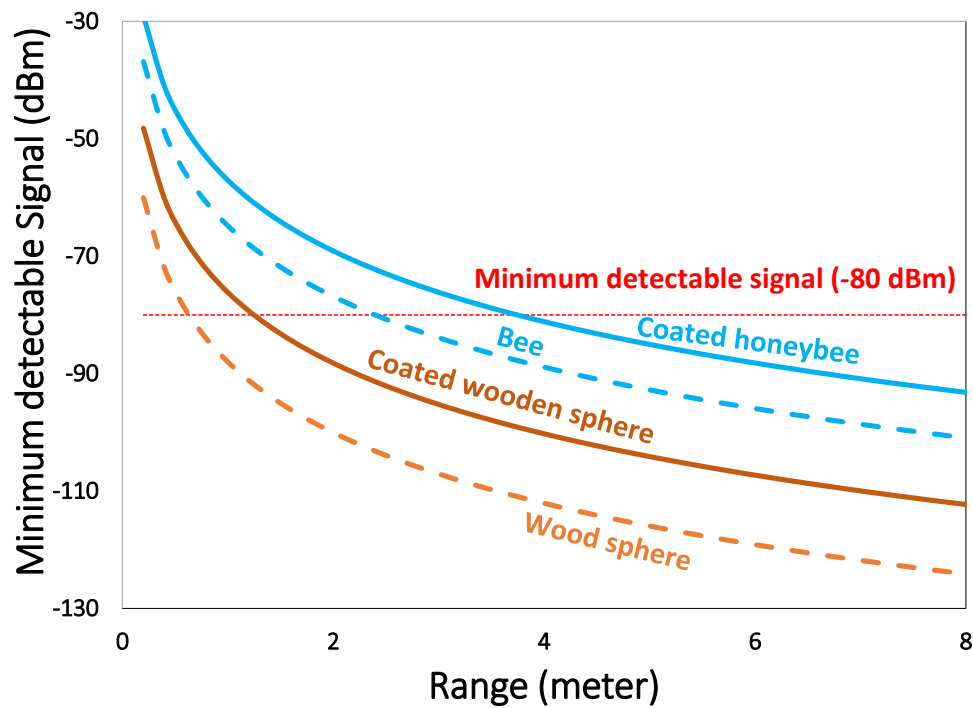
Figure 2.35: Minimum detectable signal vs range is plotted with respect to a 1 watt 5.8 GHz radar, antenna gains of 12 dBi and the respective RCS of a uncoated wooden sphere, a coated wooden sphere, an uncoated honeybee and a coated honeybee.

In order to obtain an average estimation of coating impact on honeybees, the same graph in Figure 2.36 was plotted while using the average RCS of both non-coated honeybees and coated honeybees of sizes 10 and 15 mm. The RCS values were based on the simulations that were performed on uncoated and coated bees. These RCS values were -66.14 dBsm and -47.95 dBsm for average uncoated bees and average coated bees respectively. The RCS values were plugged in the range equation to obtain the results that were plotted in Figure 2.36.

The plot showed the maximum obtainable distance for the average RCS of 10 mm and 15 mm long uncoated honeybees and coated honeybees. The uncoated bee and coated bee reach the minimum detectable signal at 1.8 and 5 metres respectively. This showed that the coated approach, provides 2.7 times increase in range as compared to the uncoated approach, which further emphasised the merits of Silver conductive coating application for increased RCS.
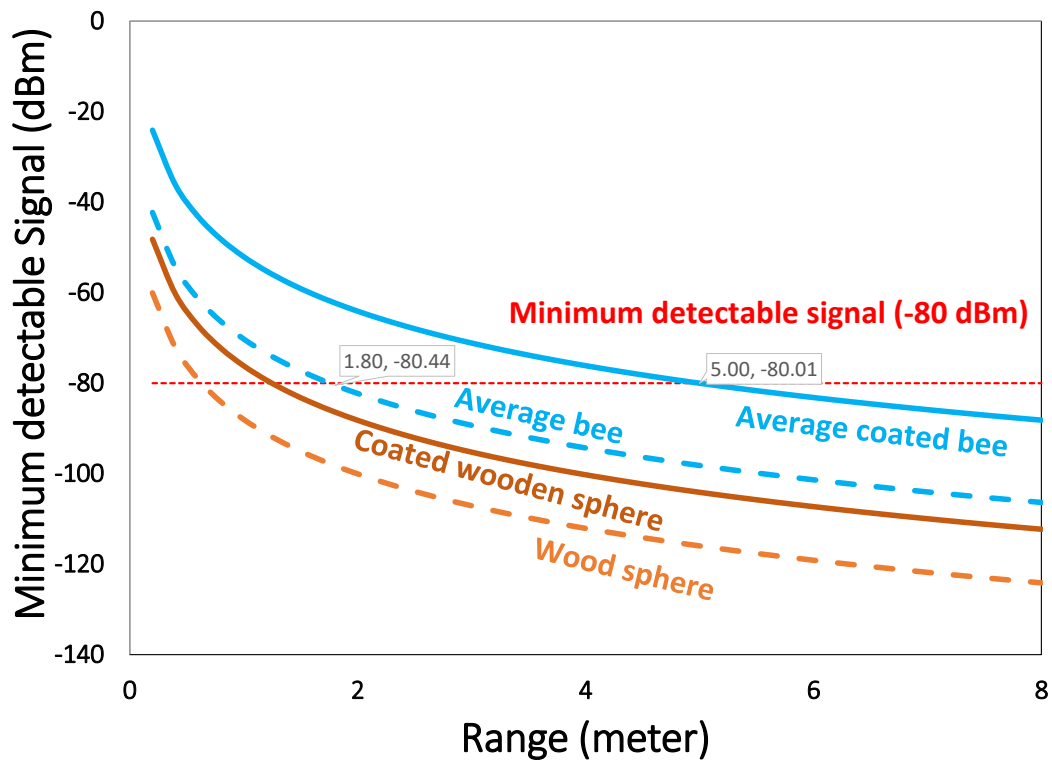
Figure 2.36: Minimum detectable signal vs range was plotted with respect to a 1 watt 5.8 GHz radar, antenna gains of 12 dBi and the respective RCS of an uncoated wooden sphere, a coated wooden sphere, average RCS of an uncoated honeybee and an average RCS of a coated honeybee.

An important coating consideration is the skin depth, which is a characteristic of electromagnetic waves that describes the depth at which the amplitude of the electric field is attenuated by 1/e or 36.8%, after propagating a distance of one skin depth [176]. This distance is small for a good conductor at microwave frequencies. Due to skin depth, electromagnetic waves tend to concentrate on the surface of a conductor, rather than penetrating the bulk of the conductor. At higher frequencies, such as 5.8 GHz, the skin depth of a conductor becomes much smaller, meaning that the electromagnetic wave only penetrates a very thin layer of the conductor. This results in an increase in the resistance of the conductor, as the current is concentrated in a smaller cross-sectional area of the conductor. This effect can cause significant energy loss in the form of heat, reducing the efficiency of microwave devices.

Chapter 3.   Design of 5.8 GHz CW Radar for Insect Monitoring

This chapter outlines the theory and methodology associated with the design and assembly of a 5.8 GHz CW radar for insect monitoring. A simulation of the radar, the radar's design, development, continued optimisation resulting in different versions of the radar and initial results are discussed within. Furthermore, this chapter touches on the RCS simulations that were conducted in chapter two, while obtaining a calibration model, experimental validations of the simulations and establishing the requirements for a dynamic insect monitoring system.

3.1 Motivation

The design and development of the 5.8 GHz radar stemmed from the need of a distant, portable and unobtrusive monitoring solution for honeybees. The current radar design was inspired from the original coffee can radar designed by Gregory Charvat at MIT [177], [178]. The radar's name was chosen due to its antennas made out of empty coffee cans, referred to as cantennas. Their system entails multiple SMA connected RF modules that allows the radar to operate in three modes; continuous wave, frequency modulated continuous wave (FMCW), and a synthetic aperture (SAR) mode. The 2.4 GHz radar system uses an analogue modulator to provide a voltage ramp, allowing the VCO to generate a RF signal that increases in frequency along with the increase of voltage of the ramp. For signal digitisation, the system comprises a laptop with a built-in sound card.
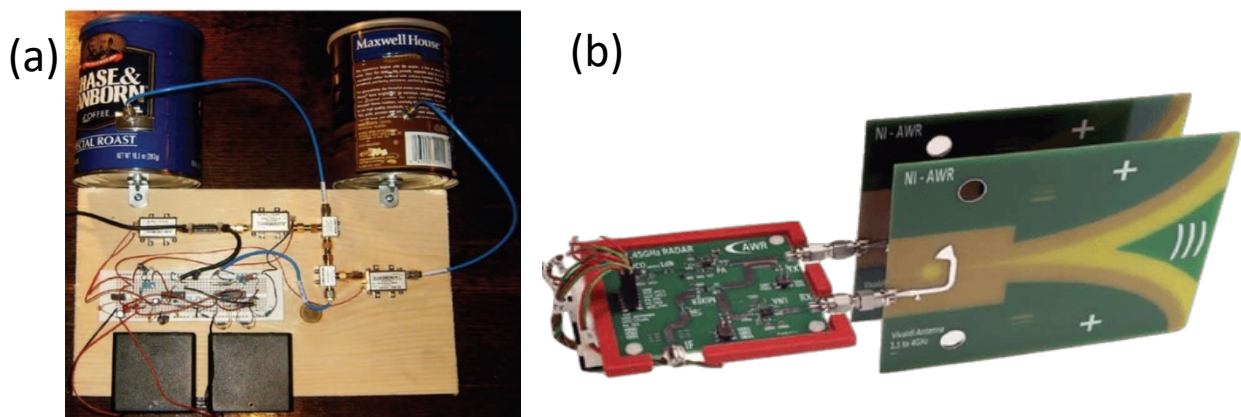
Figure 3.1: (a) 2.4 GHz coffee can radar by MIT (b) 2.4 GHz re-designed coffee can radar by AWR NI [179].

3.2 Radar Equation

The radar equation determines essential factors that dictate the radar's performance such as the received power present in the echo signal that is reflected back from the target with a specified RCS at a specific range, the transmitted power and propagation factors. These different parameters are combined in the radar equation to give an overall estimation of the radar's performance, which is naturally the first step in radar design.

The following assumes isotropic propagation with P_T being the transmitted power and no impedance mismatch between the transmitter and the antenna. The target RCS is denoted as σ, and located at range R which is assumed to lie in the far-field region of the antenna. Thus, the power density from an isotropic antenna at range can be calculated from the emitted power and considering the inverse square law spread out [112], [146]:

$$P_R = \frac{P_T}{4\pi R^2} \qquad\qquad 3.1$$

Since the radiated power is emitted using directive antennas of a certain gain, the power density from a directive antenna with a transmitting gain of G_T is then

$$P_R = \frac{P_T G_T}{4\pi R^2} \qquad\qquad 3.2$$

The incident power density upon the target is reflected in different directions depending on the target RCS. Therefore, the power density P_R reflected back to the radar receiving antenna is:

$$\frac{P_T G_T}{4\pi R^2} \times \frac{\sigma}{4\pi R^2} \qquad\qquad 3.3$$

The radar's receiving antenna Rx, receives a fraction of the echo signal re-radiated from the radar target's RCS. The radar's received power is defined as the product of the incident power density (as shown in equation 3.3) multiplied by the receiving antenna's effective area, denoted as A_e. The antenna's effective aperture area is related to the antenna's physical area through the following equation:

$$A_e = \rho_a A \qquad\qquad 3.4$$

Where A is the physical area of the antenna and ρ_a is the antenna's aperture efficiency. The received power P_R in watts is then defined as:

$$P_R = \frac{P_T G_T}{4\pi R^2} \times \frac{\sigma}{4\pi R^2} \times A_e = \frac{P_T G_T A_e \sigma}{(4\pi)^2 R^4} \qquad \text{3.5}$$

Using the above radar equation, the variables can be rearranged to obtain specific metrics. As for the maximum range of the radar R_{max}, is the range value where the target becomes undetectable by the radar. This happens when the received signal power P_R, is equal to the minimum detectable signal (MDS) denoted as P_{min}. The fundamental radar range equation for the maximum distance is defined below.

$$R_{Max} = \sqrt[4]{\left[\frac{P_T G A_e \sigma}{(4\pi)^2 P_R}\right]} = \sqrt[4]{\left[\frac{P_T G A_e \sigma}{(4\pi)^2 P_{min}}\right]} \qquad \text{3.6}$$

The antenna aperture in equation (3.4) is related to the antenna gain, where the wavelength is defined as $\lambda = c/f$, c is the velocity of propagation and f is frequency [176]. Using different antennas for transmission, assuming no impedance mismatch and the absence of polarisation mismatch to solve for effective area A_e, the equation can be rearranged to

$$A_e = \frac{\lambda^2 G_R}{4\pi} \qquad \text{3.7}$$

By substituting above equation (3.7) for gain into equation (3.5) the received echo signal power for different antenna gains G_T and G_R can be calculated as:

$$P_R = P_T \frac{G_T A_e \sigma}{(4\pi)^2 R^4} = P_T \frac{G_T \sigma G_R \lambda^2}{(4\pi)^3 R^4} \qquad \text{3.8}$$

Where G_R is the receiving antenna's gain at range R and wavelength λ. If the same antenna is used for both transmitting and receiving, then the effective area A_e and G gain have a relationship defined as:

$$G = \frac{4\pi A_e}{\lambda^2} = \frac{4\pi \rho_a A}{\lambda^2} \qquad \text{3.9}$$

By substituting equation (3.9) with Equation (3.6) initially for A_e and then for gain, two alternative radar equation forms are derived as shown in left most part and right most part of equation (3.10).

$$R_{Max} = \sqrt[4]{\left[\frac{P_T G^2 \lambda^2 \sigma}{(4\pi)^3 P_{min}}\right]} = \sqrt[4]{\left[\frac{P_T A_e^2 \sigma}{4\pi \lambda^2 P_{min}}\right]} \qquad \text{3.10}$$

Assuming the need to design a 5.8 GHz radar capable of detecting a human being (σ = 1 m^2) at a range of 100 metre, with antenna gains of 10 dBi and a transmitted power of 15 dBm. Using equation (3.8), these parameters can be inserted to find out the received echo signal at the radar, as shown below.

$$P_R = P_T \ \frac{G_T \sigma G_R \lambda^2}{(4\pi)^3 R^4} = 0.032 \cdot \frac{10 \cdot 1 \cdot 10 \cdot (0.0517)^2}{(4\pi)^3 \cdot (100)^4} = 0.032 \cdot \ 1.34 \times 10^{-8} = 4.3 \ \times 10^{-10} = -63.6 \ dBm$$

Increasing the transmitted power, decreasing the range, increasing the RCS, increasing the antenna gains are all factors that increase the received power. The radar equations can be used for the design of various types of radar systems: pulse doppler, CW, FMCW and ultra-wideband (UWB) radars. The radar of interest in this study is the CW radar, which will be described in further detail below.

3.3 CW Doppler radar

CW radars, also known as Doppler radars, utilise a CW oscillator responsible for generating a single continuous wave/tone with a constant amplitude and constant frequency. A CW radar transmits and receives constantly, thus requires no switch as in pulsed radars. CW radars can have two antennas for the Tx and Rx signal respectively, or a single antenna with a circulator or a duplexer to separate the Tx and Rx signals. CW radars can feature a low transmitted power, high sensitivity and simple architecture.

The Doppler radar, relies on the Doppler effect (Doppler frequency shift) to measure the velocity of a moving target. A change in frequency or pitch upon the motion of the source or receiver, is known as the Doppler shift. Like any other radar, the CW radar transmits and receives the reflected EM signal. However, as the target moves, the target interacts with the transmitted EM waves, which causes a change in frequency/pitch of the reflected EM wave. The Doppler effect is thus the perceived change in pitch between the source and the receiver and is proportional to the radial velocity of the target [180].

If a sound source is releasing a signal of known amplitude and frequency, the receiver should perceive the same signal if both maintained a stationary position. If the transmitter is moving towards the receiver, the receiver will receive the sound signals at a higher frequency of what is generated. This is because the receiver, is capturing more waves per second. If the transmitter is moving away, the perceived sound at the receiver appears at a lower frequency, as the number of waves being captured is less. The Doppler phenomenon explains the shift in the waveform due to the target's motion with respect

to the radiating source. The Doppler shift can be positive (blue shift) or negative (red shift) depending on the direction of the target with respect to the radiating source, where blue is towards the radar and red is away [181]. Figure 3.2 shows a custom-designed Doppler radar transmitting a signal in blue and receiving a Doppler shift in the reflected signal in blue, which can be utilised to extract the target's radial velocity.
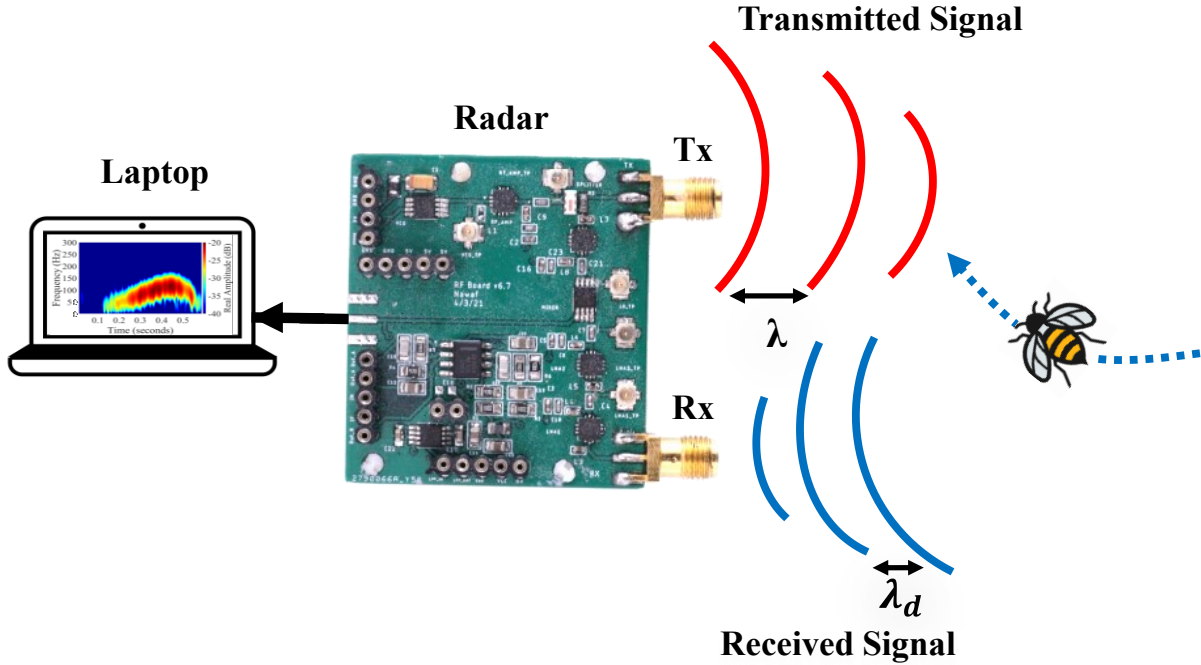
Figure 3.2: Simple illustration of the Doppler shift in blue as a result of a target's interaction with a transmitted EM signal in red and a received signal in blue.

3.3.1 CW Principle of operation

A CW radar consists of CW transceiver, which transmits/receives an unmodulated signal and is either equipped with a heterodyne receiver or a homodyne receiver. A transmitted signal expressed in the time domain is,

$$S_t(t) = cos(\omega_0 t) \hspace{4cm} 3.11$$

Where ω_0 defines the radian frequency of the transmitted RF signal, which propagates until it is reflected off a target and is received by the receiving antenna. This occurs after the reflected signal experienced phase delay and amplitude changes through its interaction with the target's RCS, which is expressed as,

$$S_r(t) = A \, cos\left(\omega_0 t + \frac{2\pi}{\lambda}\big(2R + 2d(t)\big)\right) \hspace{2cm} 3.12$$

In equation (3.12), A is the received signal's amplitude, R is the distance between the radar and the target and $d(t)$ is the target's displacement/motion. The relation

between wavelength and radian frequency is expressed below, where c is the speed of light in air and f is the frequency of operation.

$$\lambda = \frac{c}{f} = 2\pi \frac{c}{\omega}$$
3.13

Since the output of a Doppler system is a comparison between the transmitted and received signal, a comparison of sinusoid phase can be carried out by multiplication as,

$$S_r(t)S_t(t) = A \cos\left(\omega_0 t + \frac{2\pi}{\lambda}(2R + 2d(t))\right)\cos(\omega_0 t)$$
3.14

Through the application of trigonometric identity,

$$\cos a \cos b = \frac{\cos(a - b) + \cos(a + b)}{2}$$
3.15

The following equation is obtained,

$$S_r(t)S_t(t) = \frac{A}{2}\cos\left(\frac{2\pi}{\lambda}(2R + 2d(t))\right) + \frac{A}{2}\cos\left(2\omega_0 t + \frac{2\pi}{\lambda}(2R + 2d(t))\right)$$
3.16

Where the lower term of the above equation exhibits twice the frequency of the transmitted signal. The higher frequency component is thus filtered out using a low pass filter, resulting in the below signal as the received baseband signal [180],

$$x_r(t) = \frac{A}{2}\cos\left(\frac{2\pi}{\lambda}(2R + 2d(t))\right)$$
3.17

Equation 3.17 shows the baseband output of the radar is cosine of the phase. This receiver is known as a direct conversion receiver or a homodyne receiver and has only one output, thus known as a single-channel receiver [180]. Both the positive and negative Doppler shifts fold into a single frequency band after the mixer's down-conversion to baseband signal.

3.3.2 Doppler Shift

As mentioned, the CW radar operates by evaluating the phase difference between the transmitted and the received signal. The total number of wavelengths λ in a two way path, initiating from the radar to the target at range R and back towards the radar (round trip), is $2R/\lambda$, where each wavelength corresponds to a change in phase of 2π radians[177], [180]. A two-way propagation path total phase change is,

$$\varphi = 2\pi \times \frac{2R}{\lambda} = \frac{4\pi R}{\lambda} \qquad\qquad 3.18$$

Where φ is the phase. As the target moves relatively to the radar, the range R changes, which causes the phase to change as well. If the above equation is differentiated with respect to time, the rate of phase changes is provided, which corresponds to the angular frequency as shown below.

$$\omega_d = \frac{d\varphi}{dt} = \frac{4\pi}{\lambda}\frac{dR}{dt} = \frac{4\pi v_r}{\lambda} = 2\pi f_d \qquad\qquad 3.19$$

Where $v_r = \frac{dR}{dt}$ is the rate of change of range over time, also known as the radial velocity (m/s) and f_d is the Doppler frequency shift. If the radar LOS and the target's velocity factor's angle is θ, then $v_r = v\cos\theta$, where v is the magnitude of the velocity vector, or speed. The angular frequency $\omega_d = 2\pi f_d$ is the rate of change φ with time and since the carrier's signal wavelength is as mentioned in equation 3.13:

Thus, from equation (3.19),

$$f_d = \frac{2v_r}{\lambda} = \frac{2f_t v_r}{c} \qquad\qquad 3.20$$

In the above equation, f_t is the radar's frequency of operation and c is the speed of light 3×10^8 m/s. Hence, when utilising a CW radar and a Doppler shift is identified, equation 3.20 can be rearranged for the calculation of the target's radial velocity as:

$$v_r = \frac{\lambda f_d}{2} \qquad\qquad 3.21$$

Figure 3.3 illustrates the working principle of a coherent CW Doppler radar. Assuming the use of a radar in the S-band, with frequency f_c of 2.4 GHz ($\lambda = 12.49$ cm), generating a CW signal by the VCO, which is then amplified and split via a splitter between the transmitting antenna (Tx) and the mixer. Considering a target moving directly into the emitted signal of the radar, at a velocity of 60 km/h. The target would interact with the transmitted signal, causing a frequency shift proportional to the target's velocity, which is received by the receiving antenna (Rx), amplified by the low noise amplifier (LNA) and mixed in the mixer together with the reference signal referred to as the local oscillator (LO). The output of the mixer is identified as baseband signal, which would then be filtered and amplified accordingly. The baseband signal would contain the Doppler frequency (f_d) of 9.60 Hz (plus any existing static phase from the radar) as shown in the calculation based on equation (3.20),

$$f_d = \frac{2v_r}{\lambda} = \frac{2 \times 16.66 \text{ m/s}}{12.49 \text{ cm}} = 266 \ Hz$$

The filtered and amplified baseband signal is then converted into a digital signal from its original analogue format using an analogue to digital converter (ADC) and finally the digitised signal is processed for visualisation or signal processing purposes. It is important to note that the incoming and outgoing velocities observed by a Doppler radar can be either positive or negative ($\pm v$) resulting in either positive or negative Doppler shifts ($\pm f_d$). The only difference between the positive and negative velocities, is that their phases are 90° apart. Unfortunately, this is not perceivable through the architecture showed in Figure 3.3 which only outputs the absolute frequency shift without a sign or a direction. Hence, both the positive and negative Doppler shift, are observed as positive Doppler shifts.
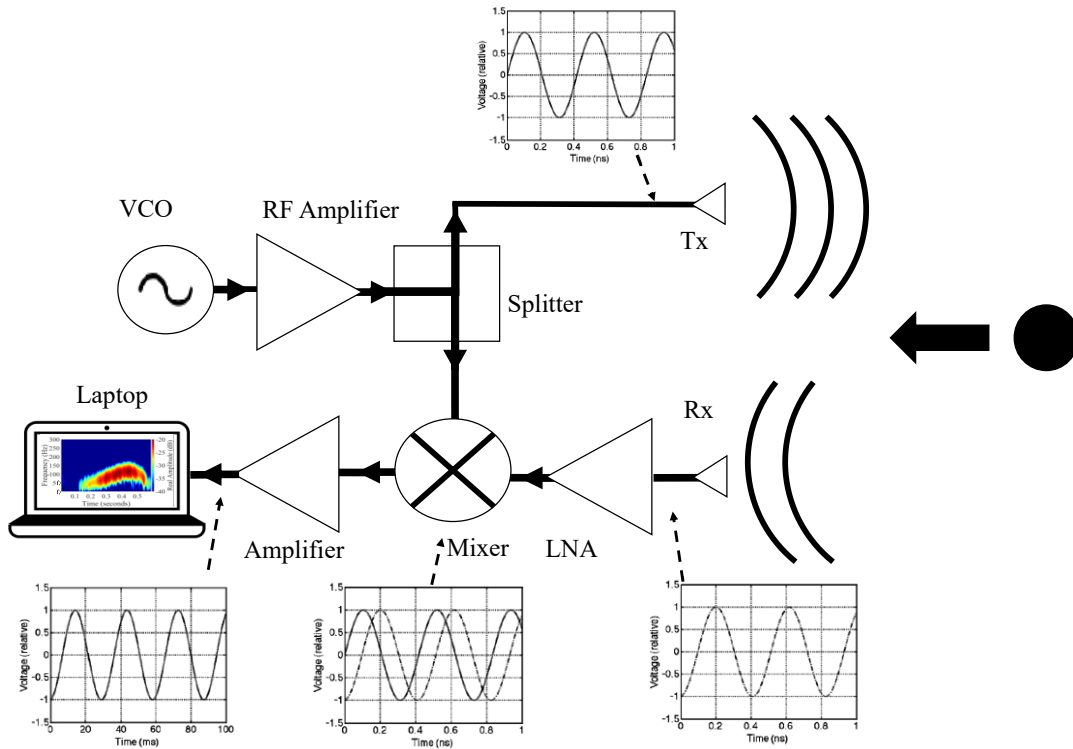
Figure 3.3: Top-level architecture of a CW Doppler radar illustrating the working principle of a coherent CW Doppler radar. The transmitted and received signal in different stages are also shown.

3.4 5.8 GHz I/Q Radar

Distinguishing the incoming and outgoing Doppler shift, can be achieved through the implementation of an I/Q architecture, which allows receiving a complex signal that has both the I and Q components. The I/Q components are signals that have the same amplitude and frequency but are out of phase by 90° (a quarter cycle). Such an implementation, would replace the common down-converter mixer module with an I/Q

mixer (also known as a quadrature mixer or image reject mixer) or with two separate mixers, where one is fed with the LO signal from the VCO and the second is fed with an LO signal that is 90° out of phase, to produce the I and Q component. A pair of signals are referred to being quadrature when the signals differ by 90° in their phase. Using such an architecture can then indicate a negative or positive Doppler shift of the target with respect to the radar, by checking which of the signals leads in phase [177].

The implementation of a quadrature receiver allows phase-coherent receivers, which enables obtaining a velocity vector rather than speed derived from Doppler's shift. Euler's equations defining complex exponential phasors can be manipulated to show [180],

$$sin(\omega t) = \frac{1}{2j}\left(e^{j\omega t} - e^{-j\omega t}\right) \: and \: cos(\omega t) = \frac{1}{2}(e^{j\omega t} + e^{-j\omega t})$$
<div align="right">3.22</div>

Where $cos(\omega t)$ and $j\sin(\omega t)$ describe the phasor's real component and the phasor's component in the imaginary (j)axis, which indicates that the cosine has both a positive component at $+\omega$ and $-\omega$, while the sine has a positive component and negative component of equal magnitude $+\omega$ and $-\omega$ respectively [180]. Knowing that

$$sin(\theta) = cos\left(\theta - \frac{\pi}{2}\right) and \: cos(\theta) = -sin\left(\theta - \frac{\pi}{2}\right)$$
<div align="right">3.23</div>

The I channel output can be derived in a similar manner to equation 3.17 as,

$$x_{rI}(t) = \frac{A}{2}cos\left(\frac{2\pi}{\lambda}\left(2R + 2d(t)\right)\right)$$
<div align="right">3.24</div>

Since the Q channel output undergoes a 90° phase shift, the output is,

$$x_{rQ}(t) = \frac{A}{2}cos\left(\frac{2\pi}{\lambda}\left(2R + 2d(t)\right) - \frac{\pi}{2}\right) = \frac{A}{2}sin\left(\frac{2\pi}{\lambda}\left(2R + 2d(t)\right)\right)$$
<div align="right">3.25</div>

3.4.1 5.8 GHz I/Q Radar Principle of Operation

A CW Doppler radar with quadrature mixer architecture is shown in Figure 3.4, which is used to illustrate the working principle of a quadrature mixer that enables positive and negative Doppler shift detection. Assuming a generated RF signal from a VCO is split equally into two signals by a splitter (splitter 1), one signal is sent to the Tx and the second split is provided as the LO signal to a splitter (splitter 3) that is built into the quadrature mixer. This signal is considered in phase with the VCO as no phase shift was

applied to this signal. A fraction of the transmitted signal reflects backs from a moving target, which encompasses a Doppler shift associated to the motion of the target.

The received signal is amplified by the LNA and passed on to the quadrature mixer, which contains a splitter (splitter 2) that splits signal $R(t)$ equally between two mixers (mixer 1 and mixer 2). The other part of the split signal in splitter 1 is referred to as the LO, which enters a splitter (splitter 3) built into the quadrature mixer that splits the signal into two equal signals, where one half enters a mixer (mixer 1) as the in-phase LO signal (channel I) and the other half is passed on to a 90° phase shifter, which causes the signal that was originally in phase with the VCO signal to lag the phase by 90°. In other architectures, splitter 3 can be replaced with a 90° splitter which provides an equal split of an in-phase signal and a quadrature signal that has a 90° phase difference. Whether this architecture or the previous architecture is used, the signal must undergo a 90° phase shift to produce the quadrature signal (channel Q).

Both mixer 1 and mixer 2 generate two down-converted signals due to being individually mixed with half the reflected signal. Both the I and Q channels are then amplified, filtered and fed into an ADC for further processing. Figure 3.4 shows a target moving towards and away from the antennas. When the target moves towards the antennas, the target's velocity is positive, which causes the I channel (in-phase channel/reference signal) to lead the Q channel.

On the other hand, if the target moves away, the target's velocity is thus negative, which causes the Q channel (signal in quadrature) to lead. Upon digitising the I and Q channel, the I channel can be considered as the real signal and the Q channel as the imaginary [177]. I/Q mixing does not have to be strictly performed using hardware, as it can also be conducted on a software level. However, the data must be digitised at an IF frequency that is shifted at least 2 times the bandwidth needed to measure negative and doppler velocities [177].
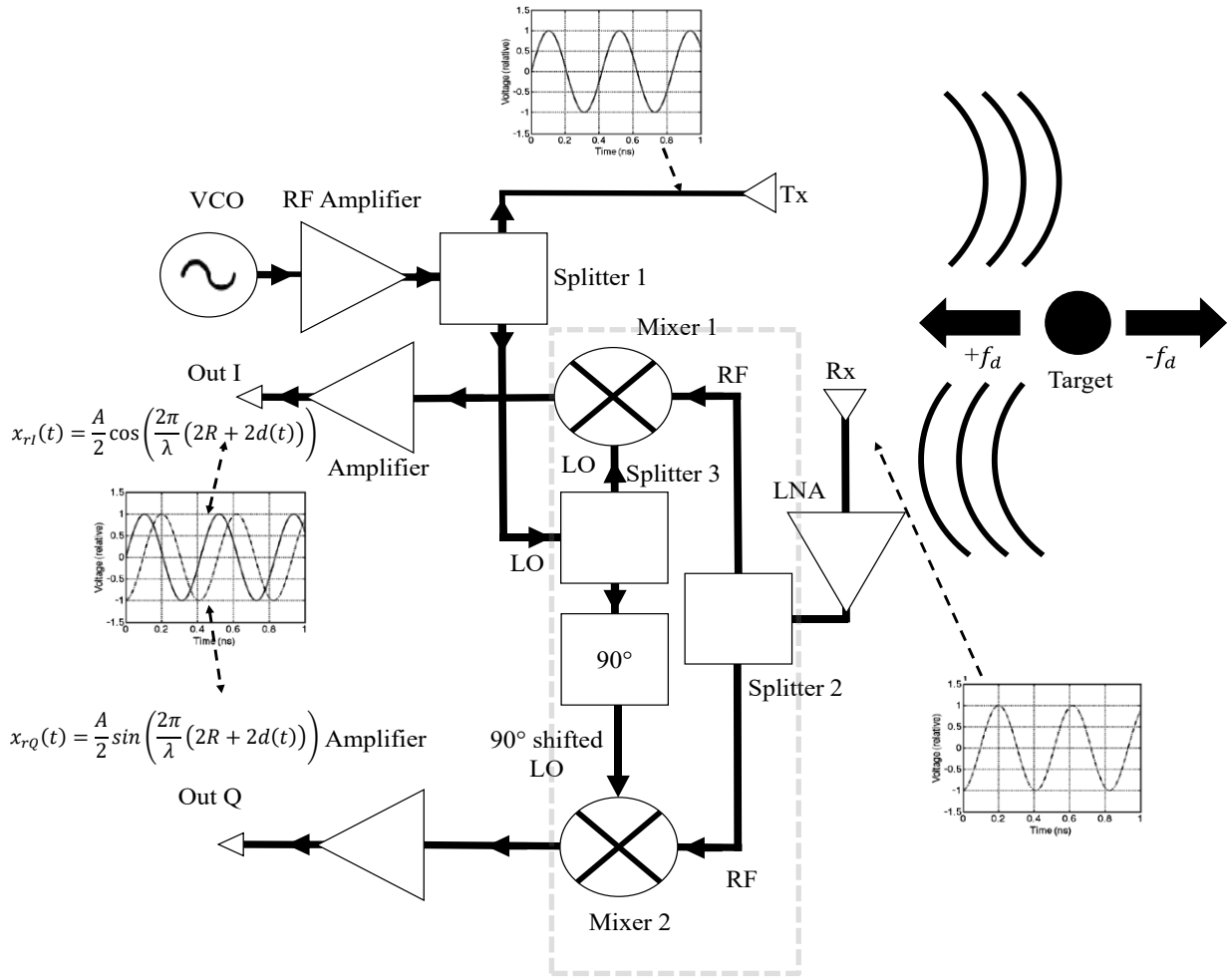
Figure 3.4: Illustrates a CW Doppler radar with a quadrature mixer architecture while displaying the signal in different stages.

3.5 5.8 GHz Radar design

The radar was required to operate in the ISM frequency band centred at 5.8 GHz. The radar must be able to detect honeybees at a suitable range, which typically requires signal amplification to receive clear honeybee signatures and keep noise to a minimum, while affording field operation. Thus, the radar should be small and portable whilst preventing board overheating due to weather and internal temperature build-up. Additionally, the system should be a low-cost and highly repeatable solution. Therefore, the key components (e.g., VCO, LNAs etc.), performance, cost and availability need to be carefully evaluated prior to their choice. Table 3.1 below summarises the technical radar requirements.

Table 3.1: Summary of radar's technical requirements

#	Parameter	Values
1	Frequency	5.8 GHz
2	Target RCS	Honeybees (-55 to -60 dBsm)
3	Range	2 to 3 metres
4	Maximum transmitted power	< 30 dBm
5	NF_{System}	< 3 dB
6	Minimum detectable signal	< -70dBm
7	Size and portability	Compact and lightweight
8	Power source	Portable battery < 12 V
9	Cost	Affordable < £100

3.6 Radar simulation

Various simulations were performed during this study in different simulation software such as National Instruments (NI) AWR Design Environment, MATLAB and Keysight ADS to tackle different aspects of the radar design. The 2.4 GHz coffee can radar [177] was redesigned as a PCB in [179] and served as a starting point for the work presented in this study. The redesign involved replicating the original coffee can radar into a portable PCB [179].

A custom 5.8 GHz radar model was designed in Keysight Advanced Design Systems (ADS) and simulated to yield the predicted Doppler shifts. The model was designed to operate under parameterised variables to control key design properties shown in Table 3.2. The simulation leveraged the ADS envelope simulation block which is suited to high frequency modulated signals and systems containing RF amplifiers, oscillators, and mixers.

The first stage of the simulation was the implementation of the model based on different functional blocks in ADS and configuring the Doppler shift in the radar. This is shown in Figure 3.5, which depicts the ADS radar model that was designed, with a description placed by each block. Additionally, each component was set to calculate its power to contribute towards the calculation of the system's link budget. The power calculation of the components is shown in Figure 3.5.

Table 3.2: Simulation parameters used in the ADS simulation.

#	Parameter	Function	Value
1	Carrier_Frequency	Defines the radar's carrier frequency	5.8 GHz
2	Transmit_antenna_Bandwidth	The bandwidth of the RF signal	400 MHz
3	Receive_Bandwidth	The bandwidth of the received signal	400 MHz
4	Transmit_Power	The power generated by the VCO	11 dBm
5	Target_Range	The range of the target	5 metre
6	Target_Velocity	The velocity of the target	5.556 m/s
7	RCS	RCS of the target	1

The first component is the VCO, which is defined as CW1, with a transmission power of 11 dBm and a centre frequency of 5.8 GHz, defined as Carrier_Frequency, providing the CW signal at our carrier frequency of choice and power of choice.
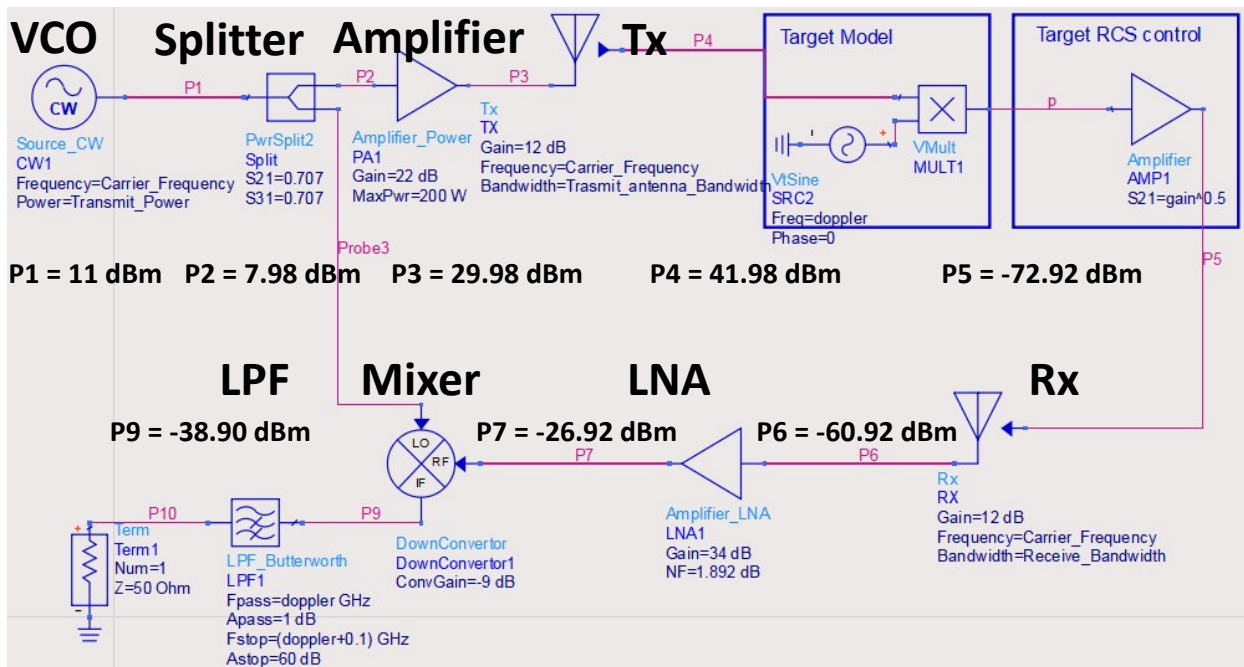
Figure 3.5: 5.8 GHz radar design in ADS.

This is followed by a 3 dB splitter defined as Split, with an equal split of 3 dB in each direction, which causes the power appearing at the at the output of power divider to be 7.989 dBm, as shown below.

$$P(dBm) = 10log10((0.5w)/1w) + 11 = 7.989\ dBm$$

119
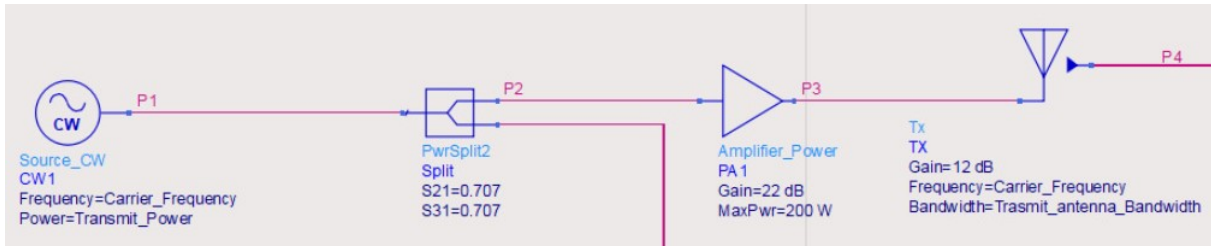
Figure 3.6: Transmission channel comprised of the VCO, 3dB Splitter, RF amplifier and Tx antenna.

A power amplifier, defined as PA1 amplifies the signal obtained from the splitter by 22 dB. At this point, the total power after passing through the amplifier becomes,

Power after amplifier = 7.989 dBm+ 22 dBm = 29.989 dBm

This is transmitted using the transmitting antenna defined as Tx, with a gain of 12 dBi. The antenna is set to have an operating frequency of 5.8 GHz and has a defined bandwidth of 400 MHz, which was defined as Transmit_antenna_Bandwidth. The total power transmitted by the antenna is

Power after Antenna = 29.989 dBm + 12 dBi = 41.98 dBm

The antenna models (shown below in Figure 3.7 as Tx and Rx) where obtained from a built-in simulation example in ADS and consist internally of an amplifier and a band pass filter to control of the antenna's gain and bandwidth respectively. The transmitted power is transmitted over a range whose value is defined as Target_Range, where it eventually reflects back from a target with an RCS and a velocity defined as RCS and Target_Velocity respectively. The transmitted signal reaches the target and is then reflected back.

The target model shown in Figure 3.7, was designed using a sine wave generator operating at the doppler frequency. The incoming signal and the sine wave signal — generated from the sine wave generator in the target model — both enter a mathematical multiplier, which performs frequency domain multiplexing. This is where the incoming signal and the Doppler sine wave signal generated are both multiplied, resulting in a Doppler shifted signal, which provided the Doppler shift of the radar simulation.

The Doppler shifted signal then interacts with the Target RCS control block to account for the target's RCS. This unit internally consists of an amplifier, where the RCS parameter in the simulation, controls the gain of the amplifier.
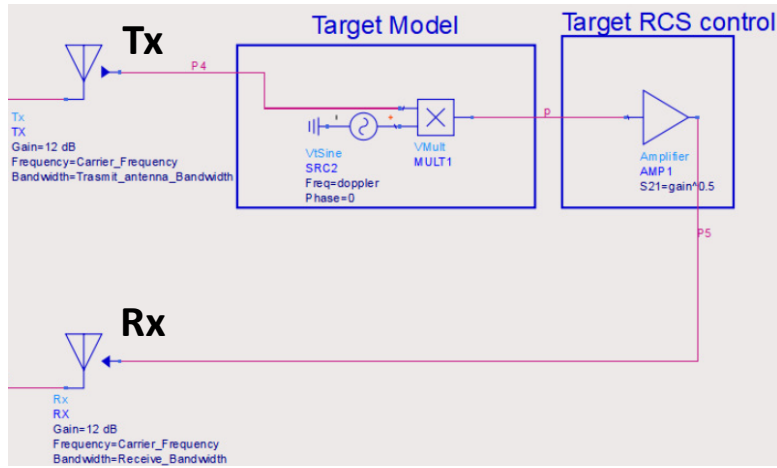
Figure 3.7: Tx and Rx to transmit and receive the signal respectively. The two blocks responsible for the Doppler shift and RCS are Target model and Target RCS block respectively.

Thus, the higher the RCS, the higher the gain of the amplifier in the custom RCS block. The gain of the RCS control block was calculated using

$$P_r = \frac{Pt \cdot Gt}{(4\pi R^2)^2} \cdot \sigma \qquad\qquad 3.26$$

Where Pt is the transmitted power from antenna Tx, σ represents the target RCS, Gt is the antenna gain and r is the target range. Equation 3.26 (same equation as equation 3.8) allows the calculation of P_r / P_t, which is the gain of target RCS amplifier, allowing RCS tuneability. The reflected/echo signal is then received by the receiving antenna (Rx).

At this stage, the simulation's initial performance can be tested, while using the radar equation as a reference of the calculations. Considering the 5.8 GHz radar's output power of 30 dBm, Tx and Rx gains of 12 dBi, a target of 1 m², a range of 25 metres, the simulated received power at the antenna was found to be equal to −60.355 dBm. The calculated received power using the theoretical radar equation (3.8/3.26) was −60.624 dBm, which was slightly different, yet showed very close approximation to the simulated model.

Increasing the RCS of the target from 1 m² (human RCS) to 100 m², (automobile RCS) would theoretically increase the received power where an RCS increase of 10-fold from 1 m² to 100 m² adds approximately 20 dBm. The RCS of a 100 m² resulted in a simulated received power of −40.355 dBm, while the theoretically calculated received power was equal to −40.011 dBm. This received power in comparison to that of the human case was indeed an increase of 20 dBm, which demonstrated the validity of the simulations and its correlation to theoretical estimations.

The received signal by the receiving antenna (Rx) is amplified by an LNA, defined as LNA1, with a gain of 34 dB and a noise figure of 1.892 dB. Note that in the original system two LNAs were used, each with a gain of 17 dB and a noise figure of 1.8 dB. These were combined into one LNA with their cascaded noise figure used as the component's noise figure.

This is then down-converted in a mixer defined as Downconverter1, with a conversion gain of -9 dB. The mixer produced the IF signal which was passed through to a low pass filter (LPF) defined as LPF1. The LPF centre frequency (f_c) was set to Doppler frequency as it is the signal of interest. The LPF's stop band and start band were set as 3 Hz and f_c + 100 MHz respectively. Any other signal beyond f_c +100MHz was attenuated by 60 db. This was finally terminated in the 50-ohm load Term1 termination. The simulation excluded the baseband amplifier which further amplified the filtered baseband signal from 30 to 90 dB (depending on which baseband amplification module was used).

The simulation conducted reflects the general behaviour of a 5.8 GHz Doppler radar. Assuming a human target of σ =1 m^2, moving with a velocity of 20 km/h (5.556 m/s). The Doppler frequency is plotted in Figure 3.8, which shows a maximum Doppler shift of 214.8 Hz with a received power of -35.355 dBm. Upon using equation 3.15 to calculate the doppler shift using a 5.8 GHz radar, for a 20 km/h target, the doppler shift was found to be 214.832 Hz, which was the same value as observed in the simulation. This confirmed the simulation model to match the theoretical calculations of the doppler shift.
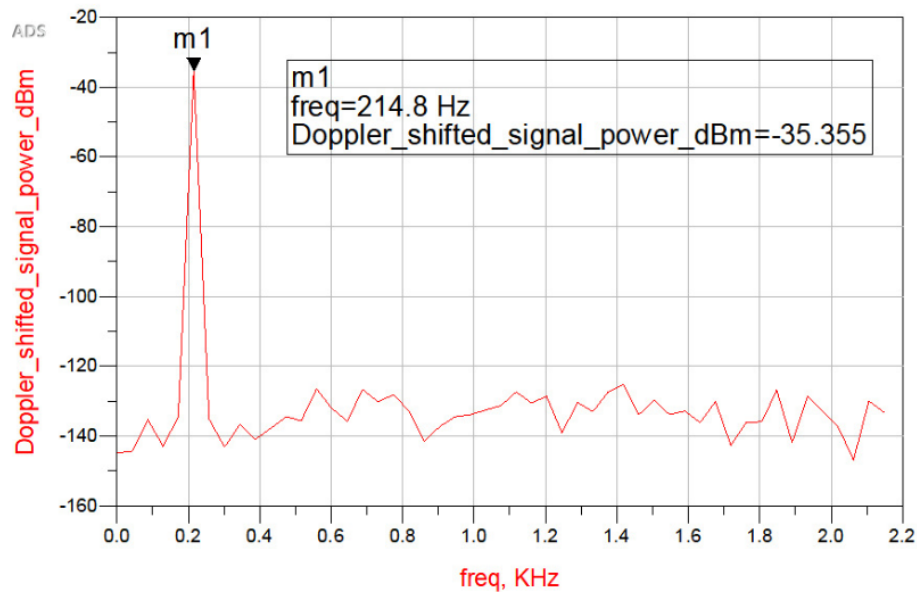
Figure 3.8: 214.8 Hz Doppler shift of human target travelling at a speed of 20 km/h.

3.6.1 Impact of RCS, Range and Velocity change

The theoretical implications of the RCS, range and velocity on a radar target are known. Yet, the RCS and range are critical parameters that dictate the overall power received by the radar, where even the slightest changes can alter the radar output. To further illustrate the impact of the RCS, range and velocity on the simulation, the aforementioned factors were parameterised and swept across a range of values using individual parametric sweeps.

3.6.1.1 RCS change

The RCS sweep was initiated from 1 to 50 m^2 with a step of 12.25 to illustrate the impact of the RCS increase while keeping the velocity at 5.556 m/s and range at 2 metres. As expected, the magnitude (dBm) of the filtered IF output of the radar was increased per sweep step from an initial 7.621 dBm to 24.610 dBm as shown in Figure 3.9.
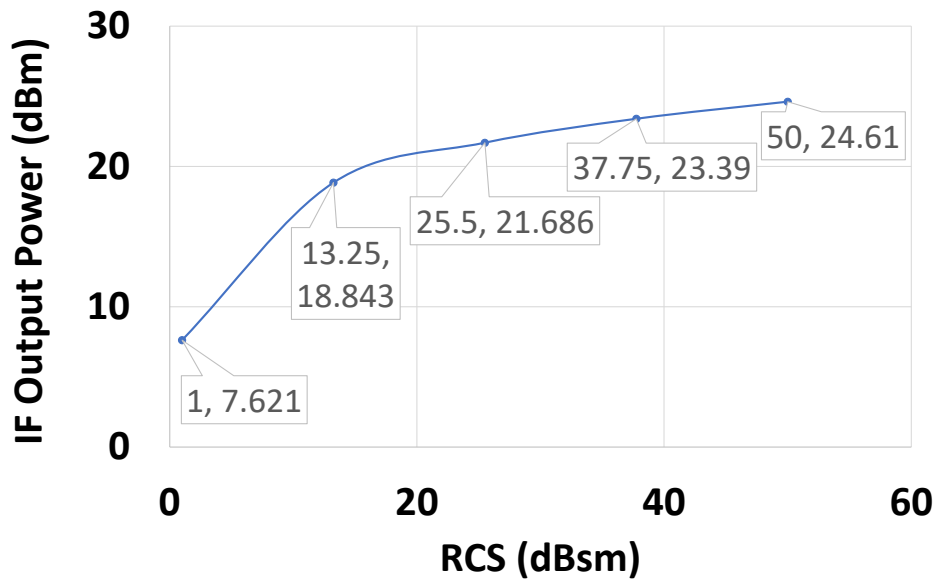
Figure 3.9: RCS sweep and its impact on the radar's IF output power while keeping range and velocity constant.

3.6.1.2 Range change

The range sweep was initiated from 3 to 7 metres with a step of 1 metre to illustrate the impact of the range increase, while keeping the velocity at 5.556 m/s and RCS at 1 m^2. In theory the longer the range the lower the power/magnitude of the received signal. As expected, the magnitude (dBm) of the filtered IF output of the radar was decreased per sweep step from an initial 0.577 dBm at 3 metres to a final -14.142 dBm at 7 metres. This is shown in Figure 3.10.
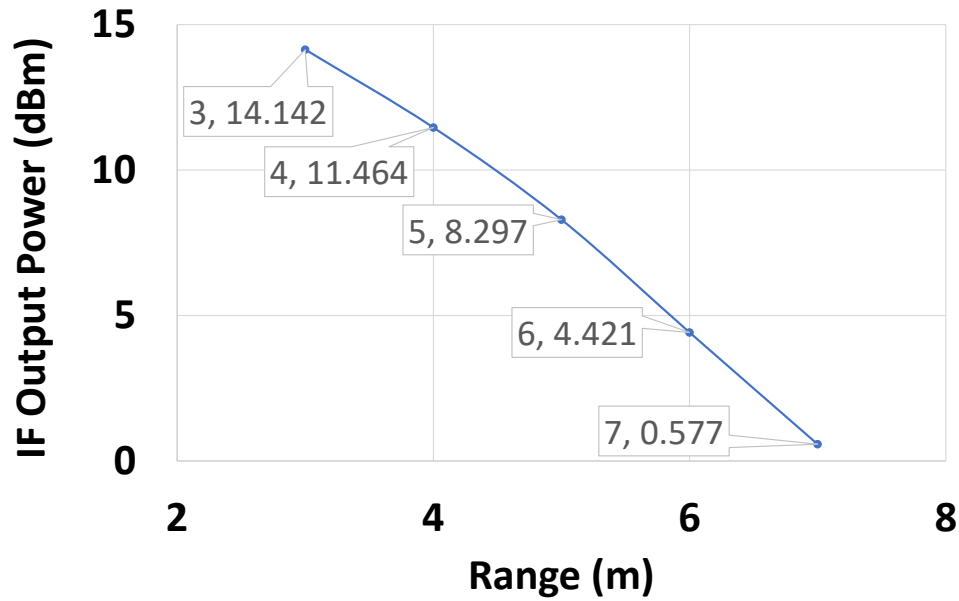
Figure 3.10: Range sweep and its impact on the radar's IF output power while keeping RCS and velocity constant.

3.6.1.3 Velocity change

The velocity sweep was initiated from 2 to 10 m/s with a step of 2.7 m/s to illustrate the impact of the velocity change, while keeping the range at 2 metres and RCS at 1 m². In theory, since both RCS and range are fixed, the only changing attribute would be the Doppler shift. As expected, the magnitude (dBm) of the filtered IF output of the radar remained fixed as the velocity of the target does not affect the signal's magnitude but impacts the Doppler shift. The different Doppler shifts of the target velocity sweep are shown in Figure 3.11 which demonstrated an increase in shift as the velocity of the target increases.
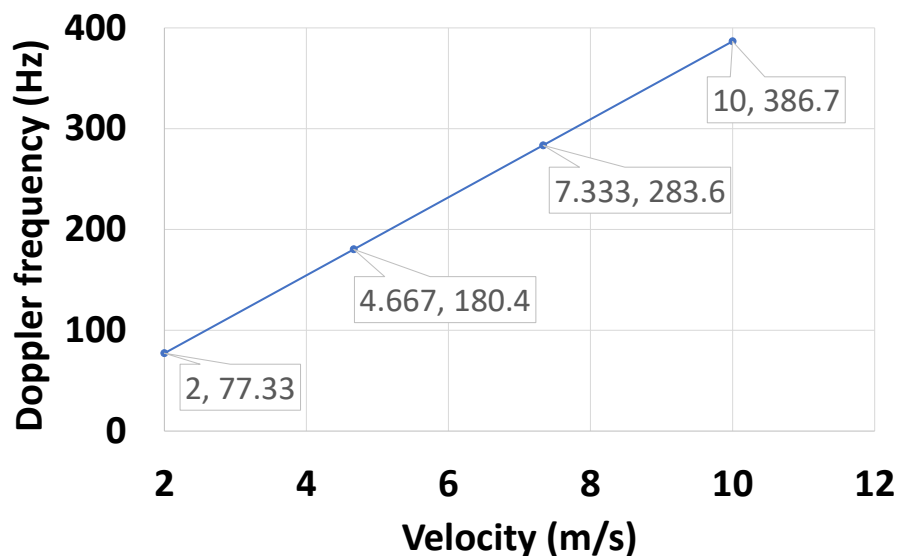
Figure 3.11: Velocity sweep and its impact on the Doppler shift while keeping RCS and range constant.

The plot in Figure 3.11 shows four Doppler frequency peaks, which can be verified by calculating their speed/Doppler shift using the simulated Doppler shift or the parameterised velocity in Figure 3.11. Considering m1, the peak of the target moving at a velocity of 2 m/s, resulted in a Doppler shift of 77.33 Hz. Upon calculating its velocity from equation (3.16), to verify the Doppler shift, the resulting velocity of the simulated Doppler shift of m1 was $\frac{\lambda f_d}{2} = \frac{51.8 \text{ mm} \times 77.33 \text{ Hz}}{2} = 2.002 \ m/s$, which agrees with the results of the simulation.

3.7 5.8 GHz Doppler radar versions

Over the time of the study, three different radar version were designed and built with multiple iterations of each version as continuous improvements were implemented. The first radar version (V1) was the 5.8 GHz Doppler radar based on interconnected RF modules, which acted a prototype radar and is referred to as 5.8 GHz radar V1. The second radar version was a 5.8 GHz CW Doppler radar integrated on a custom PCB board for ease of transportation, experimentation and cost reduction. This is referred to as the 5.8 GHz radar V2. The need for in-phase and quadrature (I/Q) data, inspired an upgrade on the radar, which resulted in an interconnected RF module-based radar with I/Q detection. Moreover, the lack of signal digitisation, low noise power regulation, integration and portability in the RF module-based radar with I/Q detection, inspired the design of the third radar. This was the 5.8 GHz I/Q PCB radar with power regulation and signal digitisation, integrated on a single custom PCB board. This is referred to as 5.8 GHz radar V3. These three radar versions are described below along with their performance attributes.

3.8 5.8 GHz Doppler Radar (V1)

The 5.8 GHz frequency choice weighed signal quality, monitoring range, and the availability of low-cost off-the-shelf components. Figure 3.12 below shows the RF modules along with the 12 V regulator, gain circuit, low pass filter, analogue to digital converter and a laptop. The figure also integrated the link budget, where the power transmitted (P_T) is 30.5 dBm and L_C are the cable losses which added approximately to -0.5 dB. This resulted in an effective isotropic radiated power (EIRP) of approximately 42.5 dBm, which can be reduced to 30 dBm by decreasing the antenna gain or adding attenuators prior to the antenna to comply with the UK radio equipment regulations [182].
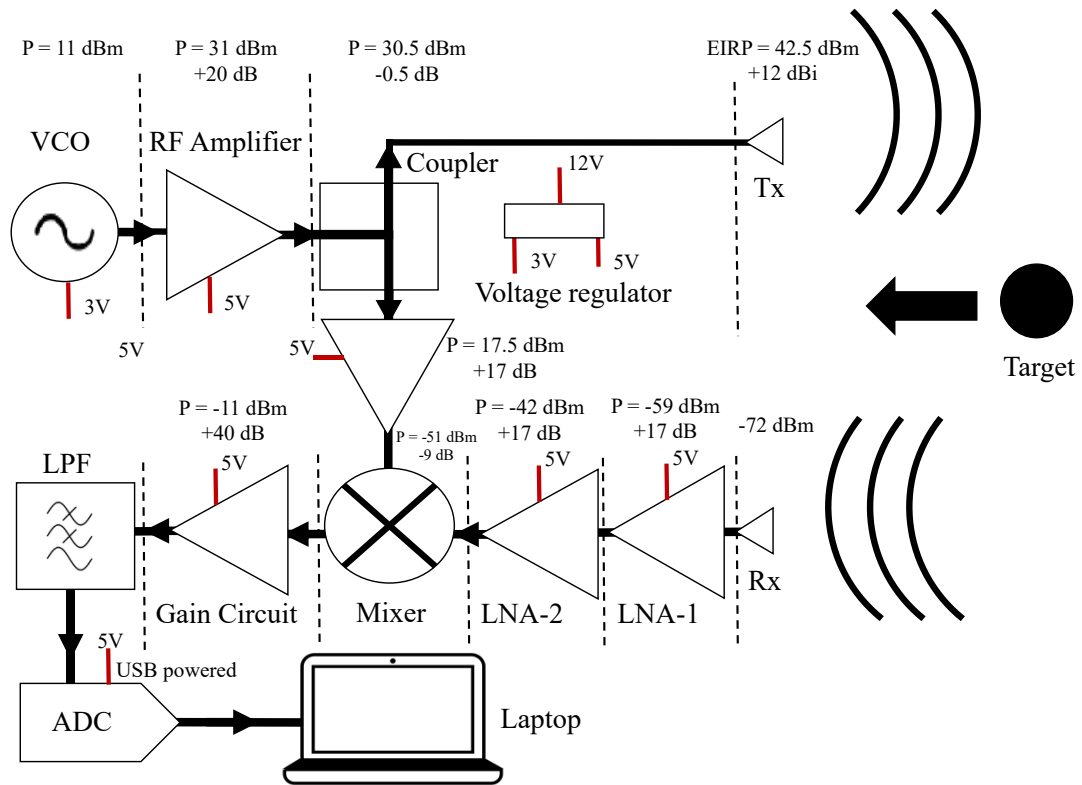
Figure 3.12: System diagram of the V1 radar including a link budget calculation.

Upon using the 2nd term of equation 3.8, the theoretical maximum distance can be calculated considering an output power of 30 dBm, antenna gains of 12 dBi and different targets descending in RCS value (Car σ = 100 m², Human =1 m² and insect= 10^{-5} m²) [146]. Figure 3.13 shows the three targets maximum detectable signal against range. The maximum distance for a car, a human and an insect were calculated as 154 metres, 48.8 metre and 2.8 metre respectively. The V1 radar — also referred to as the prototype radar — was comprised of RF evaluation boards summarised in Table 3.3.

Table 3.3: Radar RF boards used for the prototype radar

#	Device	Part Number	Parameters
1	VCO	HMC358MS8GE	5.8 GHz VCO, 11 dBm out
2	Power Amplifier	HMC408LP3	20 dB, PSat 32.5 dBm
3	Low Noise Amplifier	HMC717ALP3	14.5 dB gain, 1.3 dB NF
4	Low Noise Amplifier	2x HMC392ALC4	17 dB gain, 1.8 dB NF
5	Double Balanced Mixer	HMC219BMS8GE	9 dB conversion loss
6	20 dB coupler	HDH-06020GID	20 dB coupling
7	Antennas	Antennas Tx and RX,	12 dBi ,15 dBi and 17 dBi
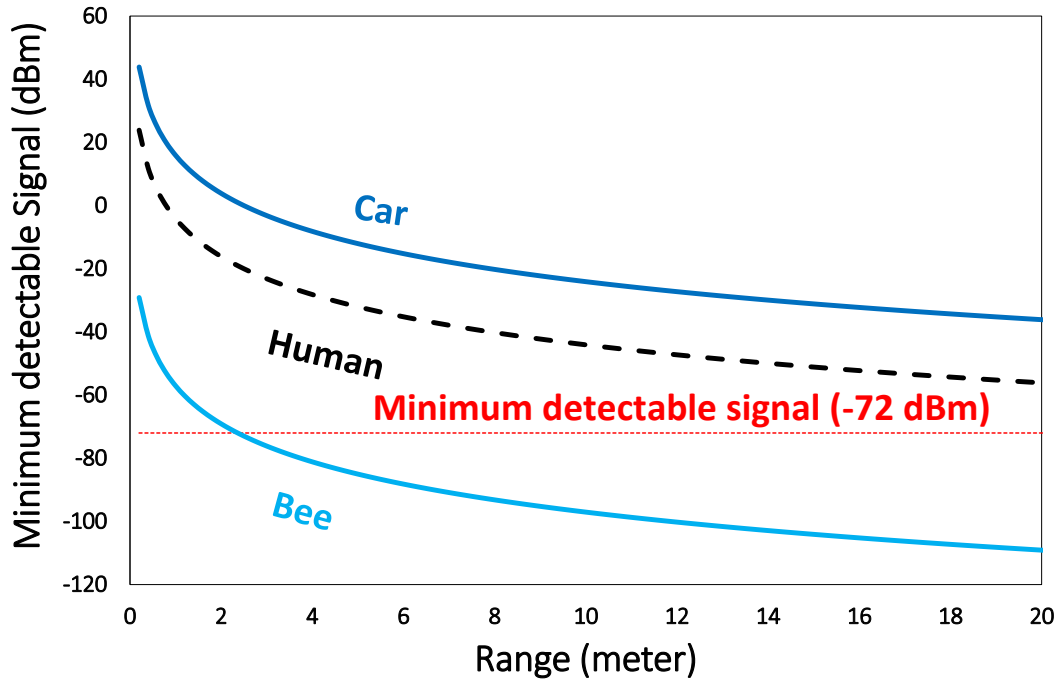
Figure 3.13: Maximum detectable signal against range for a car, a human and a bee with RCS of 100 m², 1 m² and 10^-5 m² respectively, considering the 5.8 GHz prototype with 12 dBi gain (Tx and Rx).

While the assembled prototype radar [183] demonstrated a proof of concept, it comprised of multiple costly interconnected evaluation boards (overall $3000) placed on a clipboard, making it the size inconvenient for experiments and unaffordable. Thus, the radar was re-designed on a custom 41.75 mm² PCB which focused on portability and affordability. This radar is referred to as the 5.8 GHz radar V2. The components used, reason behind their choice and their testing is discussed in the following sections.

3.8.1 VCO

The VCO chosen was the HMC358MS8GE with low phase noise (-110 dBc/Hz) and 11 dBm power output. A custom PCB was designed using Autodesk EAGLE to manufacture a 2-layer PCB on FR4 with a dielectric constant of 4.58 leading to a track width of 0.293 mm for a 50 Ω impedance termination. The JLC7628 PCB stack up with a thickness of 1.6 mm was used for fabrication by JLCPCB [184]. Both evaluation and custom in-house VCOs were tested for their tuneability and their output power in Figure 3.14. The in-house PCB is shown as an inset in Figure 3.14(a).
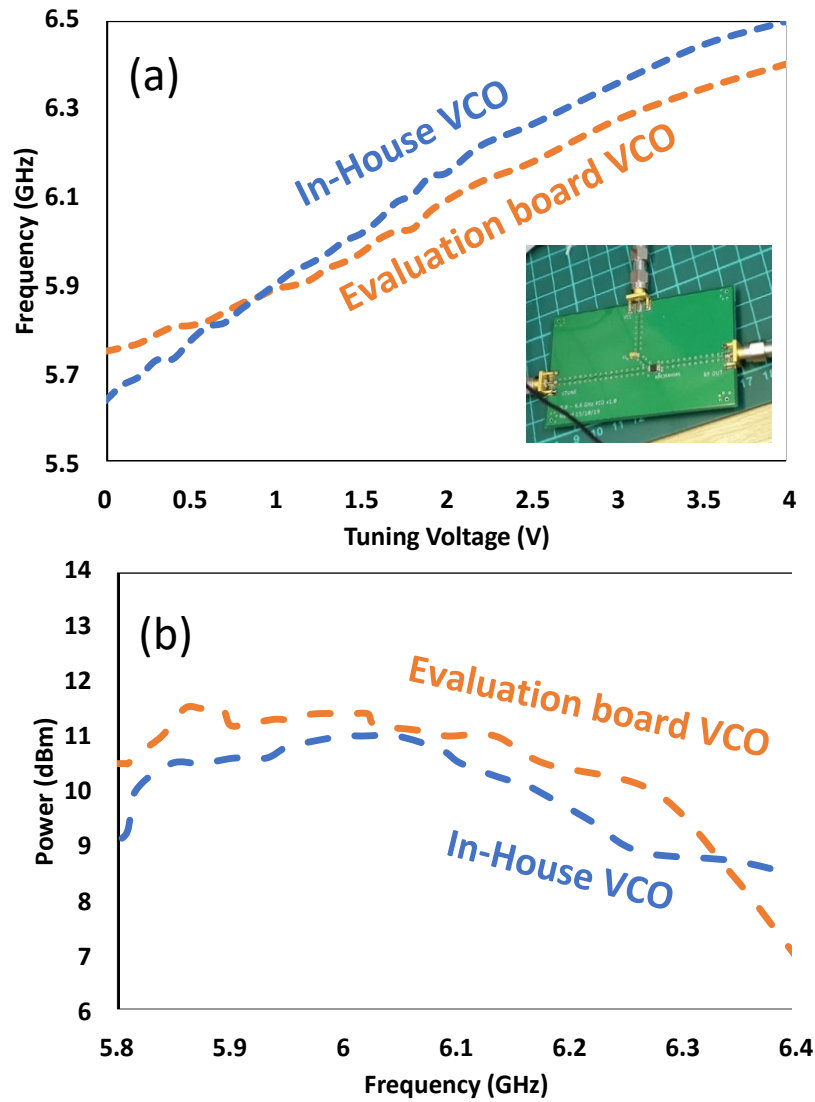
Figure 3.14: (a) Testing the linearity of the evaluation board VCO (orange) and in-house assembled VCO (blue). Inset shows the in-house assembled VCO(b). Testing the output of the evaluation board VCO (orange) and in-house assembled VCO (blue).

3.8.2 RF Amplifier

The output power from the VCO was ⌣11 dBm, and in order to obtain an approximate overall power output of 30 dBm, a RF amplifier was required. Initially the HMC717ALP3E RF amplifier with a 14.5 dB gain was used for this purpose, which would provide a maximum power output of 25.5 dBm. Though this was still a suitable output power and was used for initial experiments, it would still lack the ability to produce an output power of ⌣30 dBm. As an alternative, the HMC408LP3 was used which adds 20 dB to the 11 dBm output of the VCO resulting in around 30 dBm. 50 dB attenuation was used to preserve the spectrum analyser from excess power and for heat regulation.

To test the output under continuous wave and frequency modulation, a triangular wave generator was connected to the VCO's Vtune port, with the VCO's output connected to the input port of the amplifier. The amplifier's output was connected to the 50 dB attenuation, which was connected to the input port of a spectrum analyser. The output reported on the spectrum analyser was sweeping from 5.6 GHz to 6 GHz with an output of approximately -19.5 dBm to -21 dBm respectively (negative due to the 50 dB attenuators in place). This can be seen in Figure 3.15.

This indicated that the measured output power from the power amplifier was approximately ranging from 29 dBm to 30.5 dBm (when the 50 dB attenuation was removed). Repeating the same experiment, while replacing the evaluation board VCO with the in-house VCO measured -22 to -25.5 dBm, indicating a power output of 24.5 to 28 dBm. A lower output of several dBm was acceptable considering it was an in-house board.

Figure 3.16 shows the S21 parameters of both the HMC408LP3 and HMC717ALP3E evaluation boards. The HMC408LP3 evaluation board resulted in an S21 of 20 dB when removing the 50 dB attenuation. The combination of 20dB and the VCO's 11 dBm would result in the required 30 dBm output, deeming the HMC408LP3 a suitable RF amplifier. As for the V2 radar, the HMC408LP3 RF amplifier in the transmission channel was replaced with the HMC392ALC4 due to its poor performance as a custom PCB.
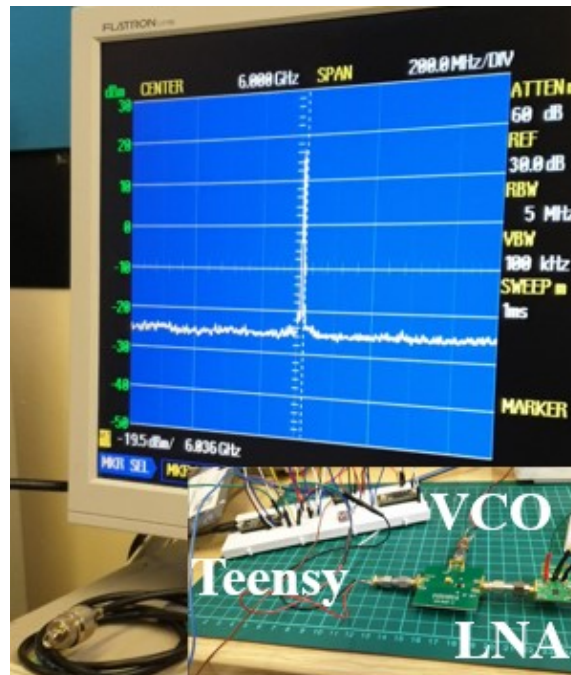
Figure 3.15: The output of the amplified signal with 50 dB attenuation. Inset shows a Teensy 3.2 microcontroller, VCO and LNA.
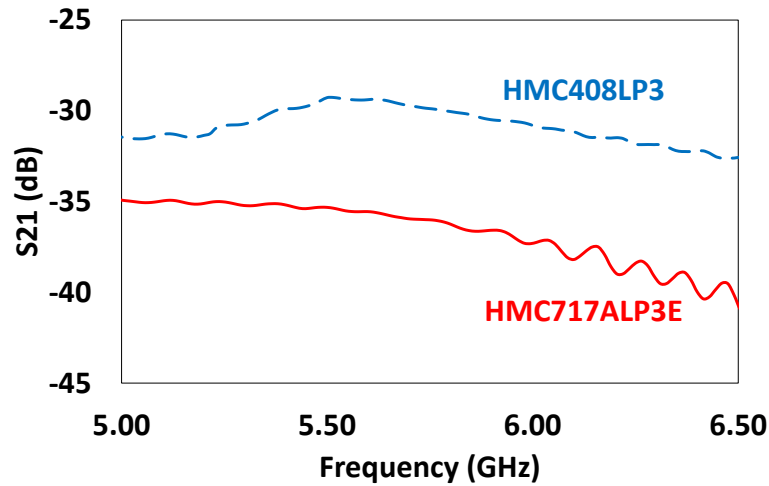
Figure 3.16: Measured S21 values of the HMC408LP3 evaluation board (blue dashed) and HMC717ALP3E evaluation board (red solid) while being connected to a combination of 50 dB attenuators to decrease their output power.

3.8.3 Coupler and Antennas

The amplified signal was required to be routed to two paths; the transmission antenna and the down-converting mixer. This can be done using different components such as splitters, couplers or circulators. The V1 radar employed the HDH-06020GID 20 dB directional coupler, as it provides unequal power splitting to maximise the transmitted signal, while the V2 radar used a 3 dB splitter (SCN-2-65+) as this splitter was obtained as a free of cost sample component and a 3 dB split was deemed adequate.

Different antennas were examined, where high gain antennas were preferred as they contributed towards the increase of the EIRP and supported placing the radar opposite the hive. At the early stages of the study two custom Yagi-Uda antennas were designed and used (more details in Appendix H). However, these were later replaced with two commercial antennas, where the first antenna was a 5.8 GHz plate antenna, with a gain of 17 dBi, a beamwidth of 40° vertical and 16° horizontal. The second antenna was a patch antenna with a gain of 16 dBi and a beamwidth of 42° both horizontally and vertically.

3.8.4 Receiver LNAs

The reflected power expected from the target is a weak signal, which naturally contains noise. The receiving channel needs to amplify, filter and process this signal with the least amount of added noise. Thus, it is important to use amplifiers with a low noise figure.

The noise figure (NF) is a measurement of how much a device degrades the quality of the given signal. It provides a quantifiable estimation of how much the signal to noise ratio (SNR) of the input signal (S_i/N_i) to the SNR of an output signal (S_o/N_o). It is used to quantify the degradation of the signal and is often expressed in dB. There are various sources of noise, such as thermal noise, EM noise, shot noise and power induced noise. When discussing low noise amplifiers, the NF is an important specification and is calculated using the following formula

$$NF = 10 \cdot log_{10} F \qquad\qquad 3.27$$

Where NF is the noise factor expressed in dB and $F = \frac{S_i/N_i}{S_o/N_o}$. Each component in the system contributes to a certain level of noise which is cumulatively expressed in the overall NF of the system (NF_{System}). However, the most significant NF that is induced to the receiving end of the system is influenced by the first LNA in the channel. The NF signal chain is expressed in the cascaded NF equation, which quantifies the total level of noise affecting the receiving channel.

$$NF_{System} = 10 \cdot log_{10} \left(F1 + \frac{F_2 - 1}{G_1} + \frac{F_3 - 1}{G_1 G_2} + \frac{F_4 - 1}{G_1 G_2 G_3} + \cdots \frac{F_n - 1}{G_1 G_2 G_3 \dots G_{n-1}} \right) \qquad 3.28$$

Where F_n and G_n are the channel's noise factors and gain of each stage in the receiver chain. Hence, the choice of the first receiver LNA is critical as it dictates the system's NF. The initial LNA chosen was the HMC392ALC, operating between 3.5 GHz and 8 GHz with a maximum gain of 17 dB and NF of 1.8 dB. Considering two LNAs placed in the receiving channel, the total NF_{System} was calculated using equation 3.28 as 1.829 dB. This LNA was preferred over the previous LNA as it features a higher gain and required less components. It was found that cascading two LNAs provided the optimal SNR for low RCS targets.

A radar's capability to detect weak signals, is dictated by the receiver's noise and the power of the reflected echo. The NF_{System} can be used to provide an estimation of the system's weakest detectable signal, also known as minimum discernible signal or minimum detectable signal (MDS). The MDS was calculated as

$$MDS = 10 \cdot log_{10} \left(\frac{kT}{1mW} \right) + NF_{System} + 10 \cdot log_{10} BW + SNR_{Out} \qquad 3.29$$

Where k is $1.38 \cdot 10^{-23}$ Joules/Kelvin and is known as the Boltzmann's constant, BW is the bandwidth of the receiver (400 MHz), NF_{System} was calculated as 1.829 dB and

the SNR_{Out} is the minimal required SNR for the signal's detection (commonly 10 dB to 13.4) [177]. Thus, the MDS can be calculated as -72.72 dBm.

Several PCB radar iterations took place, where in the first iteration, the two LNAs in the receiving channel were initially kept similar (HMC392ALC4) to V1 radar (prototype radar), resulting in a similar NF_{System} and MDS. The second iteration of the V2 radar replaced the HMC392ALC4 in the transmission channel with the PMA3-83LN+ as it provided a higher gain, lower noise figure and much lower cost. The third iteration replaced all the HMC392ALC4 with PMA3-83LN+ for the transmitting channel and the PMA3-83LNW+ (obtained as samples) for the receiving channel. The new LNAs also reduced current requirements, provided better thermal properties and were less problematic to solder. The PMA3-83LN+ has a NF of 1.3 dB and a minimum gain of 18 dB, while the PMA3-83LNW+ has a similar gain and a slightly lower NF of 1.2 dB.

Due to the reduced NF and higher gain, this contributed towards a lower NF_{System} and lower MDS, equal to 1.217 dB and -73.33 dBm respectively in the third iteration.

For all iterations of the V2 radar board, the power regulation and USB based signal digitisation remained the same in this version of the radar as the previously used methods in the evaluation board prototype. The power regulation used is mentioned in Appendix E.

3.8.5 Mixer

A mixer consists of three ports; radio frequency port (RF), LO and intermediate frequency port (IF). The RF port is where the received signal f_{RF} is fed, which originates from the reflected signal travelling back to the receiving antenna. The LO port is fed with a known frequency f_{LO} that originates from the system's oscillator (original frequency source), as a reference frequency. The utilisation of an LO port defines whether a radar's architecture is coherent (with LO signal) or incoherent. The mixer's output is at the IF port. This provides two pairs of frequencies, which are a result of multiplications in the time domain of the two signals (f_{RF}, f_{LO}) resulting in f_{IF} as shown in Figure 3.17. The upper term in the equation shown in Figure 3.17 ($f_{RF} - f_{LO}$) is the product of the down-conversion, where the outcome is a low frequency product. The low frequency product is the difference between the two mix signals f_{RF} and f_{LO}. While the lower term ($f_{RF} + f_{LO}$) is the product of up-conversion, a higher frequency product that is not required.

$$f_{IF} = \begin{cases} f_{RF} - f_{LO} \\ f_{RF} + f_{LO} \end{cases}$$
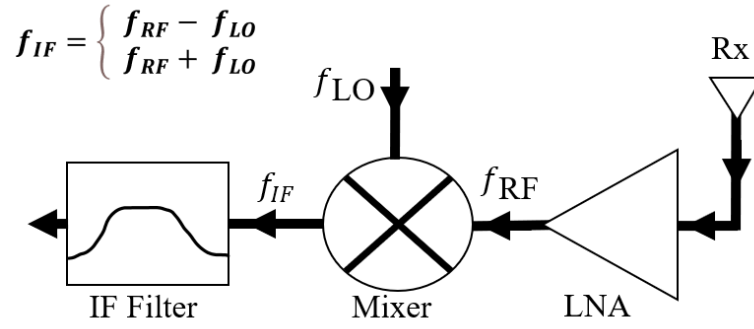
Figure 3.17: Diagram of a Mixer. Inset shows the product of the up-conversion and down-conversion.

Mixers are manufactured using active devices or by diodes, causing mixers to have a poor isolation between the three ports. As a result, spurious signals from the LO and/or RF leak into the IF signal, which is the reason behind the need of a filtering mechanism for the IF signal.

Two different passive double balanced mixer ICs were tested (HMC219B and HMC218B). The HMC219B has a higher isolation between LO to RF, higher isolation between LO to IF and isolation between RF to IF of 40 dB, 35 dB and 22 dB respectively. Another important property is the LO drive level of 13 dBm, which is a power requirement that needs to be reached in order for the mixer to operate. The HMC219B has a higher conversion loss of 9 to 11 dBm. As for the HMC218B, it has the same LO drive of 13 dBm, a lower isolation between LO to RF and a lower isolation between LO to IF of 38 dB and 32 dB respectively. In order to have a functional mixer, an amplifier was required to be inserted prior to the mixer input to satisfy the input power requirement of the mixer. Once the LO drive has been provided, the IF output signal of $f_{RF} - f_{LO}$ would be visible with an oscilloscope. Both the HMC219B and HMC218B were designed on a PCB. The output port of both mixers is an SMA connector, connected to a coaxial cable which was spliced on one SMA end to support soldering it to a wire as shown in Figure 3.18(a).

3.8.6 Low pass filter

The IF signal that is obtained from the mixer is a low frequency signal. As mentioned earlier, the low frequency IF output would be contaminated with a combination of spurious signals from the RF signal and the LO signal. One method of reducing this, is through using a low pass filter (LPF). In order to do so, it is important to estimate the maximum Doppler shift of the target, to ensure that the LPF is able to cover its frequency range.

A honeybee's fastest flying speed is 32 km/h [185], which according to equation 3.16 corresponds to a maximum Doppler shift of 345 Hz. Hence, the LPF must preserve frequencies below 345 Hz. The LPF of choice was the MAXIM7408, which is a fifth order tuneable LPF IC, with an operational range of 1 Hz to 15 KHz [186]. The LPF operates with a low power, low noise and low distortion, while allowing the choice of the centre frequency as

$$f_{OSC\,(KHz)} = \frac{k}{C_{OSC}\,(pF)}$$

3.30

Where $f_{OSC\,(KHz)}$ is the centre frequency in KHz, $C_{OSC}\,(pF)$ is the capacitor value in pF and $k\,(27 \times 10^3)$ is a variable given in the datasheet. The LPF centre frequency was set at 5 KHz and was tested as shown in Figure 3.18(b) below.
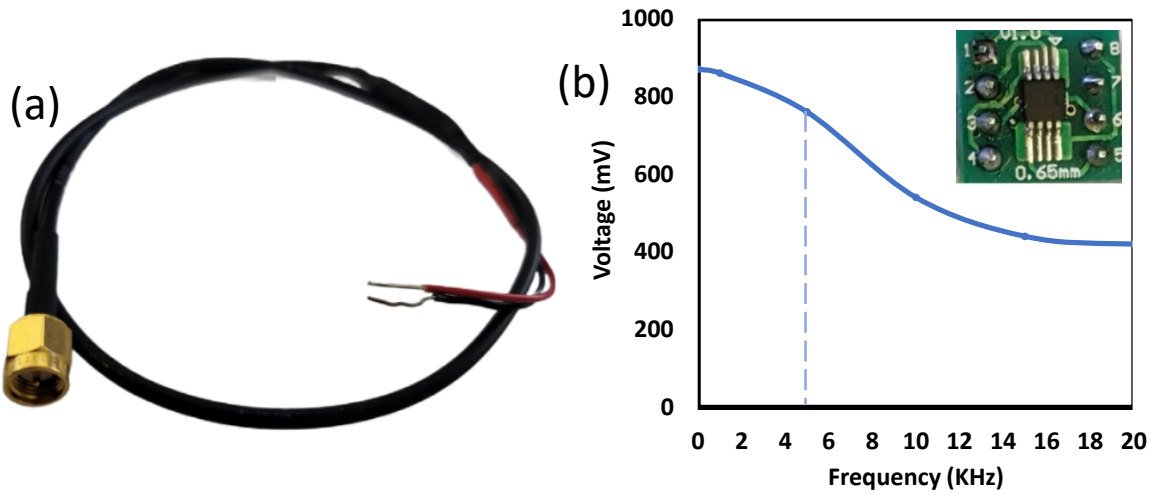
Figure 3.18: (a) Sliced SMA cable for the IF signal's connection to the rest of the system. (b) Testing the MAXIM7408 with an input of ~900 mV, while setting the centre frequency at 5 KHz. Inset shows the MAXIM7408 LPF PCB.

3.8.7 Gain block

The filtered down-converted IF signal is still considered a low power signal of ⌣50 mV peak to peak (Pk-Pk) which is in need of amplification. This is where a gain block was utilised to amplify the IF signal. During early prototyping stages, the amplification was achieved by using a TL974 operational non-inverting amplifier to provide a tuneable voltage gain of up to 91.9. The gain of the amplifier was determined by the resistor in the negative terminal and the feedback resistor. A variable gain circuit can be achieved by using a potentiometer instead of a fixed resistor, which would increase the flexibility of the amplifier. The maximum gain is calculated below, providing the tunability range of the variable gain amplifier.

$$Av_{MAX} = 1 + \frac{R_{Feedback}}{R_1} = 1 + \frac{20K\Omega}{220\Omega} = 91.9 \qquad \text{3.31}$$

Cascading another non-inverting amplifier adds versatility to the gain stage of the circuit by adding further amplification. Since this was an early stage of the study, it was attempted to obtain a high gain to support the detection of low RCS targets. Hence, a total of three non-inverting amplifiers were used, each with a variable gain of 91.9. The gain value was a theoretical value and was dependent on the resistor tolerances. Since resistor tolerance can cause values to deviate to some extent, the 91.9 was not always reached.

Prior to using the amplifiers, all gain stages would be tuned down to their lowest value and gradually increased until obtaining a suitable signal. Upon testing the gain stages, (stage one, two and three) of the amplifier, it was found that a maximum voltage gain of ~89 can be achieved per stage. This was tested by using an input of 50 mV which resulted in an output of 4.48 V, indicating a voltage gain of $\frac{4.48}{0.05} = 89.6$ (amplification of 39.046 dB). Since the devices were rail-to-rail operational amplifier, powered by a 5 V rail, the output power was capped below 5 V. This cap can always be increased by swapping the amplifier's 5 V wire with the main 11.7 V wire that originates from the LiPo battery.

Using maximum gain setting resulted in a highly amplified and distorted signal. The implemented potentiometers allowed the control of the gain which was used to control the noise figure. While testing the circuit it was realised that the wires of the circuit were hazardous, problematic and inconvenient to carry around on a breadboard. Hence, the circuit was combined with the MAXIM 7408 LPF and populated on a PCB as shown in Figure 3.19.
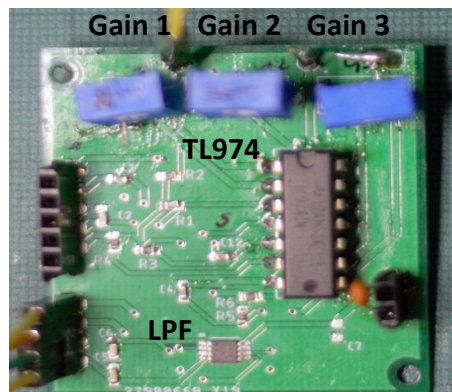
Figure 3.19: TL974 operational amplifier with the MAXIM 7408 LPF in a custom PCB. The design provided three output pins each pin (labelled as gain 1, gain 2 and gain 3) providing a gain controlled by its potentiometer. This allowed amplification flexibility through separate gain outputs that can be cascaded or used individually.

For initial in-door testing, the potentiometers were used to increase the gain until a suitable signal is observed on the oscilloscope. A signal of ~125 mV (from its initial ~50 mV) was found suitable for testing, indicating a voltage gain of 13.97 dB. Simple finger motions and hand gestures were measured with an immediate response on the oscilloscope (shown in Appendix O).

3.8.8 Analogue to Digital Converter

In order to process the analogue IF signal, it is required to be converted to a digital signal, which is the function of an analogue to digital converter (ADC). The ADC would have to operate at a low frequency range, preferably starting from as low as possible (Hz range). Initially, a Raspberry Pi was intended as a microcontroller that could process the signal. However, a Raspberry Pi does not have a built in ADC and thus requires an external ADC either via its USB port or a custom PCB design.

Different ADCs were experimented with, where finally an external Startech USB audio adapter was used [187]. The audio adapter uses a CM6206 chipset that is compatible with a Windows operating system and accepts audio input via a 3.5 mm mini-Jack. The chipset has a resolution of 16-bits and supports a 2 channel ADC input, while supporting a maximum input voltage of 5.5 V [188]. The ADC operates at a frequency range of 16 Hz to 19.2 KHz, which is suitable for its intended purpose. The USB ADC requires a 3.5 mm mini-Jack to be inserted in the device's line-in port. This required stripping the audio jack from one end and connecting it to the output of the amplified IF signal.

Using the ADC, the radar's output (of the amplified and filtered signal) was recorded in 16-bit wave formats and sampled at 44.1 KHz. In other words, the USB ADC would convert the analogue signal obtained from the amplifier to a digital signal, which can be recorded on the computer as audio input using an audio recording software such as Audacity [189]. The 44.1 KHz sampling rate was deemed sufficient to prevent aliasing and to satisfy the Nyquist theorem, where the sample rate must be at least two times the highest frequency (400 Hz) recorded. The recorded signal can then be saved as an audio file (.wav) and processed using a digital signal processing software such as MATLAB [190].

3.8.9 Further modifications

The V1 radar, the voltage regulators, the waveform generator, the gain block and the LPF were connected and tested. The change in the combined circuitry and the wiring is shown in Figure 3.20, which displays the transition from hazardous and problematic wiring to PCBs.

To further reduce the PCBs, the PCB for voltage regulation + waveform generation and the PCB for gain + LPF were combined in a single PCB as shown in Figure 3.20(c). This provided a better portability and significantly decreased the wiring even further, which reduced potential issues in field testing. The V1 radar consumed 336 mA of current via a 11.7 V battery, to produce an EIRP of 34 dBm when equipped with the HMC932ALC4 in the transmission channel.

Upon replacing the HMC932ALC4 with the HMC408LP3, the V1 radar consumed 1086 mA of current and produced an EIRP of 42.5 dBm. This prototype served as an initial performance baseline that was expected for the custom PCB radars. The V1 radar shown in 3.20 was replaced with the V2 radar which utilised the integrated baseband board when performing outdoor experiments.

In efforts to further reduce the number of boards and improve the performance, the baseband amplifier was re-designed and integrated onto the V2 radar. The previous amplifier was found to exhibit noise in the lower frequency band of the signal (50/60 Hz), which can be reduced when using an amplifier with a high common mode rejection ratio (CMMRR). Thus, the new amplifier of choice was the OPAx365 by Texas instruments, which provides a 100 dB CMMRR, low noise, fast settling time and contains two op amps per IC, supporting 120 dB amplification.

The amplifier was built as a two-stage active inverting operational bandpass filter, with a low cut-off frequency of 3 Hz and a high cut off frequency of 408 Hz. The high cut off frequency, low cut off frequency and gain were identified using the following equations respectively.

$$High\ Cutoff\ Frequency = \frac{1}{2\pi R_1 C_1} \qquad 3.32$$

$$Low\ Cutoff\ Frequency = \frac{1}{2\pi R_2 C_2} \qquad 3.33$$

$$Passband\ Gain = \frac{-R_2}{R_1} \qquad 3.34$$
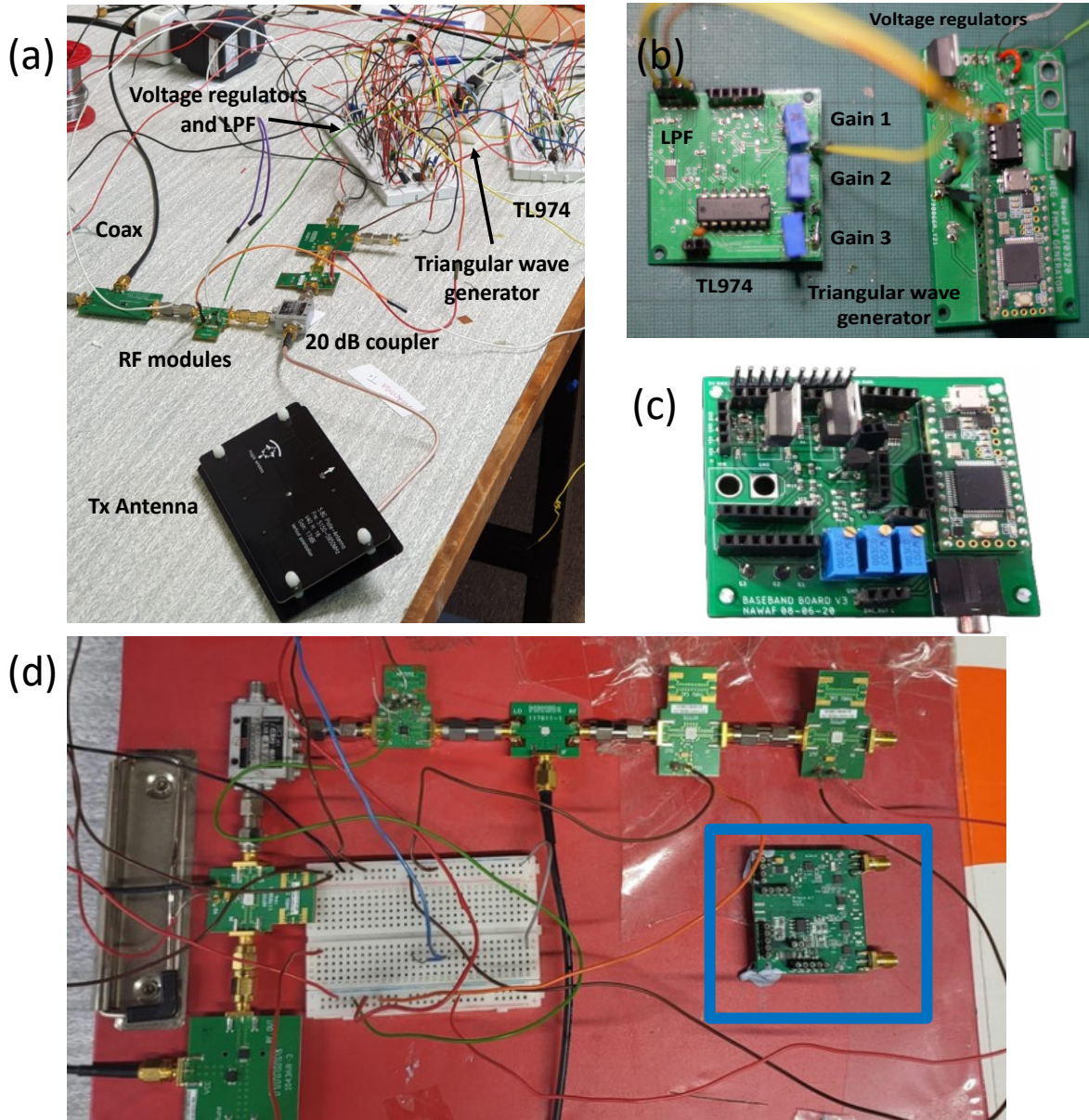
Figure 3.20: (a) Three breadboards making up the TL974 gain circuit, the Teensy 3.2 triangular wave generator, voltage regulators + LPF and RF modules (b) The reduction of the breadboards into two single boards; the gain + LPF board and the voltage regulator + Teensy LFM generator(c) The reduction of the two PCBs into a single PCB providing the function of the Teensy LFM generator, voltage regulation, gain and LPF. (d) The V1 radar placed on a clipboard for portability compared with the integrated PCB of the V2 radar shown in the blue box.

The choice of 408 Hz was due to the maximum speed of a honeybee being 32 km/h, which at 5.8 GHz corresponds to 345 Hz based on equation 3.16. Thus, eliminating the need of a LPF. The amplifier was simulated while setting the gain in the first and second stage as high as 390 (51.8 dB) and 500 (53.9 dB) respectively. This provided an overall amplification of 105.7 dB, which was based on two stages, where the 1st stage can be used separately or cascaded. The baseband amplifier was simulated below in Figure 3.21(a) while the output of the simulation is shown in Figure 3.21(b).
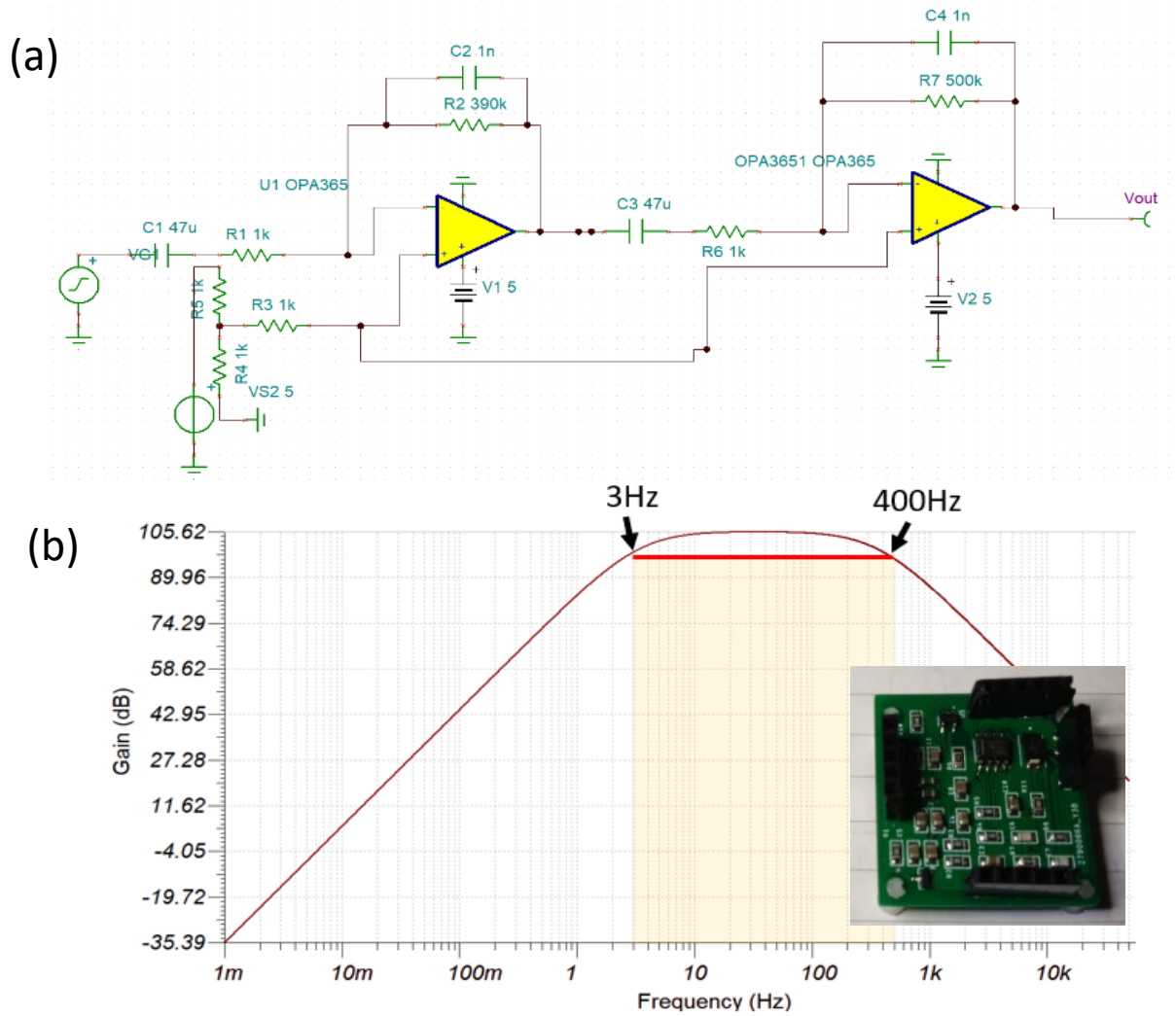
Figure 3.21: (a) OPA365 simulation circuit (b) Simulation results of the two-stage amplifier showing a total of 105.62 dB with a passband of 3 Hz to 400 Hz. Inset shows the OPA365 on a custom PCB.

The new baseband amplifier suited the intended application in terms of noise level, bandwidth, gain and frequency response and was thus prepared on a custom PCB as shown in Figure 3.21(b) as an inset. The OPA365 amplifier footprint was reduced and thus found suitable to be integrated on the radar board, while isolating the amplifier from the RF section on the PCB. Based on several tests with the 105.7 dB amplification, the second stage was replaced with a potentiometer to evaluate how much gain was needed in the second stage. It was found that an overall of ~60 dB would be sufficient to maintain an acceptable signal to noise ratio for targets as small as honeybees.
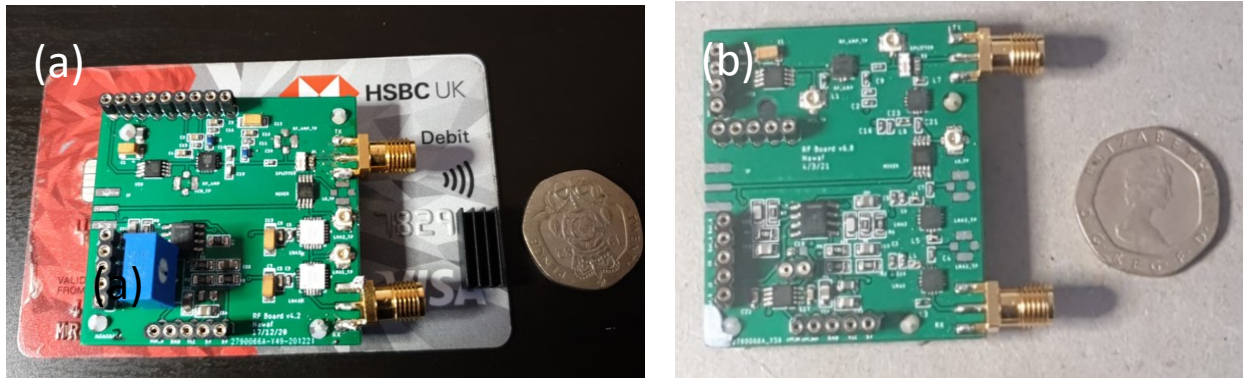
Figure 3.22: (a) 2nd Iteration of the V2 radar PCB with the PMA3-83LN+ (b)Third iteration of the V2 radar PCB with the PMA3-83LN+ and PMA3-83LNW+. Both radar PCBs show the integrated baseband amplifier, where the integrated amplifier in (a) and (b) had fixed resistors.

The first gain stage was thus reduced to 31.8 dB by setting R1 to 10 KΩ and R2 to 390 KΩ while the second stage was increased to 33.9 dB by setting R1 to 10 KΩ and R2 to 500 KΩ. This provided an overall 65.8 dB amplification if both stages were cascaded, from the previously simulated value of 105.7 dB.

3.8.10 Preliminary results

The V2 radar was compared to the V1 radar, where a series of tests were conducted to evaluate the signal. Among such tests was walking away from the radar and back towards the radar to obtain a decreasing amplitude (as the target moves away), followed by an increasing amplitude (as the target returns to the radar). A less noisy signal was observed upon comparing the third iteration radar board with the V1 radar. Upon later investigations, it was found that the noise received in the signal was due to the laptop's charging cable transformer and nearby power sockets that affected both radars at that time. When these external factors were removed, the performance of the V2 radar experienced less noise compared to the V1 radar (Shown in Appendix F). Upon testing the output power of the V2 radar using a spectrum analyser it was found that the radar's total output power was not matching that of its theoretical performance. The link budget of the radar (shown in Figure 3.23) estimated a total EIRP of 43.5 dBm and a power of 28.5 dBm, while the measured output power was 14 to 16 dBm at the antenna's output port, resulting in an EIRP of 31 to 33 dBm. Though the 14 to 16 dBm power output was lower than expected, the 31 to 33 dBm EIRP was sufficient using 17 dBi antennas.
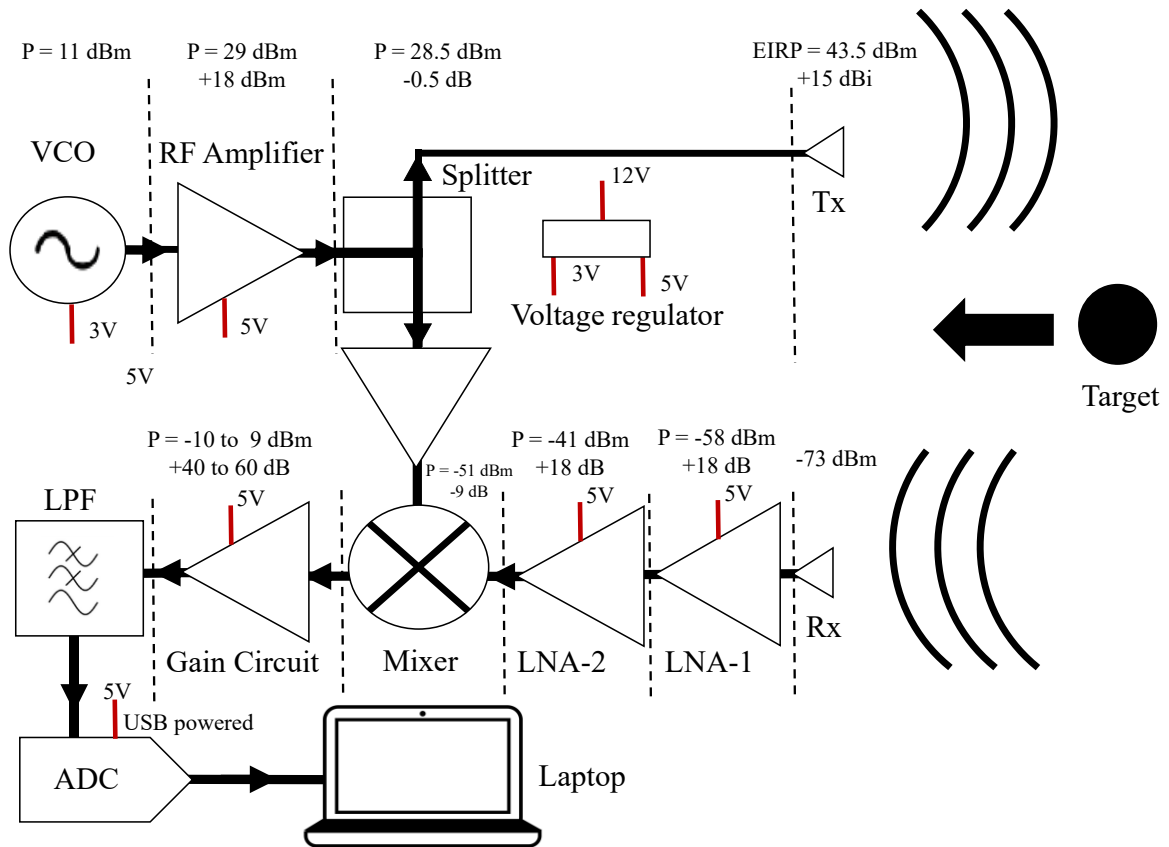
Figure 3.23: Link budget of the 5.8 GHz radar V2 third iteration.

This could still be increased upon changing the antenna's gain, using an active antenna with a built-in gain module or adding an evaluation board amplifier via an SMA connector. The maximum detectable signal of a car, human and an insect, were calculated as 130 metres, 41.4 metre and 2.3 metre respectively. The reasons behind the decrease in power are further elaborated upon in section 3.10.1 and further in Appendix K.

3.9 5.8 GHz I/Q Doppler PCB Radar

Though both the V1 radar and V2 radar were used for outdoor field experiments, there was still room for improvement. Both radars had external power regulation units, a down-converting mixer and an external USB-based ADC for signal digitisation, which was found to impose digital noise into the IF signal based on which USB port was used. This radar — referred to as V3 — combined the full power regulation and the ADC along with the RF components and the baseband amplifier on the same PCB, whilst replacing the down-converting mixer with an I/Q mixer capable of target direction discrimination. This provided a complete plug-and-play I/Q radar solution on a single portable board. Figure 3.24 shows the circuit diagram of the I/Q PCB radar along with the theoretical link budget calculation.
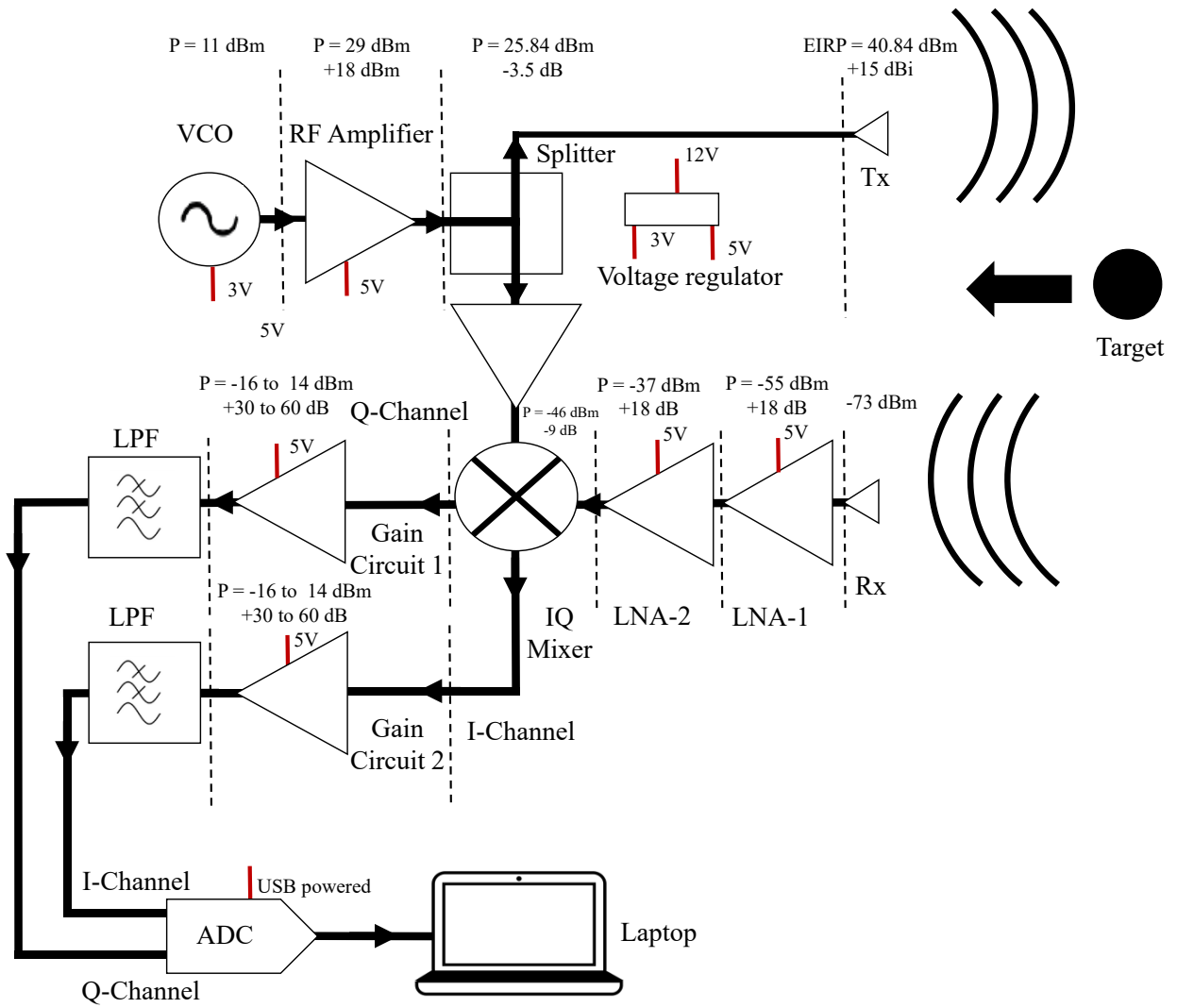
Figure 3.24: Circuit diagram and link budget of the V3 5.8 GHz I/Q radar. The circuit illustrates the I/Q mixer providing an I-channel and a Q-channel.

This board used the same RF components in the receiving channel as the previous V2 radar, causing a similar NF_{System} and MDS, equal to 1.217 dB and -73.33 dBm respectively. The radar was designed on a 4-layer PCB, while using 50Ω Conductor Backed Coplanar Waveguide (CBCPW) transmission lines. This version added the remaining functions that were used externally to the PCB, including the full power regulation, a dual-channel ADC and audio CODEC, a I/Q mixer instead of the previous double balanced mixer and a 3.5 mm audio Jack output port for ease of use with a signal processor. The plug-and-play compatibility of the V3 radar would allow any inexperienced user to utilise the radar for experiments and could support live machine learning integration on a microcontroller due to its built-in power regulation, ADC and audio Jack. The PCB's size was a total of 98 mm × 64 mm. Figure 3.25 shows a 3D CAD model obtained from Autodesk FUSION of the V3 I/Q radar PCB designed in EAGLE.
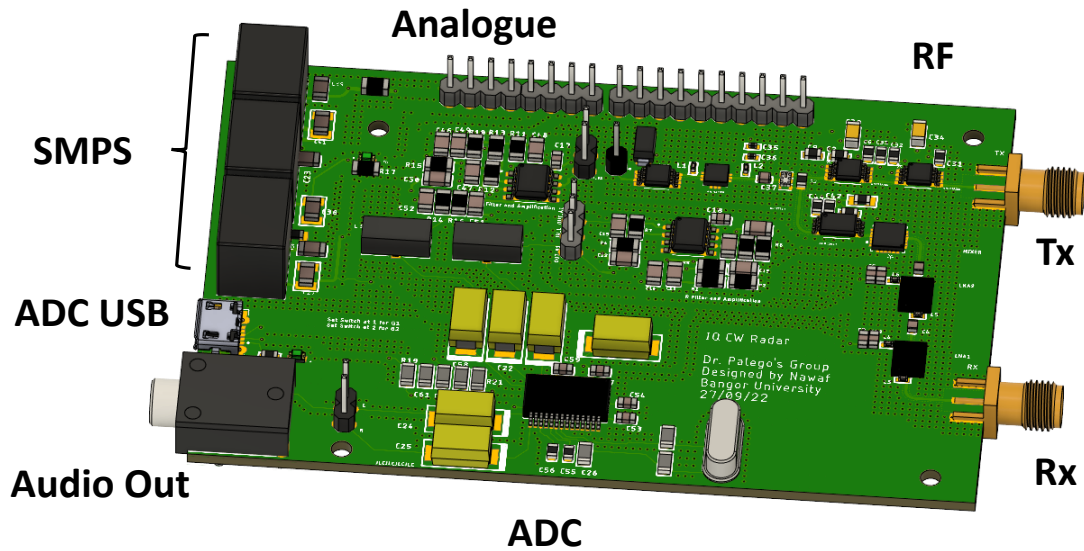
Figure 3.25: 3D CAD model of the 5.8 GHz I/Q V3 radar showing the main parts of the board.

3.9.1 Integration of power regulators

High performance and RF systems require low noise power supplies to achieve an optimal performance. The previous radars (V1 and V2) used linear voltage regulators (LVRs). Though the LVRs were able to regulate the power effectively, the LVRs rapidly increased in temperature and required heat sinks to absorb their heat. The issue with LVRs heating is twofold. Firstly, the heat resonates down the pins of the LVR, which are soldered to the board. While heat may dissipate into the heatsinks, a portion dissipates into the board, which in return increases the temperature of the board. This could lead to the board's temperature increasing which could cause components to malfunction and cause additional noise induced in the board. This is especially the case when dealing with RF components, as an increase in temperature could cause a significant shift in amplifier and VCO performance.

The second issue with LVRs was their poor power efficiency. The heat generated is power from the battery due to the LVRs poor power efficiency during its power regulation, which causes a power efficiency of as low as 27% [191]. A suitable replacement may be the use of Switch Mode Power Supplies (SMPS), as their power efficiency reaches to 90% and above [191]. The SMPS used in the V3 radar were the K7805-2000R3 and K7803M-1000R3 for 5 V and 3 V respectively, which both have an efficiency of up to 96%. Another advantage of SMPS over LVRs is that SMPS are developed with internal filtering that filters AC noise. The SMPS do not heat up, which eliminates the need of heatsinks, causing the power regulation solution to become smaller and lighter in

weight. Despite their benefits, SMPS can induce switching noise. Thus, when choosing SMPS for noise sensitive applications, it is important to look at the switching frequency, which for the selected SMPS was 400 KHz (400 KHz >> frequency of interest). This was 10 times larger than our frequency of interest (400 Hz), deeming it a suitable SMPS. Additionally, the V3 radar board was equipped with a LPF capable of filtering out high frequencies.

In mixed signal boards (analogue, digital, High frequency RF and power), power is often provided from different power domains, to prevent fast digital switching noise to couple into the sensitive analogue supply rail, thus degrading the performance. However, using different power domains increases both cost and system complexity while decreasing the portability. A suitable method implemented in the V3 radar board to filter the power supply noise allowing clean power supply rails was the use of a ferrite bead connected in series with the power rail. This passive component, filters noise which is dissipated via heat. Common filtering applications connect capacitors to ground on both sides of the ferrite bead, which forms a low-pass filter network to reduce high frequency power supply noise [192].

The SMPS improvement over LVRs and their impact on the signal was clearly observed during initial tests, which is demonstrated in Figure 3.26. Though one 5 V SMPS was enough for the radar, a spare 5 V SMPS was added to act as a substitute if the first were to fail. A final change to the power regulation was the addition of an LED as an indicator to when the SMPS started regulating the voltage.
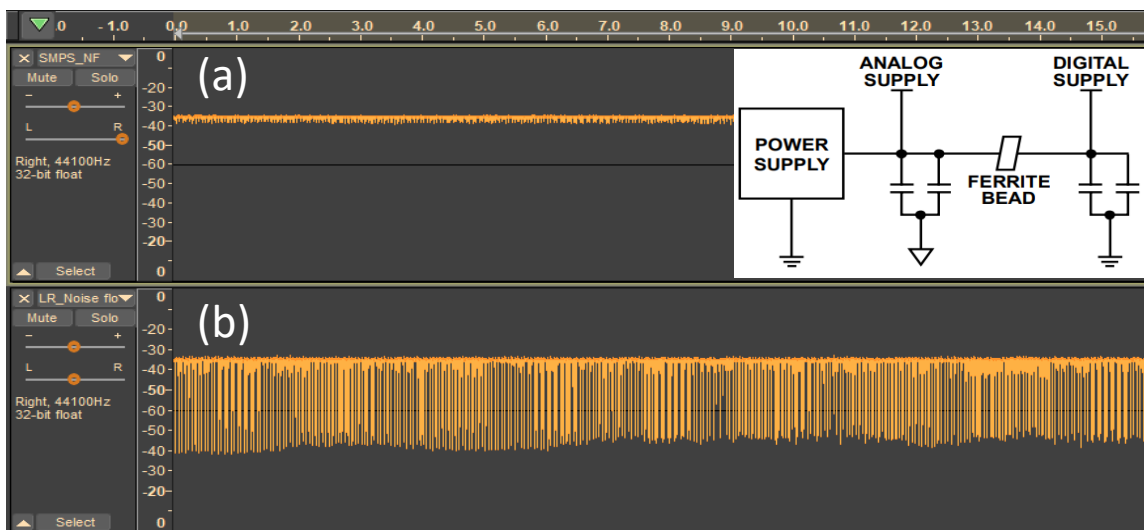
Figure 3.26: (a) Radar signal of recorded noise floor using SMPS for voltage regulation showing a much cleaner signal compared to the LVRs (b) Radar signal of recorded noise floor using LVRs for voltage regulation. Inset shows the recommended way of connecting a ferrite bead to the power supply rail [192].

3.9.2 Quadrature mixer

Experiments conducted on both the V1 radar and V2 radar, demonstrated the lack of direction discrimination in the Doppler shift, which is known to manifest in a positive or a negative doppler shift ($\pm f_d$). In a double balanced mixer that performs up-conversion or down-conversion, the negative Doppler shift is only distinguishable from a positive Doppler shift by its phase [177]. This is because the positive Doppler shift is observed as an in-phase signal, while the negative Doppler shift appears as a 90° phase shift [177]. Thus, a double-balanced mixer is unable to distinguish the difference between a positive and a negative Doppler shift [177]. This can be achieved through the implementation of an I/Q architecture, which allows receiving a complex signal that has both the I and Q components. The I/Q components are signals that have the same amplitude and frequency but are out of phase by 90° (a quarter cycle). Such an implementation, would replace the common down-converter mixer module with an I/Q mixer.

The HMC525ALC4 was used as the I/Q mixer, which operates from 4 to 8.5 GHz with a conversion loss of 8 dB. As a passive device with no DC bias requirements, it still requires a minimum LO of 15 dBm to operate reliably. The I/Q mixer produced two outputs, where each output needed to be amplified. Thus, this required two amplifier circuits to be fitted on the board. The same operational amplifiers discussed in section 3.8.9 were used. Since these were designed to provide a dual stage output, each output stage was designed to be controlled with a DIP switch to allow the user to choose the amplification required (from low to high). In other words, this allows the user to decide upon using a single amplification stage (~30 dB) or a dual amplification stage (~65 dB) using a convenient DIP switch placed on the PCB.

3.9.3 Analogue to Digital Converter

Both V1 radar and V2 radar lacked on-board signal digitisation and required the use of an external USB-based ADC instead. Though this provided a means of signal digitisation, it still required the use of an external hand-held USB ADC, which hindered portability and leaked digital noise from the USB port into the signal. This was noticed to vary from USB port and laptop used. Further, to support remote and/or live microcontroller-based radar monitoring an on-board ADC was necessary.

The on-board ADC needed to provide a dual channel operation to digitise both I and Q channels, with a resolution not lower than 12-bit and should allow the user to have minimal involvement in its installation. The chosen ADC was the PMC2902 stereo (dual channel) USB codec (ADC/DAC) with line-out.

The ADC is equipped with a USB chip interface allowing it to be USB bus powered and to be fully compliant with USB specifications. The ADC comes with 16-bit resolution and has sampling rates of up to 48 KHz. The chip's USB controller allowed seamless automatic integration with a computer's operating system, where the ADC's chip is automatically detected and installed.

The ADC supported USB power which may be convenient, but less efficient. Using USB power can impact the signal's integrity by imposing digital noise along the power provided to the USB. This would provide the same digital noise issues experienced with the external ADC. The PMC2902 circuit diagram (Figure 3.27(a)), was modified to receive power from the SMPS instead and fitted with an LED. Figure 3.27(b) shows the old ADC USB adapter, which was no longer required.

Figure 3.27: (a) PMC2902 circuit diagram (b) V3 I/Q radar placed next to discarded ADC that was no longer needed.

3.10 Preliminary results

Upon testing the V3 radar, it was found to provide the lowest noise floor and provided radar readouts with lower noise levels as compared to the other two radars (V1 radar and V2 radar). This was believed to be due to the addition of SMPS, ferrite beads and the elimination of digitally induced noise. The radar's portability and extended functions provided a complete plug-and-play radar experience. The radar board and different functions of the board are shown in Figure 3.28(a).

The addition of the I/Q mixer provided the V3 radar with means of direction identification. This is demonstrated in Figure 3.28(b), which shows a variety of hand gestures that were recorded and plotted as spectrograms. When moving the hand away from the radar a negative shift can be clearly observed and when moving the hand towards the radar a positive shift was observed. An interesting observation was the quick hand movement towards the radar, which occurred at 4 seconds. Upon looking closely at around 2 to 3.5 seconds, a negative shift is seen twice. This is where the hand was firstly withdrawn after a series of movement towards and away.
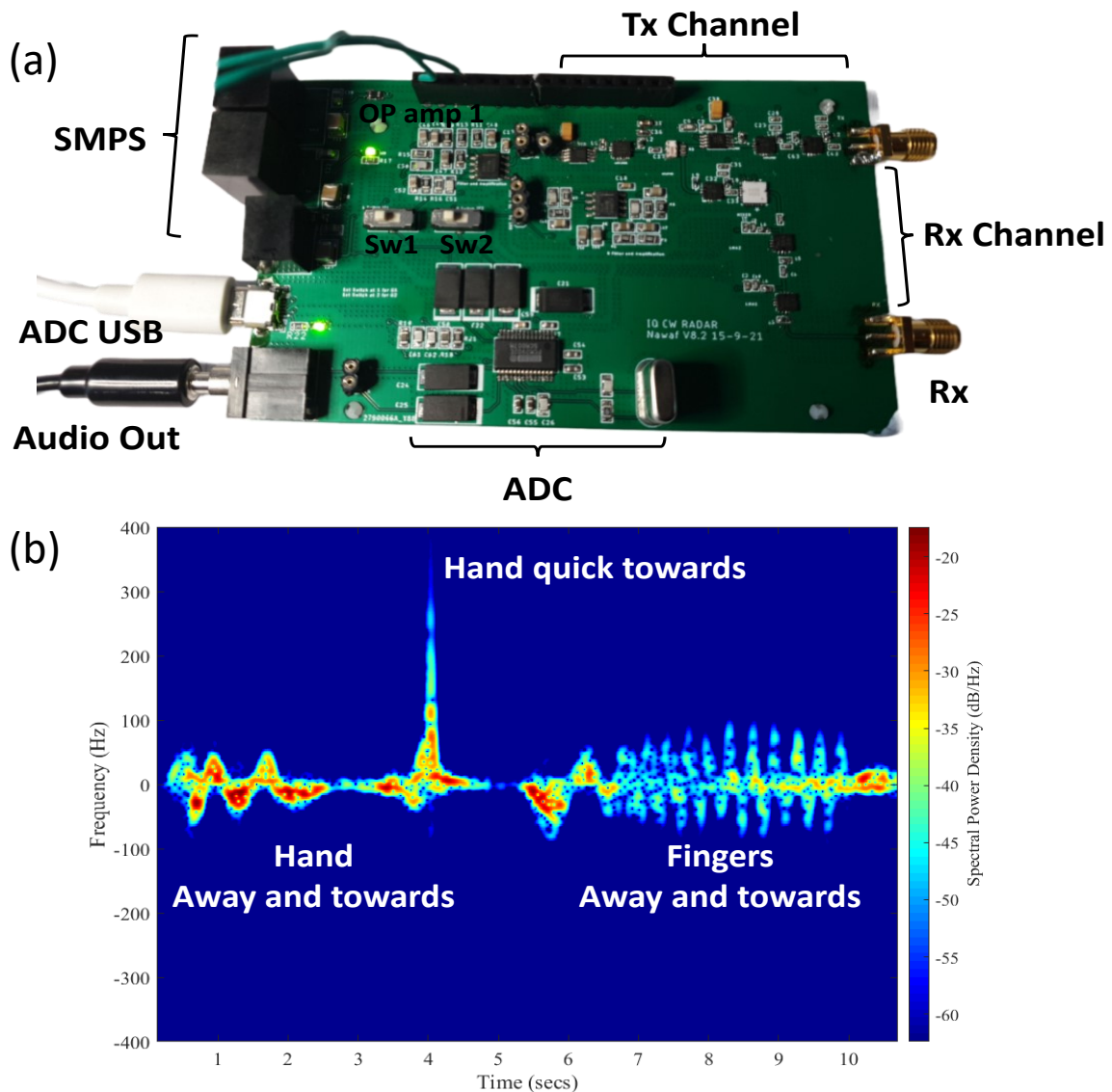
Figure 3.28: (a) Finalised V3 I/Q radar board illustrating different sections of the board (b) V3 I/Q radar board test signals showing clear positive and negative Doppler shifts recorded.

The hand was finally moved away at around 2 seconds (1st negative Doppler), and then moved back again (2nd negative Doppler) to create more momentum in order to be able to move the hand quick towards the radar again, causing the positive Doppler peak at 4 seconds. It was interesting to observe how such minor hand movements were clearly recorded. It was also noticed that the radar was able to record I/Q signatures from targets as small as fingers.

The measured output power was between 7 and 8 dBm, which was lower than expected and resulted in an EIRP of 24 to 25 dBm. The maximum detectable signal of a car, human and a bee, were calculated as 48.8 metre, 15.2 metre and 0.9 metre respectively. Upon comparing the performance of all three different radar versions, this version provided the most functionalities while having the lowest transmitted power.

3.10.1 Power output analysis and potential solutions

Upon further investigations into increasing the radar PCB performance, the 50 Ω SMA (DC to 18 GHz) and its pin connection to the 4-layer FR4 radar board (ε_r=4.6) were modelled and simulated in CST. This initial performance showed an S21 and S11 of -2.74 and -3.6 dB, which indicated that 47% was reflected back. This reflection was much higher than anticipated and can cause a significant reduction in the expected output signal. The wide transition from the SMA's pin to trace can cause a high shunt capacitance, which could result in an impedance mismatch. A method of reducing the shunt capacitance is by implementing a "cut ground" under the pad, which in return increases the strip's ground reference layer [193], [194].

By increasing the trace width to 0.38 mm (from 0.29 mm), setting the gap between trace and ground pour to 0.07 mm and implementing a 2nd layer ground cut-off of 5.75×3.75 mm the S11 was reduced to -32.89 dB, which resulted in a reflection of 0.0514% from the initial 47%. This is shown in Figure 3.29, where the S21 is shown in green (visible at -0.228 dB) and S11 is shown in red. Note that since the SMA was designed to operate from DC to 18 GHz, the S21 is designed to operate from as low as DC, but further optimised to have its peak performance at 5.8 GHz, which explains why the base level is not 0 dB. Based on the simulation outcomes, a series of transmission lines were manufactured and tested using a VNA, which indicated a lower S11 for the cut-off compared to the S11 of the PCB without cut-off. The simulations and transmission lines are described with further detail in Appendix K.
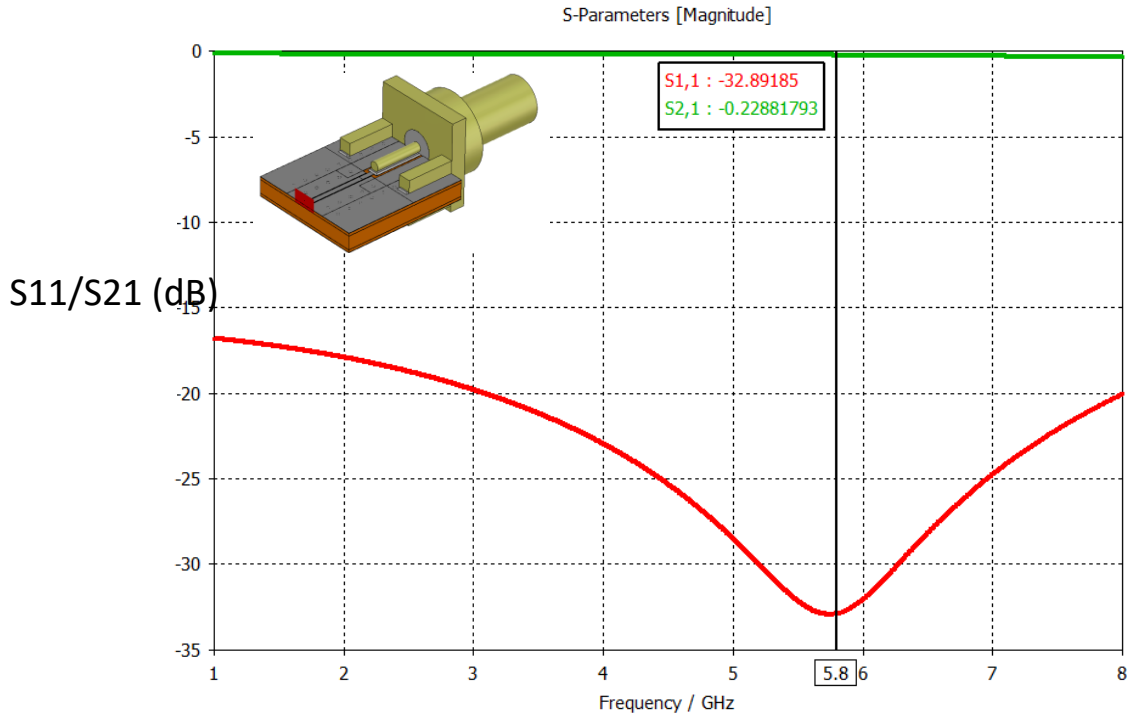
Figure 3.29: S-Parameter plot of the 4-layer FR4 PCB with 2nd layer ground cut-off showing the S21 in green and S11 in red. Inset illustrates the simulated SMA and 4-layer board PCB with 2nd layer ground cut-off.

3.11 Digital Signal Processing

All monitored radar signals were digitised, recorded and saved as .wav files, allowing the signals to undergo digital signal processing. Common methods of digital signal processing were the Fourier transform, the discrete Fourier transform and the scalogram, which are further described in Appendix R.

3.11.1 Spectrograms

Short Time Fourier Series (STFT) examine a signal's frequency content as a time window is moved, which then generates a two-dimensional time-frequency distribution plot called the spectrogram. Spectrograms are commonly used to plot time-varying spectral density over time-varying signals and are commonly used in radar signal processing. Spectrograms are Spectro-temporal presentations, and provide the change in frequency content of a signal over time. Spectrograms are generated from a series of overlapping signals (which depends on the windowing size) [195], [196] and are defined as,

$$Spectrogram\ (t, \omega) = |STFT\ (t, \omega)| \hspace{2cm} 3.35$$

Signals of practical interest are long enough to be broken down into smaller sections, such as a recorded speech separated into words, or a radar signal separated into

distinctive radar signatures. The STFT, splits the data into windows and calculates the fast Fourier transform (FFT) over each window of the presented data rather than using the Fourier transform to an entire signal over a long window. A common rule of thumb is to have 5 to 10 periods of the signal in each window [180]. The resolution of an STFT is a trade-off between frequency resolution and time resolution, where a large window produces a high frequency resolution but a low time resolution and vice versa [196], [197]. A wide range of window functions exist (e.g., Hamming, Gaussian, Hanning, Kaiser-Bessel), where windows generally should reduce the sidelobe interference in spectrograms by tapering to zero smoothly [197].

3.12 Radar Calibration

The first step in preparing the radar for insect monitoring was the calibration of the radar. This involved observing the radar's signatures upon monitoring miniature targets and confirming its ability to record a signal with an adequate SNR. The previous sections demonstrated the functionality of the radar in recording signatures as small as finger gestures (Appendix O) with capability of providing clear different gestures which can easily be discriminated visually. The true challenge was experimentally identifying targets a small as bees, such as steel spheres mentioned in chapter 2.

3.12.1 Steel spheres as radar targets

The radar was placed with both Tx and Rx pointing upwards and nine 4 mm steel spheres were dropped from a height of 2 metres upon the radar's antennas, where the radar captured the sphere's free fall under gravitational force. Since the antennas were pointing upwards, the entire free fall duration of the 4 mm steel spheres was captured. The recorded radar signatures were plotted using STFTs and examined, to identify the peak magnitude value of the falling spheres. The 4 mm steel sphere's plotted STFT magnitude was normalised to the simulated peak RCS magnitude obtained from the simulations of the 4 mm steel sphere (-64.6 dBsm discussed in chapter 2). Although a calibration model for the 4 mm steel sphere obtained was considered sufficient, smaller diameter steel spheres were also experimented with. In addition to the initial nine 4 mm spheres, three 3 mm spheres and three 2 mm steel spheres were also dropped from the same distance, to replicate the procedure. STFT plots of these are shown in Figure 3.30.
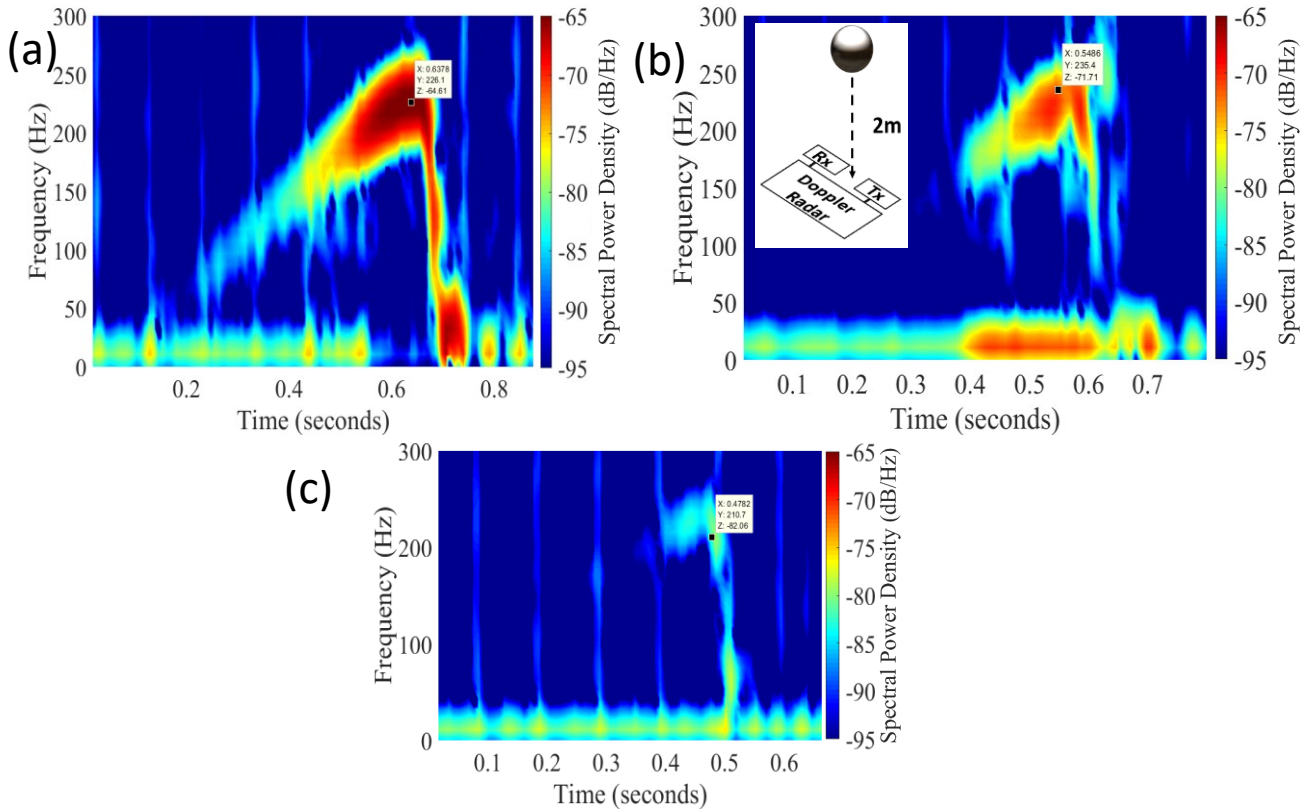
Figure 3.30: STFTs of two metre drop of steel spheres indicating the peak RCS plotted for (a) 4 mm steel sphere (b) 3 mm steel sphere (c) 2 mm steel sphere. Inset shows the experimental setup.

This was performed to measure and validate the RCS measurement and repeatability for lower target RCS. The STFTs of the three samples are shown in Figure 3.30(a)-(c), which illustrate a 4 mm steel sphere measured RCS of −64.82 dBsm, 3 mm as −74.73 dBsm and 2 mm as −79 dBsm respectively.

Table 3.4 summarises the targets that were used for the RCS experiment alongside their simulated and experimental RCS values. This demonstrated that the RCS calibration method was in close approximation with simulated RCS values. For the steel spheres of 4 mm, 3 mm and 2 mm the deviation between measured and simulated RCS values was 0.2, 1.5 and 3.1 dBsm respectively. This is plotted in Figure 3.31, which shows the experimental values as symbols. It was observed that the symbols, converged with the simulated steel sphere RCS curve.

Table 3.4: RCS targets used for RCS experiment and their simulated RCS values.

Target	Average RCS measurement (dBsm)	Simulated RCS (dBsm)
4 mm Steel sphere (n=9)	−64.43	−64.6
3 mm Steel sphere (n=3)	−70.01	−71.6
2 mm Steel sphere (n=3)	−79	−82.1
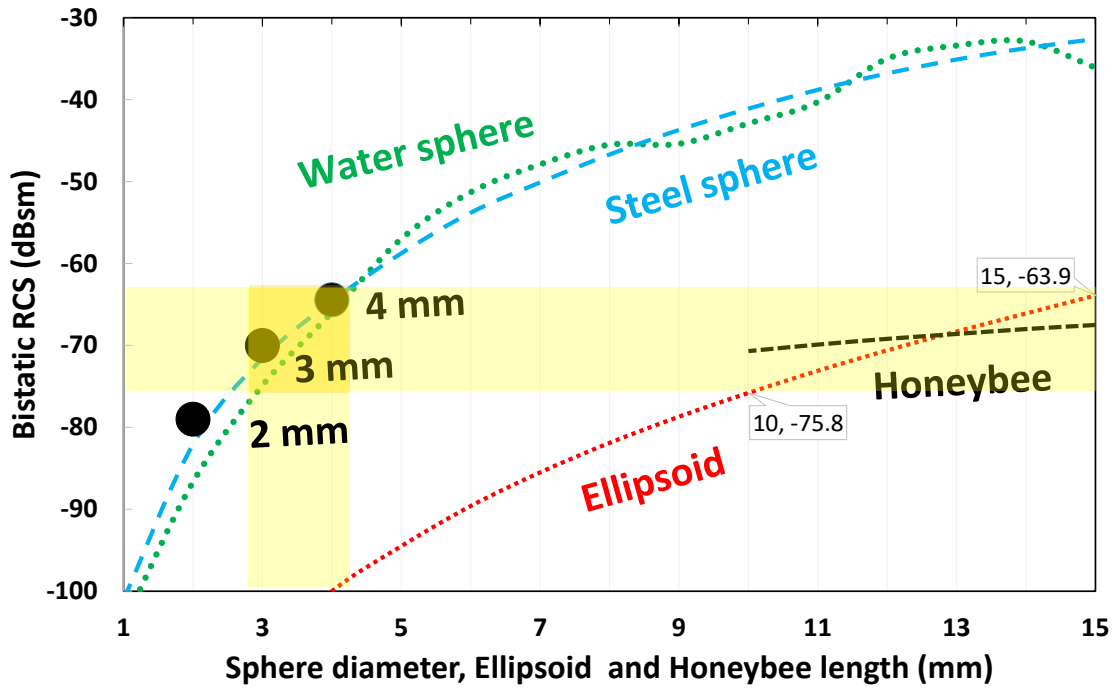
Figure 3.31: Simulated RCS values of steel spheres, water spheres, a honeybee and an ellipsoid. The yellow highlighted area shows a region of RCS convergence where different simulated targets intersect. The 3 black circles indicate the average experimental values recorded of the 4 mm steel sphere, 3 mm steel sphere and 2 mm steel sphere.

This indicated that the experimental setting matched that of the simulation. It can also be seen that the symbols of 3 to 4 mm steel spheres, perfectly aligned within the dark yellow band where the RCS overlapped with that of an ellipsoid, honeybee, water sphere and steel sphere, further confirming the 3 to 4 mm steel sphere's suitability for honeybee RCS approximation.

3.12.2 Measuring steel sphere's Doppler shift

In order to extract the Doppler shift from free-flying honeybees, an experiment was required to demonstrate accurate Doppler shift extractions. One of such experiments was the free fall experiment of a 4 mm steel sphere, where the initial velocity and acceleration were known as the gravitational acceleration, which dictated the velocity of the free-falling steel sphere once the sphere was released from its initial stationary position.

The 4 mm steel sphere was released from a height of 2 metres. The fall was recorded with a video camera that allowed slowing the frames (providing slow-motion effect) to aid in accurately identifying the starting point of the sphere's fall and the ending point. Upon examining the footage, the total time for the sphere's free fall was found to be

0.64 seconds. Since the sphere was falling with an acceleration strictly imposed by Earth's gravitational acceleration, equal to 9.80665 m/s², while the initial velocity of the sphere (pre-drop) was 0 m/s and the total duration of the free fall was 0.64 seconds, the free fall velocity prior to the sphere hitting the ground can be calculated as,

$$v_{free\ fall} =\ v_{initial}\ + g\ \times t_{free\ fall} = 0 + 9.80665\ \times 0.64\ = 6.263\ \text{m/s} \qquad 3.36$$

Where $v_{initial}$ is the initial velocity of the sphere (pre-drop), g is gravitational acceleration (9.806650 m/s²) and $t_{free\ fall}$ was the time duration of the fall. Using the Doppler shift equation (3.15), the Doppler shift of the steel sphere considering a speed of 6.263 m/s was calculated as,

$$Doppler\ shift = \frac{2\times6.263}{51.6\ mm} = 242.75\ \text{Hz} \qquad 3.37$$

The Doppler shift can be observed in the plotted spectrogram of the steel sphere's free fall in Figure 3.32. The peak magnitude of the radar signature was found around approximately 240 Hz, which corresponded to a speed of 6.20 m/s. This indicated an accurate Doppler shift-based velocity extraction with an error of 0.06 m/s. Though this error was observed, the error margin was considered minimal.
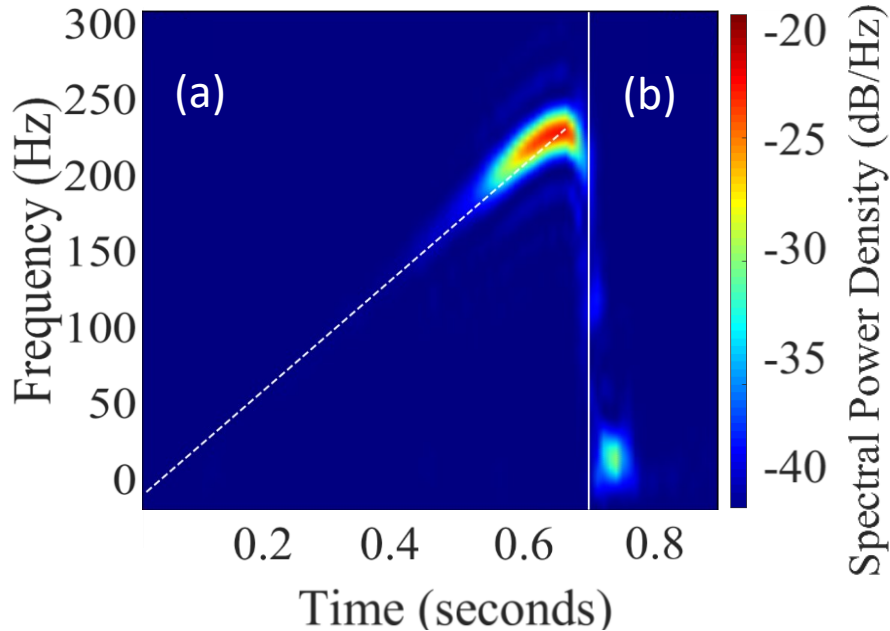
Figure 3.32: STFT of 4 mm steel sphere drop showing a comparison along gravitational acceleration, illustrated as white dashed gradient. (b) Effect of steel sphere bounce after the initial drop.

3.13 Pendulum sphere experiment

This method was implemented after the initial calibration stage to further fine tune the radar sensitivity. A servo motor was used, connected to an Arduino Uno and programmed to establish a 0 to 180° sweep. Upon tying a 15 cm thin thread, glued to the 4 mm steel sphere, it allowed the plastic rotator on the servo's motor to establish a pendulum with the earlier used calibration target (4 mm steel sphere) as the pendulum's bob as shown in Figure 3.33.

Figure 3.33: Steel sphere moving in a pendulum setup placed in front of the 5.8 GHz V1 radar. Inset shows the Arduino and stepper motor connection.

The pendulum was placed at 0.5 metre distance from the radar. Oscillations of approximately 30° were allowed perpendicularly to the radar antenna's main beam axis. In the early stages of calibration, this method kept the radar target (sphere) continuously moving, allowing the user to gradually adjust the gain settings of the amplifier until a satisfactory signal was observed. All experiments up to this point were performed using double balanced mixer architecture. However, during this experiment the double balanced mixer was replaced with an I/Q mixer (HMC525ALC4) to identify a positive and negative Doppler shift. The first pendulum radar target in the experiment was a thread without a bob. This allowed the study of the pendulum's thread impact on the signal, along with the servo motor's plastic rotator. The recorded result was plotted as an STFT with no observable signal for the thread. The next radar target was a 4 mm wooden sphere, which was previously simulated in section 2.6. Note that the minimum detectable signal of the 5.8 GHz radar was −72.72 dBm. Upon examining the STFT plot of the wooden pendulum, a minimal signal was observed, which could not be considered a pendulum signal due to its insignificance. Upon connecting a steel sphere to the pendulum, a clear pendulum signal was observed in the STFT result. These are collectively plotted in Figure 3.34.

Both wooden spheres and steel spheres had the same diameter, while maintaining similar experimental parameters (range, antenna gain, transmitted power etc.), where one may argue that they both should be perceived equally by the radar. Yet this was not the case. This was due to the wooden sphere's lower RCS as both spheres were of different material with different electrical conductivities and dielectric constants. Recall the wooden sphere simulation in section 2.6 that resulted in a simulated RCS value of −83.9 dBsm, which was much lower compared to the steel sphere's simulated RCS of −64.6 dBsm. Considering the minimum detectable signal of this radar's version was −72.72 dBsm, any signal lower than the measured value would not be detected, explaining why the wooden sphere was not detected.

3.14 Coated wooden sphere pendulum experiment

Recall from section 2.6 where the 4 mm wooden sphere was coated with a 100 μm Silver coating (σ=6.30×10^7 S/m). This caused RCS increased to an average value of 11.77 dBsm, reaching −72 dBsm from the initial −83.9 dBsm. To test this, a wooden sphere was coated with a single brush stroke of conductive Silver-paint. The coated wooden sphere along with the uncoated wooden sphere are shown as a series of insets in Figure 3.34. The coated wooden sphere was placed in the same pendulum setup used for the steel sphere and the wooden sphere, while maintaining similar experimental parameters. Upon plotting the coated wooden sphere's STFT, a signal was observed which indicated a clear pendulum behaviour. The signal was not as weak as the uncoated wooden sphere, yet not as significant as the steel sphere. Arguably one may suggest that the coated wooden sphere's recorded magnitude resided between that of the uncoated wooden sphere and the steel sphere.

The different audio files of the pendulum experiment, including the pendulum without a target (thread only), uncoated wooden sphere, coated wooden sphere and steel sphere were combined as a single audio file and processed through an STFT in MATLAB to visualise the increase in signal magnitude shown in Figure 3.34. Each target was labelled and placed in a dashed box, along with its inset. Figure 3.34 clearly indicated an increase in magnitude as it progresses from left to right, which indicated no sphere to steel sphere respectively.
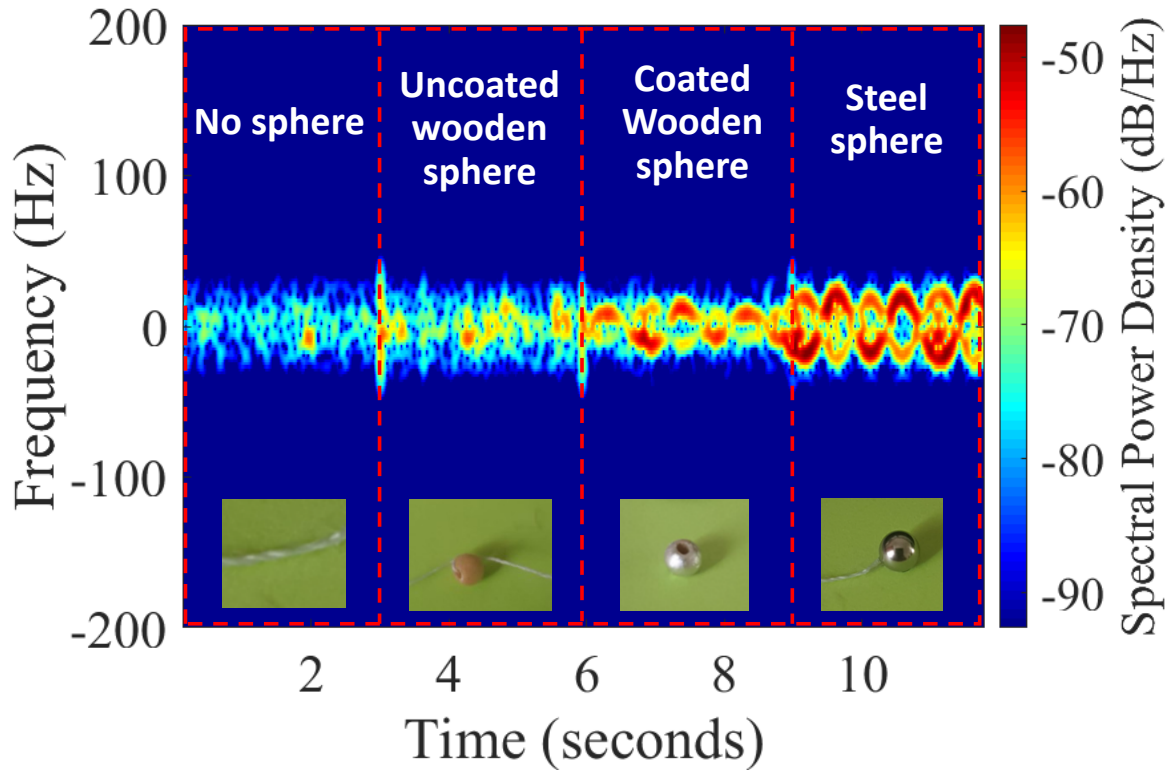
Figure 3.34: Signal magnitude increasing as pendulum target increases in RCS. The four wave files were combined (separated by red-dashed box) to demonstrate the increase in amplitude. Inset shows the targets.

To further illustrate the importance of the increasing magnitude of the uncoated wooden sphere, coated wooden sphere and steel sphere in the demonstrated pendulum setup, a plot is shown in Figure 3.35. The plot showed the minimum detectable signal of -72.72 dBm and the three mentioned radar targets.

The Figure shows a horizontal red dashed line and a vertical blue dashed line which represent the minimum detectable signal and the distance of the pendulum radar experiment 0.5 metres respectively. The lower magnitude of the wooden sphere indicated the undetectability of a 4 mm uncoated wooden sphere due to its lower RCS (-83.9 dBsm), which was below the radar detection threshold (-72.72 dBsm), coating the wood sphere with a ~100 μm Silver layer was predicted to increase the RCS to a detectable RCS of -72.06 dBsm based on simulations. This was indeed the case as demonstrated in Figure 3.33. The impact of the coating on the wooden sphere's detection range was shown in Figure 3.35. Due to the coating, the wooden sphere maximum radar range was increased from 0.4 metres to 1.2 metres.
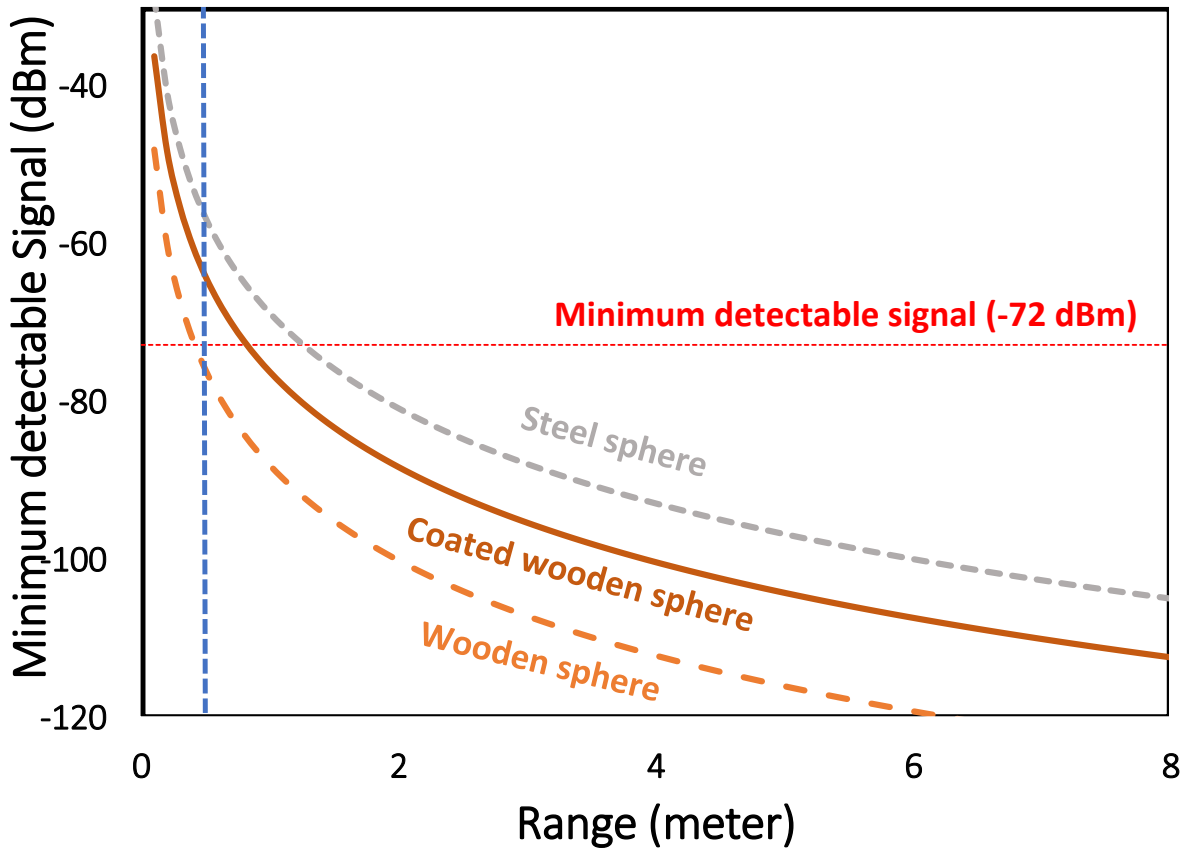
Figure 3.35: Increased detection range of coated wooden sphere compared to wooden sphere. Steel sphere acts as a reference signal to the wooden sphere's RCS. Note that the coated wooden sphere is below the steel sphere, and the uncoated wooden sphere is even lower.

Upon investigating the plot in Figure 3.35, the uncoated wooden sphere seemed to intersect with the 0.5 metre vertical line where the wooden sphere's simulated RCS is equal to -75.95 dBsm. Though this is technically out of the detectable range of the radar, the resulting signal in Figure 3.34 showed an unrecognisable signal. There were faint indicators of a signal being present at 3.3, 4.3 and 5.5 seconds, which still were deemed too weak to identify. One may argue that the sphere was swinging into and out of the radar detection capabilities, which at times indicated a weak signal as the pendulum approached the radar and at other times resembled noise as the pendulum was furthest away. Due to the signal being unidentifiable, it was not considered a reliable pendulum signal which was in agreement with the uncoated wooden sphere simulation.

3.15 Honeybee RCS Extraction

Upon establishing an effective method for RCS extraction, outdoor experimental trials were conducted with the V1 radar. The radar was placed at a 2-metre distance, facing a honeybee hive as shown in Figure 3.36. This was based on the maximum radar range for the V1 5.8 GHz radar (2 metres). The radar setup included a laptop for signal digitisation which was performed via the USB ADC adapter and a mobile phone to record the radar monitoring. The video recordings permitted visual cross-validation of honeybee activity, which were later used to extract honeybee behaviour as separate wave files. The setup is shown in Figure 3.36.
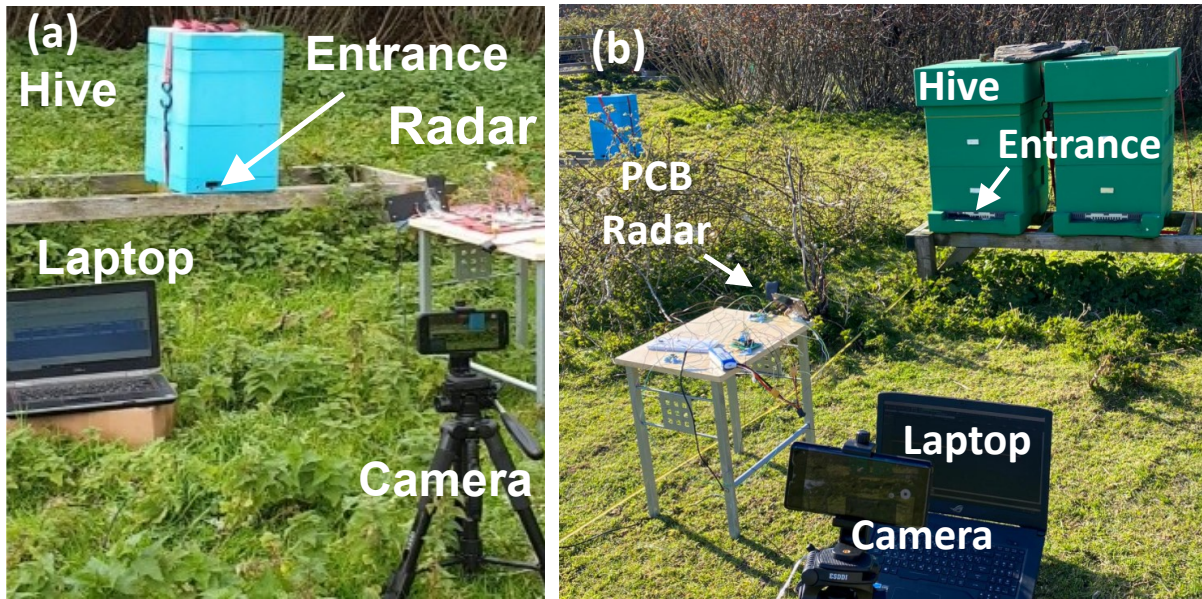
Figure 3.36: (a)Radar setup for honeybee monitoring using the V1 radar. (b) Radar setup for honeybee monitoring using the V2 radar.

Using the initial baseband amplifier, testing the radar's performance before an outdoor experiment was important. This was particularly important to address the V1 radar's variable gain, which at times may drift from the pre-set values as a result of potentiometer tolerances. Hence, prior to recording bee activity, the radar was calibrated with the 4 mm steel sphere. The radar would then be placed in front of the hive to monitor bee behaviour. The radar was powered by a 12 V LiPo battery which could ensure approximately two hours of operation. The laptops supporting the experiments were powered by their internal battery, which had afforded similar operation time. To support longer data collection, three laptops were used, along with three 12 V LiPo batteries, which allowed approximately 6 hours operation. The radar-based honeybee monitoring was conducted in Henfaes Research Centre in Abergwyngregyn on dry days with minimal wind and farm animal interruptions.

After the data collection session, the radar recorded audio file and the video recorded footage were played alongside one another to cross-correlate the radar signatures found on the audio file with video recorded evidence. This allowed confirming the extraction of sections that only correlated to honeybee signatures. The video recorder, recorded both the laptop screen — which indicated the signatures that were being recorded — while simultaneously recording the events at the entrance of the hive. This assured that both the audio recorded signatures and the video recorded signatures were present in the recorded video, for post-experimental radar signature labelling.

An example of five labelled honeybee signals are shown in Figure 3.37(a), while their corresponding STFTs are shown in Figure 3.37(b). The five honeybee signature examples demonstrated in Figure 3.37(a), showed an increasing amplitude as bees rapidly left the hive, while the returning bee illustrated a stretched out, lower speed signal. This was observed in both the time domain signals and frequency domain signals. Figure 3.37(b) showed the RCS values of the monitored honeybees ranging from −58.82 to −62.89 dBsm.
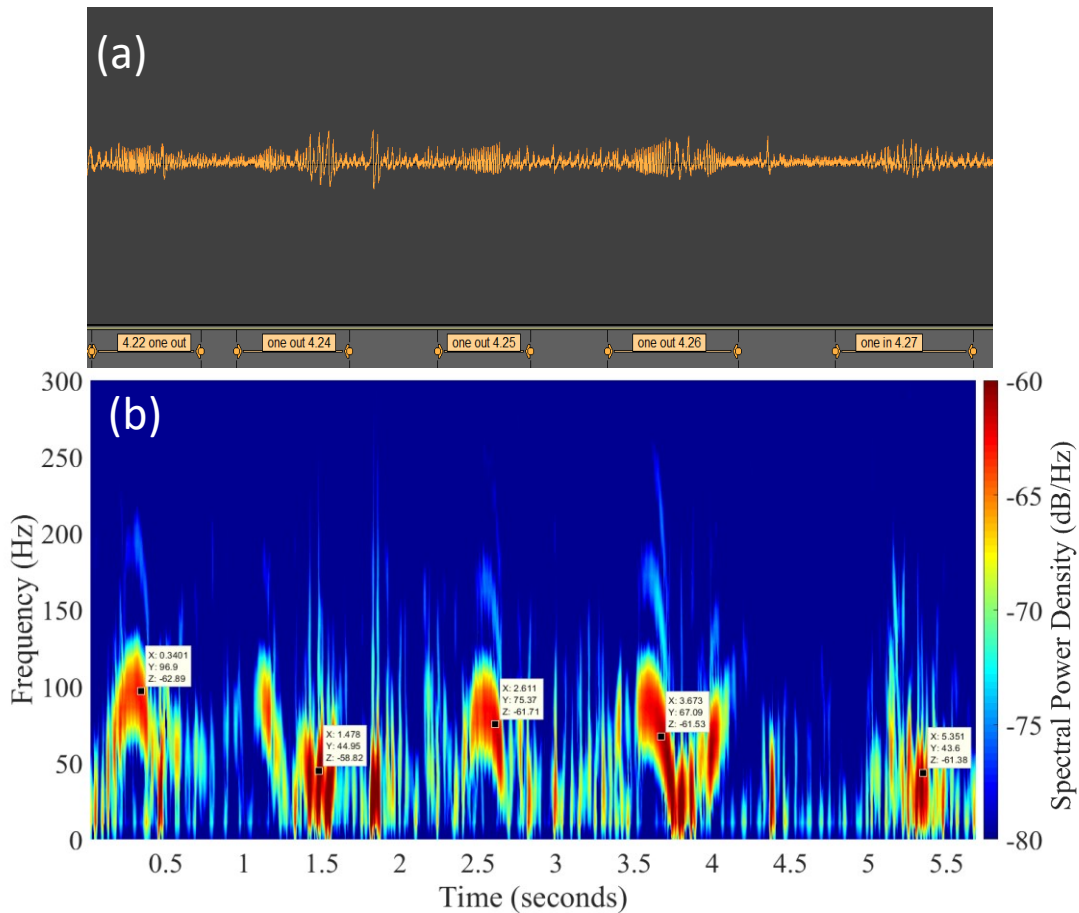
Figure 3.37: (a) Labelled audio file in Audacity showing each bee signature in an oscillogram plot (b) The same audio file represented as an STFT using MATLAB, showing the bee signatures in the frequency domain, while marking their signature to return the approximated RCS value.

Upon investigating the Doppler shift of the recorded signals, the first outgoing honeybee signal indicated a shift of 130 Hz which corresponds to a speed of 12 km/h. While the last incoming honeybee signal indicated an initial shift of 64 Hz that reduced to 32 Hz, which represented an initial speed of 5.95 km/h and a final landing speed of 2.97 km/h.

The rest of the recorded free-flying honeybee signatures were verified using the recorded footage and labelled as demonstrated to analyse their RCS signal. The overall RCS values measured for both the departing and arriving bees (n=164) ranged between −55 to −60 dBsm ± 3 dBsm, which was close to the maximum simulated RCS of a 15 mm long ellipsoid and 15 mm honeybee RCS of −63.7 dBsm and −67.5 dBsm respectively. These RCS values filled a literature gap in honeybee RCS at 5.8 GHz, whilst demonstrating the largest sample size of honeybees used for RCS extraction to date, where the second largest sample size was only extracted for 11 honeybees at 24 GHz [120]. Upon further efforts to investigate the convergence of the simulated honeybee RCS to the measured values, it was found that the dielectric constant when set to K=38 caused RCS values of honeybees 10 to 15 mm in length to increase to −71.5 to −60.72 dBsm respectively. Experimentally validating the dielectric constant of bees would thus make a compelling side study. It was observed that the RCS was changing as the bee flew across the radar's monitoring range, which was expected and mentioned in the literature review. The variations in the bee's body size, complex wingbeats and their aspect angle with respect to the doppler radar might affect the measured RCS values [118], [119]. The aspect angle was deemed to be a large contributor towards changes in RCS values, as the RCS is greatly dependent on polarisation [118], [119]. The aspect angle is an angle between the insect's body axis and the LOS of the radar. Polarisation angle can similarly have a high effect on the RCS, as it results in different scattering properties. This is due to the orientation of the electric field and magnetic field vector relative to the insect's body. Figure 3.38 provides an illustration of the plane of polarisation, insect body axis and polarisation angle. Note that in each event a different RCS main lobe magnitude is recorded. The bee model dimensions of length, width and height are positioned with respect to the Z, X and Y-axis.

Figure 3.38(a) measured an RCS of −70.7 dBsm, while the EM wave impinged the X-axis with the electric field (E-field) and magnetic field (H-field) in the Y and Z-axis respectively. This is the situation if the insect's body axis was perpendicular to the radar's EM wave.
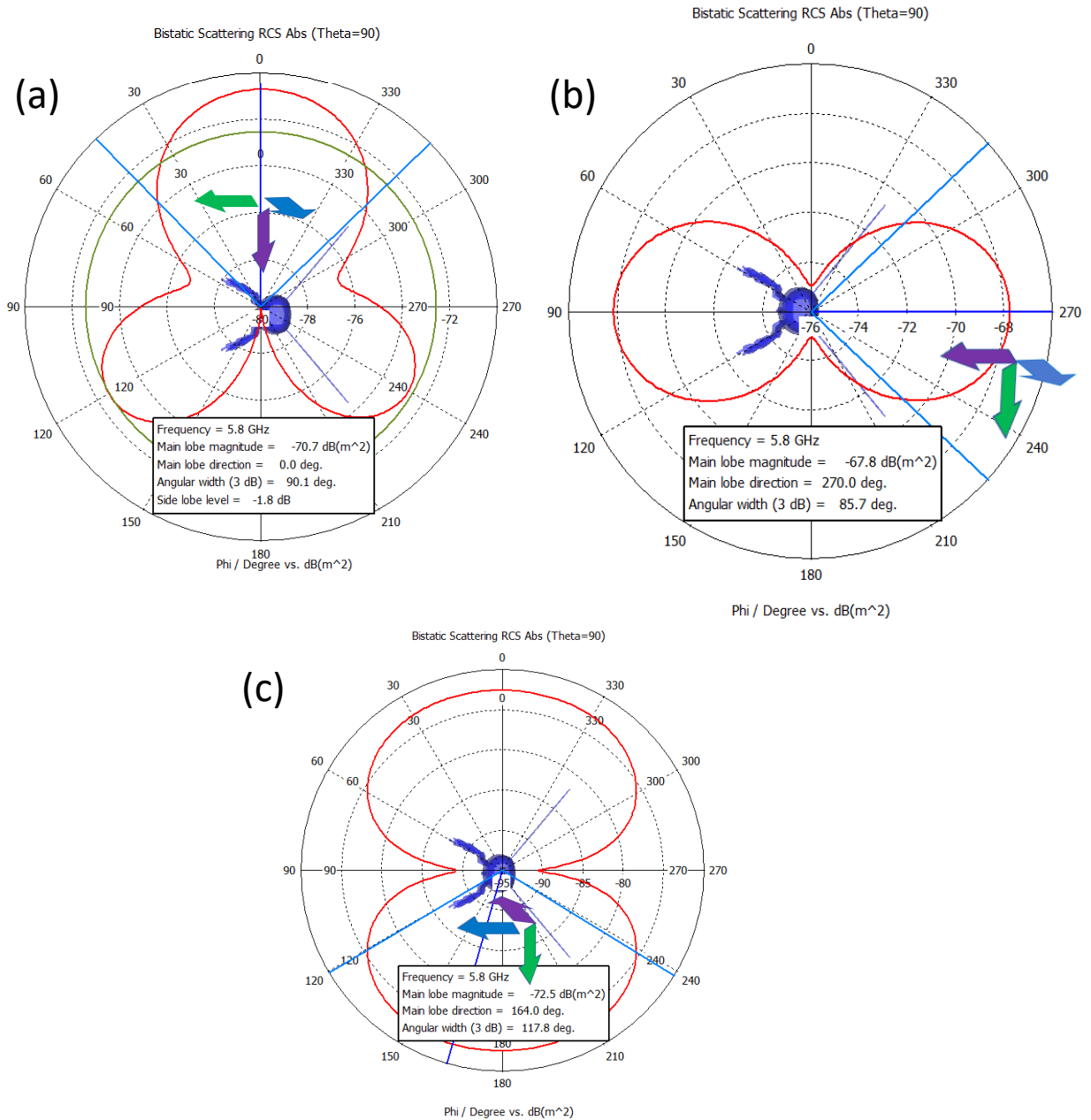
Figure 3.38: Polar plot illustration of interaction of EM waves with insect showing EM wave's propagation direction, electric field and magnetic field in purple, green and blue respectively (also shown in the blue cone). (a) EM wave normal to X-axis. (b) EM wave normal to Y-axis. (c) EM wave normal to Z-axis.

When the orientation of the insect's body axis changes to Figure 3.38(b), where the EM wave impinges the Y-axis, the scattered EM energy changes with respect to the E-field, H-field and (polarisation). This results in an RCS magnitude of −67.8 dBsm. Similarly, when the EM wave impinges the Z-axis as the insect changes orientation, the RCS magnitude changes to −72.5 dBsm. Figure 3.39 shows the 3D farfield plots, which illustrates a three-dimensional visualisation of the EM scattering, which demonstrates the impact of the insect's body axis. Three different illustrations are shown in Figure 3.39(a)-(c), which demonstrate the significance of polarisation.
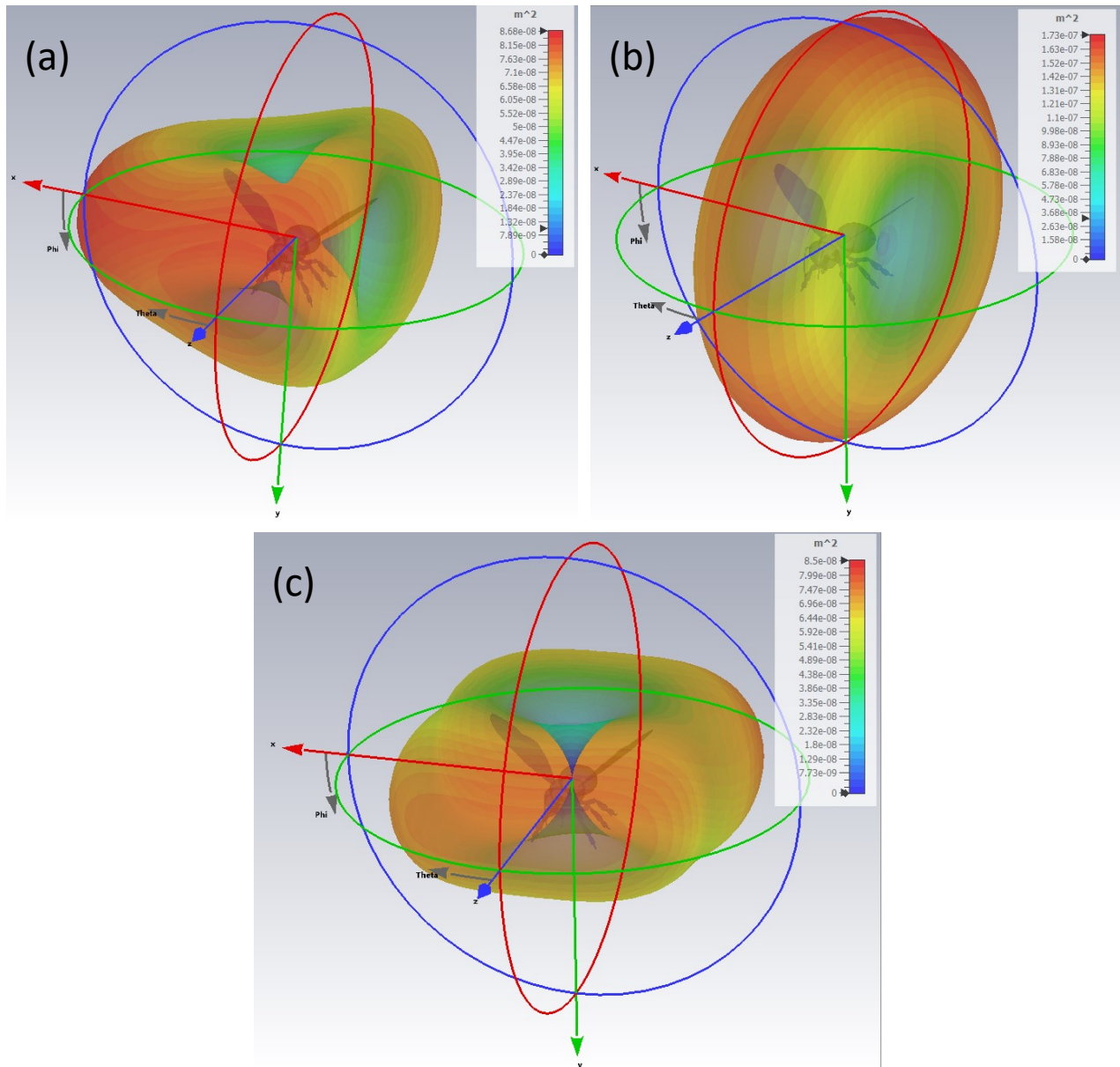
Figure 3.39: 3D Farfield illustration of interaction of EM waves with insect showing EM wave's propagation. (a) EM wave normal to X-axis. (b) EM wave normal to Y-axis. (c) EM wave normal to Z-axis.

The combined effect of wingbeat rate, the displacement of the insect in the radar's beam and even insect breathing—though the breathing may not be detected as such a wavelength— can create amplitude modulations in the returned radar signal, which are referred to as temporal modulation [119], [198]. Temporal modulations are believed to have a large impact on RCS measurements of flying insects. Additionally, factoring in the bee's complex dielectric constant, it is expected that the measured RCS somewhat deviates from the simulated RCS expectations.

3.16 RCS increase of Honeybee

Additional investigations were directed at increasing the honeybee's RCS as means to enhance detection range without drastic hardware changes (adding amplifiers, changing antennas, increasing frequency etc.). While higher RCS could be achieved at 10.5 GHz, or 24 GHz [120], frequency increase was ruled out to maintain the low-cost and commercial availability of the present components, along with coherence with earlier pollinators telemetry systems [91], [183], [199].

While section 2.6 explored EM simulations of a coated wooden sphere to hypothesise metal-coating based RCS increase, Section 3.14 demonstrated the possibility of RCS increase through the coated wooden sphere pendulum experiment. Similarly, Silver coating was also expected to enhance honeybee detection range, also through no hardware modifications.

The bee model adopted in section 2.5, was coated with a Silver layer, which aimed at maximizing the bee's coated surface while not impairing its flight capacity nor obstructing the breathing ability, by avoiding coating of bee wings and breathing spiracles. Feasibility of applying metallic coating was experimentally tested which showed honeybee *seta* with length ranging from 300 to 900 µm.

The bee's surface available for coating favours distribution of Silver coating in a closely packed arrangement that could approach the performance of the coating layers used for the RCS study. As shown in Figure 3.40 and Figure 3.41 the RCS and detection range improvement for a radar with an MDS of -72.72 dBm with a target of an average sized (12.5 mm long) partially coated honeybee could achieve an increase of 17.7 dBsm and a maximum range of 3.4 metre. When considering a large-coated honeybee of 15 mm long, the maximum range obtained can reach up to 4.2 metres.
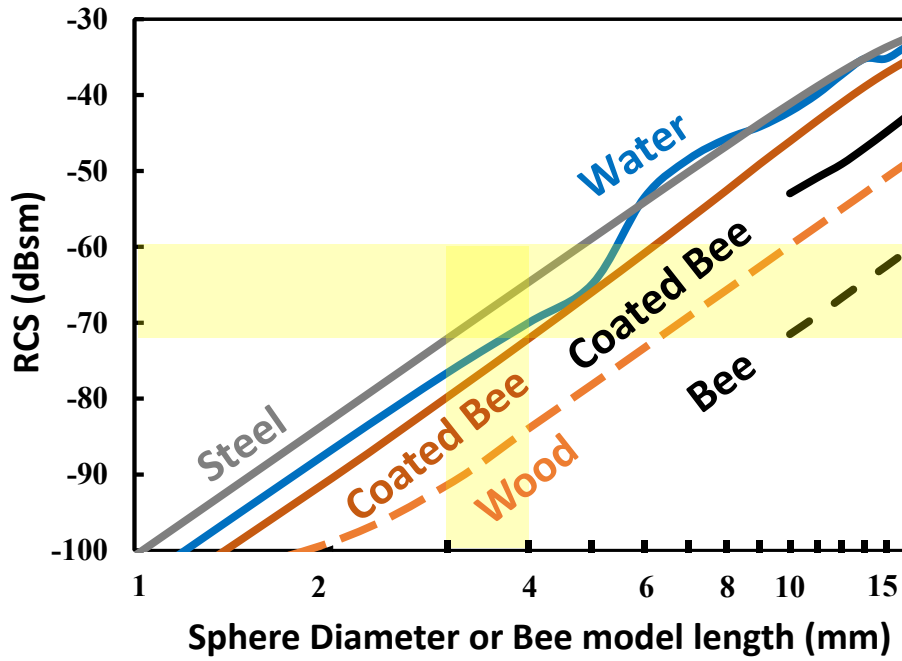
Figure 3.40: Simulated RCS values of steel spheres, water spheres, wooded spheres (coated and uncoated) and a bee (coated and uncoated).

Such RCS enhancement can be interesting to dynamic tracking applications, as it drastically reduces tag load along with challenges in higher frequency modules. However, for near-hive monitoring via stationary transceivers, the 2-to-3-meter range achieved while avoiding the invasiveness/inconvenience of the coating process might be preferable.
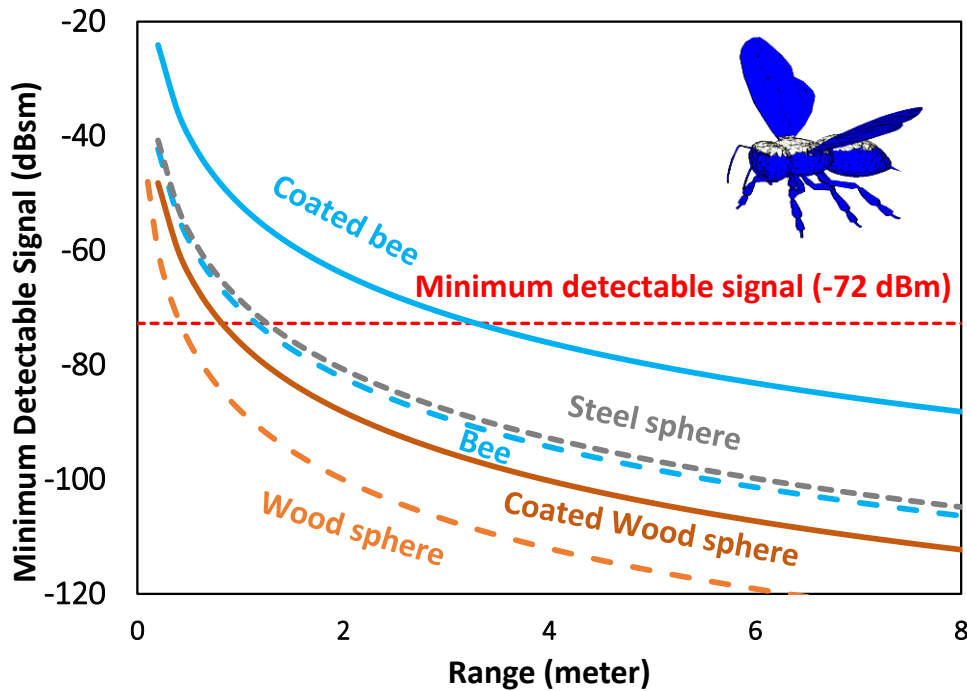
Figure 3.41: Increased detection range of both coated wooden sphere and coated bee. Coated bee displayed as an inset.

Chapter 4. Dynamic Insect Monitoring

This chapter correlates between simulated signals and recorded honeybee signals. It outlines the experimental work that was conducted for dynamic insect radar monitoring and shows machine learning integration using honeybee monitoring data collected from the radar. It further discusses the experimental work that involved the micro-Doppler effect, which includes simulated honeybee micro-Doppler and experimental micro-Doppler features that present wingbeat frequency and human vital sign detection.

4.1 Pendulum Simulation

The previous chapter introduced pendulum signatures that were recorded using the V1 radar during early calibration stages, where the pendulum was used to aid in radar calibration. This was performed by swinging a 4 mm steel sphere in front of the radar until a clear signal was recorded. A similarity was found between the pendulum signals and the radar monitored honeybee signals. In order to correlate the honeybee signatures to the pendulum swings, a simulation model of a pendulum swing —originally designed and programmed by V. Chen in [196] — was modified to reflect the experimental parameters of the pendulum experience performed in this study. The equations and the derivations of the pendulum are illustrated in [196]. As for the total force acting on a pendulum, this is comprised of the acceleration and mass of the pendulum. The pendulum equation, obtained from [196], is shown below and derived in Appendix Q.

$$mL \ \frac{d^2\theta}{dt^2} = -mg \ sin\theta \qquad\qquad 4.1$$

Where m is the pendulum bob's mass (0.2610 gram for 4 mm steel sphere), L is the length of the string (15 cm), θ is the swinging angle and $\frac{d^2\theta}{dt^2}$ is its second time derivative. The equations can then be re-written as two first-order ordinary differential equations (ODE) by denoting the angular velocity $\Omega = \frac{d\theta}{dt}$ as shown below [196],

$$\begin{cases} \dfrac{d\theta}{dt} = \ \Omega \\ \dfrac{d\Omega}{dt} = \dfrac{g}{L} sin\theta \end{cases} \qquad\qquad 4.2$$

If the pendulum interacted with a linear friction (causing it to damp/decay), an additional term of $-2\gamma\frac{d\theta}{dt}$ is added, which should be proportional to the angular frequency. The pendulum equation then becomes [196],

$$\frac{d^2\theta}{dt^2} + 2\gamma\frac{d\theta}{dt} + \omega_0^2 sin\theta = 0 \qquad 4.3$$

Where γ is the damping constant and $\omega_0 = (\frac{g}{L})^{1/2}$ is the angular frequency of free oscillation's. The equation of the pendulum with the linear friction can be written as a set of first order ODEs as [196],

$$\begin{cases} \dfrac{d\theta}{dt} = \Omega \\[2ex] \dfrac{d\Omega}{dt} = +2\gamma\Omega = \dfrac{g}{L}sin\theta \end{cases} \qquad 4.4$$

The simulation model represented a pendulum oscillation which comprised of a small bob and a string attached to a pivot as shown in Figure 4.1. The pendulum's bob swings towards and away along the *y*-axis at (*x*=0 and *z*=0) from the radar under the influence of gravity (9.80665 m/s²). The length of the string L and the diameter of the pendulum's bob were 15 cm and 4 mm respectively, similar to the experimental parameters.
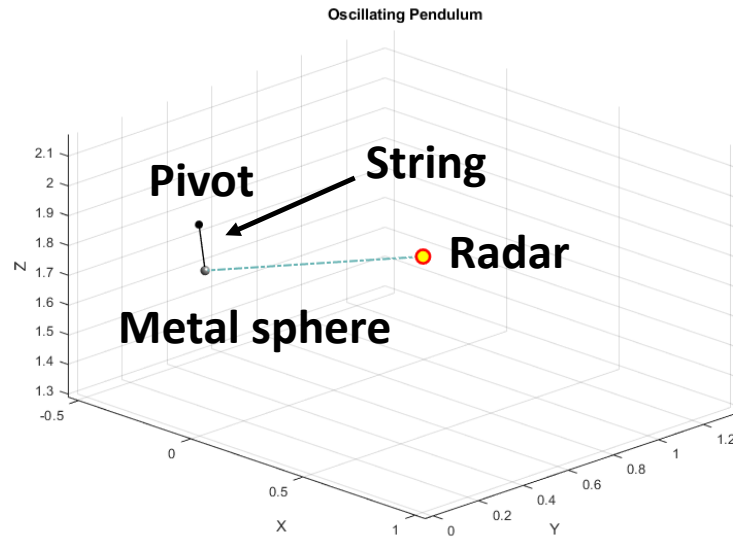
Figure 4.1: Animation of the pendulum with a string of 15 cm and a steel sphere of 4 mm diameter swinging back and forth with respect to the radar.

The simulation was set to allow the pendulum to swing back and forth as shown in Figure 4.1, which resembled the experimental pendulum swing. Figure 4.2(a) and (b) demonstrated the back-and-forth pendulum signature in the simulation and in an experimental setting using the V3 I/Q radar respectively.
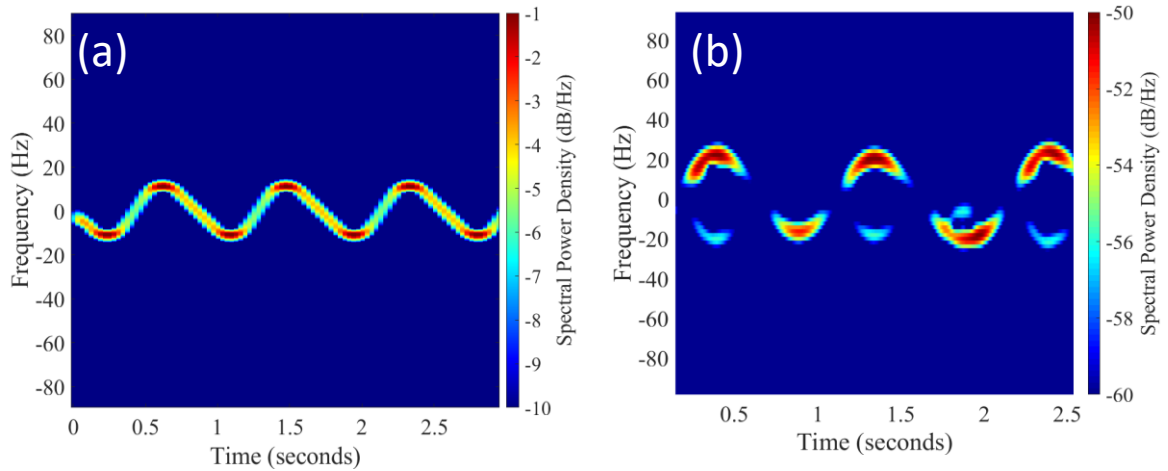
Figure 4.2: Spectrograms of 5.8 GHz pendulum swinging back-and-forth (a) in a simulation setting (b) in an experimental setting.

When the pendulum swings, it is when the pendulum initiates the drop from left to right (or vice versa) where the speed of the pendulum is the highest. Hence, in terms of Doppler shift, the highest shift recorded is when the pendulum's bob descends from either side of the swings to the pivot point of the pendulum. These maximum Doppler shifts can be observed in Figure 4.2(a) and (b), as peaks and troths, where ± Doppler shift indicates the swing's direction (towards or away). As for the peak amplitude of the signal in Figure 4.2(a) and (b), this relies on the positioning of the radar, as the amplitude depends on the proximity of the pendulum's bob. The radar was placed in a position where it was in line with the maximum Doppler shift. This meant that as the bob approached its maximum speed below the pivot point as it swings from left to right, the bob comes into close approximation with the radar and thus records the highest amplitude signal, which also coincides with the maximum speed. Experimentally, it was noticed that, these left to right swings — heading towards the radar — (shown in Figure 4.2(b)) had a higher amplitude compared to the opposing movement, that swings from right to left (away from the radar). It was noticed that the simulation did not take this into account and future changes should be applied to the simulation to attenuate the reflection from the pendulum's bob as it moves away. Note that the detected radar signatures in Figure 4.2(b) are noisier compared to the ideal simulation scenario where no external noises are present in Figure 4.2(a), but still capture the front-and-back signatures of the pendulum, with clear enough resolution. Additionally, discrepancies are observed in the spectral power density recorded as it is a comparison between an ideal simulation setting and the experimental process. Finally, a faint signal in the simulation seemed to connect the peaks and valleys

of the simulation, which was believed to be a continuation pattern of the swinging sphere. This was not clearly observed by the radar in the experiment.

Another example of pendulum swing series are shown in Figure 4.3(a)-(c). The experiment involved using the prototype radar (no I/Q), where the pendulum was kept at a range of 0.5 metres. The system was able to record different signals based on their interaction with the radar. Upon initial inspections of the radar signatures, and the video recorded footage, it was found that the recorded pendulum signals were distinguishable from one another based on their type of motion. Figure 4.3(a) illustrated the intensity and frequency of the signal to gradually increase over time, which indicated the pendulum coming closer to the radar as the acceleration of the pendulum increased forcing the pendulum to swing faster, while Figure 4.3(b) showed the opposite behaviour, representing a deceleration. Figure 4.2(b) demonstrated an equal behaviour where the pendulum swings towards and away from the radar, intrinsically varying from Figure 4.3(c), which showed a diagonal swinging behaviour.
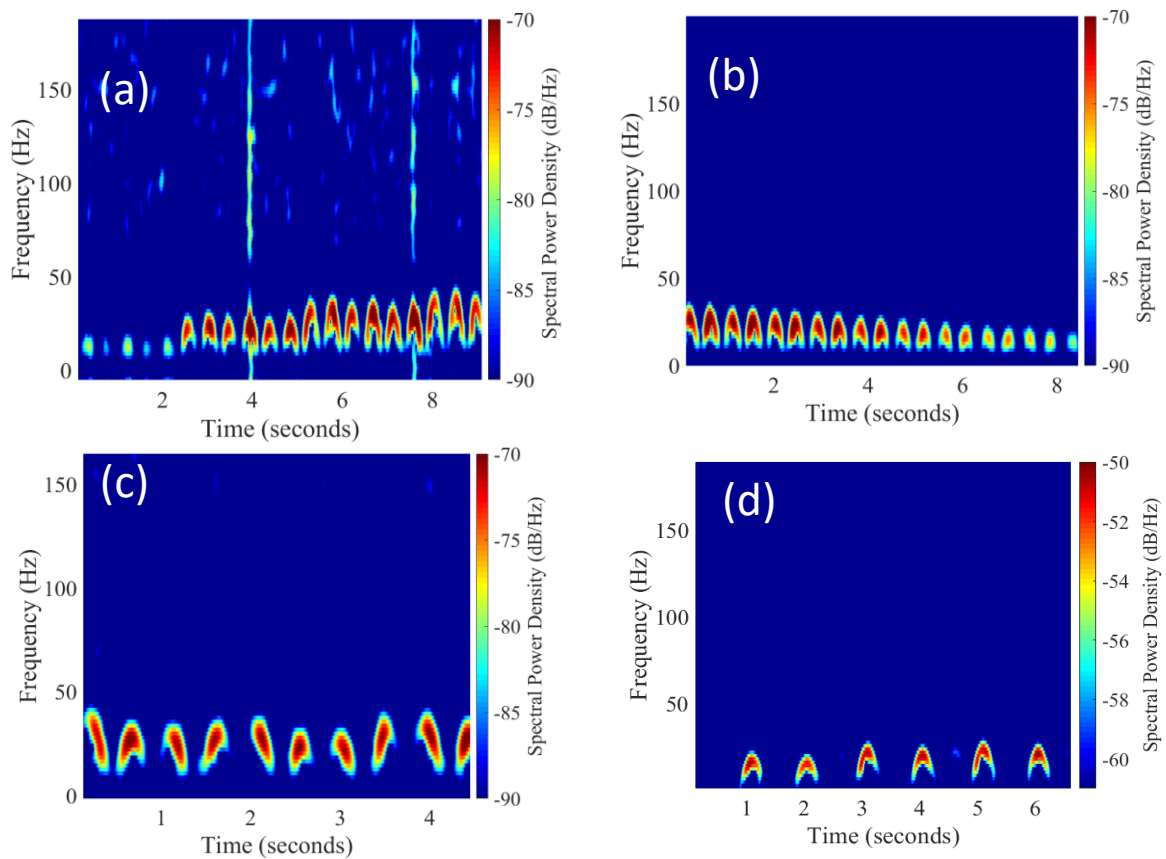
Figure 4.3: Pendulum experiment showing different signals (a) acceleration (b) deceleration (c) diagonal signals (d)back and forth.

These were all signals that could be easily identified due to the change of signal intensity and frequency, where the frequency shift was a clear indicator of increments/decrements in speed, while the intensity was an indicator of how close pendulum was to the radar. Since discrimination of different pendulum signals can easily be performed with the human eye based on the different signals demonstrated in Figure 4.3, it is believed that a machine learning model would easily be able to identify different classes of pendulum movements. This is due to machine learning models sometimes outperforming humans at tasks such as image identification [200], [201].

4.1.1 Pendulum and Bee correlation

From the radar's perspective a pendulum moving towards the radar is a signal that increases in both speed and magnitude as the sphere (pendulum's bob) comes in close approximation to the radar. This indicates the first half of the pendulum swing, while the second half of the pendulum swing is the pendulum returning to the opposite direction. Both these pendulum events had similar features to departing/returning bees, where approaching bees increase in both magnitude and frequency. A bee flying straight out of the hive towards a radar —from the radar's perspective— is a quick signal with an increasing speed and an increasing magnitude that reaches its peak as it approaches the radar and decays rapidly as the bee flies out of the radar's field. This was found to share similarities with the first half of the pendulum swing that approached the radar, as the pendulum's speed increased while it swung towards the radar (indicating the first half of the swing). The pendulum then reversed back and continued the pendulum swing in the opposing direction, where it completed the second half of the swing.

The first half of the approaching pendulum is illustrated and labelled in Figure 4.4(e)(f), which both as a spectrogram and as an oscillogram may appear as a leaving bee to an untrained eye. While a bee returning to the hive would approach the radar first, increasing the signal's magnitude as it comes closer to the radar, where the magnitude and frequency then decays as the bee slows itself to enter the hive.
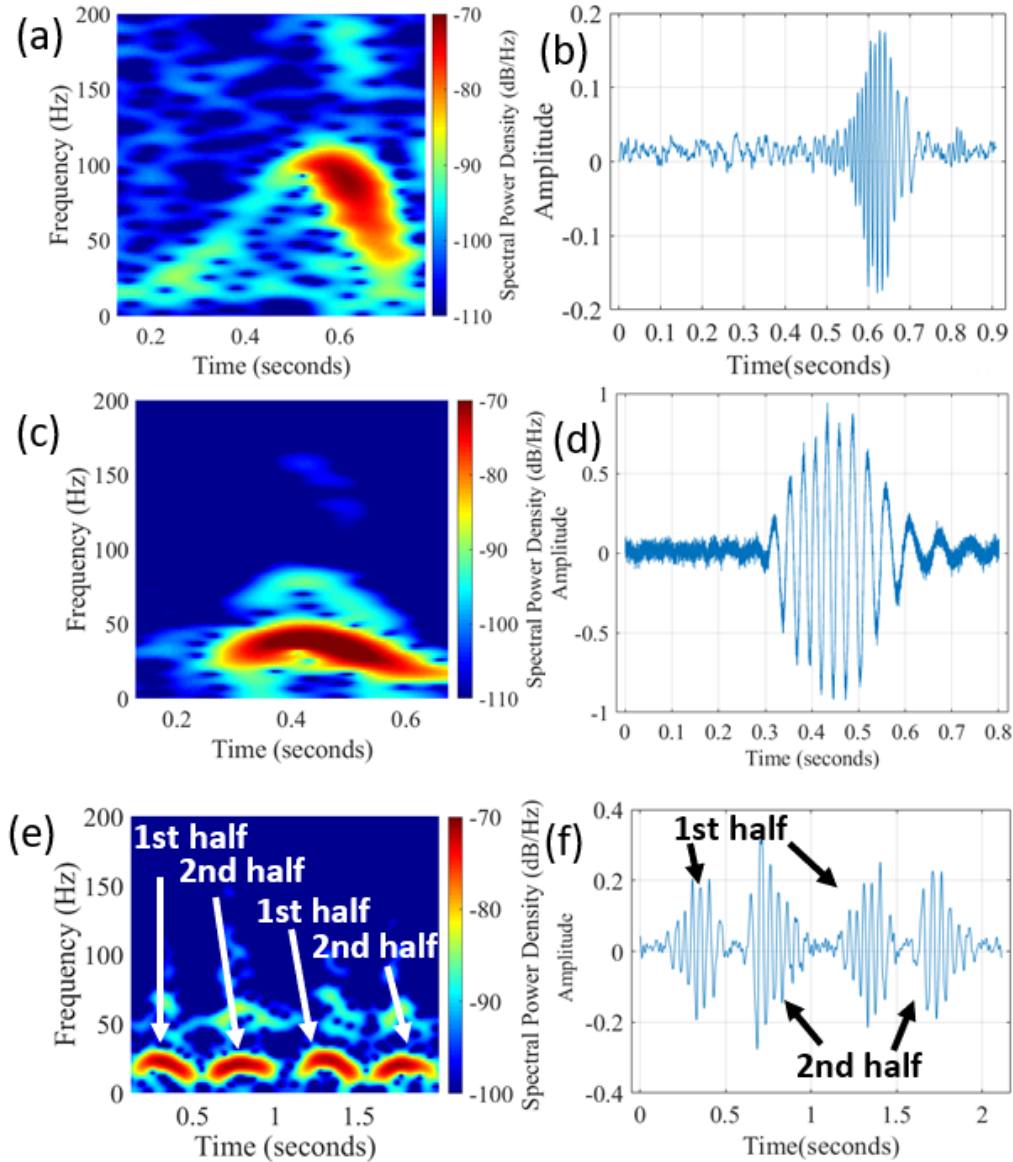
Figure 4.4 Spectrograms of (a)bee leaving (c) bee returning (e) two cycles of a pendulum swinging towards and away. Oscillograms of (b) bee leaving (d) bee returning (f) two cycles of a pendulum swinging towards and away.

The bee flies at a slower pace as it returns from foraging at an initial peak of 44 Hz (~4.1 km/h) to then slow down to 25 Hz (2.32 km/h), with a signal duration of 211.5 ms, representing a longer low frequency shift (shown in Figure 4.4(c)(d)). The arriving honeybee's signal was double the length and nearly half the velocity of the departing

honeybee in Figure 4.4(a)(b). Figure 4.4(a) and (c) are two different honeybee flight events that can be visually discriminated from one another, in a similar manner to differentiating the different pendulum signals in Figure 4.3.

A degree of correlation can be observed with the pendulum and honeybee signals, yet honeybee signals are complex. This complexity makes it difficult to be matched with that of the pendulum Doppler shift. Additionally, replicating bee signals using sphere dropping or controlled pendulum swings lacked the flying speed of honeybees, the complex temporal amplitude modulations induced on the returning radar signal and lacked different key honeybee motion types (e.g., broadside flight) [119], [198].

Hence, a simulation approach was implemented to correlate key bee flight movements to experimental signals that were observed. A simulation model from [196] was adopted and modified to suit the study's experimental parameters. A 4 mm sphere was modelled which was moved at a velocity and acceleration of choice towards/away from the radar, at a pre-defined radar location to represent the bee's flight. The sphere's movements are summarised in Table 4.1 and case 1 to 4 are demonstrated in Figure 4.5(a)-(d) as spectrograms. Note that the sphere in Figure 4.5(a)-(c) flew at 1 m/s, while (d) flew at 5 m/s, which explains the increased Doppler shift in (d). Figure 4.5 shows the simulated spectrograms (on the left) and their respective oscillogram representations (on the right). Additionally, Figure 4.5 shows insets of recorded bee signals.

Table 4.1: Summary of simulated sphere movements

Case	Movement type
1	Constant target speed towards radar
2	Constant target speed away from radar
3	Constant target speed in broadside direction
4	Constant target speed passing above radar
5	Constant target acceleration towards radar
6	Constant target acceleration away from radar
7	Constant target acceleration in broadside direction
8	Target linearly decreasing acceleration
9	Target linearly increasing acceleration
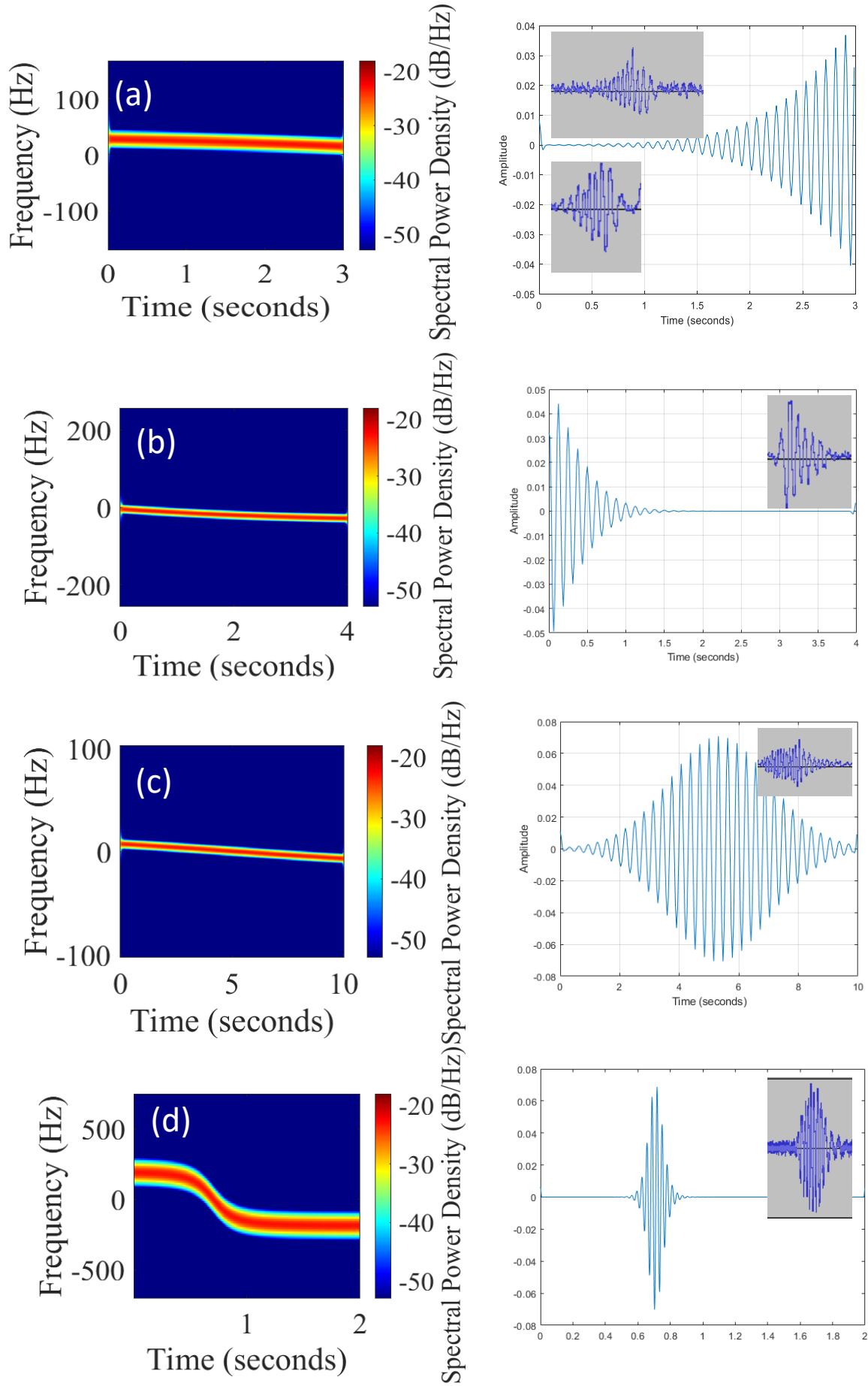
Figure 4.5: Main simulated sphere movements (a) Case1 (b)Case2 (c)Case3 (d)Case4.

The spectrogram's FFT points were stored in a complex double array (512 × 512), where each row was plotted with respect to time, which displayed 512 lines of the spere's interaction with the radar. By extracting the envelop of the plot, applying amplitude modulation and plotting the outcome, an oscillogram signal was achieved (displayed on the right of each case), which converged towards recorded signals obtained during the experiments (displayed as insets).

4.1.2 Bee signal discrimination

Departing and arriving bee were discriminated through Doppler measurements. Bees departing from the hive rapidly, flew out accelerating in an ascending trajectory. This was observed as an increasing Doppler shift. By contrast, bees arriving resulted in a decreasing Doppler shift due to the bee's deceleration as it approached the hive for landing. Figure 4.6(a) demonstrates a departing bee event, which illustrates the increase in Doppler frequency, peaking at 170 Hz. This indicated a flying speed of 15.81 km/h. The increase in Doppler shift, shows that the bee was initially flying at a speed of 1.1 m/s and then accelerated to 4.39 m/s (15.81 km/h) with an acceleration of 10.2 m/s^2.

Upon comparing the bee's acceleration, it was found that it approached the gravitational acceleration (9.8 m/s^2) observed when dropping the 4 mm sphere. By contrast, Figure 4.6(b) showed a returning bee event, with a decreasing Doppler frequency, which peaked at 96 Hz. This indicated an initial flying speed of 8.93 km/h. The bee was decelerating from its initial speed of 2.48 m/s (8.93 km/h) to a final 0.7 m/s before landing at the hive. The signals shown in Figure 4.6(a) and (b), emphasised departing and returning honeybee's signature which were short bursts of high/increasing frequency and pro-longed low/decreasing frequency respectively.
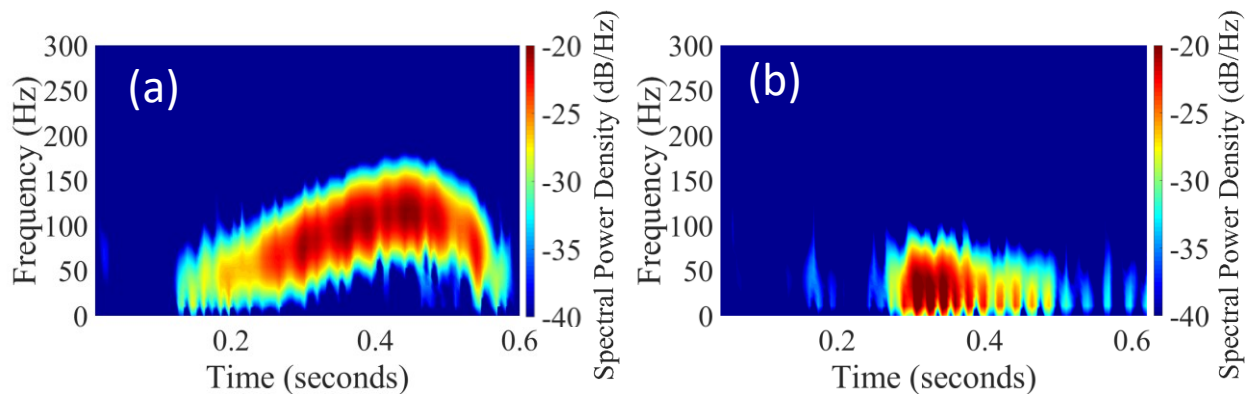
Figure 4.6: Radar readouts of (a) honeybee departing from its hive demonstrating an increase in Doppler shift as it flies in a straight ascending trajectory. (b) Honeybee returning to its hive, demonstrating decrease in Doppler shift as it arrives at the entrance in a more errant pattern.

Similar to the previously shown pendulum signals' capability of being visually classified, the current bee signatures also supported classification. The difference between departing and returning honeybee Doppler shifts can thus be utilised to integrate machine learning techniques for the development of an autonomous classification system.

4.2 Machine Learning integration

It was found that manual correlation of Doppler signatures using video footage was difficult, time consuming, and impractical for in-field bee activity assessment. Hence, utilising artificial intelligence (AI) to automate such an approach was investigated by the research group and carried out by another group member to showcase the radar's extended capabilities with AI [183]. Due to the radar's ability to record Doppler shift of targets as small as honeybees, while providing a high enough resolution and SNR, it was possible to integrate Machine learning (ML) applications. Such applications could support hive access logging, hive activity evaluation, foraging evaluation and indirect estimation of foraging time. These algorithms include Neural Networks (NNs) and random forest.

The main goal of the machine learning integration was to autonomously identify bee events such as departing, incoming and hovering bees. The most efficient approach to the implementation of the classification model was the use of a NN built through the random forest algorithm, while processing the audio files using linear prediction (LP) features. This was attempted using two methods; spectrogram based and audio based.

4.2.1 Two class/Binary spectrogram-based image classification

A small spectrogram dataset (n = 600) of monitored honeybees was used for the classification of departing and incoming bees via identification of the signal's intensity and overall signal signature. A window size of approximately 0.4 seconds was used to further splice the data into 1250 pieces.

Honeybee flight spectrograms were used for NN based image prediction, which contained both the pretrained and naïve elements of the audio [202]. The use of spectrogram (visual representations) prediction of audio signatures is commonly used, due to improvements in NN based image prediction [203].

The processed data was split into a 4:1:1 ratio of training, validation, and test data for both cases. The NN reached a maximum accuracy of 88.7% with a Binary Cross

Entropy loss (BCEL) of 0.43. The BCEL compares each of the probabilities that were predicted to an output that can be either 1 or 0, to which it then calculates a score that penalises the probabilities based on their distance of the actual value. The aim of the BCEL is to converge towards zero, which associates a lower loss. This was the first attempt of radar integration with ML techniques using the MobileNet V2 architecture, which allowed autonomous discrimination of incoming and outgoing flights of honeybees, further extending the possible applications of the radar [183]. This integration can enhance the probability of correctly identifying entering/leaving bees from a hive, automate unobtrusive honeybee logging, and opened the possibility to monitor more complex honeybee behaviour.

4.2.2 Three-class/Ternary audio-based prediction

Honeybee behaviour observed was complex and not limited to simple entering/leaving events. Though the in and out prediction (binary classification) is useful in applications that evaluate honeybee behaviour, it lacks the classification of other honeybee behaviour. Several additional honeybee movements were noticed, where the most commonly noticed behaviour — other than the in and out flights — was honeybees hovering at the entrance. Honeybee hovering is a behaviour where the honeybee does not enter or leave the hive, but remains flying side to side while facing the entrance. An example of a hovering event is shown in Figure 4.7 below.
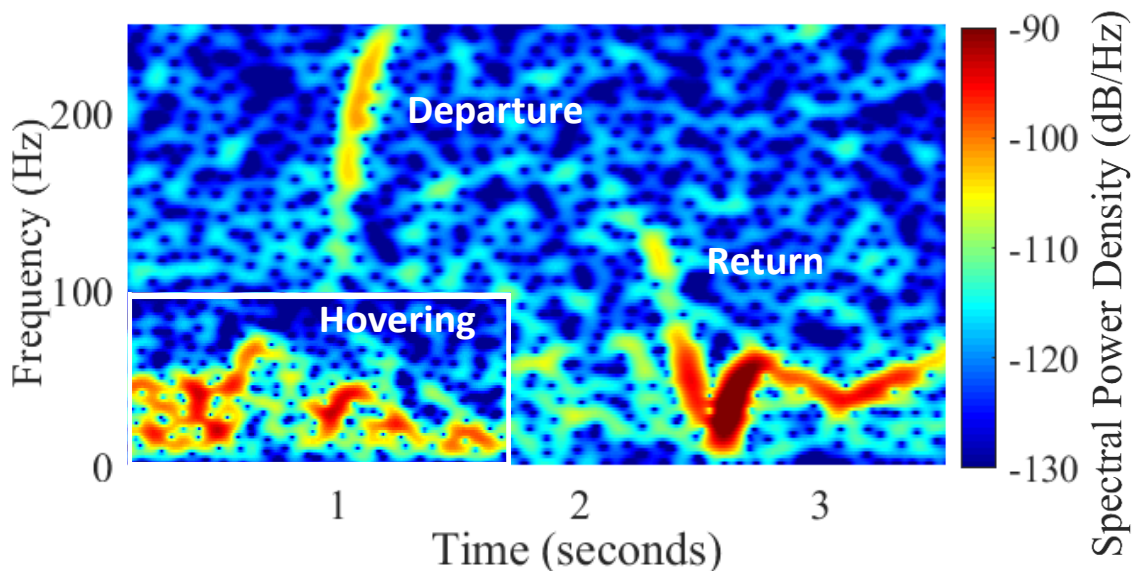
Figure 4.7: Three different honeybee signatures monitored.

Such hovering behaviour happens frequently at the entrance and can be correlated to honeybee orientation flights, where young bees hover around the entrance to memorise the location of the hive [204]. The bee's free movement at times involves moving forward, backwards and side to side. A visual illustration of departing, arriving and hovering honeybees are shown in Figure 4.8 as red, blue and orange arrows respectively.
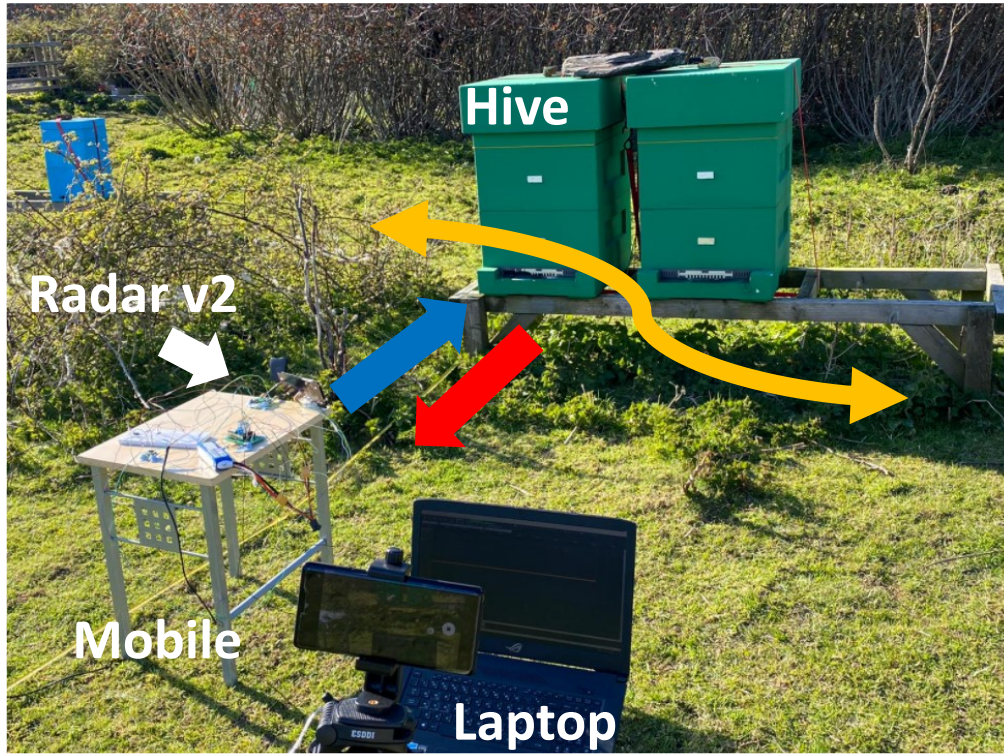
Figure 4.8: V2 radar setup with blue arrow, red arrow and orange arrows representing arriving, departing and hovering honeybee flights respectively.

The classification of this signal would deem valuable towards both research and commercial applications. In commercial applications, it could act as a metric for evaluating young bee exploration flights, as such exploration flights are good indicators of hive growth and strength [204]. From a research perspective, the decrease of orientation flights was attributed to the presence of non-lethal doses of neonicotinoids. Thus, the increase/decrease of orientation flights could be evaluated to assess the impact of different neonicotinoids [27]. This type of study is not limited to pesticides but can also be conducted in different settings, such as near radio/cellular towers, power lines and other sources containing an element of high frequency/radiation. Successful identification of hovering could contribute towards the elimination of false positive identifications of towards/away signals that are caused by hovering signals.

The previous two-class model used spectrograms, which was found to be computationally expensive. Since the radar output signals were already recorded as audio files, while containing relevant data at low frequencies (< 1 KHz), audio files were thus used. The audio files were divided into similar segments of 0.4 seconds (∼70 kB per file), with each being checked for a minimum signal. This concluded the final data set to be approximately 700, 600 and 200 bee signals entering leaving and hovering around the hive respectively.

Support vector machines (SVMs) using line spectral frequencies (LSF) showed a prediction accuracy of 93.97%, which was the highest result in ternary classification. The loss value was reported as 0.2667. This was much higher than the original binary classification accuracy (88.7%). The NN with LSF came second in prediction accuracy of 89.22%, with a loss value of 0.2933.

It is believed that if the V3 I/Q radar was used, the visual differences between the three classes would expand and thus leading to a higher prediction accuracy. This could potentially allow classification of multiple other signals as direction (with respect to the radar).

The integration of ML, whether binary classification or ternary classification provided high prediction accuracy, which demonstrated the radar's potential for classification-based applications. This could pave the path for unobtrusive and autonomous species classifications and real time monitoring of hives, polytunnels and/or wild woodland.

4.3 Micro-Doppler

Rotation of structures and mechanical vibration imposed on a transmitted radar signal may generate a frequency modulation on the received echo and as a result create sidebands about the Doppler frequency shift. The vibration-induced modulation is known as the micro-Doppler phenomenon [195]. Micro-Doppler phenomenon can be considered as a characteristic of the interaction between a vibration source and the target body [197]. Any target could produce micromotions (small motions) such as a walking human, drone propellors, bird wing flaps, and even insects wing beats. The micro-Doppler effect of a vibrational target in a radar setting would only be produced if the vibration rate and the displacement of the vibration are high enough. In equation 4.5, if the vibrational scatterer

azimuth and elevation angle (αp , β) are zero (in the LOS of the radar) the Doppler frequency reaches the maximum value of

$$f_D = \frac{2}{\lambda} D_v \, f_v \cos\beta \, \cos\alpha \, p \cos\omega_v \, t \text{ , while } \alpha \, p \text{ ,}\beta = 0, \qquad 4.5$$

$$f_D = \frac{2}{\lambda} D_v \, f_v \qquad\qquad 4.6$$

Where D_v is the amplitude of the vibration and f_v is the vibration rate. The micro-Doppler is thus correlated to the frequency band used, where the higher the frequency the more observable the micro-Doppler signature is [196]. The micro-Doppler is a time-varying frequency shift that can be extracted from a radar output signal in coherent Doppler radars. A common way of presenting micro-Doppler signatures is in a joint time-frequency analysis, such as the STFT.

4.4 Simulation and analysis of insect micro-Doppler shifts

A series of honeybee micro-Doppler simulations were performed based on a flying bird micro-Doppler simulation in [196]. The simulated radar position and wavelength was adjusted to reflect that of the experimental setup. The flapping and motion kinematics can be found in [196]. The simulations demonstrated the case for a honeybee with no wings, only wings and the case with wings flapping at a fixed frequency, which are explained in the next sections.

4.4.1 Honeybee body only Micro-Doppler simulation

To understand the individual impact of the bee's body and its wings on the simulation, both were simulated individually. The body of the honeybee was simulated as an ellipsoid with dimensions a= 15 mm, b=3 mm and c = 3 mm. The bee model was set to travel at a constant speed of 5 m/s towards and past radar as shown in Figure 4.9(a). The ellipsoid's RCS was calculated using the ellipsoid RCS equation 2.10 (in chapter 2). Both the bee's position and angular deviation were calculated from the starting point at each step, while updating the spectral power density from the radar's directivity and path loss. The simulation flight path was chosen to include flight towards and away from the radar, due to experimental observations made while using the radar outdoor. It was noticed that bee mostly approached the radar and flew above the radar as they headed towards their destination (whether departing or leaving). Hence, the simulated flight path of the bee was extended to display events past the radar.
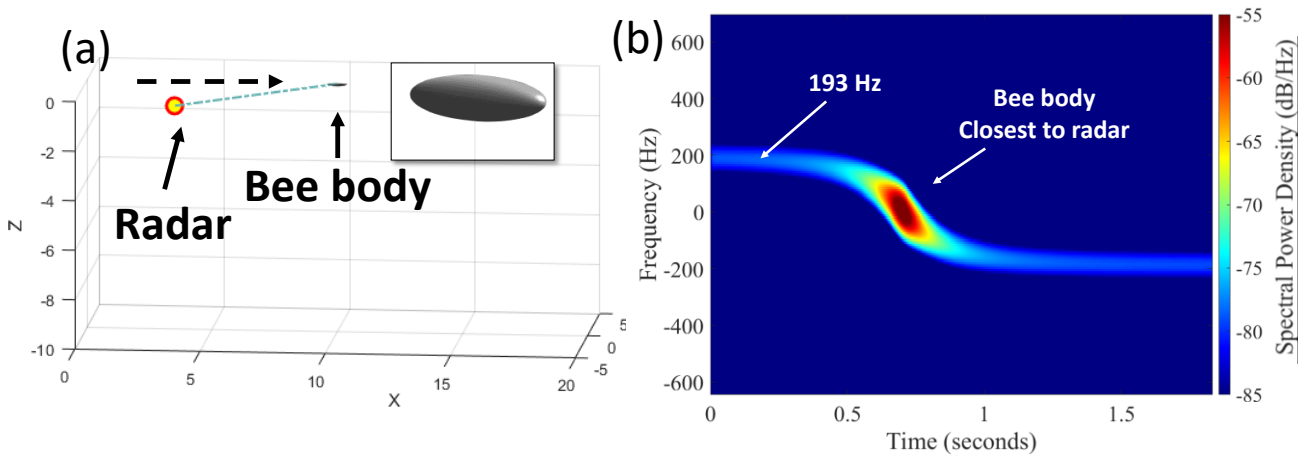
Figure 4.9: (a) Bee body moving towards and past the radar at a constant velocity of 5 m/s. Inset displays the ellipsoid. (b) Spectral response of the bee before and after passing the radar.

Inspecting Figure 4.9(b) revealed three transitional segments. The first segment (0 to 0.5 seconds) was a constant spectral band, centred at the Doppler shift (193 Hz), which theoretically corelated to the calculated Doppler shift of a 5 m/s moving target at 5.8 GHz. Due to the target moving towards the radar and maintaining a horizontal path with no changes in speed and elevation, the spectral signature, amplitude response and the corresponding Doppler shift was fixed. In the second segment (0.5 to 1 second), the bee progressed from flying towards to flying past the radar. This demonstrated a transitional area from a positive Doppler shift of 193 Hz towards a negative Doppler shift of -193 Hz. This was also the area where the bee's body was closest to the radar, hence the increased amplitude. The third segment (1 to 1.5 seconds) displayed the bee flying away from the radar as opposed to the initial flight towards the radar. This showed a negative Doppler shift, while having a similar spectral band as observed in the first segment. Further, since the bee wings were excluded in this simulation, no wingbeat frequencies were observed.

4.4.2 Honeybee wings only Micro-Doppler simulation

The simulation was edited to only display the simulation effects of honeybee wings. Two wings were modelled on each side of the ellipsoid as smaller ellipsoids set to be 9.97 mm long, 3 mm wide and 1 mm thick. When simulating the wings only, with no wingbeat frequency set for the wings, a similar spectral signature as Figure 4.9(b) was observed. This was due to the wings following the same behaviour as the body in the previous simulation, since no wingbeat flapping frequency was set. Upon setting the wingbeats to 200 Hz, as shown in Figure 4.10, a clear spectral band around 193 Hz was observed, while other spectral bands around intervals of 200 Hz were also displayed.
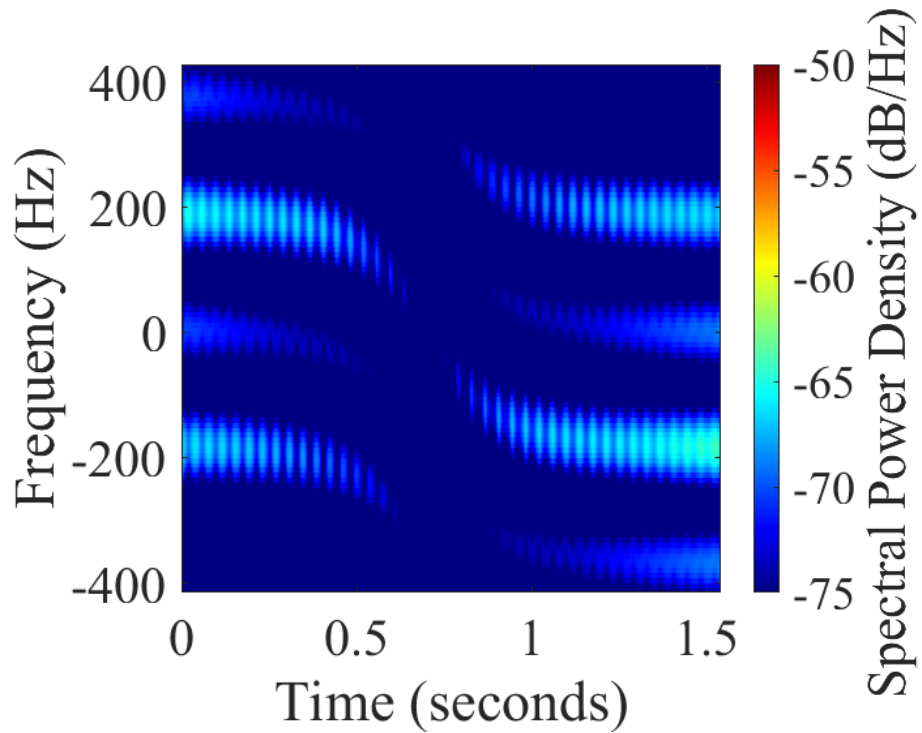
Figure 4.10: Simulated wingbeats showing a clear Doppler shift at 193 Hz and micro-Doppler signatures caused by wingbeats at intervals of 200 Hz.

The 200 Hz bands were micro-Doppler features imposed on the signal due to the rapid beats of the wings. This additional spectral band was not observed in previous body-only or non-beating wings simulations, which indicated that their presence was caused due to the addition of wingbeat frequency.

4.4.3 Honeybee body with wings Micro-Doppler simulation

Similar simulation parameters were set, where the combination of both wingbeats and body were simulated. This simulation provided a full study of the micro-Doppler simulation, which displayed the bee maintaining its Doppler frequency, while the wingbeats displayed micro-Doppler features at the set wingbeat frequency (200 Hz).

Similarly, the signal shown in Figure 4.11, displayed the same overall signature that can be split up into three segments as explained earlier. The combinational effect of wingbeats + body can be clearly observed as a main Doppler signal, where the ~200 Hz band is observed as a stronger intensity signal compared to Figure 4.10 and 4.9(b). This is due to the wings being in level with the body, to increase the overall RCS.
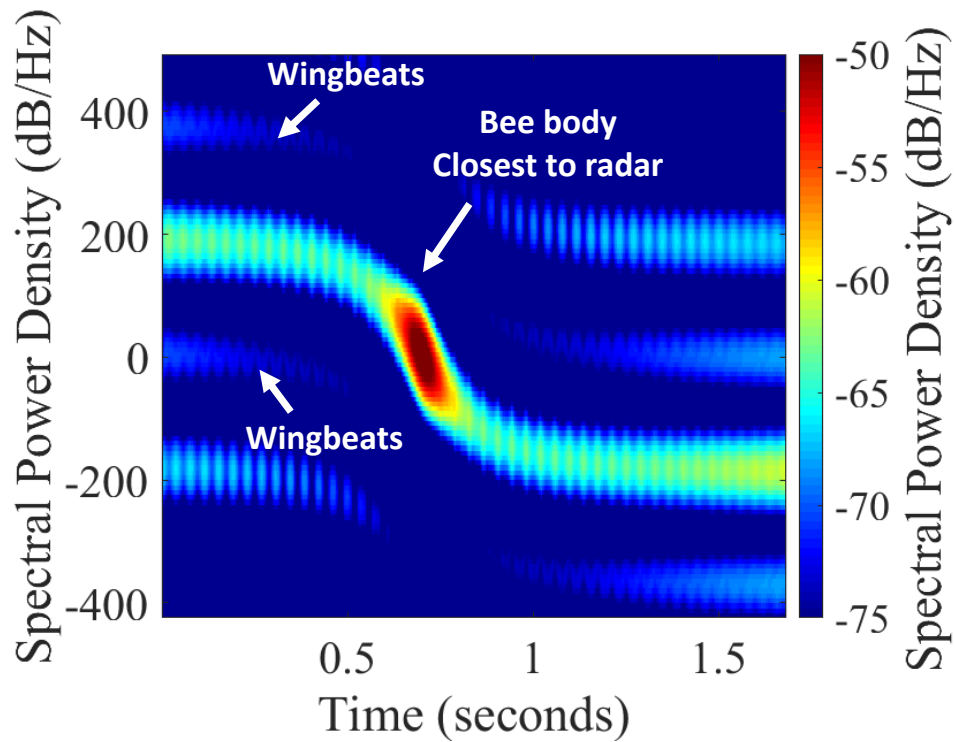
Figure 4.11: Full study of the micro-Doppler simulation displaying main Doppler frequency and micro-Doppler.

The test was repeated while changing the bee's body speed from 5 m/s to 0.05 m/s to simulate a scenario where a bee would flutter in a contained environment. The simulation output shown in Figure 4.12 demonstrates a centred Doppler shift of the bee's body at 19.3 Hz, while displaying wingbeats at ∼±200 Hz.
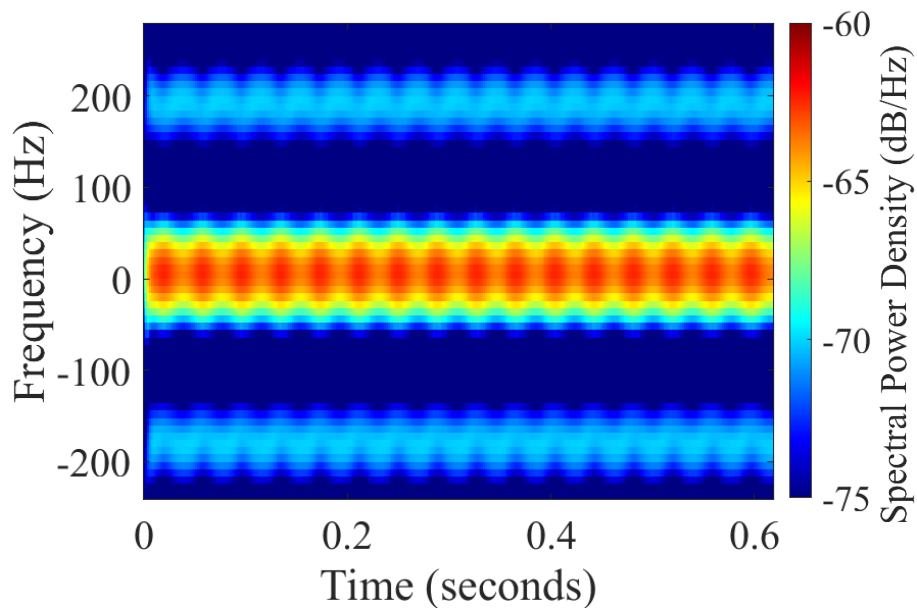
Figure 4.12: Simulation of fluttering bee displaying main Doppler frequency at 1.93 Hz and micro-Doppler wingbeats at 185 Hz.

4.5 Radar measurements of vibrational signals

To verify the radar's ability to measure vibrational signatures, it was first tested with a mechanical shaker and a thin copper wire driven by a Thandar TG503 Function Generator. This involved the use of the V1 radar, where the double balanced mixer was used (no I/Q). The function generator controlled the vibrational frequency of the shaker, which dictated the oscillations of the freestanding copper wire. The vibrational frequency of the function generator was manually stepped from 5 Hz to 160 Hz, which caused oscillations of ±1 mm on the copper wire, while it was placed 50 cm away from the radar. The setup is illustrated in Figure 4.13(a), while the radar readout plotted as an STFT is shown in Figure 4.13(b). Figure 4.13(b) shows captured vibrational signals that were observed from the copper wire, which increased in frequency as the wire's vibrational frequency were manually increased via the function generator during the experiment. This demonstrated the radar's capability to record vibrational increase on the copper wire, which was limited by the mechanical shaker's frequency response. The radar readouts were processed in MATLAB as STFTs, with a window size of 256 and an overlap of 250.
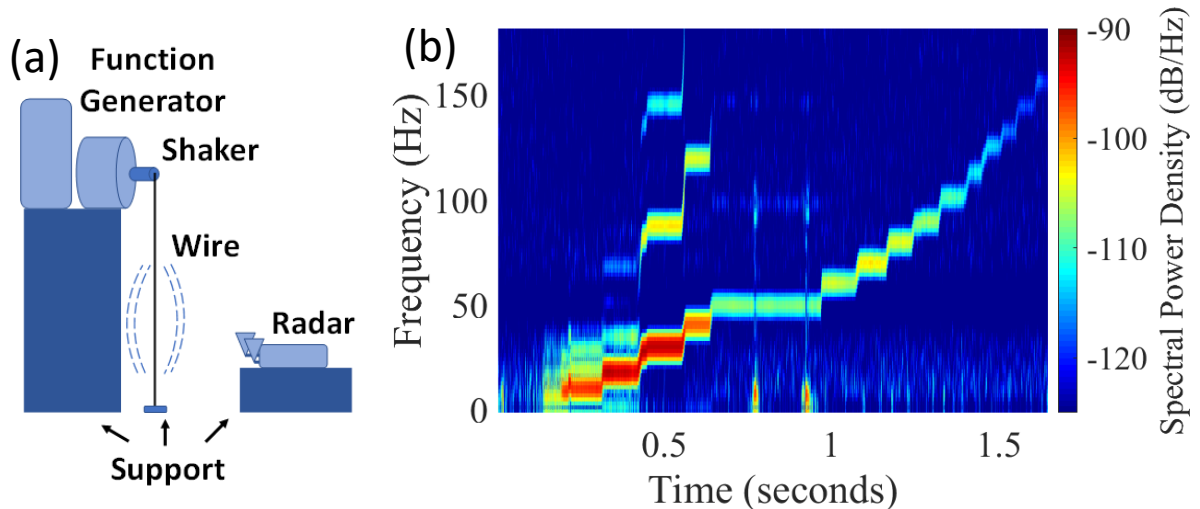
Figure 4.13: (a) setup of the vibration detection experiment (b)STFT plot of copper wire vibrations from 5 to 160 Hz induced by the mechanical shaker.

4.5.1 Insect wingbeats

In a similar setup to that of the copper wire, a bumblebee was placed in a transparent plastic case in front of the radar at a distance of 15 cm. A video camera was placed to record the radar recordings and the movement of the bumblebee to provide a visual correlation of the radar recorded signals. After the radar observations, video segments that indicated interesting movements such as fluttering, dashing, rubbing its

limbs against the box while not flying were carefully observed, extracted and compared to the radar readouts.

The STFT in Figure 4.14(a) illustrated the recorded radar signature of a bumblebee flapping its wings repeatedly in the plastic container. The STFT showed a concentration of signals at the lower frequency band along with four ~1 second horizontal bursts at around 125 Hz. Further, it was found that the 125 Hz coincided within common bumblebee wingbeat frequencies [205]. Moreover, the horizontal micro-Doppler features matched exactly the timing of the bee's wingbeat bursts when cross-referenced with the video footage. In addition to the visual rapid wing motion during the matched segments, additional buzzing was audible at the same matching segments. Upon further inspection, vertical line segments such as the ones displayed between 20 and 23 seconds were visually correlated to rapid limb rubbing, as the bumblebee was moving its limbs against the container. Though these segments were observed to be mostly correlated to limb movement, it was difficult to decorrelate them from the bee's main body motion.

In order to add further insight to the bumblebee's wingbeat, the same experiment was repeated, while replacing the double balanced mixer with the I/Q mixer. The outcome of the radar recording is shown in Figure 4.14(b), which similarly illustrated a wing beat pattern around 170 to 185 Hz in both the positive and negative spectrum. Since the video footage of wingbeats matched precisely with the radar observed micro-Doppler shifts, it was confirmed that these ± micro-Doppler shifts originated from the bumblebee's wings.

Interestingly enough, the simulation of a fluttering bee shown in Figure 4.12 (illustrated in Figure 4.14(b) as the lower inset) displayed a close resemblance to the experiment shown in Figure 4.14(b). This was observed in the centred Doppler shift that reflected the body of the fluttering insect (present in both Figure 4.12 and 4.14(b)), and the wingbeat bands around ±185 Hz (present in both Figure 4.12 and 4.14(b)). The centre Doppler shift band and ±micro-Doppler wingbeats were observed on other data samples that were inspected for wingbeats. To demonstrate the potential application of insect wingbeat classification, a honeybee was used for a similar experiment. The output of the file is displayed as an STFT in Figure 4.15(a) and (b), which showed a micro-Doppler wingbeat frequency of 220 to 240 Hz and 226 Hz respectively. Both the same files were also studied using FFTs, which demonstrated peaks in the same frequency band for each Figure. Evidently, this was well within the expected frequency as honeybee wingbeat frequency reported in literature was 220 to 250 Hz [205], [206].
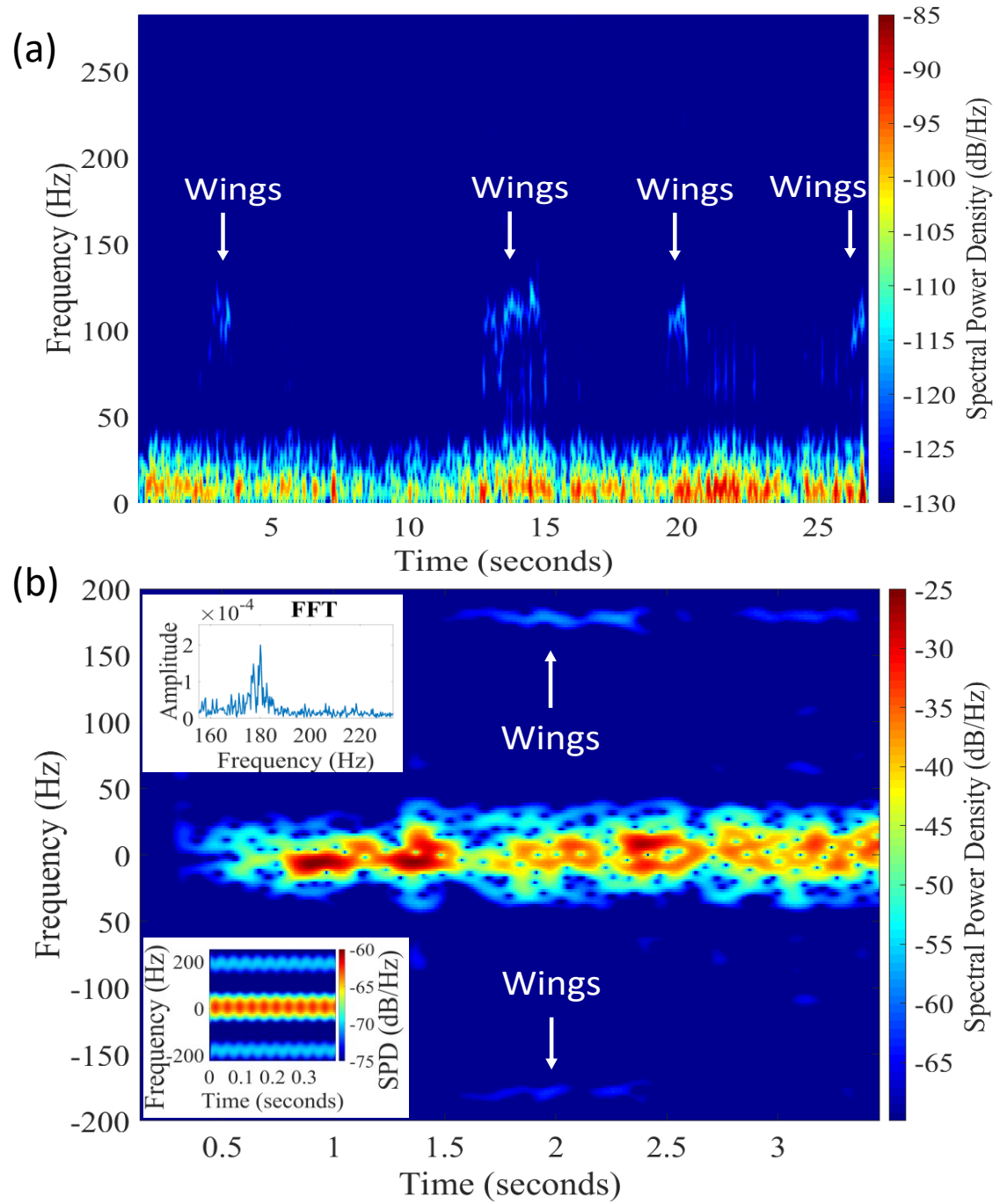
Figure 4.14: Micro-Doppler wingbeat frequency of (a) bumblebee using double balanced mixer (b)bumblebee using I/Q mixer. Upper inset shows an FFT highlighting the wingbeat frequency. Lower inset shows a simulated flight at 0.05 m/s of a honeybee with wingbeats at 185 Hz.
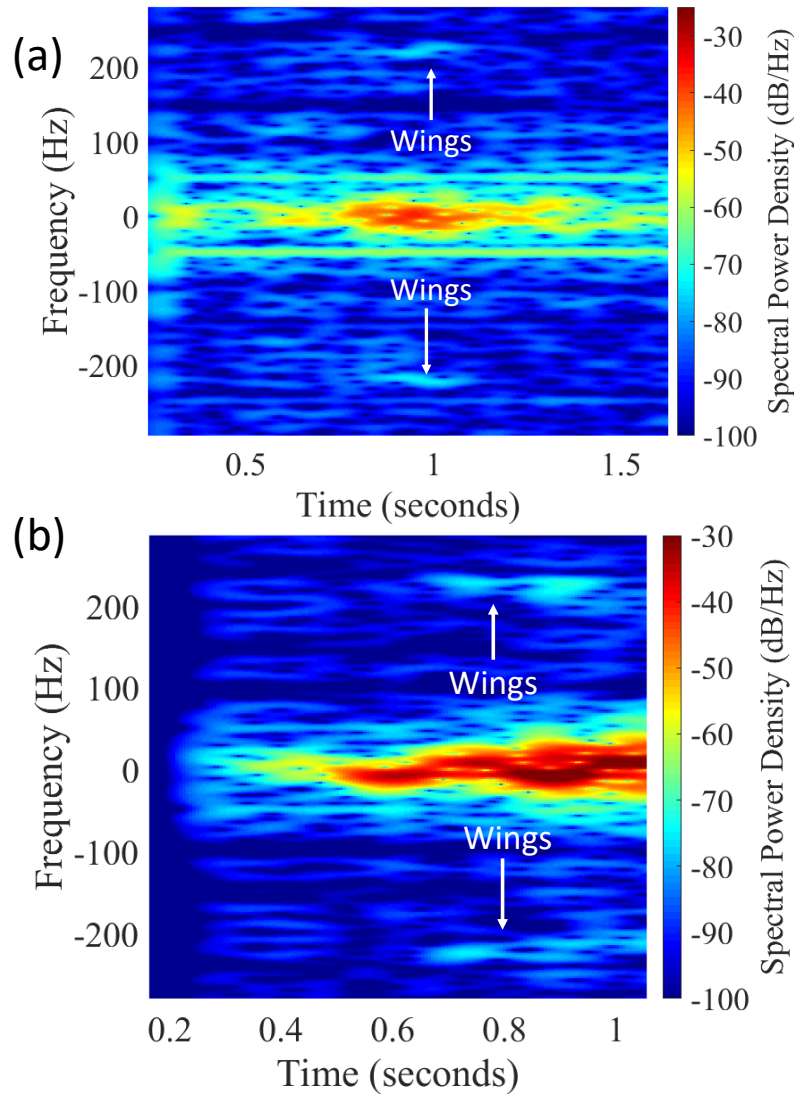
Figure 4.15: Micro-Doppler wingbeat frequency of (a) honeybee with wingbeat micro-Doppler frequency of 220 to 240 Hz (b) honeybee with wingbeat micro-Doppler frequency of 226 Hz.

Despite the radar's low frequency of operation, insect wingbeats were detected with adequate resolution. A higher signal resolution could be achieved with a higher frequency radar, as shorter wavelengths additionally match the size of the insect/wings in comparison to lower frequencies.

Furthermore, it was evident that micro-Doppler related experiments require a low-noise environment. The demonstrated micro-Doppler experiments were performed indoors where electrical appliances, power adapters, cooling fans (laptop, PCs, refrigerators) and even electrical sockets can induce noise. This was noticed strongly around 50 Hz, which caused harmonics further up the frequency in increments of 50 Hz (100 Hz, 150 Hz, 200 Hz etc.). These were required to be filtered out using software-implemented notch filters operating at 50 Hz intervals. Although this resulted in a less noisy STFT, valuable spectral information in these intervals would be filtered out as well.

The bumblebee and honeybee wingbeat differences demonstrated the radar's ability to distinguish different wingbeat frequencies as expected through the initial mechanical shaker experiment. This capability allows the potential discrimination of different insect species based on their wingbeat frequencies. The implementation of such a classification model can be supported through spectrogram, audio files or even FFTs and could result in a wide range of applications suitable for a commercial and/or academic setting.

4.5.2 Vital sign detection

Cardiopulmonary activities create periodic deformations on the chest wall, which in respiration can be between 4 mm to 12 mm and 0.035 mm to 1 mm for heartbeats [207]. A single channel radar is sufficient for the detection of heartbeats/respiration, as the phase changes are proportional to amplitude changes in the recorded signal [180], [208]. The rate of a heartbeat/respiration can be extracted by counting the waveform's total recorded peaks (oscillogram). Another method is to display the recorded result in a spectrogram.

Due to the radar's ability to detect micro-sized targets and their various vibrational frequencies, the radar's suitability for vital sign detection was evaluated. The vital signs of interest that were detected were breathing, coughing and heartbeats. The radar was placed at a distance of 25 cm from a 30-year-old target's chest, while the target maintained uninterrupted breathing for a period of 7 seconds as shown in Figure 4.16(a). Figure 4.16(a) shows the radar recorded signal as a spectrogram, where periodic events of low frequency (< 10 Hz) and high spectral power density (>−35 dB/Hz) were correlated with breathing and heartbeat.
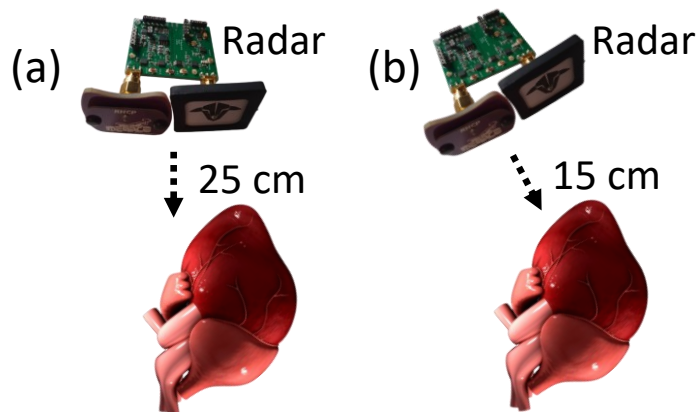
Figure 4.16: V2 Radar setup for (a) breathing and cough experiment (b) heartbeat experiment.

A manual timer was initiated, while the breathing recording was repeated, and interrupted by three intentional coughs between 1.5 seconds and 2.5 seconds, shown in Figure 4.17(b). This clearly showed three distinctive cough events that can be separated from one another, which also matched the recorded time. To focus on biologically relevant content, the range of the monitored frequency was reduced to 100 Hz, which also rescaled the spectral density.

Both figures showed a horizontal band at 120 Hz, which were due to the laptop's fan, as the blades rotated at 40 cm distance away from the radar. Further, both figures demonstrated harmonics that appeared vertically above signals. This was especially the case when inspecting the cough events as the displacement caused by coughing was much larger compared to breathing, which caused prominent harmonic tones.

The radar was then moved closer to a 15 cm distance from the target's chest at an angle of 15° to account for the heart's left offset as illustrated in Figure 4.16(b). The radar recorded signals are shown in Figure 4.18(a) and (b), which demonstrated a heartbeat signal during two normal breathing cycles and a heartbeat signal while holding breath respectively. Since the radar was moved closer, the amplitude of the breathing signals in both breathing cycles (∽1 to 4 seconds and ∽5 to 8 seconds) increased, which is shown in Figure 4.18(a). The natural pause (∽4 to 5 seconds) in between the breathing cycles showed a signal which was believed to be related to the target's heartbeat.
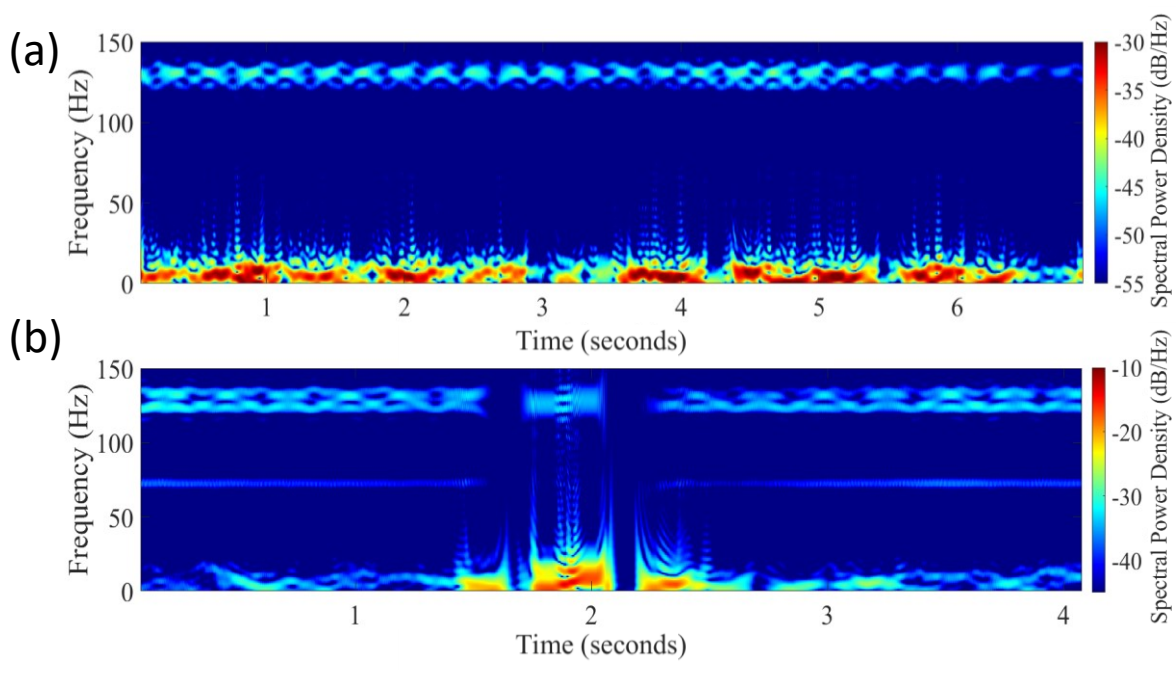
Figure 4.17: Comparison between (a) uninterrupted breathing (b) breathing with 3 intentional coughs between 1.5 and 2.5 seconds, which were recorded using the V2 radar.
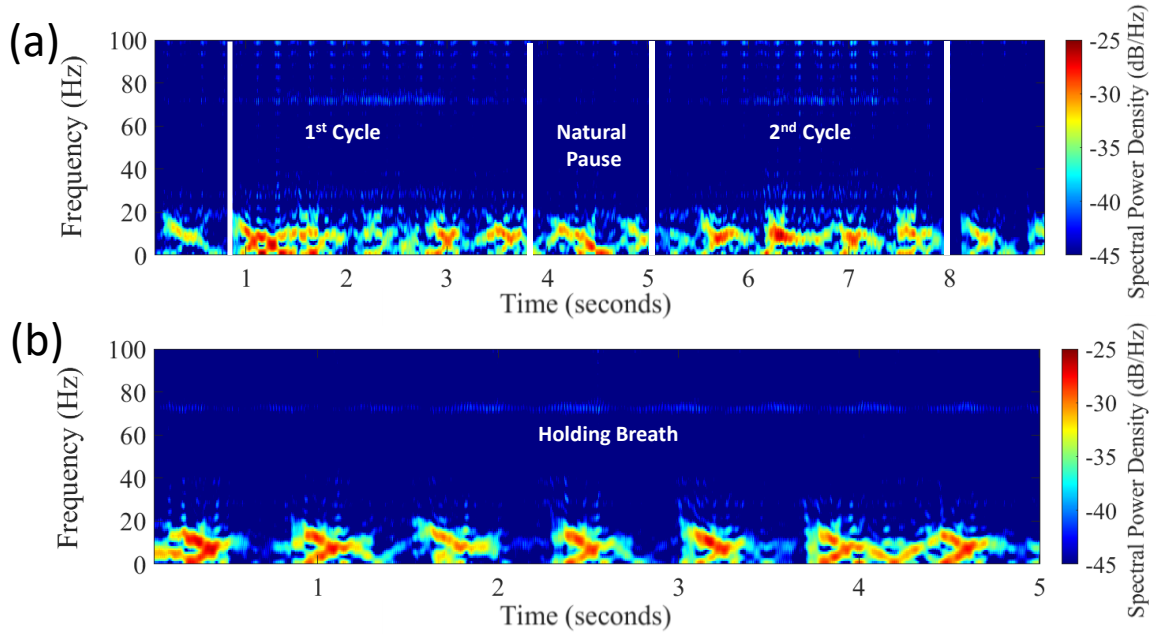
Figure 4.18: Heartbeat comparison (a) while breathing normally (b) while intentionally withholding breath, which were recorded using the V2 radar.

To confirm the heartbeat signal, breathing and movements were withheld, while the radar recorded the target's heartbeats. The periodic signal shown in Figure 4.18(b) matched the experimenter's pulse of 94 beats per minute (bpm). An X shaped signature was observed, which may be correlated to acceleration and deceleration phases in atrioventricular dynamics, supporting the hypothesis that the radar can be used for heartbeat detection.

While the previously demonstrated breathing, coughing and heartbeat signals were demonstrated using the V2 radar, another attempt was made using the V1 radar. This radar used higher gain antennas 12 dBi (Tx) and 17 dBi (Rx), to contribute to a higher EIRP. The radar was placed at a distance of 50 cm, pointing directly towards the chest of a 33-year-old human target, while the human target withheld his breath and movements during this experiment. The experimenter manually calculated his pulse to result in 96 bpm. The recorded signal is shown as an STFT in Figure 4.19, which depicted clear heartbeat signals. Figure 4.19 also displays an inset, which illustrated the FFT of the heartbeat signal, indicating a peak at 1.6 Hz (represented 96 bpm). To further verify the heartbeat rate, a closer look at the signals revealed that the 5 seconds mark displayed the start of a new heartbeat peak, which indicated that from 0 to 5 seconds, a total of 8 heartbeat signals were recorded. This resulted in a calculated heartbeat rate of 96 bpm, which matched that of the calculated heartbeat.

188
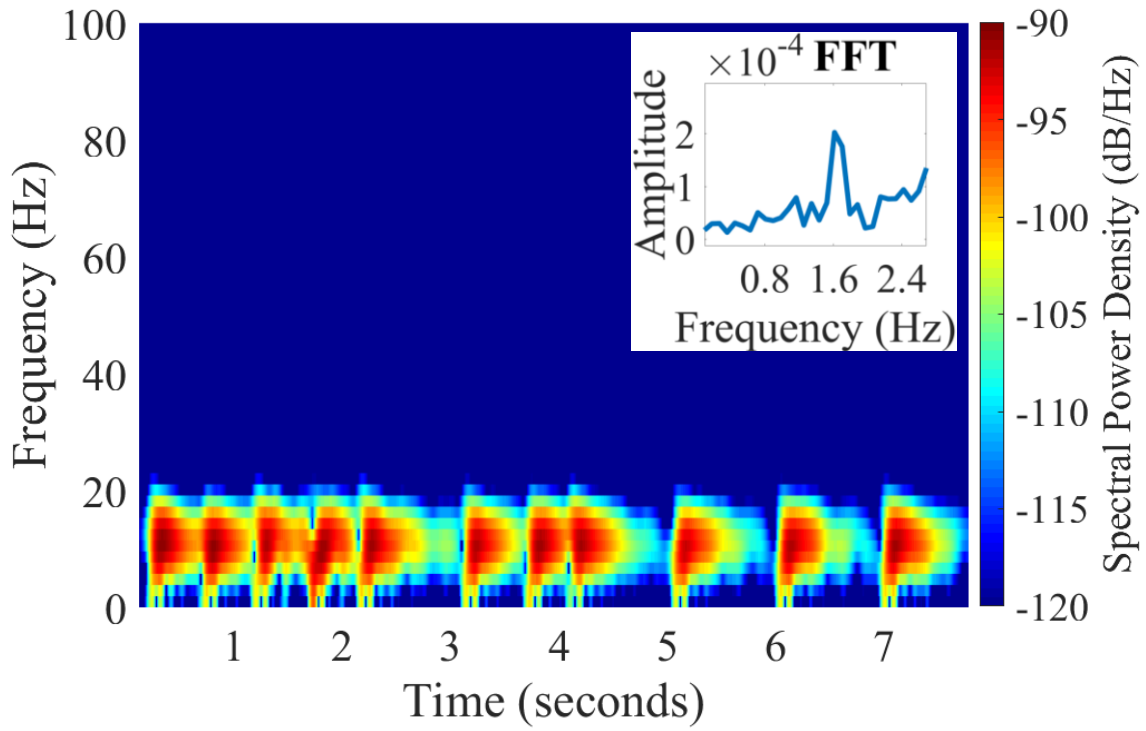
Figure 4.19: Heartbeat signals recorded using the V1 radar. Inset shows the FFT of the heartbeat which indicated the presence of a peak at 1.6 Hz (96 beats per minute).

A comparison can be drawn from both heartbeat plots, where the difference was distance and angle. The X-signature observed in Figure 4.18(b) is no longer visible in Figure 4.19 as the radar was placed directly in front of the experimenter's chest. Hence it was believed that the X-signature was a result of the 15° angular offset.

It is important to consider that the heartbeat detection in Figure 4.19 may more likely be a result to the detection of chest displacement than that of cardiovascular movements within the experimenter's chest. This can be concluded from the pulse-like signature in Figure 4.19 when compared to the X-shaped signature in 4.19(b). Furthermore, the distance between the radar and chest was larger which also indicates that the signatures in Figure 4.19 may have been chest displacements. Finally, the radar's incident power reflection at the air-skin interface and surface reflection may reach 50% and more than 90% respectively [180], which at a distance of 50 cm makes it challenging to perceive cardiovascular movements as opposed to a distance of 15 cm.

Whether monitoring insects, wingbeats or heartbeats, one of the limitations present in the 5.8 GHz radar is the frequency of operation. Other systems utilise a higher frequency (such as 24 GHz) [120], [128], [209][120], [128], where observing honeybees with 24 GHz is relatively easier compared to a 5.8 GHz radar. This is due to the wavelength

of the 24 GHz being more than 4 times smaller (λ=12.5 mm) compared to 5.8 GHz (51.68 mm), allowing it to match closer to the actual the size of a bee (10 mm to 15 mm).

With a wavelength smaller than the target, the resolution would be high enough to obtain a clear signature of the insect, and further aid signal separation when observing multiple honeybees. A shorter wavelength would also allow higher resolution micro-Doppler signals, afford separation of micro-movements from the overall Doppler shift, which may appear as a single motion in a 5.8 GHz radar. Such movements can include in-hive vibrations/communication signals (e.g., waggle dance, quacking, tooting), minute body movements (limbs) a finer wing beat resolution.

Figure 4.20 overlays 24 GHz steel sphere and water sphere RCS simulations against 5.8 GHz steel sphere and water sphere RCS simulations. This compared the RCS simulation results performed by [120] against the RCS simulation results performed in this study [183]. As expected, the simulation resulted in a higher RCS at 24 GHz, for a steel sphere and water sphere. These were orders of magnitudes larger than that achieved in the 5.8 GHz simulation, confirming the challenges from 5.8 GHz detection.
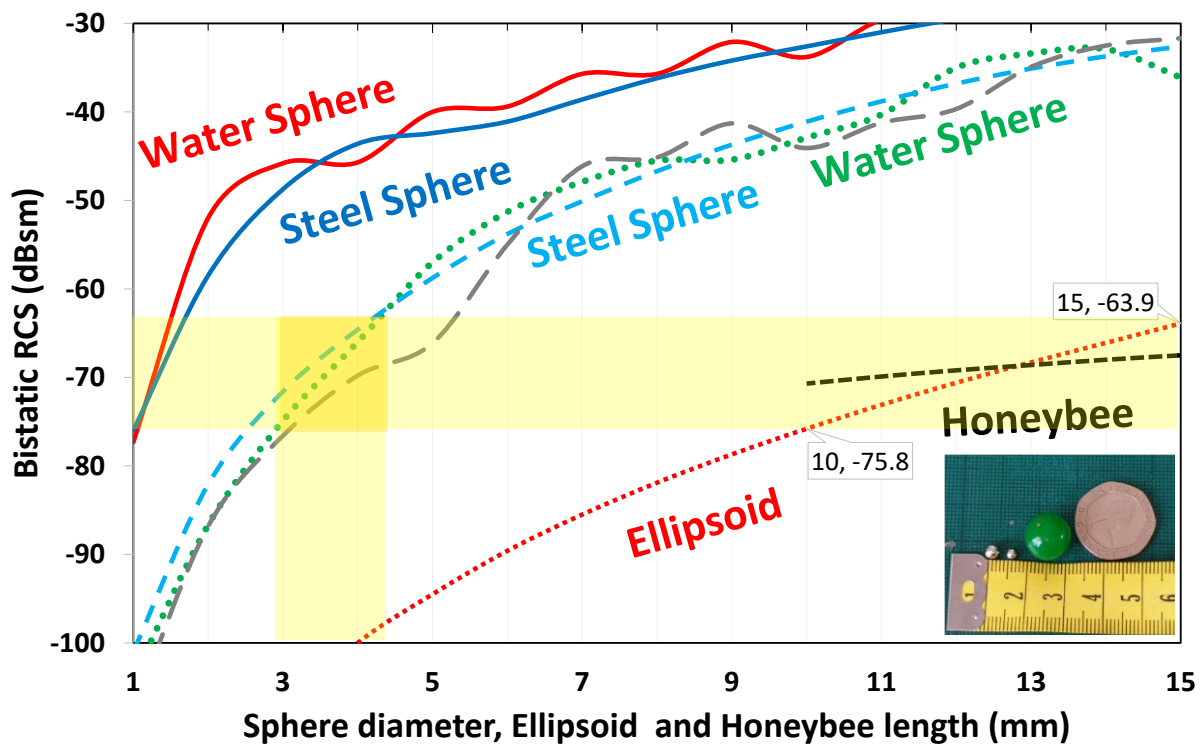
Figure 4.20: Simulation combination of calibration targets used and their approximation to water spheres. Solid lines are simulations for a 24 GHz radar while the rest (dashed and dotted lines) are for 5.8 GHz radar. Yellow highlight indicates the RCS values for spheres from 3 to 4 mm. Inset displays different targets used. From left to right these were, 4 mm, 3 mm, 10 mm hydrogel sphere and 20 pence coin for size reference.

To further demonstrate the difference between signal resolution, Figure 4.21 shows an experimental comparison between the 5.8 GHz radar and a commercial 24 GHz CW radar (similar to the one used in [120], [128], [209]) for a 4 mm steel sphere used in a pendulum setting. The output power of the 24 GHz radar module was 16 dBm, which was less compared to that of the 5.8 GHz radar. Yet, the 24 GHz pendulum signature resulted in a higher/finer resolution. This is shown Figure 4.21(b) in the higher frequency signal component of the pendulum signal, indicating a tail-like feature (shown closer in the insets), unlike the 5.8 GHz. Although this signal is less complex compared to a honeybee's signal, it provides an adequate representation of the higher resolution obtained with higher frequency as illustrated in Figure 4.21.

However, the 5.8 GHz frequency of choice was considered due to a collection of reasons that deemed it more favourable compared to other frequencies such as its monitoring range versus signal quality trade-off, the availability of off-the-shelf components, the low cost of the components and the ability to still manufacture PCBs using cheaper RF boards. Most importantly, the 5.8 GHz choice supported the integration with existing RF systems that are available within the research group.

Another disadvantage of CW radar results is leakage from the transmitter to the receiver. A portion of the transmitted signal can leak via the antennas or coupling circuitry. This unwanted leakage causes the radar to have low-frequency noise and DC offset if not properly removed. Further, reflected signals from stationary objects and noise sidebands are also received. Although stationary objects do not result in a Doppler shift (as no movement is involved), they may contribute to further noise.
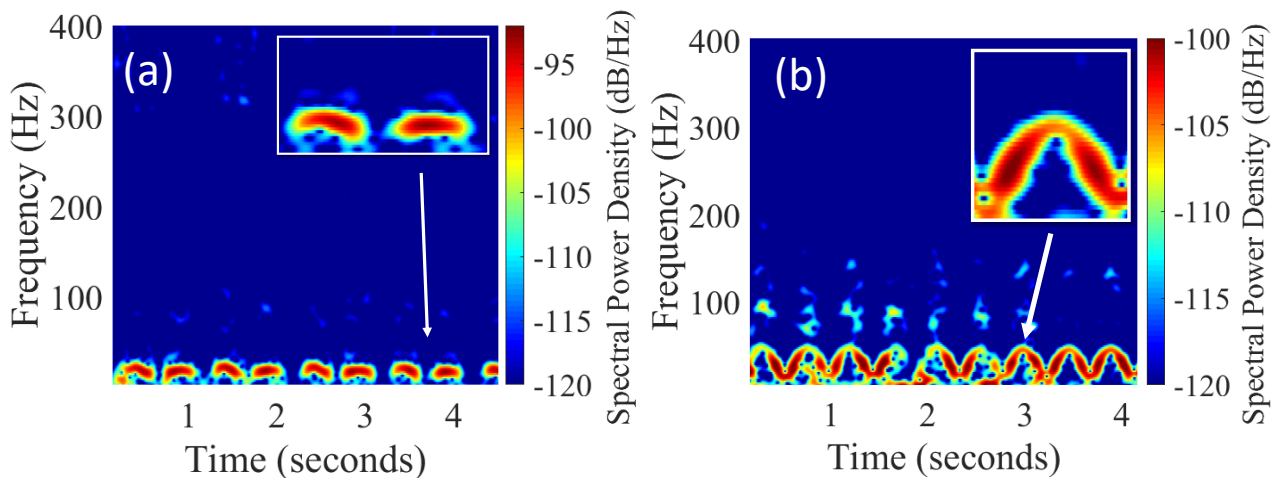
Figure 4.21: Pendulum signature of (a) 5.8 GHz V1 radar (b) 24 GHz radar. Insets shows a closer view of the pendulum signature to demonstrate resolution differences, where a clear tail-like feature can be observed when using a 24 GHz radar.

Chapter 5.   Conclusion and Future Work

This chapter reviews the study's most important findings. Current insect monitoring and tracking methods involve the use of a tagging system that impacts both the insect and the environment negatively. The current radar system was capable of unobtrusive insect monitoring from a 2 to 3-meter distance, while demonstrating micro-Doppler capabilities and high prediction accuracies when coupled with machine learning.

5.1 Conclusion

Chapter 2 studies insects as radar targets, while specifically investigating honeybee RCS at 5.8 GHz, which was found to be a research gap. Multiple simulations were performed, which when combined together, converged to provide a simulated value of a honeybee's RCS that was matched with a 3- 4 mm steel sphere and an ellipsoid within honeybee dimensions. This chapter also provided a rationale for the radar's placement to face the hive and studied the possibility of coating a honeybee, where the use of the SEM encouraged coating the upper part of the thorax and abdomen with 100 μm.

Chapter 3 presented a simulation of a 5.8 GHz Doppler radar for a target with a variable RCS, range and velocity. The chapter discussed the main radar boards designed and assembled starting with the V1 radar, the V2 radar and finally concluding with the plug-and-play V3 I/Q radar. This chapter also discussed a calibration method using 4 mm steel spheres to tune the radar's sensitivity and approximate a honeybee RCS. Releasing the spheres from a 2-metre distance, normalising their magnitude to the simulated value, and repeating the experiment 9 times resulted in an average RCS of −64.43 dBsm. The sphere's drop was recorded to extract the target's Doppler shift, which upon manual calculation — using gravitational force as velocity — was found to be accurate with a minor error of 0.06 m/s. A pendulum experiment was performed to evaluate the RCS increase of 100 μm Silver coated wooden sphere, which was only detectable after the application of the coating, thus correlating the simulated RCS value of both wooden sphere and coated wooden sphere to an experimental setting. The same simulation and theoretical study was applied to a honeybee, which resulted in a 17.7 dBsm RCS increase and a maximum range of 3.8 metre (reaching 4.2 metres for 15 mm long bees) from its original 2.4 metres.

Chapter 4 discussed the correlation of bee signals which comprised of a pendulum simulation and experiments to show shared signature attributes of target movements with

respect to the radar. A simulation that controlled the movement, location, velocity and acceleration of a sphere was implemented to demonstrate several sphere movement scenarios while drawing similarities to bee signals obtained from field experiments. Honeybee signals recorded during field experiments were demonstrated, while displaying the difference in departing and returning honeybees, which allowed signal discrimination. Interestingly enough, the radar recorded honeybee signals seemed to have similar signatures to audio recorded data of honeybees. This was concluded upon comparing Figure 1.15(a) and (c) with radar recorded data.

Machine learning techniques were explored in chapter 4, where spectrograms of departing and returning honeybees were processed as LSP and random forest was used for the implementation of a NN, achieving a maximum accuracy of 87.83% with a Binary Cross Entropy Loss of 0.4274. Another machine learning implementation (processing the data as .wav files), where LSF approach was employed using SVMs for Ternary classification. This provided a Ternary accuracy rate of 93.37% with a loss of 0.2667.

Micro-Doppler signals were investigated, following a series of honeybee wingbeat micro-Doppler simulations. Experimental micro-Doppler signatures were recorded and demonstrated for bumblebee and honeybee wingbeats, which matched the insect's documented wingbeat in literature. This was achieved without the use of high frequency radars and changes applied to the radar board. Finally, the radar was further utilised for vital signs monitoring, where a heartbeat, breathing and coughs were recorded and visually classified. The radar was able to provide accurate chest displacements, which matched the experimenters' bpm.

The study focused on adapting a highly sensitive 5.8 GHz Doppler radar for near hive monitoring, which provided enough resolution to distinguish basic insect motion and wingbeats. The integration of machine learning techniques and artificial intelligence allows endless applications to be envisaged, where classification models can be built to monitor the world's most economically beneficial insect, the honeybee. This can be further expanded to incorporate wingbeats as a classification method which would pave the way for various insect classification applications. The results presented in this study act as a proof of concept, while demonstrating a wide range of potential applications suitable for both academic and commercial environments. Suggestions for future work are discussed in the next section given further time.

5.2 Future work

The versatility of the radar allows multiple integrations that can further expand its applications. Its plug-and-play capability enables it to be used for a wide range of experiments, regardless of the experimenter's educational background or expertise. Additionally, given further time, several modifications and experiments would have taken place to enhance its performance and test its capabilities, which are discussed below.

5.2.1 Remote monitoring

The radar allows easy integration with different microcontrollers. This encourages the use of the radar remotely, through online access to a microcontroller. Since the V3 I/Q radar board combined the necessary functions to operate as a stand-alone-radar with plug-and-play capability and minimal user involvement, remote operation was briefly tested. This provides further flexibility with data collection and eliminated the need for operator presence at the site. By adding a USB camera looking outwards (in the direction of the antennas), the user can monitor the hive and the recorded values simultaneously, which can be later used for signal labelling thus, providing an ideal setting for machine learning integration. This was briefly attempted as shown in Figure 5.1, as a proof of concept, to allow remote data collection while monitoring both the data collection process and the target.
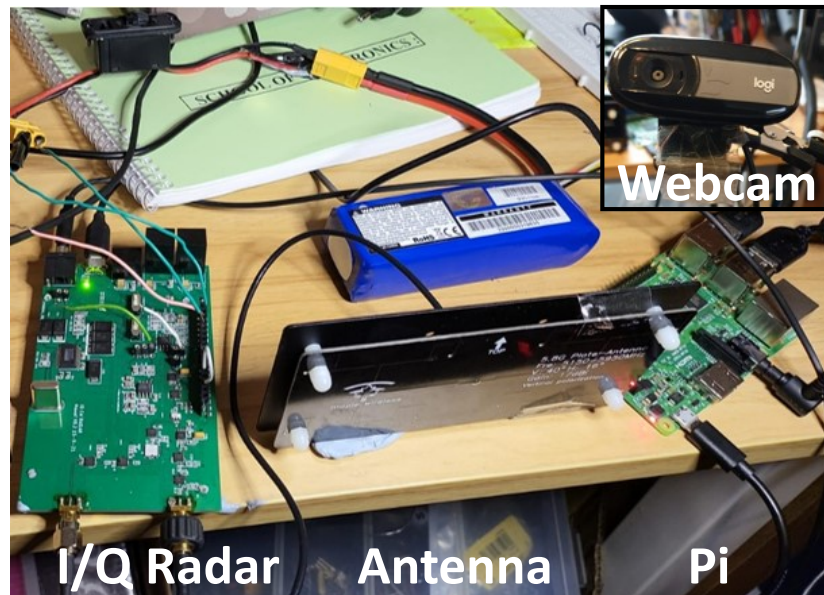
Figure 5.1: Remote data collection using the V3 I/Q radar and Raspberry Pi. Inset shows the webcam used.

While any microcontroller could be used, A Raspberry Pi was used to provide a simple proof of concept for remote radar recording. To enable this functionality, it required

the installation of a remote desktop software on the Raspberry Pi, Audacity, a USB webcam and a streaming software. This would allow the webcam to continuously act as a streaming service which was accessible upon opening the streaming URL.

Figure 5.2 shows a demonstration of accessing the Raspberry Pi remotely to record radar signatures. The radar was powered by a 12 V LiPo battery, while the Pi was powered by a portable power-bank. Using a laptop, a remote desktop connection was established by connecting to the Pi's IP and the Pi's Audacity software was executed. By connecting to the streaming URL from a personal device, the webcam stream was found visible. Upon initiating the recording, the Pi started to record the monitored radar signatures. Normally, a Raspberry Pi is not capable of processing recorded audio as it lacks an ADC for audio digitisation. However, this is now possible with the V3 I/Q radar's capability of digitising audio. Highlighted areas in Figure 5.2 demonstrate the Pi's usage and that the streaming service was functional. Remote data recording provides the potential of managing multiple radar devices given that each radar device has a stable internet connection. This proof of concept encourages future data collection to take place remotely.
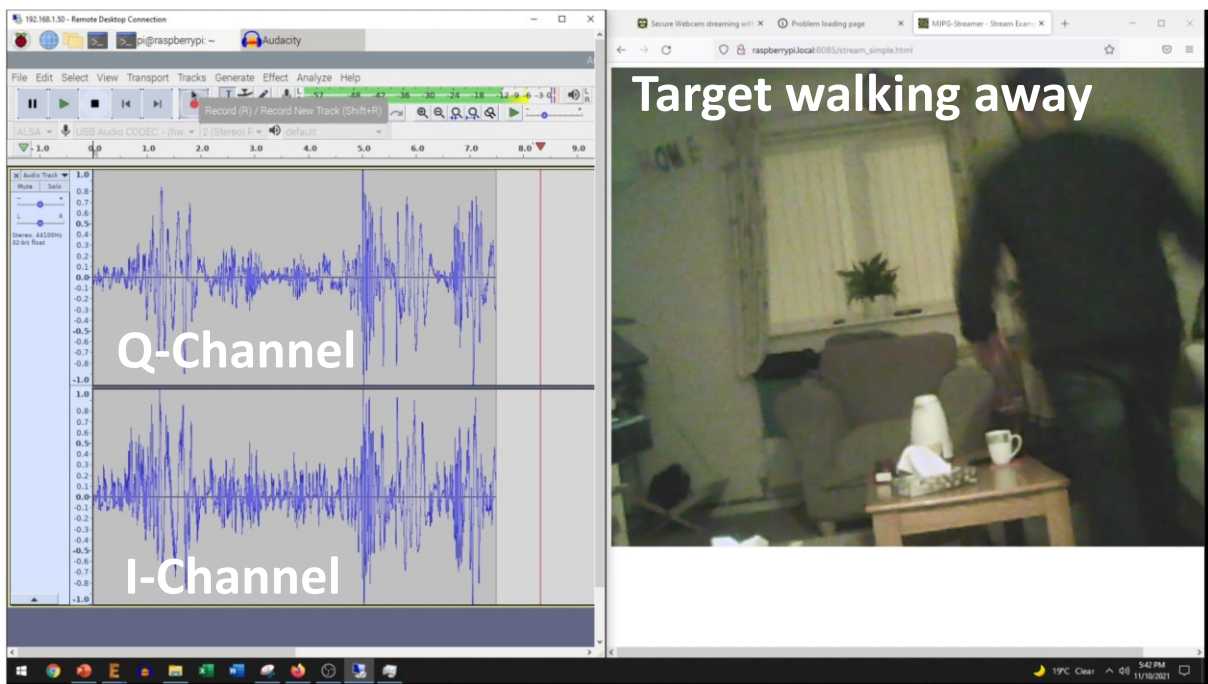
Figure 5.2: Remote data collection using the V3 I/Q radar integrated with a Raspberry Pi. The two open windows on the desktop, correspond to a remote desktop connected to the Raspberry Pi and the streaming service connected to the Pi's webcam.

5.2.2 Monitoring vibrational signals

By placing the radar facing out of the hive, the radar would be close enough to record various vibrational signals such as "queen piping" and "queen quacking", which is a 1 second long signal at ~400 Hz signal and a 200 to 350 Hz signal respectively [125],[210]. This leads up to two applications, where the first is simple monitoring of such frequencies to alarm the hive-owner as such signals are believed to be associated to hive swarming. The second application is based on the fact that the piping signals increase in frequency (from 200 to 550 Hz) —though generally observed ~400 Hz — as the queen matures in age, which allows the radar to aid in the presence of the queen and the potential identification of the queen's age [210]. Figure 5.3 was reproduced from [125], which shows quacking and tooting signals that were recorded using a piezoelectric accelerometer installed in the centre frame of the hive [125]. If bees are preparing to swarm, the queen toots and the worker bees confine the other queens by feeding them [210]. These vibrational signatures can be recorded using the radar in a non-obtrusive manner as opposed to [125]. Further integration of machine learning techniques can predict swarming events using the queen's communication as early indicators.
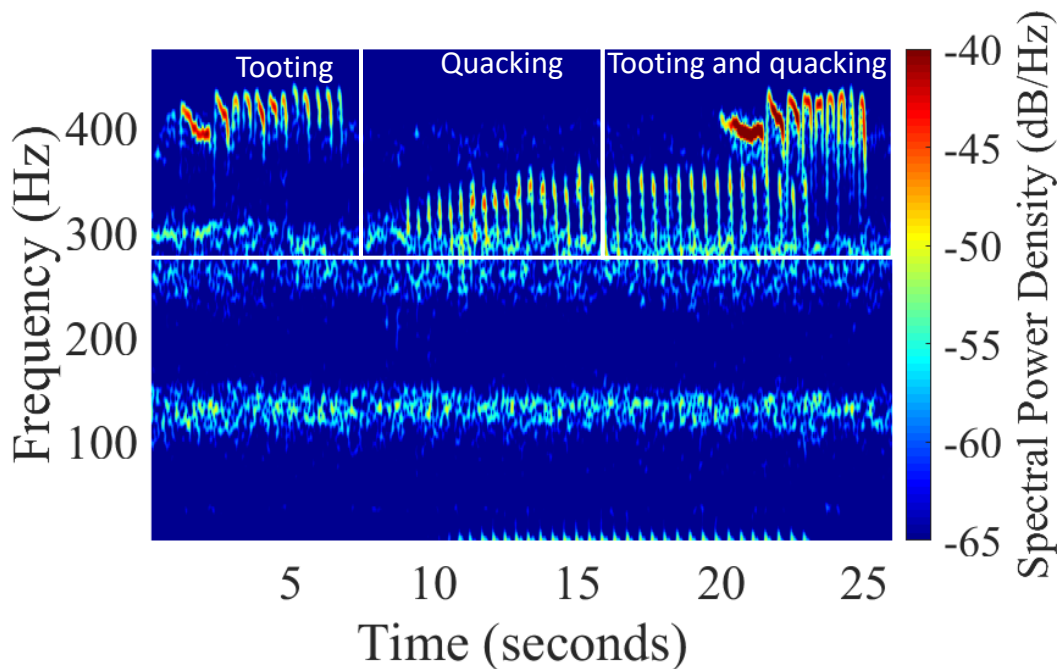
Figure 5.3: Tooting, quacking and a combination of both signals. Reproduced from supplementary files in [125].

5.2.3 Real-time classification

The remote monitoring capability can be further extended upon implementing a real time classification of radar signals. Using a machine learning implementation of

either Binary or Ternary classification. Using a machine learning implementation of either Binary or Ternary classification of a hive could provide interesting data for analysis. Especially, when the data is correlated to other hive metrics such as reproductive success, pollination success and general hive health. This would provide hive owners with live evaluations of their hive by assessing honeybee traffic. Further, the capability of logging traffic, could provide a daily log of the amount of bees that departed and the amount that returned. Collecting and studying this data can provide early indicators of colony weaknesses (i.e., if departing bees >> returning bees), allowing hive owners to potentially engage in early colony stress investigations to obtain a maximum pollination efficacy. This is interesting for both bee farms and commercial applications (soft fruit industries) that require bee behaviour monitoring, which may be applied to a hive, a polytunnel or even a flower patch. A microcontroller suitable for such an application would be the NVIDIA Nano Jetson.

An interesting application for a commercial setting would be the placement of radars at entrances and exits of polytunnels to estimate the bee traffic within the tunnels. Adding a layer of insect classification through wingbeats could further reveal whether the pollinating occurring within the tunnel is a result of farm bees or wild bees. Similarly, polytunnel monitoring can be applied to assess the traffic in a newly built tunnel, allowing measurement of the time duration needed for the new tunnel's traffic to reach that of the older tunnels. It can also provide insightful tunnel related metrics that allow a soft fruit company to re-evaluate the number and location of farm bees to further increase/reduce tunnel traffic. This example is shown in Figure 5.4

Figure 5. 4 Example of a polytunnel monitoring system that logs entries and exits out of a polytunnel for polytunnel performance evaluation.

Another insightful study would be the placement of the radar near specific flower patches and new fruit strains, in order to identify whether such strains encourage/discourage bee activity.

The addition of a solar panel would allow the radar to maintain operation through a renewable energy source. The solar panel would continuously charge a battery which powers the radar, while coupled with live hive monitoring capabilities and wireless data transmission, an environmentally friendly solution can be provided as illustrated in Figure 5.5.
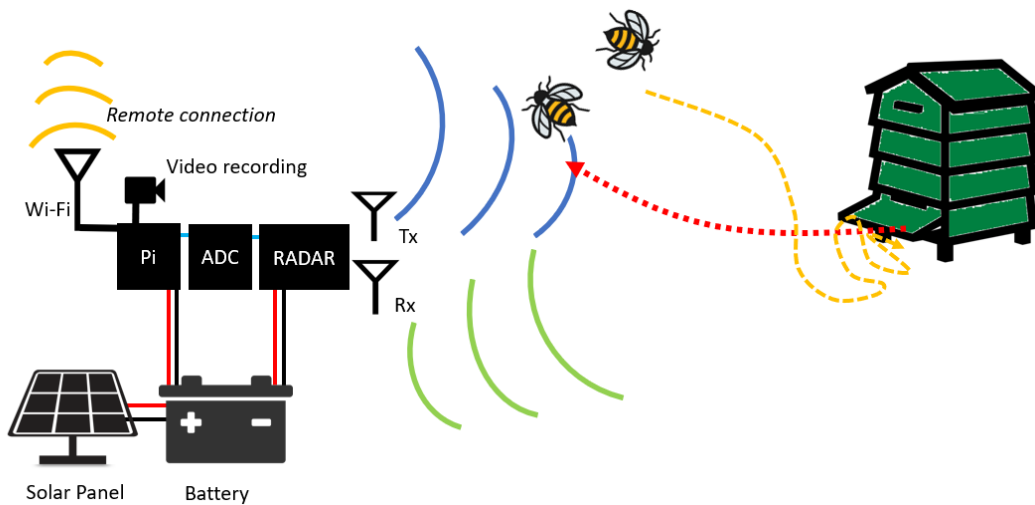
Figure 5.5: a solar panel-based radar for hive monitoring.

Table 5.1 shows the power calculations that took place to determine the solar panel and external battery required to run a maximum of five days without sunshine. The power calculations considered the radar board and a Raspberry Pi 3 processor, which consume ∽10Ah per day, resulting in a 100 Ah battery for five days.

Table 5.1: Power calculations for setting up a solar panel-based radar for hive monitoring

#	Component	Voltage (v)	mA per hour (mAh)	Watt
1	VCO	3	100	
2	LNA	5	58	
3	LNA	5	58	
4	LNA	5	58	2
5	Op Amp	5	4.6	
6	LPF	5	1.15	
7	Pi3	5	550	2.75
Total current per hour (mA)			279.75+550 = 830	4.75

5.2.4 Pesticide-inflicted behaviour assessment via radar monitoring

Bee logging can be used to evaluate a hive's performance when exposed to different doses of pesticide. Monitoring the number of incoming and outgoing bees, their velocity and performing a daily count can be used to plot daily metrics that can be compared with hives that are not exposed to pesticides. The implementation of such a comparison and a daily report of bees entering/leaving can indicate the impact of the pesticide on the colony. The same method can be used to assess the impact of different types/doses of pesticides.

5.2.5 Radar Modifications

Though the radar produced satisfactory bee recordings at a non-obtrusive range, further adjustments can be made to increase the performance. Ground cut-off was shown to support a higher output power in the V3 I/Q radar. However, this was only implemented at the output SMA of the radar. Upon further PCB transmission line inspections, it was found that a combination of a thin SMA pad, a 2nd layer ground cut-off (5.75×3.75 mm) and via fencing spaced at $\lambda/20$ (2.58 mm), delivered a higher S21 (-1.29 dB) in comparison to a PCB with no 2nd layer ground cut-off, which showed an S21 of -2.15 dB. The increase of PCB performance shows that performance of FR4 PCB can be enhanced. This can be further investigated in a simulation and experimental setting to enable fabricating high frequency PCB using affordable FR4 PCBs.

The usage of different PCB material is also encouraged for future work. In fact, another simulation studied the impact of a Roger's sheet, which strongly encouraged the usage of a Roger's RO4350B (ε_r=3.8) laminate resulting in a S11 of -36.33 dB (0.023% reflection). This is mentioned in more detail in Appendix K. Hence, future fabrication of the radar board using a high frequency supporting laminate would certainly result in a higher performance.

The V3 I/Q radar board was compact at the size of 104.6 mm $\times$ 64.6 mm. Yet, the board supported further reductions in size, as the bottom layer was unpopulated with components. Upon the removal of the two amplifier circuits and the ADC to the bottom layer, the overall board size can be reduced to 60 mm^2 board.

5.2.6 Coating experiments

Coating experiments were limited to the coated wooden sphere and several preliminary experiments on coated bees and coated hydrogel spheres that showed a minor

increase in magnitude compared to non-coated counterparts under similar monitoring conditions. Given more time, a more comprehensive and controlled study would have taken place to correlate the increase of magnitude with nanoparticle coating.

5.2.7 I/Q machine learning

Though this was not performed yet as the V3 I/Q radar was developed at a later stage in the study, it is believed that the additional directional parameter can potentially aid in classification, pushing the accuracy even higher. A suggested study would be the comparison of the current ternary classification approach to a classic signal processing technique such as the Hidden Markov Model (HMM). Though the application of HMM to the data extracted with the double balanced mixer, for ternary classification resulted in a poor accuracy of 53%. It is believed that with I/Q data, more robust classification algorithms can be built that could increase the prediction accuracy.

Applying machine learning techniques can provide insightful hive related predictions, allowing hive owners to mitigate different events to increase their overall yield. By monitoring hive performance and predicting hive yield, commercial farmers can be a step ahead of colony activity/traffic decline, where such predictions can be applied to hives, polytunnels and flower patches.

An interesting point that can be further explored with machine learning, is whether the classification algorithms are strictly looking at the amplitude and the signature of the signal or whether the algorithm is also incorporating the wingbeats increasing and decreasing in the signals. These minute signatures may be invisible to the human eye, (in both audio and spectrograms) but may be visible and even processed by the algorithm, although the signals were not manifested as micro-Doppler signatures. Identifying whether data un-seen by the human eye is contributing towards the classification is a compelling research question.

5.2.8 Insect classification

This application was briefly touched on, where the radar's capabilities can be utilised to classify different insects based on their wingbeats and maximum flight speed. To the authors knowledge, no 5.8 GHz radar-based insect classification system exists. Such a classification system is valuable as it can indicate the presence of predatory/invasive species (e.g., European hornet, Asian hornet, wasps). This can then be used to alert the hive owner allowing early involvement prior to endangering the colony.

5.2.9 Challenges with monitoring insects in real-time

This study demonstrated the feasibility of monitoring insects using a low-cost 5.8 GHz radar. The use of radar technology for insect monitoring makes a compelling reason due to its lower cost, lower power requirements, compact size, and functionality through low visibility conditions (unlike cameras). However, it requires overcoming several challenges to develop a reliable low-cost insect monitoring radar.

One of the major challenges, that was successfully addressed during this study is the detection of targets as small as honeybees at 5.8 GHz, while maintaining a reasonable monitoring distance. In addition to these challenges, other difficulties arise that are related to the complex flying behaviour of honeybees. Honeybees do not fly in straight lines, and their flight behaviour is not simply inwards and outwards of a hive. This makes detection difficult as a range of false positives can be recorded due to their random motion. Honeybee monitoring is performed best when individual bees enter/leave a hive, whereas in a realistic scenario this is not the case. A small number of bees flying around the hive, can still be within the radar's detection capabilities. However, when a large number of bees are hovering at the entrance, the monitoring process becomes more challenging.

Additionally, various surrounding factors such as animals, other insects, vegetation and even wind can induce noise, or contribute to an increased rate of false positives in honeybee detection. These complexities are present in both offline monitoring (post-recording processing) and real-time monitoring.

In addition to the above challenges, real-time monitoring requires a powerful microcontroller (NVIDIA Nano Jetson) that can effectively handle monitoring and parse data fast enough to a running machine learning algorithm that automatically detects the behaviour, to then label the event. Furthermore, the radar's placement in relation to the hive (as shown in Figure 5.6) needs to be maintained in terms of angle, elevation and distance throughout testing and experimentation phases. This is due to the fact that any variation within the aforementioned parameters compared to variables the model was originally trained with, will become inconsistent and may result in inaccurate predictions. Thus, real-time monitoring is a topic where future work could be dedicated to, as its successful implementation possesses the potential to open a multitude of research and commercial opportunities.
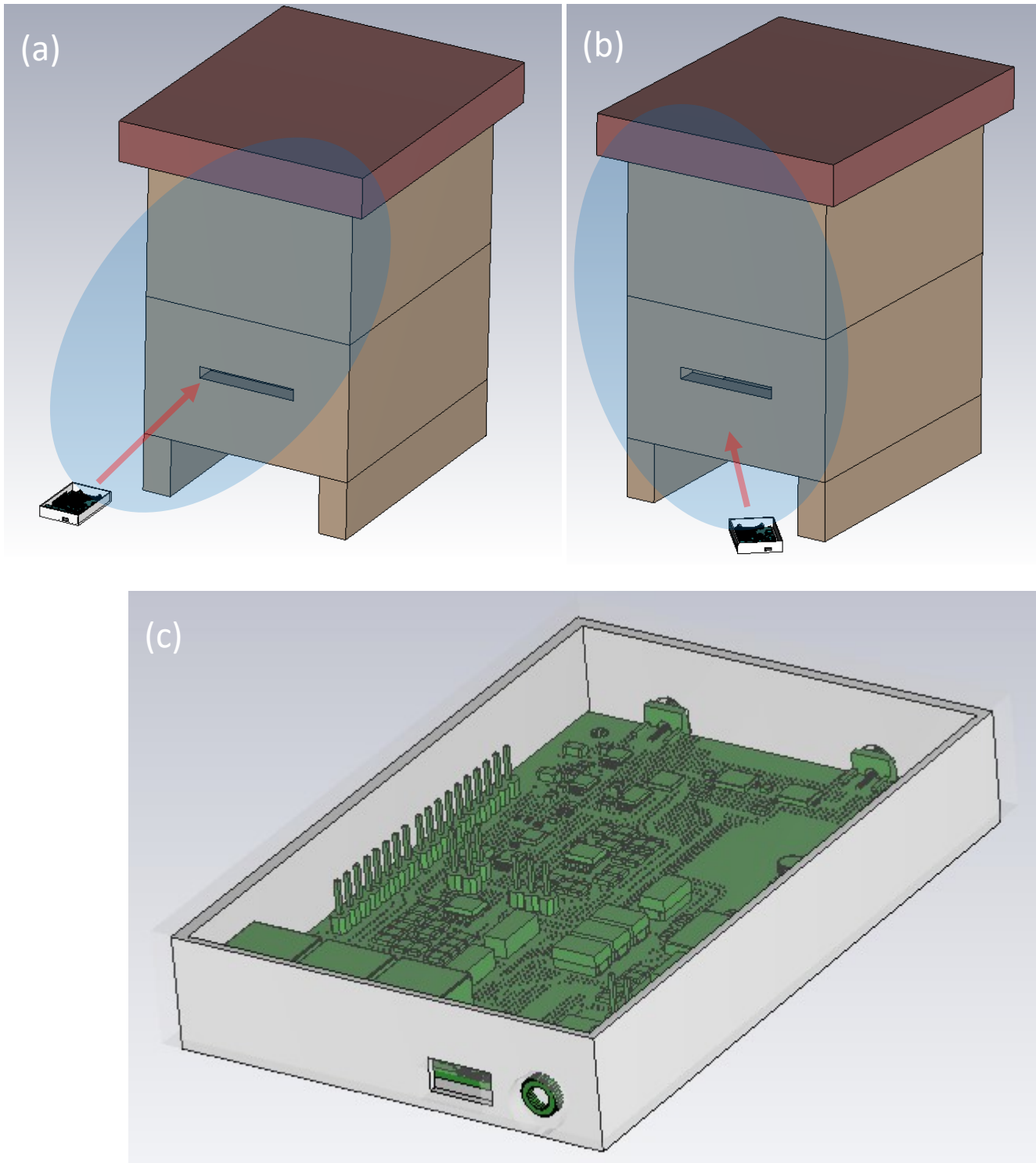
Figure 5.6: Importance of radar placement modelled in CST Microwave Studio (a) radar placed perpendicular towards hive entrance (b) Radar placed with a slight angle and at a closer distance (c) Closer up image of the V3 I/Q Radar placed in an enclosure.

REFERENCES

[1]   F. Sánchez-Bayo and K. A. G. Wyckhuys, "Worldwide decline of the entomofauna: A review of its drivers," *Biol. Conserv.*, vol. 232, no. January, pp. 8–27, 2019, doi: 10.1016/j.biocon.2019.01.020.

[2]   D. E. Chamberlain and R. J. Fuller, "Local extinctions and changes in species richness of lowland farmland birds in England and Wales in relation to recent changes in agricultural land-use," *Agric. Ecosyst. Environ.*, vol. 78, no. 1, pp. 1–17, 2000, doi: 10.1016/S0167-8809(99)00105-X.

[3]   C. A. Hallmann *et al.*, "More than 75 percent decline over 27 years in total flying insect biomass in protected areas," *PLoS One*, vol. 12, no. 10, 2017, doi: 10.1371/journal.pone.0185809.

[4]   J. Ollerton, R. Winfree, and S. Tarrant, "How many flowering plants are pollinated by animals?," *Oikos*, vol. 120, no. 3, pp. 321–326, 2011, doi: 10.1111/j.1600-0706.2010.18644.x.

[5]   E. Öckinger and H. G. Smith, "Semi-natural grasslands as population sources for pollinating insects in agricultural landscapes," *J. Appl. Ecol.*, vol. 44, no. 1, pp. 50–59, 2007, doi: 10.1111/j.1365-2664.2006.01250.x.

[6]   D. H. Morse, "The Insectivorous Bird as an Adaptive Strategy," *Annu. Rev. Ecol. Syst.*, vol. 2, no. 1, pp. 177–200, 1971, doi: 10.1146/annurev.es.02.110171.001141.

[7]   L. H. Yang and C. Gratton, "Insects as drivers of ecosystem processes," *Curr. Opin. Insect Sci.*, vol. 2, pp. 26–32, 2014, doi: 10.1016/j.cois.2014.06.004.

[8]   J. Baude, M., Kunin, W. E., Boatman, N. D., Conyers, S., Davies, N., Gillespie, M. A. K., Morton, R. D., Smart, S. M., & Memmott, "Historical nectar assessment reveals the fall and rise of floral resources in Britain," *Nature*, vol. 530, no. 7588, pp. 85–88, 2016, doi: https://doi.org/10.1038/nature16532.

[9]   A. Newbold, T., Hudson, L. N., Hill, S. L. L., Contu, S., Lysenko, I., Senior, R. A., … Purvis, "Global effects of land use on local terrestrial biodiversity," *Nature*, vol. 520, no. 7545, pp. 45–50, 2015, doi: https://doi.org/10.1038/nature14324.

[10]   IPBES, *The assessment report of the Intergovernmental Science-Policy Platform on Biodiversity and Ecosystem Services on pollinators, pollination and food production. S.G. Potts, V. L. Imperatriz-Fonseca, and H. T. Ngo (eds).* 2016.

[11] H. S. Hines HM, "Bumble bee (Hymenoptera: Apidae) diversity and abundance in tallgrass prairie patches: effects of local and landscape floral resources," *Environ. Entomol.*, vol. 34, pp. 1477–84, 2005.

[12] N. M. Carvell C, Meek WR, Pywell RF, "The response of bumblebees to successional change in newly created arable field margins," *Biol. Conserv.*, vol. 118, no. 3, pp. 327–339, 2004, doi: https://doi.org/10.1016/j.biocon.2003.09.012.

[13] D. Goulson, G. C. Lye, and B. Darvill, "Decline and conservation of bumble bees," *Annu. Rev. Entomol.*, vol. 53, pp. 191–208, 2008, doi: 10.1146/annurev.ento.53.103106.093454.

[14] C. S. Osborne JL, "Managing habitats for pollinators in farmland," *Asp. Appl. Biol.*, no. 40, pp. 207–215, 1994.

[15] L. P. Suchail, S., Guez, D. & Belzunces, "Characteristics of imidacloprid toxicity in two Apis mellifera subspecies," *Environ. Toxicol. Chem.*, no. 19, pp. 1901–1905, 2000.

[16] T. W. Trusts, "Bad news for bees: Government reverses ban on bee-killing neonicotinoids," 2021. https://www.wildlifetrusts.org/news/bad-news-bees-government-reverses-ban-bee-killing-neonicotinoids (accessed Oct. 15, 2022).

[17] D. Goulson, "An overview of the environmental risks posed by neonicotinoid insecticides," *J. Appl. Ecol.*, vol. 50, no. 4, pp. 977–987, 2013, doi: 10.1111/1365-2664.12111.

[18] A. Jeschke, P., Nauen, R., Schindler, M. & Elbert, "Overview of the status and global strategy for neonicotinoids," *J. Agric. Food Chem.*, no. 59, pp. 2897–2908, 2011.

[19] P. Pollack, *Fine Chemicals: The Industry and the Business*. New Jersey: John Wiley & Sons, Inc, 2011.

[20] M. Tapparo, A., Marton, D., Giorio, C., Zanella, A., Solda, L., Marzaro and E. Al., "Assessment of the environmental exposure of honeybees to particulate matter containing neonicotinoid insecticides coming from corn coated seeds," *Environ. Sci. Technol.*, no. 46, pp. 2592–2599, 2012, doi: doi: 10.1021/es2035152.

[21] M. Marzaro, M., Vivan, L., Targa, A., Mazzon, L., Mori, N., Greatti and E. Al., "Lethal aerial powdering of honey bees with neonicotinoids from fragments of maize seed coat," *Bull. Insectology*, no. 64, pp. 119–126, 2011.

[22] D. Lye, G.C., Jennings, S.N., Osborne, J.L. & Goulson, "Impacts of the use of nonnative

commercial bumble bees for pollinator supplementation in raspberry," *J. Econ. Entomol.*, no. 104, pp. 107–114, 2011.

[23] H. C. Yang, E.C., Chuang, Y.C., Chen, Y.W. & Chang, "Abnormal foraging behavior induced by sublethal dosage of imidacloprid in the honey bee (Hymenoptera: Apidae).," *J. Econ. Entomol.*, no. 101, pp. 1743–1748, 2008.

[24] N. Han, P., Niu, C.Y., Lei, C.L., Cui, J.J. & Desneux, "Quantification of toxins in a Cry1Ac+CpTI cotton cultivar and its potential effects on the honey bee Apis mellifera L," *Ecotoxicology*, no. 19, pp. 1612–1619, 2010.

[25] G. & S. Mommaerts, V., Reynders, S., Boulet, J., Besard, L., Sterk and G., "Risk assessment for side-effects of neonicotinoids against bumblebees with and without impairing foraging behaviour," *Ecotoxicology*, no. 19, pp. 207–215, 2010.

[26] P. et al. Henry, M., Beguin, M., Requier, F., Rollin, O., Odoux, J.-F., Aupinel, "A common pesticide decreases foraging success and survival in honeybees.," *Science (80-.).*, no. 336, pp. 350–351, 2012.

[27] J. Fischer, T. Müller, A. K. Spatz, U. Greggers, B. Grünewald, and R. Menzel, "Neonicotinoids interfere with specific components of navigation in honeybees," *PLoS One*, vol. 9, no. 3, pp. 1–10, 2014, doi: 10.1371/journal.pone.0091364.

[28] P. & Moritz, R.F.A., de Miranda, J., Fries, I., Le Cont, Y., Neumann and R. J. Paxton, "Research strategies to improve honeybee health in Europe," *Apidologie*, no. 41, pp. 227–242, 2010.

[29] Department for Environment Food & Rural Affairs, "Statement on the decision to issue – with strict conditions – emergency authorisation to use a product containing a neonicotinoid to treat sugar beet seed in 2021," 2021. https://www.gov.uk/government/publications/neonicotinoid-product-as-seed-treatment-for-sugar-beet-emergency-authorisation-application/statement-on-the-decision-to-issue-with-strict-conditions-emergency-authorisation-to-use-a-product-containing-a-neonicoti (accessed Oct. 15, 2022).

[30] J. E. Losey and M. Vaughan, "The economic value of ecological services provided by insects," *Bioscience*, vol. 56, no. 4, pp. 311–323, 2006, doi: 10.1641/0006-3568(2006)56[311:TEVOES]2.0.CO;2.

[31] IPBES and FAO, "The regional Report for Africa on Pollinators and Pollination and food production," pp. 1–49, 2016.

[32]   R. Portus, "An ecological whodunit: The story of colony collapse disorder," *Soc. Anim.*, pp. 1–19, 2020, doi: 10.1163/15685306-BJA10026.

[33]   A. D. Barnosky *et al.*, "Has the Earth's sixth mass extinction already arrived?," *Nature*, vol. 471, no. 7336, pp. 51–57, 2011, doi: 10.1038/nature09678.

[34]   A. M. Klein *et al.*, "Importance of pollinators in changing landscapes for world crops," *Proc. R. Soc. B Biol. Sci.*, vol. 274, no. 1608, pp. 303–313, 2007, doi: 10.1098/rspb.2006.3721.

[35]   N. Carreck and I. Williams, "The economic value of bees in the UK," *Bee World*, vol. 79, no. 3, pp. 115–123, 1998, doi: 10.1080/0005772X.1998.11099393.

[36]   M. H. Allsopp, W. J. de Lange, and R. Veldtman, "Valuing insect pollination services with cost of replacement," *PLoS One*, vol. 3, no. 9, 2008, doi: 10.1371/journal.pone.0003128.

[37]   J. Chisel, "Honey Bees Impact on the U.S. Economy," *Univ. Puget Sound Econ. Theses*, 2015, [Online]. Available: http://soundideas.pugetsound.edu/economics_theses/98.

[38]   POST, "Insect pollination POST note," *Parliam. Off. Sci. Technol.*, no. 348, pp. 1–4, 2010.

[39]   T. D. Breeze, A. P. Bailey, K. G. Balcombe, and S. G. Potts, "Pollination services in the UK: How important are honeybees?," *Agric. Ecosyst. Environ.*, vol. 142, no. 3–4, pp. 137–143, 2011, doi: 10.1016/j.agee.2011.03.020.

[40]   C. Press and C. Press, "Bumblebees : Their Behaviour and Ecology . By Dave Goulson . Bumblebees : Their Behaviour and Ecology by Dave Goulson Review by : Reviewed by Kristina Niovi Jones The Quarterly Review of Biology , Vol . 79 , No . 3 (September 2004), p . 315 Published by," vol. 79, no. 3, 2014.

[41]   J. Memmott, N. M. Waser, and M. V. Price, "Tolerance of pollination networks to species extinctions," *Proc. R. Soc. B Biol. Sci.*, vol. 271, no. 1557, pp. 2605–2611, 2004, doi: 10.1098/rspb.2004.2909.

[42]   D. F. M. Keith S. Delaplane, *Crop Pollination By Bees*. New York: CABI Publishing, 2000.

[43]   D. Goulson, E. Nicholls, C. Botías, and E. L. Rotheray, "Bee declines driven by combined Stress from parasites, pesticides, and lack of flowers," *Science (80-.).*, vol. 347, no. 6229, pp. 1–16, 2015, doi: 10.1126/science.1255957.

[44] F. Sánchez-Bayo, D. Goulson, F. Pennacchio, F. Nazzi, K. Goka, and N. Desneux, "Are bee diseases linked to pesticides? - A brief review," *Environ. Int.*, vol. 89–90, pp. 7–11, 2016, doi: 10.1016/j.envint.2016.01.009.

[45] R. Underwood and D. VanEngelsdorp, "Colony Collapse Disorder: Have We Seen This Before?," *Bee Cult.*, no. May, pp. 13–18, 2007.

[46] D. E. Chamberlain, R. J. Fuller, R. G. H. Bunce, J. C. Duckworth, and M. Shrubb, "Changes in the abundance of farmland birds in relation to the timing of agricultural intensification in England and Wales," *J. Appl. Ecol.*, vol. 37, no. 5, pp. 771–788, 2000, doi: 10.1046/j.1365-2664.2000.00548.x.

[47] J. C. Grixti, L. T. Wong, S. A. Cameron, and C. Favret, "Decline of bumble bees (Bombus) in the North American Midwest," *Biol. Conserv.*, vol. 142, no. 1, pp. 75–84, 2009, doi: 10.1016/j.biocon.2008.09.027.

[48] W. K. Chemnitz Christine and Rehmer Christian, "Insect Atlas 2020 – Facts and figures about friends and foes in farming," pp. 10–11, 2020.

[49] T. N. G. for the Netherlands, "Agricultural subsidies," 2021. https://www.rijksoverheid.nl/onderwerpen/landbouw-en-tuinbouw/landbouwsubsidies (accessed Aug. 18, 2021).

[50] N. Dudley and S. Alexander, "Agriculture and biodiversity: a review," *Biodiversity*, vol. 18, no. 2–3, pp. 45–49, 2017, doi: 10.1080/14888386.2017.1351892.

[51] H. Goulet and L. Masner, "Impact of herbicides on the insect and spider diversity in eastern Canada," *Biodiversity*, vol. 18, no. 2–3, pp. 50–57, 2017, doi: 10.1080/14888386.2017.1351398.

[52] C. Vidau *et al.*, "Exposure to sublethal doses of fipronil and thiacloprid highly increases mortality of honeybees previously infected by nosema ceranae," *PLoS One*, vol. 6, no. 6, 2011, doi: 10.1371/journal.pone.0021550.

[53] M. Alburaki, S. Boutin, P. L. Mercier, Y. Loublier, M. Chagnon, and N. Derome, "Neonicotinoid-coated Zea mays seeds indirectly affect honeybee performance and pathogen susceptibility in field trials," *PLoS One*, vol. 10, no. 5, pp. 1–20, 2015, doi: 10.1371/journal.pone.0125790.

[54] M. Alburaki *et al.*, "Honey bee survival and pathogen prevalence: from the perspective of landscape and exposure to pesticides," *Insects*, vol. 9, no. 2, pp. 1–15,

2018, doi: 10.3390/insects9020065.

[55] L. Tison *et al.*, "Honey Bees' Behavior is Impaired by Chronic Exposure to the Neonicotinoid Thiacloprid in the Field," *Environ. Sci. Technol.*, vol. 50, no. 13, pp. 7218–7227, 2016, doi: 10.1021/acs.est.6b02658.

[56] G. Kairo *et al.*, "Nosema ceranae, Fipronil and their combination compromise honey bee reproduction via changes in male physiology," *Sci. Rep.*, vol. 7, no. 1, pp. 1–14, 2017, doi: 10.1038/s41598-017-08380-5.

[57] J. S. Pettis, N. Rice, K. Joselow, D. Van Engelsdorp, and V. Chaimanee, "Colony failure linked to low sperm viability in honey bee (Apis mellifera) queens and an exploration of potential causative factors," *PLoS One*, vol. 11, no. 2, pp. 1–10, 2016, doi: 10.1371/journal.pone.0147220.

[58] J. W. Lee, H. Kwon, and B. Lee, "Design consideration of UHF RFID tag for increased reading range," *IEEE MTT-S Int. Microw. Symp. Dig.*, pp. 1588–1591, 2006, doi: 10.1109/MWSYM.2006.249638.

[59] K. Finkenzeller, *RFID Handbook*, Third Edit. Wiley, 2010.

[60] J. Landt, "The history of RFID," *IEEE Potentials*, vol. 24, no. 4, pp. 8–11, 2005, doi: 10.1109/MP.2005.1549751.

[61] S. Streit, F. Bock, C. W. W. Pirk, and J. Tautz, "Automatic life-long monitoring of individual insect behaviour now possible," *Zoology*, vol. 106, no. 2003, pp. 169–171, 2006, doi: 10.1078/0944-2006-00113.

[62] M. Donelli and M. Manekiya, "Development of environmental long range RFID sensors based on the modulated scattering technique," *Electron.*, vol. 7, no. 7, 2018, doi: 10.3390/electronics7070106.

[63] C. W. Schneider, J. Tautz, B. Grünewald, and S. Fuchs, "RFID tracking of sublethal effects of two neonicotinoid insecticides on the foraging behavior of Apis mellifera," *PLoS One*, vol. 7, no. 1, pp. 1–9, 2012, doi: 10.1371/journal.pone.0030023.

[64] L. Hou, M. Verdirame, and K. C. Welch, "Automated tracking of wild hummingbird mass and energetics over multiple time scales using radio frequency identification (RFID) technology," *J. Avian Biol.*, vol. 46, no. 1, pp. 1–8, 2015, doi: 10.1111/jav.00478.

[65] G. B. Zydlewski, G. Horton, T. Dubreuil, B. Letcher, S. Casey, and J. Zydlewski, "Remote

monitoring of fish in small streams: A unified approach using PIT tags," *Fisheries*, vol. 31, no. 10, pp. 492–502, 2006, doi: 10.1577/1548-8446(2006)31[492:RMOFIS]2.0.CO;2.

[66]   S. Sumner, E. Lucas, J. Barker, and N. Isaac, "Radio-Tagging Technology Reveals Extreme Nest-Drifting Behavior in a Eusocial Insect," *Curr. Biol.*, vol. 17, no. 2, pp. 140–145, 2007, doi: 10.1016/j.cub.2006.11.064.

[67]   E. J. H. Robinson, T. O. Richardson, A. B. Sendova-Franks, O. Feinerman, and N. R. Franks, "Radio tagging reveals the roles of corpulence, experience and social information in ant decision making," *Behav. Ecol. Sociobiol.*, vol. 63, no. 5, pp. 627–636, 2009, doi: 10.1007/s00265-008-0696-z.

[68]   P. de Souza *et al.*, "Low-cost electronic tagging system for bee monitoring," *Sensors (Switzerland)*, vol. 18, no. 7, pp. 1–21, 2018, doi: 10.3390/s18072124.

[69]   C. D. LeMunyan, W. White, E. Nyberg, and J. J. Christian, "Design of a Miniature Radio Transmitter for Use in Animal Studies," *J. Wildl. Manage.*, vol. 23, no. 1, p. 107, 1959, doi: 10.2307/3797755.

[70]   "© 1964 Nature Publishing Group," *Galapagos Tortoise Mar. Iguana Deep Body Temp. Meas. by Radio Telem. , 204(4956), 355–358. doi10.1038/204355a0*, 1964.

[71]   W. Daniel Kissling, D. E. Pattemore, and M. Hagen, "Challenges and prospects in the telemetry of insects," *Biol. Rev.*, vol. 89, no. 3, pp. 511–530, 2014, doi: 10.1111/brv.12065.

[72]   J. Růžičková, "Radio telemetry of ground beetles : Habitat use and movement activity of Carabus ullrichii," Palacký University Olomouc, 2018.

[73]   M. Liégeois, P. Tixier, and L. Beaudoin-Ollivier, "Use of Radio Telemetry for Studying Flight Movements of Paysandisia archon (Lepidoptera: Castniidae)," *J. Insect Behav.*, vol. 29, no. 2, pp. 199–213, 2016, doi: 10.1007/s10905-016-9554-4.

[74]   M. Wikelski, D. Moskowitz, J. S. Adelman, J. Cochran, D. S. Wilcove, and M. L. May, "Simple rules guide dragonfly migration," *Biol. Lett.*, vol. 2, no. 3, pp. 325–329, 2006, doi: 10.1098/rsbl.2006.0487.

[75]   S. Levett and S. Walls, "Tracking the elusive life of the Emperor Dagonfly Anax imperator Leach," *J. Br. Dragonfly Soc.*, vol. 27, no. 1, pp. 59–68, 2011.

[76]   D. Moskowitz and M. May, "Adult tiger spiketail (Cordulegaster erronea Hagen)

habitat use and home range observed via radio-telemetry with conservation recommendations," *J. Insect Conserv.*, vol. 21, no. 5–6, pp. 885–895, 2017, doi: 10.1007/s10841-017-0027-7.

[77] P. D. Lorch and D. T. Gwynne, "Radio-telemetric evidence of migration in the gregarious but not the solitary morph of the Mormon cricket (Anabrus simplex: Orthoptera: Tettigoniidae)," *Naturwissenschaften*, vol. 87, no. 8, pp. 370–372, 2000, doi: 10.1007/s001140050743.

[78] C. Watts and D. Thornburrow, "Habitat use, behavior and movement patterns of a threatened New Zealand Giant Weta, deinacrida heteracantha (anostostomatidae: Orthoptera)," *J. Orthoptera Res.*, vol. 20, no. 1, pp. 127–135, 2011, doi: 10.1665/034.020.0112.

[79] M. Tini *et al.*, "A stag beetle's life: sex-related differences in daily activity and behaviour of Lucanus cervus (Coleoptera: Lucanidae)," *J. Insect Conserv.*, vol. 21, no. 5–6, pp. 897–906, 2017, doi: 10.1007/s10841-017-0029-5.

[80] L. Drag and L. Cizek, "Radio-Tracking Suggests High Dispersal Ability of the Great Capricorn Beetle (Cerambyx cerdo)," *J. Insect Behav.*, vol. 31, no. 2, pp. 138–143, 2018, doi: 10.1007/s10905-018-9669-x.

[81] R. S. Pasquet *et al.*, "Long-distance pollen flow assessment through evaluation of pollinator foraging range suggests transgene escape distances," *Proc. Natl. Acad. Sci. U. S. A.*, vol. 105, no. 36, pp. 13456–13461, 2008, doi: 10.1073/pnas.0806040105.

[82] M. Hagen, M. Wikelski, and W. D. Kissling, "Space use of bumblebees (Bombus spp.) revealed by radio-tracking," *PLoS One*, vol. 6, no. 5, 2011, doi: 10.1371/journal.pone.0019997.

[83] P. J. Kennedy, S. M. Ford, J. Poidatz, D. Thiéry, and J. L. Osborne, "Searching for nests of the invasive Asian hornet (Vespa velutina) using radio-telemetry," *Commun. Biol.*, vol. 1, no. 1, 2018, doi: 10.1038/s42003-018-0092-9.

[84] M. Wikelski *et al.*, "Large-range movements of neotropical orchid bees observed via radio telemetry," *PLoS ONE*, vol. 5, no. 5. 2010, doi: 10.1371/journal.pone.0010738.

[85] J. Poidatz, K. Monceau, O. Bonnard, and D. Thiéry, "Activity rhythm and action range of workers of the invasive hornet predator of honeybees Vespa velutina, measured by radio frequency identification tags," *Ecol. Evol.*, vol. 8, no. 15, pp. 7588–7598, 2018, doi: 10.1002/ece3.4182.

[86]   ATS, "ATS Avian." https://atstrack.com/tracking-products/transmitters/product-transmitters.aspx?serie=A2405#close (accessed Aug. 28, 2021).

[87]   LOtek, "Lotek Nanopin." https://www.lotek.com/products/nanopin/ (accessed Aug. 28, 2021).

[88]   G. Contracts, "US government contracts," 2020. https://www.governmentcontracts.us/government-contracts/opportunity-details/NBD00159445434800013.htm?searchText=GPS (accessed Aug. 28, 2021).

[89]   S. C. Chang, F. M. Yaul, F. O. Sullivan, D. M. Otten, J. H. Lang, and E. Initiative, "Harvesting Energy from moth vibrations during flight," *Int. Work. Micro Nanotechnologies Power Gener. Energy Convers. Appl.*, pp. 3–6, 2009.

[90]   T. Reissman, R. B. MacCurdy, and E. Garcia, "Electrical power generation from insect flight," *Act. Passiv. Smart Struct. Integr. Syst. 2011*, vol. 7977, p. 797702, 2011, doi: 10.1117/12.880702.

[91]   J. Shearwood *et al.*, "C-Band Telemetry of Insect Pollinators Using a Miniature Transmitter and a Self-Piloted Drone," *IEEE Trans. Microw. Theory Tech.*, vol. 69, no. 1, pp. 938–946, 2021, doi: 10.1109/TMTT.2020.3034323.

[92]   J. R. Riley and A. D. Smith, "Design considerations for an harmonic radar to investigate the flight of insects at low altitude," *Comput. Electron. Agric.*, vol. 35, no. 2–3, pp. 151–169, 2002, doi: 10.1016/S0168-1699(02)00016-9.

[93]   J. R. Riley *et al.*, "Tracking bees with harmonic radar," *Nature*, vol. 379, no. 6560. pp. 29–30, 1996, doi: 10.1038/379029b0.

[94]   M. E. O'Neal, D. A. Landis, E. Rothwell, L. Kempel, and D. Reinhard, "Tracking insects with harmonic radar: A case study," *Am. Entomol.*, vol. 50, no. 4, pp. 212–218, 2004, doi: 10.1093/ae/50.4.212.

[95]   D. MASCANZONI and H. WALLIN, "The harmonic radar: a new method of tracing insects in the field," *Ecol. Entomol.*, vol. 11, no. 4, pp. 387–390, 1986, doi: 10.1111/j.1365-2311.1986.tb00317.x.

[96]   J. L. Woodgate, J. C. Makinson, K. S. Lim, A. M. Reynolds, and L. Chittka, "Life-long radar tracking of bumblebees," *PLoS One*, vol. 11, no. 8, pp. 1–22, 2016, doi: 10.1371/journal.pone.0160333.

[97]   J. L. Woodgate *et al.*, "Harmonic radar tracking reveals that honeybee drones navigate

between multiple aerial leks," *iScience*, vol. 24, no. 6, p. 102499, 2021, doi: 10.1016/j.isci.2021.102499.

[98]   J. C. Makinson, J. L. Woodgate, A. Reynolds, E. A. Capaldi, C. J. Perry, and L. Chittka, "Harmonic radar tracking reveals random dispersal pattern of bumblebee (Bombus terrestris) queens after hibernation," *Sci. Rep.*, vol. 9, no. 1, pp. 1–11, 2019, doi: 10.1038/s41598-019-40355-6.

[99]   J. S. Brebner *et al.*, "Bumble bees strategically use ground level linear features in navigation," *Anim. Behav.*, vol. 179, no. September, pp. 147–160, 2021, doi: 10.1016/j.anbehav.2021.07.003.

[100] M. Beekman and F. L. W. Ratnieks, "Long-range foraging by the honey-bee, Apis mellifera L.," *Funct. Ecol.*, vol. 14, no. 4, pp. 490–496, 2000, doi: 10.1046/j.1365-2435.2000.00443.x.

[101] J. M. Mola and N. M. Williams, "A review of methods for the study of bumble bee movement," *Apidologie*, vol. 50, no. 4, pp. 497–514, 2019, doi: 10.1007/s13592-019-00662-3.

[102] Bernd Hein, *Bumblebee Economics*. Harvard University Press, 2004.

[103] G. Dubois and V. Vignon, "First results of radio-tracking of Osmoderma eremita (Coleoptera: Cetoniidae) in French chestnut orchards," *Rev. d'Ecologie (La Terre la Vie)*, vol. 63, no. SUPPL. 10, pp. 131–138, 2008.

[104] E. Drinkwater, E. J. H. Robinson, and A. G. Hart, "Keeping invertebrate research ethical in a landscape of shifting public opinion," *Methods Ecol. Evol.*, vol. 10, no. 8, pp. 1265–1273, 2019, doi: 10.1111/2041-210X.13208.

[105] E. Feuerbacher, J. H. Fewell, S. P. Roberts, E. F. Smith, and J. F. Harrison, "Effects of load type (pollen or nectar) and load mass on hovering metabolic rate and mechanical power output in the honey bee Apis mellifera," *J. Exp. Biol.*, vol. 206, no. 11, pp. 1855–1865, 2003, doi: 10.1242/jeb.00347.

[106] J. Kim, M. Jung, H. G. Kim, and D. H. Lee, "Potential of harmonic radar system for use on five economically important insects: Radar tag attachment on insects and its impact on flight capacity," *J. Asia. Pac. Entomol.*, vol. 19, no. 2, pp. 371–375, 2016, doi: 10.1016/j.aspen.2016.03.013.

[107] F. Batsleer *et al.*, "The neglected impact of tracking devices on terrestrial

arthropods," *Methods Ecol. Evol.*, vol. 11, no. 3, pp. 350–361, 2020, doi: 10.1111/2041-210X.13356.

[108] L. Roquer-Beni *et al.*, "A novel method to measure hairiness in bees and other insect pollinators," *Ecol. Evol.*, vol. 10, no. 6, pp. 2979–2990, 2020, doi: 10.1002/ece3.6112.

[109] Bernd Heinrich, *The Hot-Blooded Insects*. Springer International Publishing, 1993.

[110] B. Bruderer, "The study of bird migration by radar. Part 2: Major achievements," *Naturwissenschaften*, vol. 84, no. 2, pp. 45–54, 1997, doi: 10.1007/s001140050348.

[111] W. Develop-, "Bird Detection by Radar America . Indeed , with the introduction of higher-powered Bvss , Bird Detectio • by Radar tJuly," vol. 63, 1946.

[112] V. Drake and D. Reynolds, *Radar Entomology*. Wallingford Oxfordshire UK: CABI Publishing, 2012.

[113] A. Crawford, "Radar reflections in the lower atmosphere," *Proc. Inst. Radio Eng.*, pp. 404–405, 1949.

[114] R. C. Rainey, "observation of desert locust swarm using radar.pdf," *Nature*, pp. 77–77, 1955.

[115] M. Raghu, "A Study to Explore the Effects of Sound Vibrations on Consciousness," *Int. J. Soc. Work Hum. Serv. Pract.*, vol. 6, pp. 75–88, 2018.

[116] H. M. Aumann and N. W. Emanetoglu, "The radar microphone: A new way of monitoring honey bee sounds," *Proc. IEEE Sensors*, no. 2, pp. 2–3, 2017, doi: 10.1109/ICSENS.2016.7808865.

[117] H. Aumann, B. Payal, N. W. Emanetoglu, and F. Drummond, "An index for assessing the foraging activities of honeybees with a Doppler sensor," *SAS 2017 - 2017 IEEE Sensors Appl. Symp. Proc.*, pp. 7–11, 2017, doi: 10.1109/SAS.2017.7894090.

[118] A. Hajovsky, R.; Deam, A.; LaGrone, "Radar reflections from insects in the lower atmosphere.," *IEEE Trans. Antennas Propag.*, vol. 14, no. (2), pp. 224–227, 1966, doi: doi:10.1109/tap.1966.1138665.

[119] W. W. Wolf, C. R. Vaughn, R. Harris, and G. M. Loper, "Insect Radar Cross-sections for Aerial Density Measurements and Target Classification," *Am. Soc. Agric. Biol. Eng.*, vol. 36, no. June, pp. 949–954, 1993, doi: doi: 10.13031/2013.28420.

[120] H. M. Aumann, "A technique for measuring the RCS of free-flying honeybees with a

24 GHz CW Doppler radar," *IET Conf. Publ.*, vol. 2018, no. CP741, 2018, doi: 10.1049/cp.2018.0540.

[121] J. R. Riley, D. R. Reynolds, and R. A. Farrow, "The migration of Nilaparvata lugens (stål) (delphacidae) and other hemiptera associated with rice during the dry season in the Philippines: A study using radar, visual observations, aerial netting and ground trapping," *Bull. Entomol. Res.*, vol. 77, no. 1, pp. 145–169, 1987, doi: 10.1017/S0007485300011627.

[122] W. Schaefer, G, "Radar observations of insect flight," *Insect Flight Symp. R. Entomol. Soc.*, vol. 7, pp. 157–197, 1976.

[123] L. A. Lewis and S. S. Schneider, "The modulation of worker behavior by the vibration signal during house hunting in swarms of the honeybee, Apis mellifera," *Behav. Ecol. Sociobiol.*, vol. 48, no. 2, pp. 154–164, 2000, doi: 10.1007/s002650000225.

[124] A. Michelsen, W. H. Kirchner, and M. Lindauer, "Sound and vibrational signals in the dance language of the honeybee, Apis mellifera," *Behav. Ecol. Sociobiol.*, vol. 18, no. 3, pp. 207–212, 1986, doi: 10.1007/BF00290824.

[125] M. T. Ramsey *et al.*, "The prediction of swarming in honeybee colonies using vibrational spectra," *Sci. Rep.*, vol. 10, no. 1, pp. 1–17, 2020, doi: 10.1038/s41598-020-66115-5.

[126] M. Ramsey, M. Bencsik, and M. I. Newton, "Long-term trends in the honeybee whooping signal' revealed by automated detection," *PLoS One*, vol. 12, no. 2, pp. 1–22, 2017, doi: 10.1371/journal.pone.0171162.

[127] M. Ramsey, M. Bencsik, and M. I. Newton, "Extensive Vibrational Characterisation and Long-Term Monitoring of Honeybee Dorso-Ventral Abdominal Vibration signals," *Sci. Rep.*, vol. 8, no. 1, pp. 1–17, 2018, doi: 10.1038/s41598-018-32931-z.

[128] H. M. Aumann, M. K. Aumann, and N. W. Emanetoglu, "Janus: A combined radar and vibration sensor for beehive monitoring," *IEEE Sensors Lett.*, vol. 5, no. 3, pp. 5–8, 2021, doi: 10.1109/LSENS.2021.3056870.

[129] S. Ferrari, M. Silva, M. Guarino, and D. Berckmans, "Monitoring of swarming sounds in bee hives for early detection of the swarming period," *Comput. Electron. Agric.*, vol. 64, no. 1, pp. 72–77, 2008, doi: 10.1016/j.compag.2008.05.010.

[130] J. D. Villa, "Swarming behavior of honey bees (Hymenoptera: Apidae) in southeastern

Louisiana," *Ann. Entomol. Soc. Am.*, vol. 97, no. 1, pp. 111–116, 2004, doi: 10.1603/0013-8746(2004)097[0111:SBOHBH]2.0.CO;2.

[131] A. Avitabile, R. A. Morse, and R. Boch, "Swarming Honey Bees Guided by Pheromones1," *Ann. Entomol. Soc. Am.*, vol. 68, no. 6, pp. 1079–1082, 1975, doi: 10.1093/aesa/68.6.1079.

[132] A. Thielens, D. Bell, D. B. Mortimore, M. K. Greco, L. Martens, and W. Joseph, "Exposure of insects to radio-frequency electromagnetic fields from 2 to 120 GHz," *Sci. Rep.*, vol. 8, no. 1, pp. 1–10, 2018, doi: 10.1038/s41598-018-22271-3.

[133] K. Darney *et al.*, "Effect of high-frequency radiations on survival of the honeybee (Apis mellifera L.)," *Apidologie*, vol. 47, no. 5, pp. 703–710, 2016, doi: 10.1007/s13592-015-0421-7.

[134] M. A. Baars, "International Association for Ecology Patterns of Movement of Radioactive Carabid Beetles," *Oecologia*, vol. 44, no. 1, pp. 125–140, 1979.

[135] A. Zacepins and E. Stalidzans, "Information processing for remote recognition of the state of bee colonies and apiaries in precision beekeeping (apiculture)," *Biosyst. Inf. Technol.*, vol. 2, no. 1, pp. 6–10, 2013, doi: 10.11592/bit.130502.

[136] H. Human *et al.*, "Miscellaneous standard methods for Apis mellifera research," *J. Apic. Res.*, vol. 52, no. 4, 2013, doi: 10.3896/IBRA.1.52.4.10.

[137] A. Terenzi, S. Cecchi, S. Spinsante, S. Orcioni, and F. Piazza, "Real-Time System Implementation for Bee Hives Weight Measurement," *2019 IEEE Int. Work. Metrol. Agric. For. MetroAgriFor 2019 - Proc.*, vol. 2, no. 1, pp. 231–236, 2019, doi: 10.1109/MetroAgriFor.2019.8909252.

[138] D. Heise, Z. Miller, E. Harrison, A. Gradisek, J. Grad, and C. Galen, "Acoustically Tracking the Comings and Goings of Bumblebees," *SAS 2019 - 2019 IEEE Sensors Appl. Symp. Conf. Proc.*, pp. 1–6, 2019, doi: 10.1109/SAS.2019.8705973.

[139] J. A. Shaw *et al.*, "Polarization lidar measurements of honey bees in flight for locating land mines," *Opt. Express*, vol. 13, no. 15, p. 5853, 2005, doi: 10.1364/opex.13.005853.

[140] L. McKendrick *et al.*, "Microsatellite analysis supports the existence of three cryptic species within the bumble bee Bombus lucorum sensu lato," *Conserv. Genet.*, vol. 18, no. 3, pp. 573–584, 2017, doi: 10.1007/s10592-017-0965-3.

[141] J. R. Hagler and C. G. Jackson, "Methods for marking insects: Current techniques and future prospects," *Annu. Rev. Entomol.*, vol. 46, pp. 511–543, 2001, doi: 10.1146/annurev.ento.46.1.511.

[142] R. W. and C. K. Sarah S. Greenleaf, Neal M. Williams, "Bee Foraging range and body size," *Oecologia*, vol. 153, no. 4, pp. 589–596, 2007, doi: 10.1007/s00442-007.

[143] E. C. G. Pyke and H. Pulliam, "OPTIMAL FORAGING: A SELECTIVE REVIEW OF THEORY AND TESTS," *Q. Rev. Biol*, vol. 52, no. 2, pp. 137–154, 1977.

[144] D. G. and J. C. Stout, "Homing ability of the bumblebee Bombus terrestris (Hymenoptera: Apidae)," *J. Exp. Biol*, vol. 202, no. 12, pp. 1655–1666, 1999.

[145] E. F. Knott, J. F. Shaeffer, and M. T. Tuley, *Radar Cross Section*, Second Edi. Raleigh: SciTech Pub., 2004.

[146] M. I. Skolnik, "Introduction to Radar Systems: Merrill I. Skolnik," *Mc Grow-Hill*. 1980.

[147] S. K. Ueng and F. S. Yang, "Visual computing for scattered electromagnetic fields," *Lect. Notes Comput. Sci. (including Subser. Lect. Notes Artif. Intell. Lect. Notes Bioinformatics)*, vol. 5876 LNCS, no. PART 2, pp. 899–908, 2009, doi: 10.1007/978-3-642-10520-3_86.

[148] J. R. Riley, "A millimetric radar to study the flight of small insects," *Electron. Commun. Eng. J.*, vol. 4, no. 1, pp. 43–48, 1992, doi: 10.1049/ecej:19920011.

[149] J. R. Riley, "ANGULAR AND TEMPORAL VARIATIONS IN THE RADAR CROSS-SECTIONS OF INSECTS," *Proc. IEEE*, vol. 120, no. July, pp. 1229–1232, 1973.

[150] J. R. Riley, "Radar Cross Section of Insects," *Proc. IEEE*, vol. 73, no. 2, pp. 228–232, 1985, doi: 10.1109/PROC.1985.13135.

[151] M. I. Skolnik, *Radar Handbook*, Second Edi., vol. 53. McGraw-Hill, 1990.

[152] E. C. R. Vaughn, W. Wolf, and W. Klassen, "Quantitative analysis of radar returns from insects," *Radar, lnsect Popul. Ecol. Pest Manag.*, vol. NASA Pub, no. 2070, pp. 131–158, 1979.

[153] V. A. Drake, "Target density estimation in radar biology," *J. Theor. Biol.*, vol. 90, pp. 545–571, 1981.

[154] S. Nambari, G. Sasibhushana Rao, and K. S. Ranga Rao, "Estimation of RCS for a perfectly conducting and plasma spheres," *Lect. Notes Electr. Eng.*, vol. 372, no. June

2018, pp. 437–447, 2016, doi: 10.1007/978-81-322-2728-1_40.

[155] S. R. B. and L. J. B. Benjamin Morris Herman, *Tables of the radar cross sections of water spheres*, vol. Rep. 9. Tucson: Institute of Atmospheric Physics, 1961.

[156] N. A. W. Centre, *Electronic warfare and radar systems engineering handbook*. Pont Mugu, CA: Electronic Warfare Division, 1997.

[157] E. F. Knott, *Radar Cross Section Measurements*. New York: VAN NOSTRAND REINHOLD, 1993.

[158] D. W. Hess, "INTRODUCTION TO RCS MEASUREMENTS," *Meas. Tech.*, 2008.

[159] Y.-W. K. Hsueh-Jyh Li, *The Electrical Engineering Handbook*. San Diego: Elsevier Inc, 2005.

[160] M. A. Alves and M. C. Rezende, "Teaching Radar Cross Section Concepts To Undergraduates With a Simulation Software," *Conf. Eng. Technol. Educ.*, pp. 188–192, 2008.

[161] N. Levanon, "Radar," *Encyclopedia of Physical Science and Technology*. Elsevier, pp. 497–510, 2001.

[162] B. R. Mahafza, *Radar Systems Analysis and design using matlab*, Third Edit. New York: CRC Press, 2013.

[163] "Meteorological Applications - 2009 - Wood - Cloud-radar observations of insects in the UK convective boundary layer.pdf." .

[164] E. M. Ahmed, "Hydrogel: Preparation, characterization, and applications: A review," *J. Adv. Res.*, vol. 6, no. 2, pp. 105–121, 2015, doi: 10.1016/j.jare.2013.07.006.

[165] R. Wang *et al.*, "Insect-Equivalent Radar Cross-Section Model Based on Field Experimental Results of Body Length and Orientation Extraction," *Remote Sens.*, vol. 14, no. 3, p. 508, 2022, doi: 10.3390/rs14030508.

[166] F. I. Addison *et al.*, "Simulation of the Radar Cross Section of a Noctuid Moth," *Remote Sens.*, vol. 14, no. 6, p. 1494, 2022, doi: 10.3390/rs14061494.

[167] S. C. Pickard, R. D. Quinn, and N. S. Szczecinski, *Simulation of the arthropod central complex: Moving towards bioinspired robotic navigation control*, vol. 10928 LNAI, no. 1704366. Springer International Publishing, 2018.

[168] D. Mirkovic, P. M. Stepanian, C. E. Wainwright, D. R. Reynolds, and M. H. M. Menz,

"Characterizing animal anatomy and internal composition for electromagnetic modelling in radar entomology," *Remote Sens. Ecol. Conserv.*, vol. 5, no. 2, pp. 169–179, 2019, doi: 10.1002/rse2.94.

[169] "3D Bee model," 2023. https://open3dmodel.com/3d-models/3d-model-flying-bee-animal_135062.html.

[170] A. Thielens, M. K. Greco, L. Verloock, L. Martens, and W. Joseph, "Radio-Frequency Electromagnetic Field Exposure of Western Honey Bees," *Sci. Rep.*, vol. 10, no. 1, pp. 1–14, 2020, doi: 10.1038/s41598-019-56948-0.

[171] C. M. Reville WJ, "An evaluation of the usefulness of air-drying biological samples from tetramethylsilane in preparation for scanning electron microscopy," *J Electron Microsc*, vol. 40, no. 3, pp. 198–202, 1991.

[172] N. Aldabashi, "Work Function Tuning using Black Phosphorous, Graphene Oxide, and Conductive Graphene," Bangor University, 2018.

[173] K. A. Khan and T. Liu, "Morphological Structure and Distribution of Hairiness on Different Body Parts of Apis mellifera with an Implication on Pollination Biology and a Novel Method to Measure the Hair Length," *Insects*, vol. 13, no. 2, 2022, doi: 10.3390/insects13020189.

[174] R. Snodgrass, *Anatomy of the honey bee*. Muriwai Books, 2018.

[175] P. B. WHITE, "The pathology of Isle of Wight Disease in hive bees," *Trans. Roy. Soc. Edinb*, vol. 52, 1921.

[176] D. M. Pozar, *Microwave Engineering*, Fourth., vol. 1999, no. December. University of Massachusetts at Amherst: John Wiley & Sons, Inc, 2012.

[177] G. L. Charvat, *Small and Short-Range Radar Systems*. CRC Press, 2014.

[178] D. Schneider, "Coffee-can radar: How to build a synthetic aperture imaging system with tin cans and AA batteries.," *IEEE Spectr*, vol. 49, no. 11, pp. 24–25, 2012.

[179] J. Carroll, G. Paparisto, and D. Vye, "The 'coffee-can' radar redesigned as an inexpensive RF PCB [Application Notes]," *IEEE Microw. Mag.*, vol. 17, no. 10, pp. 62–74, 2016, doi: 10.1109/MMM.2016.2589201.

[180] A. Boric-Lubecke, Olga Droitcour, Amy D. Lubecke, Victor M. Park, Byung-Kwon Singh, *Doppler radar physiological sensing*. John Wiley & Sons, Inc, 2016.

[181] D. Maulik, *Doppler sonography: a brief history, in Doppler Ultrasound in Obstetrics and Gynecology*. Heidelberg: Springer, 2005.

[182] Ofcom, "IR 2030 – UK Interface Requirements 2030," no. April, p. 101, 2020.

[183] N. Aldabashi, S. Williams, A. Eltokhy, E. Palmer, P. Cross, and C. Palego, "Integration of 5.8GHz Doppler Radar and Machine Learning for Automated Honeybee Hive Surveillance and Logging," *IEEE MTT-S Int. Microw. Symp.*, pp. 625–628, 2021, doi: 10.1109/ims19712.2021.9574826.

[184] JLC, "www.jlcpcb.com." https://jlcpcb.com (accessed Aug. 15, 2022).

[185] L. Langstroth, *The Hive and the Honey-Bee*. Northern Bee Books, 2014.

[186] M. I. Products, "MAX7408-MAX7415," 1821.

[187] P. Id, E. Usb, S. Card, and A. Adapter, "7 . 1 USB Audio Adapter External Sound Card with SPDIF Digital Audio," vol. c, 1844.

[188] U. S. B. Hid, "CM6206," pp. 1–37.

[189] T. A. Team, "Audacity." [Online]. Available: https://www.audacityteam.org/.

[190] MATLAB, "R2018a." The MathWorks Inc., Natick, MA, USA, 2018.

[191] ADI, "AN-140 Basic Concepts of Linear Regulator and Switching Mode Power Supplies," no. October, pp. 1–16, 2022.

[192] J. Eco and A. Limjoco, "AN-1368 Ferrite Bead Demystified," *Appl. Note*, pp. 1–11, 2015, [Online]. Available: https://www.analog.com/media/en/technical-documentation/application-notes/AN-1368.pdf.

[193] F. Semiconductor, "PCB Layout Design Guidelines for Radio Board Using the MC13853 LNA," pp. 1–18, 2008.

[194] C. F. Yee, M. Mohamad Isa, A. Abdullah Al-Hadi, and M. K. Md Arshad, "Techniques of impedance matching for minimal PCB channel loss at 40 GBPS signal transmission," *Circuit World*, vol. 45, no. 3, pp. 132–140, 2019, doi: 10.1108/CW-01-2019-0004.

[195] V. C. Chen, F. Li, S. S. Ho, and H. Wechsler, "Micro-doppler effect in radar: Phenomenon, model, and simulation study," *IEEE Trans. Aerosp. Electron. Syst.*, vol. 42, no. 1, pp. 2–21, 2006, doi: 10.1109/TAES.2006.1603402.

[196] V. C.Chen, *The Microdoppler effect in Radar*, Second. Artech House, 2019.

[197] H. L. Victor C. Chen, *Time-Frequency Transforms for Radar Imaging and Signal*

Analysis. Artech House, INC, 2002.

[198] J. R. Riley, "QUANTITATIVE ANALYSIS OF RADAR RETURNS FROM INSECTS," *NASA. Wallops Flight Cent. Radar, Insect Popul. Ecol. Pest Manag.*, pp. 131–158, 1979.

[199] J. Shearwood, D. M. Y. Hung, P. Cross, S. Preston, and C. Palego, "Honey-Bee Localization Using an Energy Harvesting Device and Power Based Angle of Arrival Estimation," *IEEE MTT-S Int. Microw. Symp. Dig.*, vol. 2018-June, pp. 957–960, 2018, doi: 10.1109/MWSYM.2018.8439173.

[200] Y. Sun, Y. Chen, X. Wang, and X. Tang, "Deep learning face representation by joint identification-verification," *Adv. Neural Inf. Process. Syst.*, vol. 3, no. January, pp. 1988–1996, 2014.

[201] G. E. H. Alex Krizhevsky, Ilya Sutskever, "ImageNet Classification with Deep Convolutional Neural Networks," *Adv. neural Inf. Process. Syst.*, pp. 1097–1105, 2012, doi: 10.1201/9781420010749.

[202] Y. Dong, X., Yan, N., & Wei, "Insect Sound Recognition Based on Convolutional Neural Network," 2018, doi: https://doi.org/10.1109/ICIVC.2018.8492871.

[203] A. Owens, J. Wu, J. H. McDermott, W. T. Freeman, and A. Torralba, "Learning Sight from Sound: Ambient Sound Provides Supervision for Visual Learning," *Int. J. Comput. Vis.*, vol. 126, no. 10, pp. 1120–1137, 2018, doi: 10.1007/s11263-018-1083-5.

[204] E. A. Capaldi *et al.*, "Ontogeny of orientation flight in the honeybee revealed by harmonic radar," *Nature*, vol. 403, no. 6769, pp. 537–540, 2000, doi: 10.1038/35000564.

[205] K. Marcus J King, Stephen L Buchmann, H. Spanglar, "Activity of asynchronous flight muscle from two bee families during sonication (buzzing)," *J. Exp. Biol.*, vol. 10, no. 199, pp. 2317–2321, 1996.

[206] M. A. Jankauski, "Measuring the frequency response of the honeybee thorax," *Bioinspiration and Biomimetics*, vol. 15, no. 4, 2020, doi: 10.1088/1748-3190/ab835b.

[207] M. A. Othman *et al.*, "5.8 GHz microwave Doppler radar for heartbeat detection," *Proc. 23rd Int. Conf. RADIOELEKTRONIKA 2013*, pp. 367–370, 2013, doi: 10.1109/RadioElek.2013.6530947.

[208] O. B. Lubecke, P. W. Ong, and V. M. Lubecke, "10 GHz doppler radar sensing of

respiration and heart movement," *Proc. IEEE Annu. Northeast Bioeng. Conf. NEBEC*, pp. 55–56, 2002, doi: 10.1109/nebc.2002.999462.

[209] A. E. Souza Cunha, J. Rose, J. Prior, H. M. Aumann, N. W. Emanetoglu, and F. A. Drummond, "A novel non-invasive radar to monitor honey bee colony health," *Comput. Electron. Agric.*, vol. 170, no. August 2019, p. 105241, 2020, doi: 10.1016/j.compag.2020.105241.

[210] A. Michelsen, W. H. Kirchner, B. B. Andersen, and M. Lindauer, "The tooting and quacking vibration signals of honeybee queens: a quantitative analysis," *J. Comp. Physiol. A*, vol. 158, no. 5, pp. 605–611, 1986, doi: 10.1007/BF00603817.

[211] D. Systems, "Cst Studio Suite." 2022, [Online]. Available: https://www.3ds.com/products-services/simulia/products/cst-studio-suite/solvers/.

[212] Microchip, "MCP4921/4922 12-Bit DAC with SPI Interface," p. 42, 2007, [Online]. Available: http://ww1.microchip.com/downloads/en/devicedoc/21897b.pdf.

[213] L. T. Corporation, "LT1009 - 2.5V Reference," pp. 1–8, 1985.

[214] B. C. Wadell, "Transmission line design handbook," *Chapter*. p. 513, 1991, [Online]. Available: http://www.lavoisier.fr/livre/notice.asp?id=OS6WOOAXK2XOWK.

[215] R. Islam and R. M. Henderson, "Minimizing attenuation of coplanar waveguide on lossy silicon substrates up to 300 GHz," *IEEE MTT-S Int. Microw. Symp. Dig.*, pp. 1–3, 2013, doi: 10.1109/MWSYM.2013.6697736.

[216] M. Bailey, "General Layout Guidelines for RF and Mixed-Signal PCBs," *MAXIM Appl. notes*, vol. 1, no. Figure 1, pp. 1–14, 2011, [Online]. Available: http://www.maximintegrated.com/app-notes/index.mvp/id/5100.

[217] J. Ardizzoni, "A Practical Guide to High-Speed PCB Layout," *Analog Dialogue, vol. 39, no. 9*, pp. 1–6, 2005, [Online]. Available: https://www.analog.com/media/en/analog-dialogue/volume-39/number-3/articles/high-speed-printed-circuit-board-layout.pdf.

[218] R. Corporation, "Rogers Corporation MWI-2019 Transmission Line Modeling Software." [Online]. Available: http://www.rogerscorp.com/.

[219] E. Hammerstad and O. Jensen, "Accurate Models for Microstrip Computer-Aided Design." *IEEE MTT-S Int. Microw. Symp. Dig.*, vol. 1, no. 12, pp. 107–409, 1980, doi:

10.1109/mwsym.1980.1124303.

[220] C. N. G. Ghione, "Analytical Formulas for Coplanar," *Electron. Lett.*, no. 4, pp. 179–181, 1984.

[221] W.Hilberg, "from Approximations to Exact Relations for Characteristic Impedances," *IEEE Trans. Microw. Theory Tech.*, vol. MTT-17, no. 5, pp. 259–265, 1969.

[222] RS Components Ltd., "RS Pro Straight PCB Mount SMA End Launcher Connector, jack, Solder Termination," 2020.

[223] V. E. H. William L. Briggs, *The DFT, an Owner's Manual for the Discrete Fourier Transform*. Philadelphia: Society for Industrial and Applied Mathematics, 1995.

[224] G.-S. and J. Maria, *Digital Signal Processing with Matlab Examples, Volume 1 Signals and Data, Filtering, Nonstationary Signals, Modulation*, vol. 1. Springer, 2017.

[225] M. Parker, *Digital Signal Processing 101*, Second. Elsevier, 2017.

[226] J. M. Goupillaud and P. A. Grossman, "Cycle-Octave and Related Transforms in Seismic Signal Analysis," *Geoexploration*, vol. 23, pp. 85–102, 1984.

[227] D. F. W. Heil and C. E., "Continuous and Discrete Wavelet Transforms," *SIAM Rev.*, vol. 31, no. 628, pp. 628–666, 1989.

[228] I. Daubechies, "The Wavelet Transform, Time-Frequency Localization and Signal Analysis," *IEEE Trans. Inform. Theory,* vol. IT-36, pp. 961–1005, 1990.

[229] P. T. Combes and J. M., A. Grossmann, *Wavelets, Time-Frequency Methods and Phase Spaces*. New York: Springer-Verlag, 1989.

[230] L. Breiman, "RANDOM FORESTS," *Mach. Learn.*, no. 45, pp. 5–32, 2001, doi: http://dx.doi.org/10.1023/A:1010933404324.

[231] A. Markel, J., Gray, *Linear Prediction of Speech*. New York: Springer-Verlag, 1976.

[232] Oppenheim, A., Schafer, R., Buck, J., *et. al.*, *Discrete-time signal processing*, Vol. 2. New Jersey: Prentice Hall, 1989.

[233] G. E. A. P. A. Silva, D. F., Souza, V. M. A., Ellis, D. P. W., Keogh, E. J., & Batista, "Exploring Low Cost Laser Sensors to Identify Flying Insect Species.," *J. Intell. Robot. Syst.*, 2018, doi: https://doi.org/10.1007/s10846-014-0168-9.

[234] A. S. Academy, "Australian Space Academy." http://www.spaceacademy.net.au/spacelink/spcomcalc.htm (accessed May 15,

2023).

[235] FCC, "Radio Frequency Safety." https://www.fcc.gov/general/radio-frequency-safety-0 (accessed May 15, 2023).

[236] E. RF, "SAR Calculator." https://www.everythingrf.com/rf-calculators/sar-rf-exposure-calculator (accessed May 15, 2023).

Appendix A Honeybee SEM Images
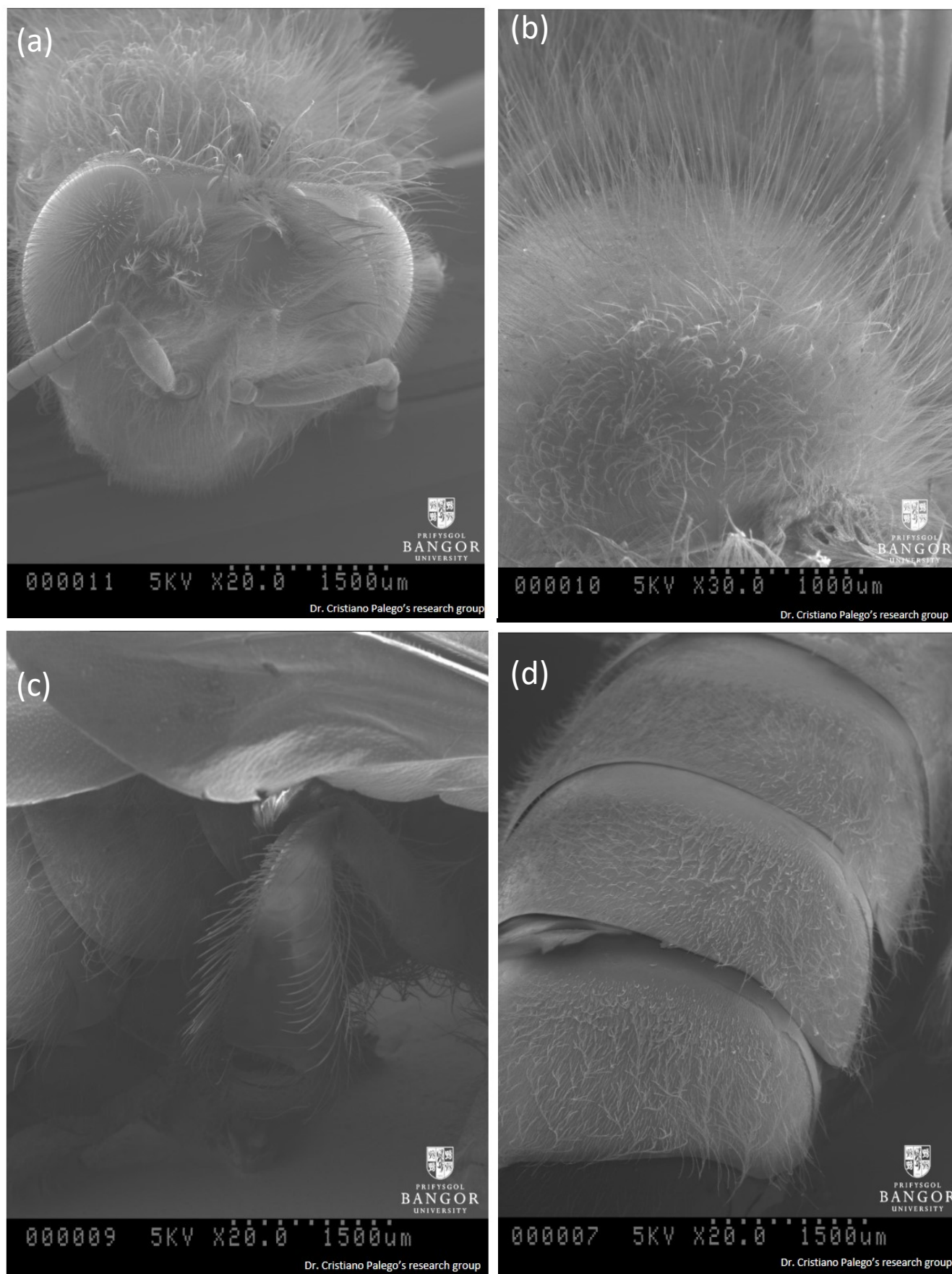
Figure A1: SEM scan of (a) honeybee head (b)thorax (c) hind leg (d) abdomen.
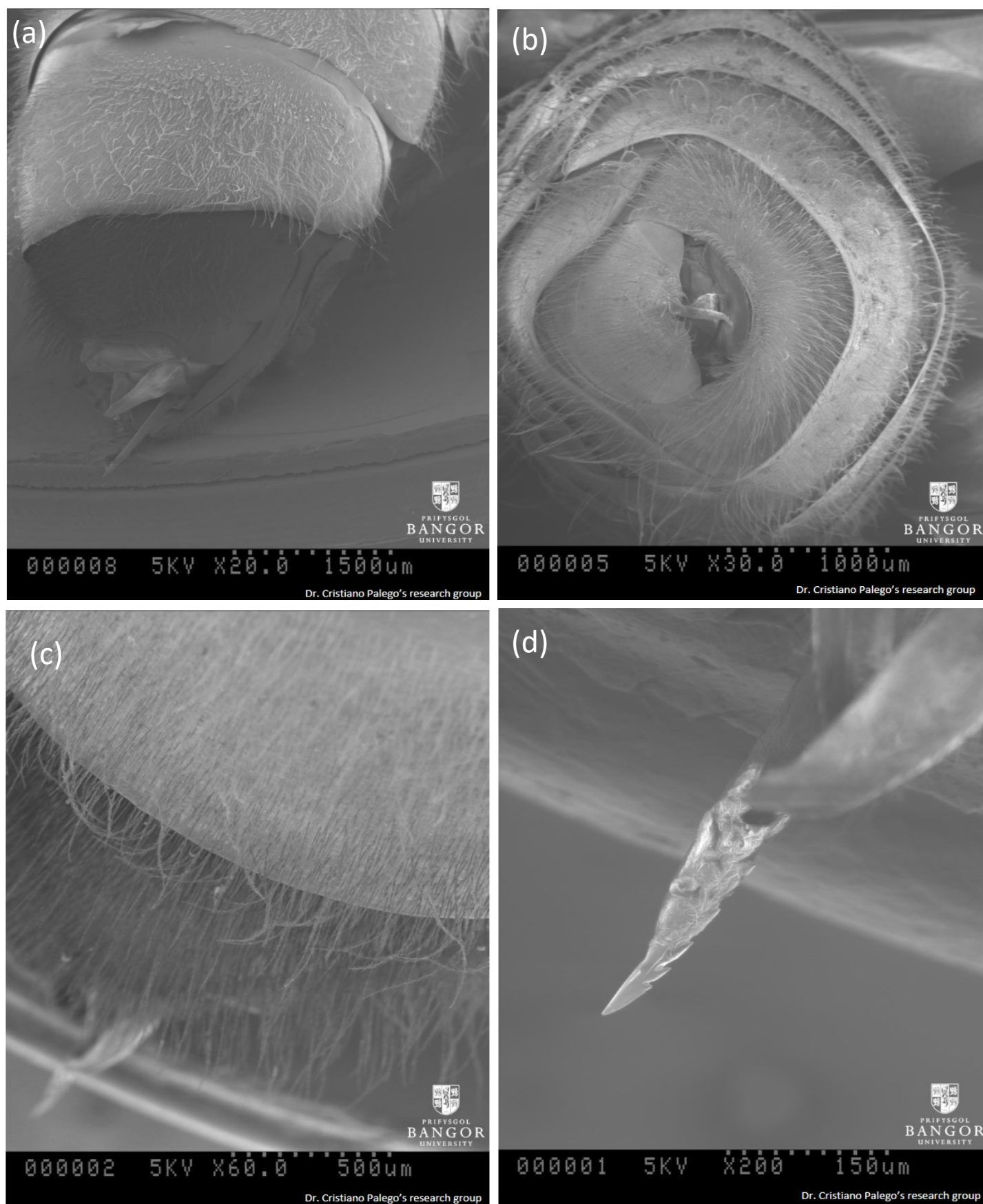
Figure A2: SEM scan of honeybee (a) abdomen (b)rear (c) abdomen showing the stinger (d) stinger.
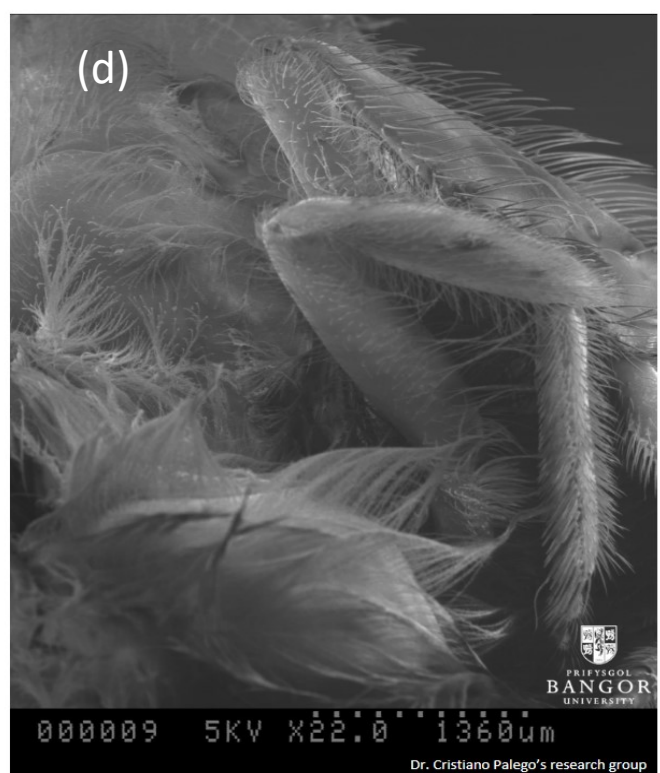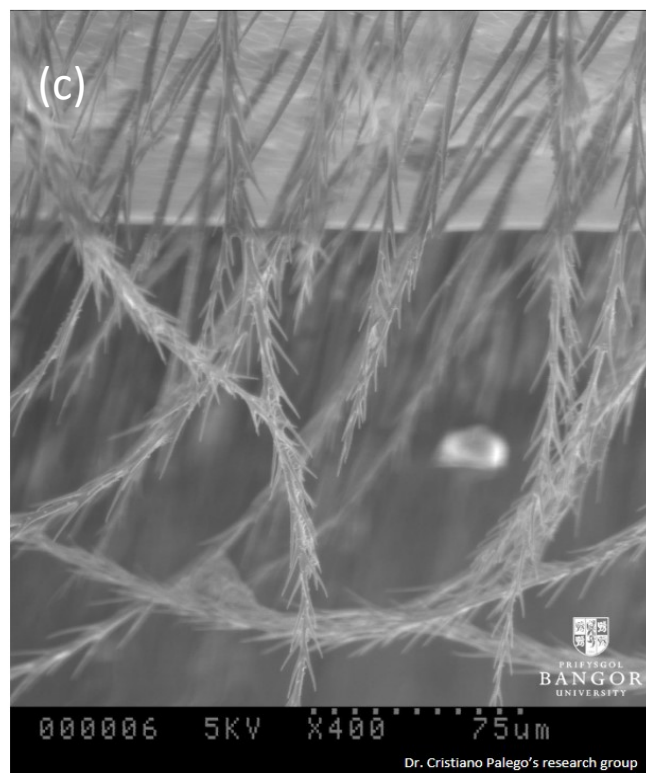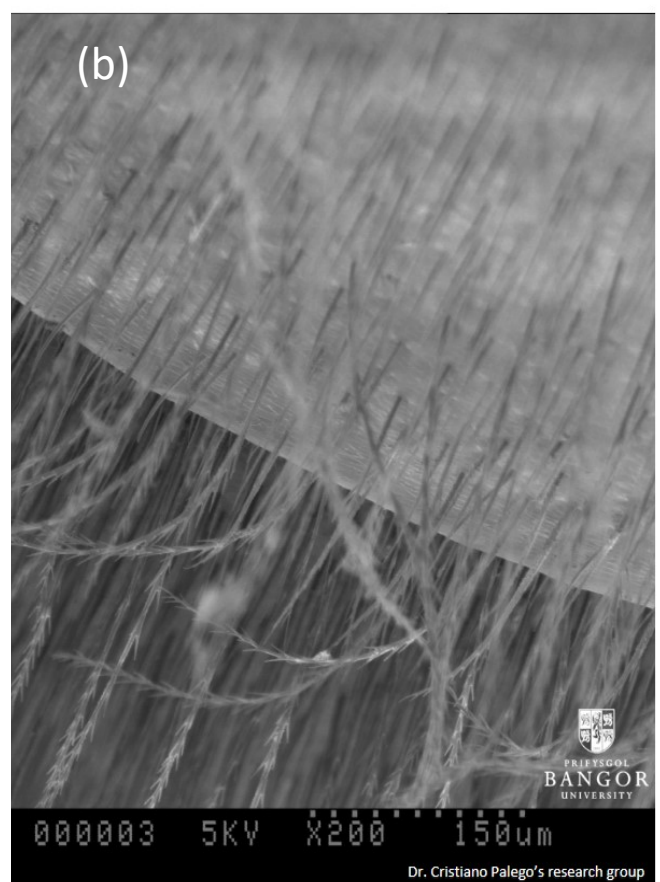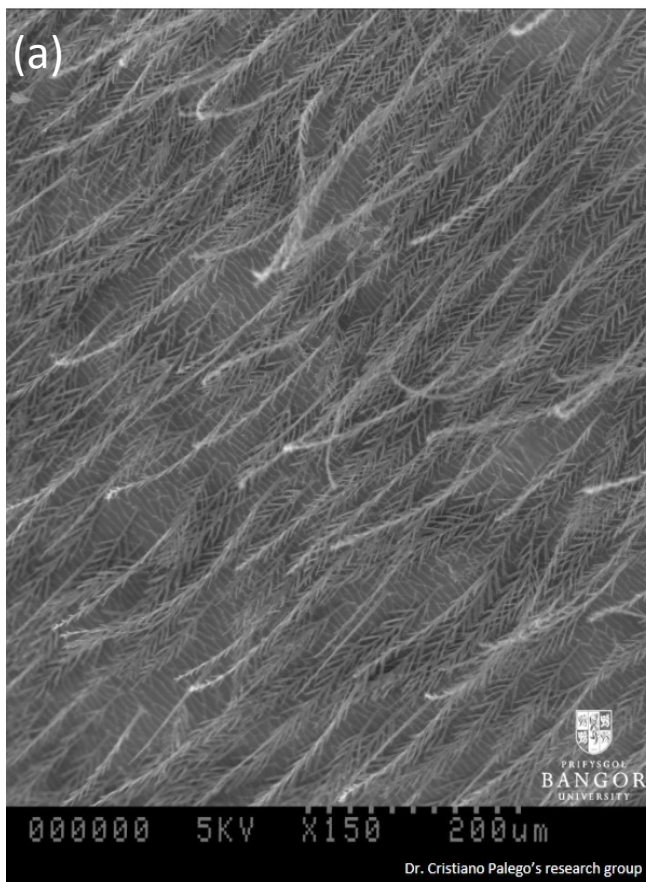
Figure A3: SEM scan of honeybee (a) 150X on Seta (b) 200X on Seta (c) 400X on Seta (d) mid leg and hind leg.
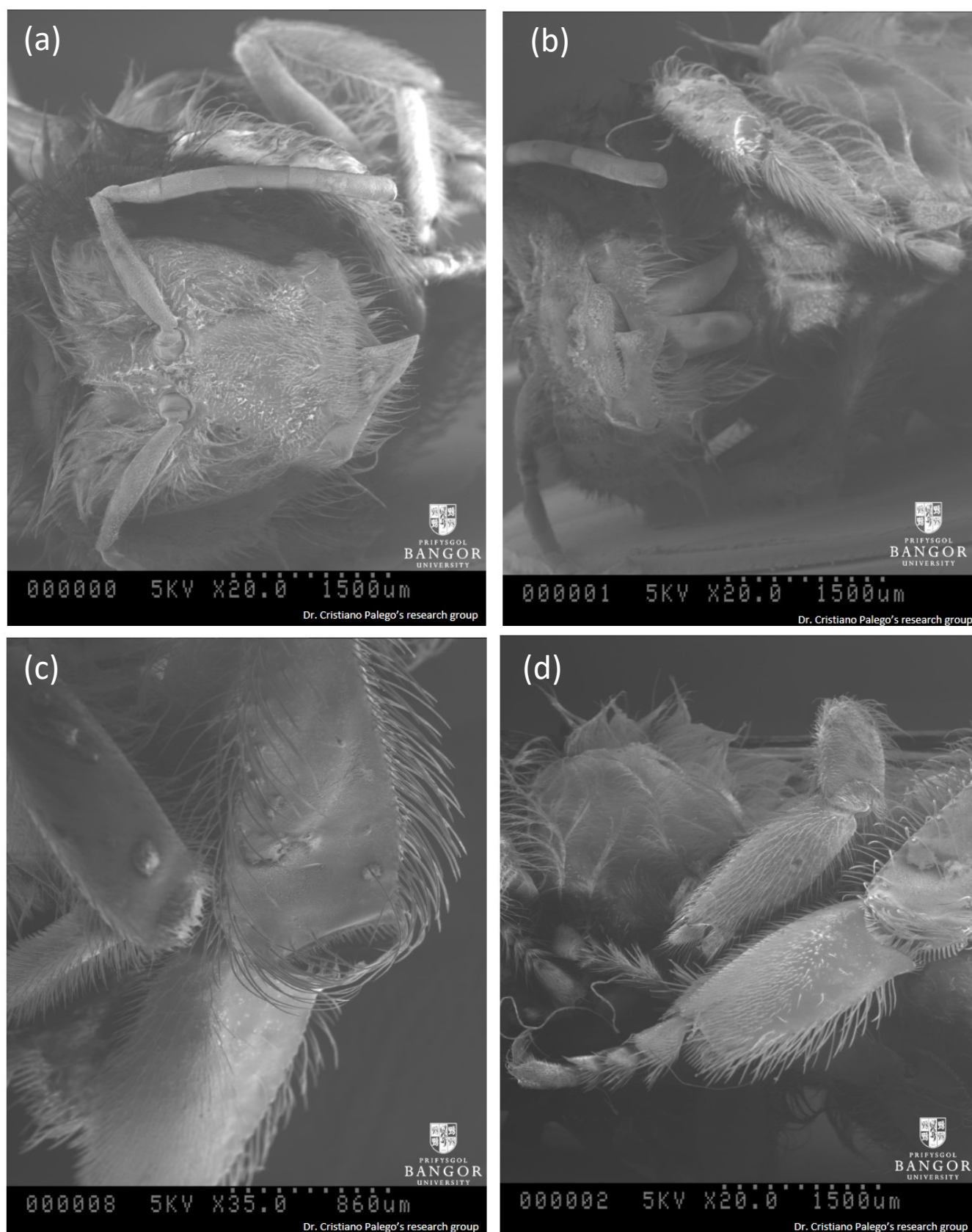
Figure A4: SEM scan of honeybee abdomen (a) honeybee head and antennas (b) honeybee head and foreleg (c) middle leg and hind leg (d) front leg and middle leg.

Appendix B CST Microwave Studio for RCS Calculation

The RCS simulations were conducted using CST Studio suite [211], a high performance EM simulation software equipped with various solvers. The Asymptotic Solver (A-solver) and the Integral equation solver (I-solver) are suitable for RCS simulations. The A-solver is preferred for large electrical sizes, while the I-solver is considered most efficient for models with multiple empty spaces [211].

Performing RCS based simulation was performed by opening CST's Microwaves & RF/Optical application area, and selecting the RCS option. In order to be able to simulate the RCS, it would require setting open (add space) boundaries and the use of an integral solver due to the integral solver's ability to sweep monostatic and bistatic RCS in both the target's elevation (Theta) and azimuth (Phi) plane. An example shown below is the simulation of a metal plate using CST Microwave Studio as an EM simulation tool. Upon following the above instructions, the resulting RCS is 0.4552 m^2. This is shown in Figure B1. The theoretical calculation of the RCS of a 100 mm^2 steel plate was performed using Equation 1.6 (chapter 1) at 5.8 GHz frequency which resulted in an RCS of 0.46 m^2. Note that the simulated RCS value and theoretical value were in close approximation.

Type	Bistatic Scattering
Approximation	enabled (kR >> 1)
Monitor	farfield (f=5.8) [pw]
Component	Abs
Output	RCS
Frequency	5.8 GHz
Total ACS	0.0000 m2
Total RCS	0.01966 m2
RCSmax	0.4552 m2
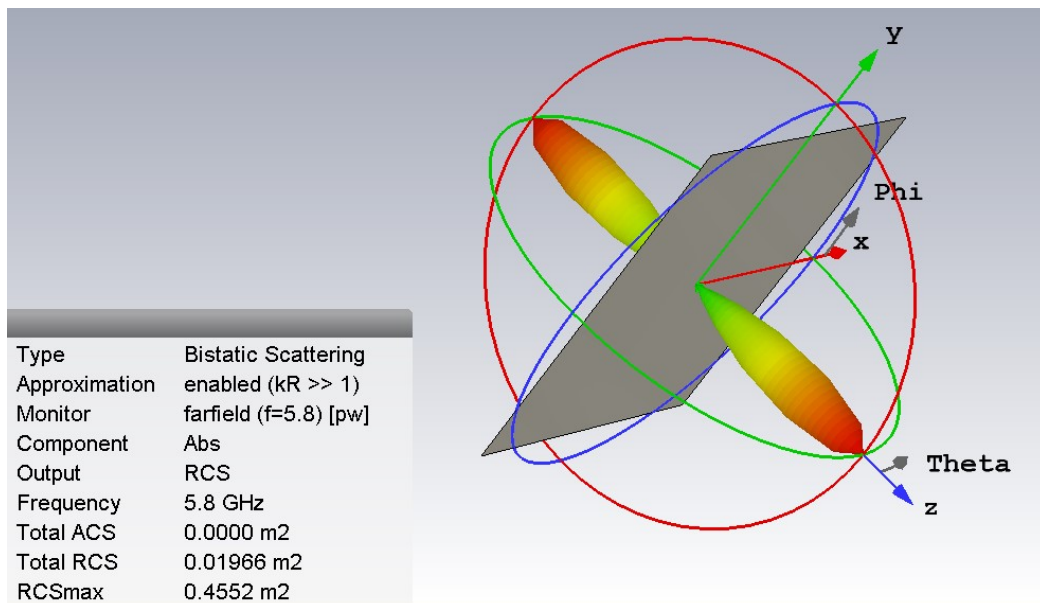
Figure B1: Simulation of flat plate of 100 m^2 RCS, which resulted in an RCS of 0.4552 m^2.

Appendix C FMCW

A CW radar utilises an unmodulated waveform for the detection of radial velocity and direction but is incapable of detecting the range of the target. In order to measure range, a timing reference in the transmitted waveform is required. This can be done by adding a modulation to the transmitted frequency or phase. The most common implemented waveform modulation is a Linear Frequency Modulation (LFM), which can be saw-toothed, triangular or even sinusoidal.
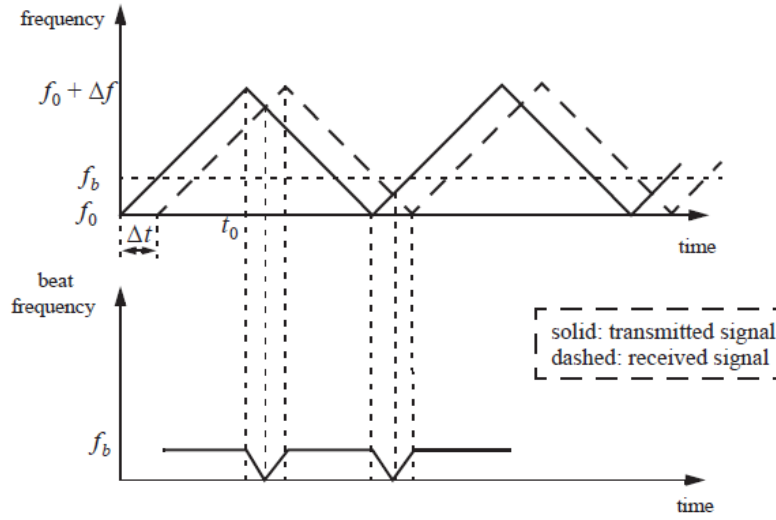
Figure C1: FMCW beat frequency f_b

Figure C1 shows the FMCW beat frequency (f_b), which is defined as the difference between the transmitted and the received signals, along with the returned waveform from a target at range R. The time delay, denoted as Δt is a measurement of the target range, defined as [162]

$$\Delta t = \frac{2R}{c} \qquad\qquad \text{C1.1}$$

The modulating frequency f_m is chosen such that:

$$f_m = \frac{1}{2t_0} \qquad\qquad \text{C1.2}$$

While the rate of frequency change $\dot{f}$ is:

$$\dot{f} = \frac{\Delta f}{t_0} = \frac{\Delta f}{\left(\frac{1}{2f_m}\right)} = 2f_m\Delta f \qquad\qquad \text{C1.3}$$

Where the peak frequency deviation is denoted as Δf. The beat frequency f_b is

$$f_b = \Delta t \dot{f} = \frac{2R}{c} \dot{f}$$

C1.4

This can be re-arranged as

$$\dot{f} = \frac{c}{2R} f_b$$

C1.5

By substituting equation (C1.3) with equation (C1.5) to solve for f_b results in:

$$f_b = \frac{4R f_m \Delta f}{c}$$

C1.6
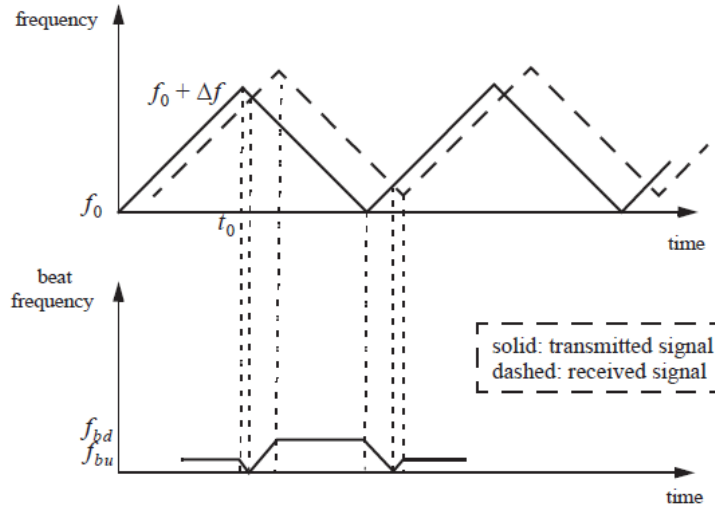
Figure C2: Transmitted and received triangular LFM

Figure C2 illustrates the transmitted and received triangular LFM, while considering the presence of a Doppler. The beat frequency is defined as

$$f_b = f_{received} - f_{transmitted}$$

C1.7

As the target moves, the received signal will contain the Doppler shift and a frequency shift, which is a result of the time delay Δt. During the positive part of the slope in Figure C2, the Doppler shift subtracts from the beat frequency, denoted here as f_{bu} (up). On the other hand, during the negative part of the slope the two terms add up, where the beat frequency here is denoted as f_{bd} (down). Consequently, for f_{bu} and f_{bd}

$$f_{bu} = \frac{2R}{c} \dot{f} - \frac{2\dot{R}}{\lambda}$$

C1.8

$$f_{bd} = \frac{2R}{c} \dot{f} + \frac{2\dot{R}}{\lambda}$$

C1.9

Where $\dot{R}$ being the range rate and the $\frac{2R}{c}\dot{f}$ being due to the range time delay as in equation (C1.1) while $\frac{2\dot{R}}{\lambda}$ is due to the Doppler of the target. To compute the range, equations (C1.8) and (C1.9) are added together, resulting in:

$$R = \frac{C}{4\dot{f}}\,(f_{bu}+f_{bd}) \qquad\qquad \text{C1.10}$$

By subtracting equation (C1.9) from (C1.8) the range rate (or the radial velocity) can be computed as,

$$\dot{R} = \frac{\lambda}{4}\,(f_{bd}-f_{bu}) \qquad\qquad \text{C1.11}$$

As shown from equation (C1.10) and equation (C1.11) both the radial velocity and the range can be calculated when utilising a CW radar with a LFM waveform. The selection of the maximum time delay Δt_{max} follows,

$$\Delta t_{max} = 0.1t_0 \qquad\qquad \text{C1.12}$$

As a result, the maximum range is defined by the following:

$$R_{max} = \frac{0.1ct_0}{2} = \frac{0.1c}{4f_m} \qquad\qquad \text{C1.13}$$

This is how both the range and radial velocity can be found using a LFM waveform. Another method that could be used to find both the range and radial velocity in a CW radar, is to employ multiple frequency schemes [162].
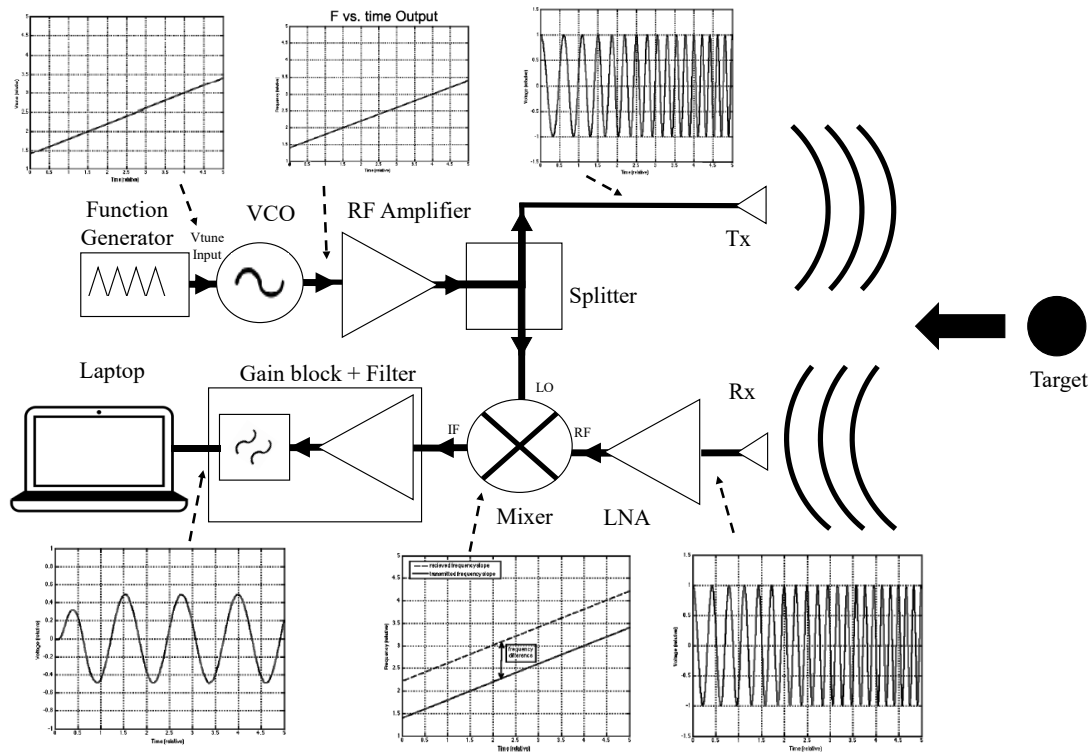
Figure C3: Illustrates a FMCW Doppler radar architecture while displaying the signal in different stages.

Figure C3 shows an FMCW radar and its main components. The figure shows the generation of a linear waveform which is fed into the Vtune port of the VCO. This causes the VCO to produce a sinusoidal waveform with a frequency that changes over time. The waveform is then amplified by the RF amplifier and split between the transmitting antenna and LO port of the mixer. Simultaneously, the linearly modulated transmitted signal is reflected back from the target, which causes a shift in the phase of the modulated signal. The shifted signal is received by the receiving antenna, which is a delayed version of the original signal. This is amplified by the LNA and fed into the RF port of the down-converting mixer. The mixer multiplies the delayed difference from the original LO signal. Due to the delay in the received signal, a consistent frequency offset can be seen, which is directly proportional to the range of the target. Thus, the larger the offset, the further the target. The product of the mixer (the difference between the LO and RF signal), is referred to as the beat frequency. Utilising Fourier analysis, the range of the target can be identified.

Appendix D Frequency modulator (Triangular wave) generator

Generating a linearly modulated (LM) wave such as a triangular wave is necessary for the implementation of a FMCW radar and is not a requirement for a Doppler radar. The application of a LM wave would take place at the frequency oscillator making it convenient to enable or disable the LM wave. There are different methods for the generation of a LM wave, where the triangular wave was chosen. Among the methods of generating an LM wave are the use of dedicated oscillator ICs, 555 timers or a direct digital synthesis (DDS) circuit, which implements fast waveform generation utilising high speed digital circuits. This is performed by generating output values from a look-up table (LUT), where the required waveforms are stored in discretised values and are then converted to an analogue signal using a Digital to Analogue Convertor (DAC). A simple method to implement this is through the use of a microcontroller built-in DAC. The issue with a microcontroller-based implementation is that digital noise may leak into the LM wave, which could contribute towards an increase in VCO phase noise. Hence, the use of a separated/dedicated DAC is preferred.

A similar approach to the DDS circuit is followed, by emulating a DDS using a microcontroller with a dedicated DAC. The DAC outputs discrete values, which are used to approximate a triangle wave using a stair-case waveform. The resolution of the triangular waveform is limited by the resolution of the DAC (the higher the bits the higher the resolution). A suitable low power DAC is the MCP4921, offering a resolution of 12 bits, high accuracy, high stability (against temperature, pressure and humidity) and a low noise performance. The voltage output of the DAC is represented by,

$$V_{Out} = \frac{V_{Ref} \times GD_N}{2^{12}}$$
D1.1

Where V_{Ref} is the reference voltage, G is the chosen gain, D_N is the digital input value and n is the DAC's number of bits (n=12) [212]. A teensy 3.2 microcontroller is used to communicate with the MCP4921 DAC using the SPI interface allowing the elimination of additional phase noise and adding greater modulation flexibility as different modulations can be programmed. The teensy is connected to the DAC using the pinout diagram in Figure D1(b).

The MCP4921 requires a V_{Ref} of 2.5 V, which can be supported using a LT1009 2.5 V reference output. The DAC's pin AVSS and LDAC are connected to ground, and a 0.1 µF and 1 µF capacitor are used at the V_{Ref} to reduce noise. Since the FMCW radar operates at a centre frequency of 5.8 GHz, the VCO is required to oscillate from 5.6 GHz to 6 GHz to produce a 400 MHz bandwidth.
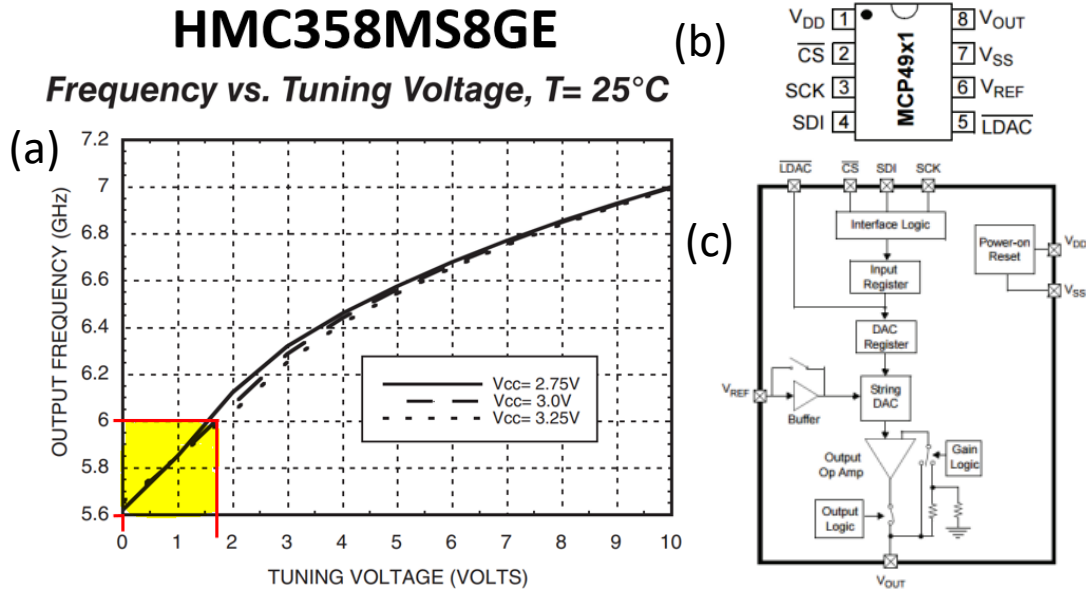
Figure D1: (a) Frequency vs tuning voltage of the HMC358 highlighting 0 V to 1.77 V which corresponds to 5.6 and 6 GHz respectively (b)MCP4921 DAC (c) Teensy 3.2 microcontroller.

The 400 MHz is achieved by programming the teensy microcontroller to generate a digital triangular waveform ramp, with an interval of 20 ms at a frequency of 20 Hz and a peak voltage of 1.77 V. The reason for choosing this frequency range was due to:

a) The centre frequency requirement of 5.8 GHz

b) The chosen 400 MHz band is least affected by voltage fluctuations as apparent from Figure D1(a).

c) This band is the most linear band of the performance. Past this point it starts losing linearity.

The microcontroller's output is fed into the DAC, resulting in the required ramp output voltage and duration. When connecting the output of the DAC to the HMC358 VCO in the Vtune port, the voltage ramp causes the VCO to oscillate a frequency ramp that changes in accordance with the applied voltage. Figure D1(a) shows the output frequency that can be achieved with respect to the Vtune port voltage of 0 V to 1.77 V highlighted.

Figure D2(a) shows the connection of the Teensy 3.2 and the MCP4921 DAC on a breadboard. The Teensy was programmed to generate the required ramp, whose output was then connected to an oscilloscope. The oscilloscope in Figure D2(b) demonstrates the ramp signal produced by the Teensy and DAC.
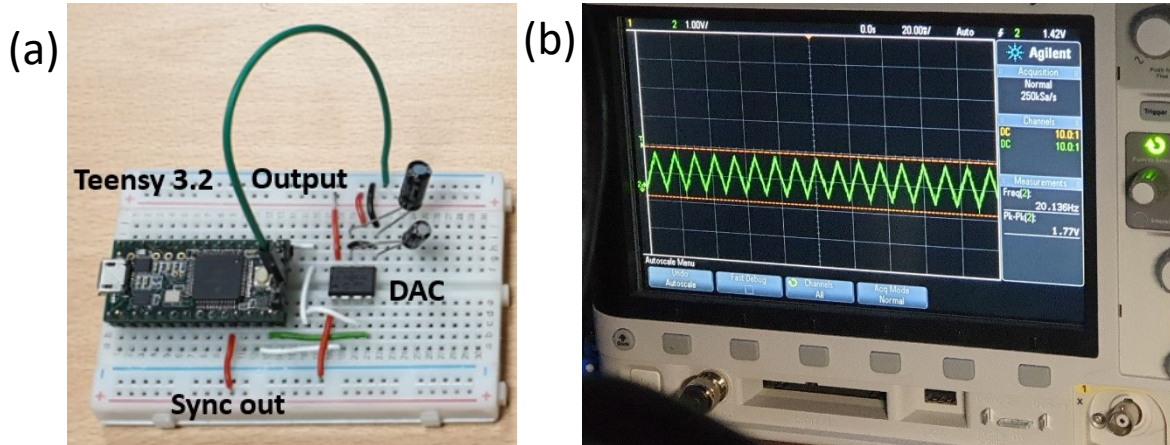
Figure D2: (a) Triangular waveform generator using a Teensy 3.2 and a MCP4921 DAC (b) Triangular waveform generated with a frequency of 20 Hz and a peak voltage of 1.77 V.

Appendix E Voltage Regulation - LVRs

Whereas the radar's initial testing was performed using two power supplies, a battery was required to support portability. At a later stage, a single power supply was used to emulate a portable power source with means of power regulation, where finally a LiPo battery was used. The radar contains components that require 5 V, 3 V and 2.5 V. The power regulation carried out for V1 and V2 radars, involved two LM317 adjustable voltage regulators in T0-220 packages. The LM317 is able to produce 1.5 A of load current in a voltage range of 1.2 to 37 V. The choice of the nominal output is dependent on a resistive divider, which makes it a simple and cost-effective method of regulating the voltage. The recommended LM317 circuit is shown in Figure E1(a). The nominal voltage is defined by:

$$V_{Out\ Regulated} = V_{Ref}\frac{(1 + R_2)}{R_1} + I_{Adj}R_2 \qquad \text{E1.1}$$

Where V_{Ref} is a 2.5 V voltage reference and $I_{Adj}R_2$ is an error term that can be neglected. Using equation E1.1 to obtain 3 V, R_2 and R_1 can be set to be 200Ω and 2 kΩ respectively. The resistor values may not provide the exact voltage output required; hence it is recommended to have R_2 as variable resistors (potentiometer). This provides a more accurate means of settling the nominal voltage, but would require a calibration prior to its use. When using the LM317, it is important to use heatsinks as power dissipation can be significant causing the LM317 to become hot. This affects the components surrounding the pins of the regulators. Thus, it is important to provide adequate heat sinking, while keeping the heat sink away from components as it is electrically connected to ground.

The LM317s were tested first using power supplies to regulate 12 V to 3 V and 5 V, and were afterwards tested using LiPo batteries of 11.1 V and 7.4 V. The required output was noticed to be stable with the heatsinks. The regulated voltage outputs per input voltages are shown in Table E1.

Table E1: Voltage inputs and resistor value for required output voltages.

Vin (v)	V required (v)	V regulated output (v)	resistance (Ω)
11.1	5	5.07	530
11.1	3	3.05	186
7.4	5	5.04	565
7.4	3	3.04	210

As for the voltage reference source used for both the voltage regulator and the DAC, the LT1009 reference IC was used. This provides a stable and precise (±0.2% accuracy) voltage reference, which requires no adjustment nor calibration [213]. Figure E1 below shows the LM317 and the LT1009 connected together to provide the power regulation and a reference voltage respectively.
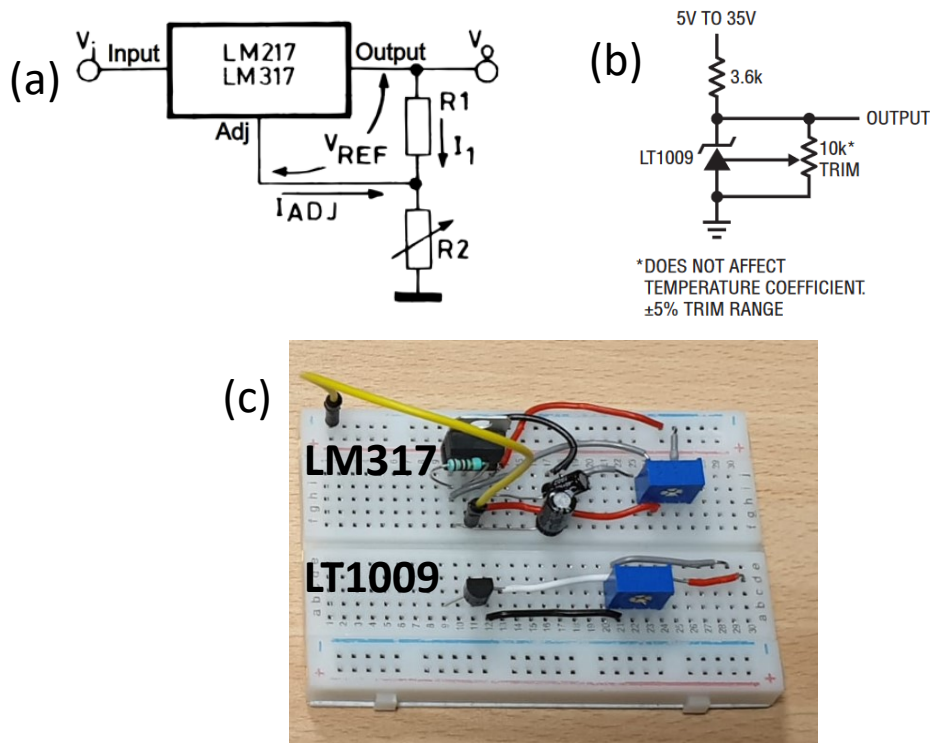
Figure E1: (a)Recommended circuit for the LM317 (b) Recommended circuit for the LT1009 (c) Breadboard showing the LM317 and LT1009.

Since the radar's use would be outdoors, having breadboard-based power units would compromise the performance. As a result, the power regulation unit was designed on a PCB, which accepts the main voltage as an input and outputs 2.5 V, 3 V and 5 V.

Appendix F Voltage Regulation - SMPs

SMPs were found to be a better alternative to LVR. SMPs were connected based on the datasheet's application circuit shown below.
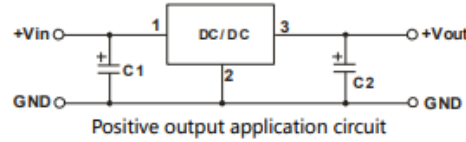
Figure F1: SMPS connection

A cleaner performance was noticed once SMPs were compared to LVRs. This was mentioned briefly in 3.9.1. Another performance example is shown below, where the signatures observed in Figure F1(a) are cleaner compared to (b) and signals are less clumped together. Another plot is shown in Figure F1(c)(d) and is this time plotted in a scalogram, where the same is observed. Note that in both figures, the left signatures were hand movements and the right signatures were finger movements.
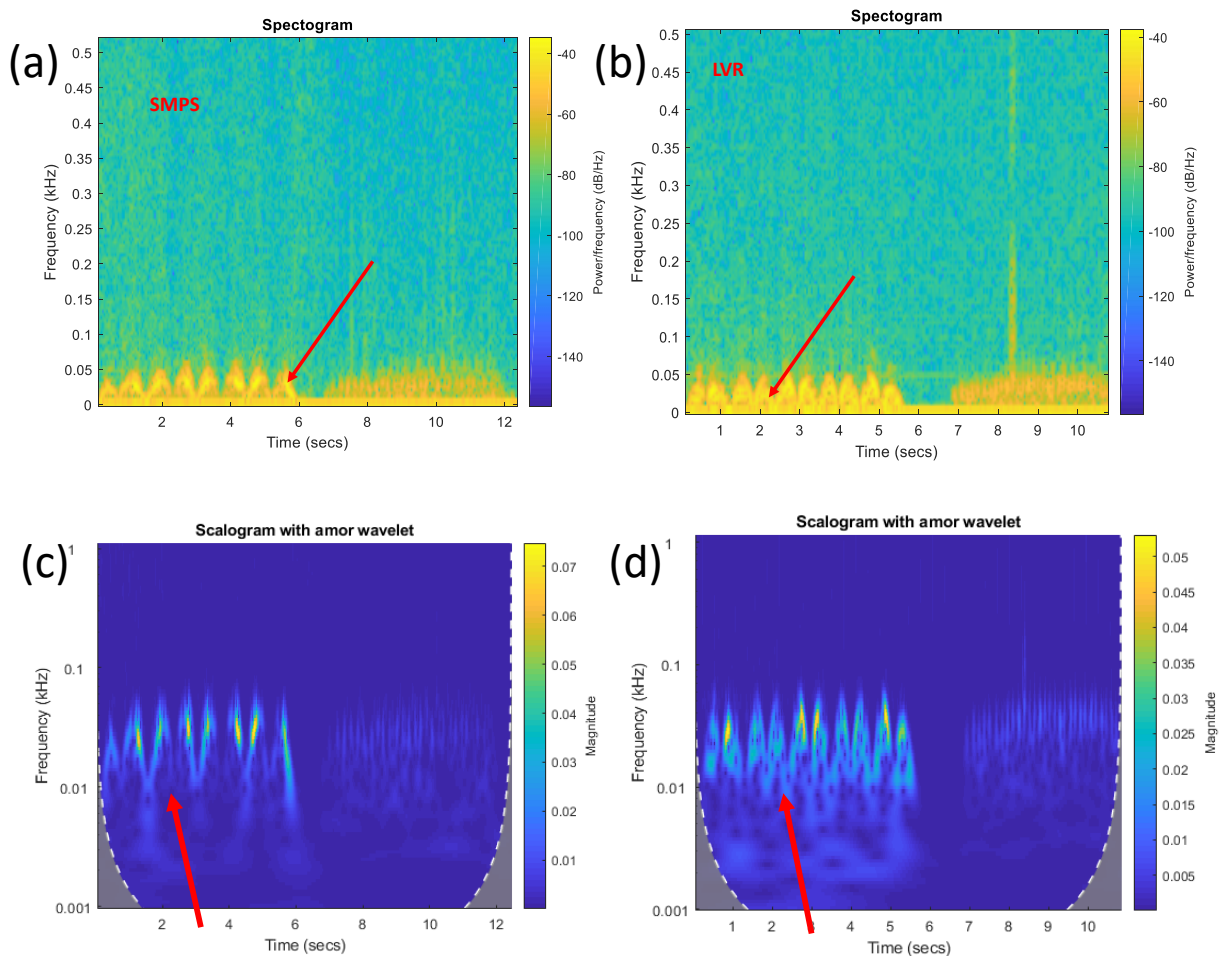
Figure F2: (a)Spectrogram of SMPS (b)Spectrogram of LVR (c) Scalogram of SMPs (d) Scalogram of LVR.

Appendix G Bill of Materials

The components used and their costs are shown below for each radar version designed and assembled. To reduce the use of the budget items 1 to 4 were obtained as evaluation boards from Analog Devices. This reduced the cost to £97.79 from the original £3088

Table G1: V1 radar

#	Component	Parameters	Cost
1	HMC358MS8GE	5.8 GHz VCO, 11 dBm out	£34.34 per part £413 Evaluation board
2	HMC717ALP3	14.5 dB gain, 1.3 dB NF	£14.19 per part £324.56 Evaluation board
3	3× HMC392ALC4	17 dB gain, 1.8 dB NF	£91.05 per part £647.82 Evaluation board
4	HMC219BMS8GE	Down-converter Mixer	£14.96 per part £309.29 Evaluation board
5	HDH-06020GID	20 dB coupler	£40 (used)
6	2×Antenna	5.8 GHz 17 dBi	£20
7	Teensy 3.2	Microcontroller for Triangular wave	£22.83
8	MCP4921	Digital to Analogue converter	£2.65
9	MAX7408	15KHz Centre Frequency LPF	£9.83
10	LM318	Voltage regulator	£0.62
11	LT1009	Voltage reference	£1.86
Total			£3088

Table G2: Third iteration of V2 radar

#	Component	Parameters	Cost
1	HMC358MS8GE	5.8 GHz VCO, 11 dBm out	£34.34
2	2×PMA3-83LN+	19.2 dB gain, 2.2 dB NF	£12.91
3	HMC219BMS8GE	Down-converter Mixer	£14.96
4	SCN-2-65+	3 dB Power Splitter	£2.75
5	2×Antenna	5.8 GHz 17 dBi	£20
6	2×PMA3-83LNW+	19 dB gain, 2.2 dB	£13.30
7	OPA2365AID	Operational Amplifier	£3.73
	Total		£128.2

Appendix G.   Bill of Materials

Table G3: V3 I/Q radar

#	Component	Parameters	Cost
1	HMC358MS8GE	5.8 GHz VCO, 11 dBm out	£34.34 per part
2	2×PMA3-83LN+	19.2 dB gain, 2.2 dB NF	£12.91
3	SCN-2-65+	3 dB Power Splitter	£2.75
4	HMC525ALC4	Quadrature mixer	£14.96 per part
5	ADC	Audio Codec	£9.8
6	2×Antenna	5.8 GHz 17 dBi	£20
7	2×PMA3-83LNW+	19 dB gain, 2.2 dB	£13.30
8	2×OPA2365AID	Operational Amplifier	£3.73
9	K78XXM-1000R3	3 V SMPS	£2.71
10	2×K78XX-2000R3	5 V SMPS	£5.33
Total			£151.38

Appendix H Antenna Design and Fabrication

Yagi-Uda antennas are known for their end-fire capability since being proposed in late 1920s [185], [186]. Microstrip antennas are known for their ease of fabrication, thin shapes, light weight, relatively low cost and their ease of integration [187]. A microstrip-fed Yagi-Uda dipole array combines the benefits of the end-fire capability with the advantages of a microstrip. The microstrip-fed Yagi-Uda dipole array employed a double-sided driven dipole elements, with a reflector which were printed on the substrate along with a number of printed director elements. This type of antenna can be optimised in terms of gain (the longer the array the more the director elements, the higher the gain), bandwidth and impedance.

The Yagi-Uda dipoles were designed based on a maximum length of an A4 paper (297 mm) to support the highest gain possible. Antenna Magus was used for the development of the antenna model, which was then exported to CST Microwave studio to study the radiation pattern. The antenna gain was calculated as 7.08 dBi, which reduced the EIRP to 28.42 dBm.

The Yagi-Uda microstrip-fed dipole antenna was designed using Antenna Magus, and imported into CST for EM simulation. The design dimensions of the antenna's elements were extracted from Antenna Magus and are displayed in Table H1. The spacing used is mentioned in Table H2. The antenna's size was 214 mm long, 39.72 mm wide, with a thickness of 0.8 mm.

Table H1: Design dimensions of antenna elements

N	Number of elements	20
Lde	Driven element length	18.47 mm
Lr	Reflector element length	39.72 mm
Sr	Spacing between reflector and centre of the driven element	7.504 mm
We	Element width	1.847 mm
Wf	Feedline width	1.556 mm
Lf	Feedline length	35.75 mm
Hs	Substrate height	800 μm
L	Substrate length	296.0 mm
W	Substrate width	55.42 mm
ε_r	Relative permittivity	4.3
tanδ	Loss tangent of the substrate	0.025
Ld1	Director 1 length	15.07 mm
Ld2	Director 2 length	14.88 mm
Ld3	Director 3 length	14.70 mm
Ld4	Director 4 length	14.52 mm
Ld5	Director 5 length	14.38 mm
Ld6	Director 6 length	14.24 mm
Ld7	Director 7 length	14.11 mm
Ld8	Director 8 length	14.00 mm
Ld9	Director 9 length	13.89 mm
Ld10	Director 10 length	13.78 mm
Ld11	Director 11 length	13.70 mm
Ld12	Director 12 length	13.64 mm
Ld13	Director 13 length	13.57 mm
Ld14	Director 14 length	13.50 mm
Ld15	Director 15 length	13.43 mm
Ld16	Director 16 length	13.38 mm
Ld17	Director 17 length	13.32 mm
Ld18	Director 18 length	13.26 mm

Table H2: Space dimensions of antenna elements

Name	Description	Value
Sd1	Spacing between director 1 and adjacent element (towards feed)	6.980 mm
Sd2	Spacing between director 2 and adjacent element (towards feed)	7.833 mm
Sd3	Spacing between director 3 and adjacent element (towards feed)	8.690 mm
Sd4	Spacing between director 4 and adjacent element (towards feed)	9.496 mm
Sd5	Spacing between director 5 and adjacent element (towards feed)	10.22 mm
Sd6	Spacing between director 6 and adjacent element (towards feed)	10.93 mm
Sd7	Spacing between director 7 and adjacent element (towards feed)	11.63 mm
Sd8	Spacing between director 8 and adjacent element (towards feed)	12.13 mm
Sd9	Spacing between director 9 and adjacent element (towards feed)	12.63 mm
Sd10	Spacing between director 10 and adjacent element (towards feed)	13.14 mm
Sd11	Spacing between director 11 and adjacent element (towards feed)	13.63 mm
Sd12	Spacing between director 12 and adjacent element (towards feed)	14.02 mm
Sd13	Spacing between director 13 and adjacent element (towards feed)	14.24 mm
Sd14	Spacing between director 14 and adjacent element (towards feed)	14.46 mm
Sd15	Spacing between director 15 and adjacent element (towards feed)	14.68 mm
Sd16	Spacing between director 16 and adjacent element (towards feed)	14.90 mm
Sd17	Spacing between director 17 and adjacent element (towards feed)	15.12 mm
Sd18	Spacing between director 18 and adjacent element (towards feed)	15.33 mm
X	Device X-dimension	39.72 mm
Y	Device Y-dimension	800 µm
Z	Device Z-dimension	229.4 mm

The EM simulation resulted in a gain of 14.9 dBi as shown in Figure H1(a). The antenna's S11 parameters were −22 dB at 5.8 GHz as indicated in Figure H1(b). Figure H1(c)-(e) show the top, bottom and side view of the antenna's spacing, elements and the naming convention used respectively.

The antenna's design was printed on PCB thermal transfer paper to create a mask. The mask was placed on a double-sided copper cladded (35 µm copper thickness) FR4 board and heated to 180 °C. Upon removing the mask, the FR4 board containing the printed mask was etched using Ferric Chloride, leaving the desired copper elements, which resulted in the final antennas shown in Figure H2(b) and (d). Figure H2(a) and (c) display the S11 parameters of the antennas. Antenna one and two obtained a S11 reading of –10 dB and –7 dB respectively at 5.8 GHz. The antennas were noticed to have their resonant frequency shifted to 6.2 GHz with a S11 reading of –29 dB for both antennas. The shift of 400 MHz could be due to poor etching and/or misalignment of feed and ground.
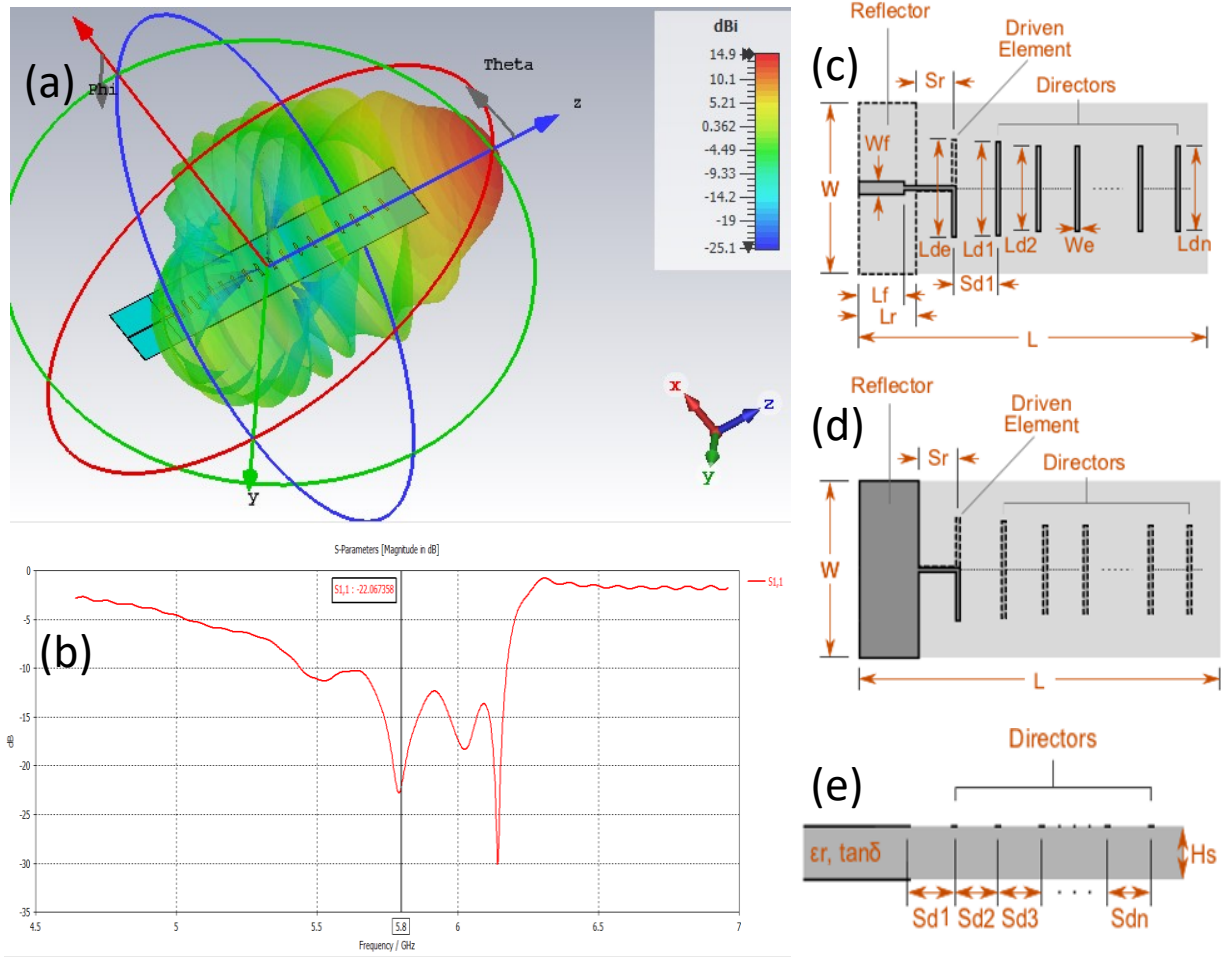
Figure H1: (a) Radiation pattern with a 14.9 dBi gain of the Yagi-Uda microstrip-fed dipole in CST (b) S11 plot of the Yagi-Uda microstrip-fed dipole in CST showing a minimum reflectivity of -22 dB. (c) Top view. (c) Bottom view. (e) Side view.

A piece of copper tape was used to tune the resonant frequency, which caused it to shift towards 5.8 GHz, as shown in Figure H2(b). This allowed a S11 value of -30 dB and -25 dB for antenna one and two respectively.

With no specialised equipment to identify the gain of our antenna, resorting to the use of Friis equation seemed suitable. The Friis equation shown in equation H1.1, calculates the amount of power at the receiving antenna, where the received power is directly proportional to the transmitted power and the gain of the antennas.

$$P_{RX} = P_{TX}G_{TX}G_{RX}\left(\frac{\lambda}{4\pi D_R}\right)^2 \qquad \text{H1.1}$$

Where P_{RX} is the power at the receiver, P_{TX} is the transmitted power, G_{TX} is the transmitting antenna's gain, G_{RX} is the receiving antenna's gain and D_R is the distance between both antennas.
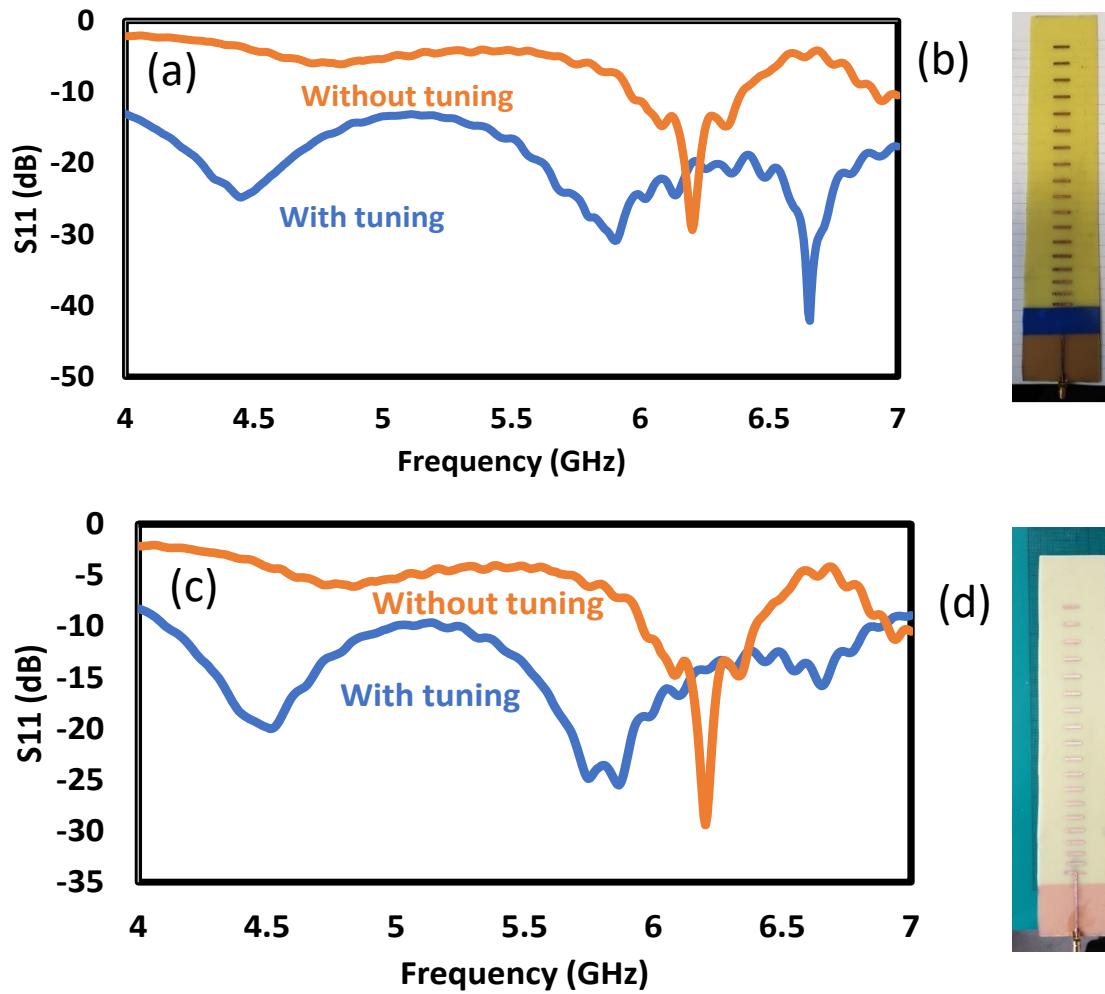
Figure H2: (a) Antenna 1 S11 value of −10 dB and −30 dB after tuning respectively (b) Antenna 1 with blue tape holding down copper tape (c) Antenna two S11 value of −7 dB and −25 dB before and after tuning respectively. (d) Antenna 2.

The combined transmitted power between the VCO and the LNA was approximately 19 dBm at a wavelength of 51.68 mm. The total losses were 1.22 dB due to the SMA connectors ($\backsim$0.1 dB × 3), coupler's insertion loss ($\backsim$0.5 dB) and SMA cable ($\backsim$0.22 dB).

Accumulating for the losses indicates a transmitted power of 17.78 dBm. The gain of the transmitting antenna was simulated as 14.9 dBi, while the gain of the commercial receiving antenna was 5 dBi from the datasheet. The distance between the transmitting and receiving antenna was 60 cm. Upon calculating the above parameters using Friis formula, the resulting received power was −5.599 dBm. Using the Spectran HF-60105 portable spectrum analyser, the measured value was found to be −13.39 dBm at 5.78 GHz. Upon using the received power in Friis equation and adjusting the wavelength to 51.86 mm to correspond with the peak signal at 5.78 GHz, the transmitting antenna's gain was calculated as 7.08 dBi using the following equation,

$$G_{TX} = \frac{P_{RX}\ (4\pi D_R)^2}{P_{TX}G_{RX}\lambda^{\ 2}} \qquad\qquad \text{H1.2}$$

This meant that the gain of the in-house fabricated antenna was about half the gain of the simulation, which reduced the EIRP to 28.42 dBm.

The impact of the antenna's length and respective increase in directors was also investigated. The length was incremented from a minimum of 60 mm and 1 director to a maximum of 296 mm and 18 directors. The length's impact on the S11 is shown in Figure H3(a) and the length's impact on the gain is shown in Figure H3(b).
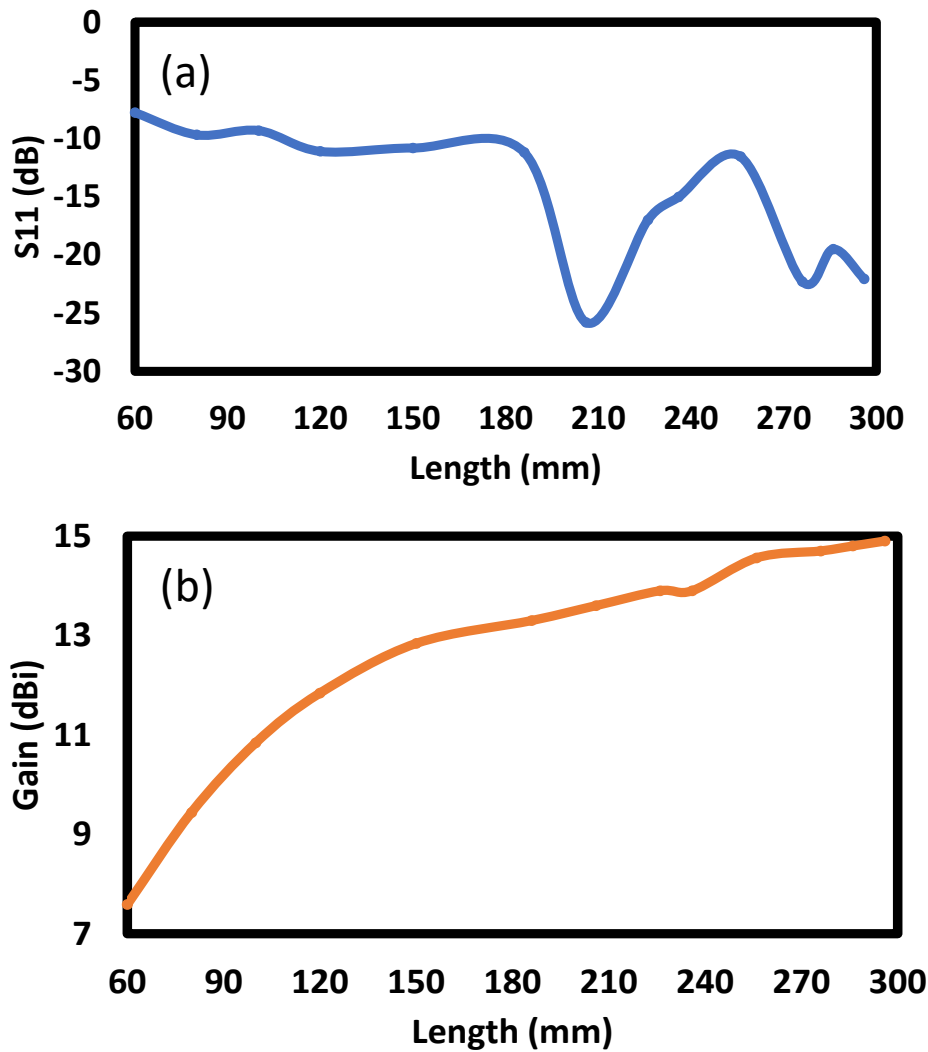

Figure H3: Investigating the impact of the antenna's length on (a) S11 (b) gain

Appendix I AWR Simulation of Coffee Can Radar

A block diagram of the original coffee can radar is shown below in Figure I1 [177], while annotations of component's output power were added manually. Note that each of the RF modules, were connected using SMA connectors with an expected loss of 0.3 dB, which finally adds up to an effective isotropic radiated power (EIRP) of ~20 dBm. The EIRP is the maximum transmitted power including the antenna's gain while excluding any losses. This was calculated using

$$EIRP = P_T - L_C + G_a \qquad\qquad I1.1$$

Where P_T is the power transmitted (13 dBm), L_C are the cable losses where in this case the losses which constitute to approximately 0.2 dBm and G_a is the antenna gain of 7.2 dBi.
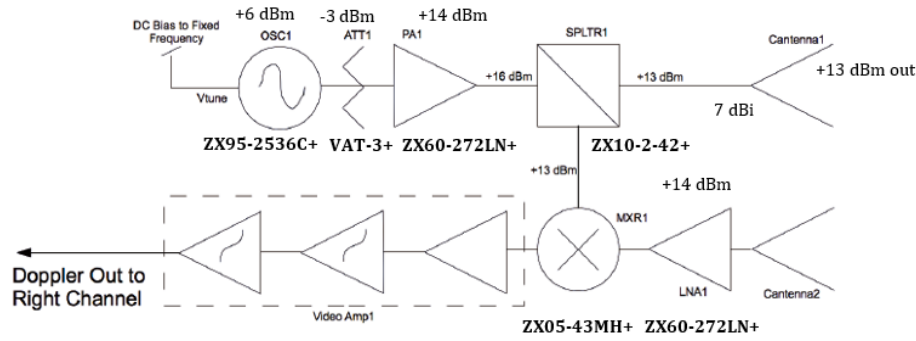
Figure I1: Original coffee can radar block diagram [177]. Manually added link budget based on their used components along with their names.

The simulation schematic shown in Figure I1, depicts the key RF and analogue components of the coffee can radar in AWR. The simulation, operating at a centre frequency of 2.4 GHz, shows a transmitting channel and a receiving channel both equipped with their cantennas (7.2 dBi gain). Additionally, the simulation takes a radar target into account with variable parameters. The RCS of the target was a human with an RCS of 1 m² ($\sigma = 0\ dBsm$) at a distance of 25 metre with a velocity of 20 km/h.
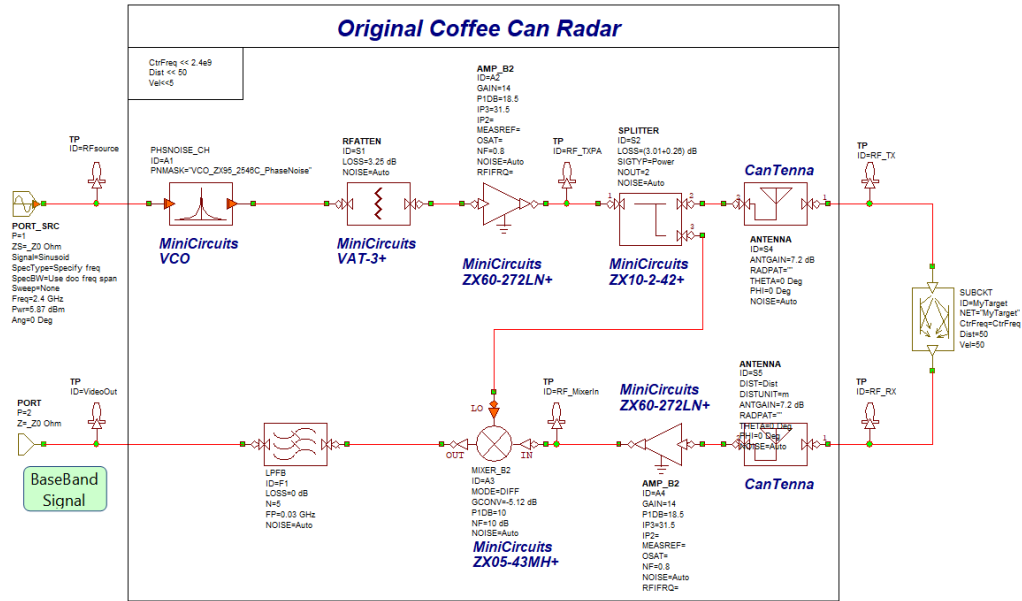
Figure I2: Original coffee can radar simulation in AWR.

Figure I3, illustrates the cascaded power of both systems, where the original radar (blue) and redesigned radar (green) had a peak transmitted power of 13 and 23 dBm respectively and an EIRP of 20 and 30 dBm respectively. The figure also shows that the original radar led with a higher power due to the VCO higher output power, but was outperformed by the redesigned radar. This is firstly due to its lower RF amplification and due to the redesigned radar's 20 dB coupler which replaced the original 3 dB splitter, causing more power to propagate towards the transmitting antenna. This consequently effected the received power of -80.6 dBm and -69.3 dBm as illustrated in the same figure at the receiving antennas of both the original and redesigned radar system.
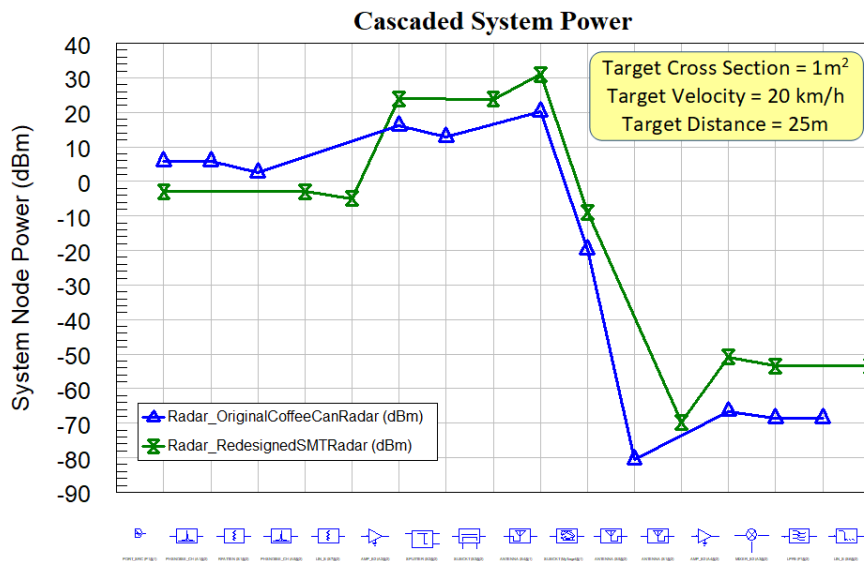
Figure I3: Cascaded system power of original coffee can radar showing a peak power of 20 dBm.

Further, Figure I4 shows the original coffee can radar and redesigned coffee can radar IF power spectrum peaks of −80.41 and −65.36 dBm of the received signal respectively. Considering the parameters of the radar simulation being variables, any of such parameters can be modified to obtain a virtual evaluation of the radar in a quick and cost-effective manner. An example could be increasing the RCS of the target from 1 m² to 100 m², which would cause the IF power spectrum peak to increase to −60.41 and −45.36 dBm for the original coffee can radar and the redesigned radar respectively.

Figure I4: Peak IF power reaching −80.41 dBm and −65.36 dBm for the original coffee can radar and the redesigned radar considering a human target of 1m² RCS at a distance of 25 m and a velocity of 20 km/h.

Appendix J CPW Design and Calculation

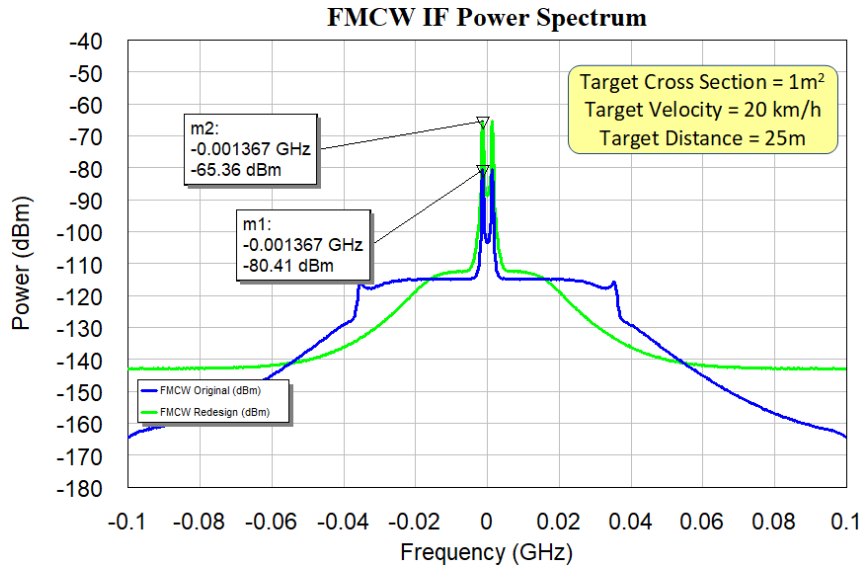A radar PCB would accommodate different signals such as unregulated voltages and regulated (3 V, 5 V, 12 V and Vtune), analogue signals, RF and digital signals. A two-layer board would have limited routing capabilities, causing it to be problematic. A four-layer board, as shown in Figure J1 on the other hand, offers more routing possibilities, delivering adequate isolation among the signals.
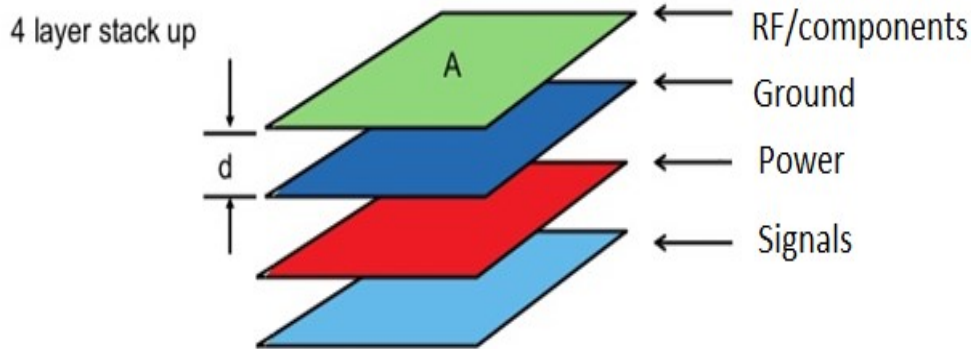

Figure J1: Four-layer stack-up that supports RF routing.

At high speed/frequency design, substrate thickness needs to be decreased to reduce spurious effects such as radiation loss [176]. Similarly, this causes the transmission line whether a microstrip, coplanar waveguide or slot-line to become narrow to an extent that it is not practical for use [176]. Among the mentioned transmission lines, coplanar waveguide (CPW) is commonly used for high speed/frequency design. The CPW has a single conductor placed in-between two ground planes on top of the substrate. Compared to a common microstrip approach or stripline, this provides an advantage of having a single centred conductor configuration, which is ideal for connecting surface mount components (SMTs) and grounding components due to the close proximity of the ground planes [176], [214]. Additionally, the dual ground planes surrounding the centre conductor offer lateral isolation. This provides additional EM interference (EMI) shielding and eliminates field lines created from the centre conductor trace [176], [214]. CPWs suffer less losses compared to striplines as in a CPW the field lines pass above the dielectric [214].

Designing a CPW requires the calculation of two main properties: the effective dielectric constant and the impedance (Z_0). To calculate the impedance, the elliptical integral K(k) needs to be used.

A CPW with a bottom ground, also known as Conductor Backed Coplanar Waveguide (CBCPW), is a structure that is a transition from a microstrip. This configuration supports routing above a ground plane, which in return provides a higher isolation [214]. Field lines are confined between the ground planes and the central conductor, though the field lines can also be terminated at the lower ground plane. A CBCPW PCB was demonstrated to provide a 0.02 dB/mm less loss compared to a CPW [215]. If a CBCPW is not properly designed, it can exhibit behaviour microstrip. This can be prevented by ensuring that the width between the centre conductor and the ground *(w)* << to the height of the substrate *(h)* [214].

For even higher isolation it is recommended to have a via fence alongside the ground of the CBCPW to tie the ground pour of the top-layer to the ground plane. This configuration is known as grounded coplanar waveguide routing and provides top-layer induced return currents with a connection to ground [216].

High speed PCB design requires adhering to a wide range of guidelines, which dictates the PCB design [216], [217]. Among such guidelines for example is to minimise long parallel runs and signal traces close proximity on the same board as it reduces inductive coupling. Another example is minimising adjacent long traces to prevent capacitive coupling [217]. Signals that require isolation such as high frequency RF signals, will need to be routed on a dedicated layer. RF signals will require to be routed on impedance-controlled lines, where the trace maintains a characteristic impedance (mostly 50 Ω). Due to CBCPW impedance-controlled traces calculations being lengthy with room for human error, various corporations provide calculation models to encourage correct design. These can be found on the website of the PCB fabricators. Among such tools is the Rogers Corporation tool which uses accurate models for computer aided design by Hammerstad and Jensen [218], [219].

Designing a CPW requires the calculation of two main properties: the effective dielectric constant and the impedance (Z_0). To calculate the impedance, the elliptical integral K(k) needs to be used as shown below [214], [220].

$$Z_0 = \frac{30\pi}{\sqrt{\varepsilon_{eff}}} \frac{K(k')}{K(k)} \qquad \text{J1.1}$$

where

$$\varepsilon_{eff} = 1 + \frac{\varepsilon_r - 1}{2} \frac{K(k')K(k_1)}{K(k)K(k_1')} \qquad \text{J1.2}$$

and

$$k = \frac{s}{s + 2W} \text{ and } k_1 = 1 + \frac{\sinh\left(\frac{\pi s}{4h}\right)}{\sinh\left(\frac{(s + 2W)\pi}{4h}\right) 2} \qquad \text{J1.3}$$

Where S is the centre conductor of the CPW, W is the gap between the conductor and ground plane, h is the thickness/height of the dielectric, K is the complete elliptic integral of the first kind and k' is equal to $\sqrt{1.0 - k^2}$. The ratio of the complete elliptic functions in equation (J1.1) is approximated by [221]

$$\frac{K(k)}{K(k')} \approx \begin{cases} \dfrac{1}{2\pi} \ln\left[2 \dfrac{\sqrt{1+k} + \sqrt[4]{4k}}{\sqrt{1+k} - \sqrt[4]{4k}}\right] & for \ 1 \le \dfrac{K}{K'} \le \infty, \dfrac{1}{\sqrt{2}} \le k \le 1 \\[4mm] \dfrac{2\pi}{\ln\left[2 \dfrac{\sqrt{1+k'} + \sqrt[4]{4k'}}{\sqrt{1+k'} - \sqrt[4]{4k'}}\right]} & for \ 0 \le \dfrac{K}{K'} \le 1, 0 \le k \le \dfrac{1}{\sqrt{2}} \end{cases} \qquad \text{J1.4}$$

The geometry of the CPW without ground, CPW with ground and grounded CPW are shown in Figure J2. A CPW with a bottom ground, also known as Conductor Backed Coplanar Waveguide (CBCPW), is a structure that is a transition from a microstrip. This configuration supports routing above a ground plane, which in return provides a higher isolation [214]. Field lines are confined between the ground planes and the central conductor, though the field lines can also be terminated at the lower ground plane.
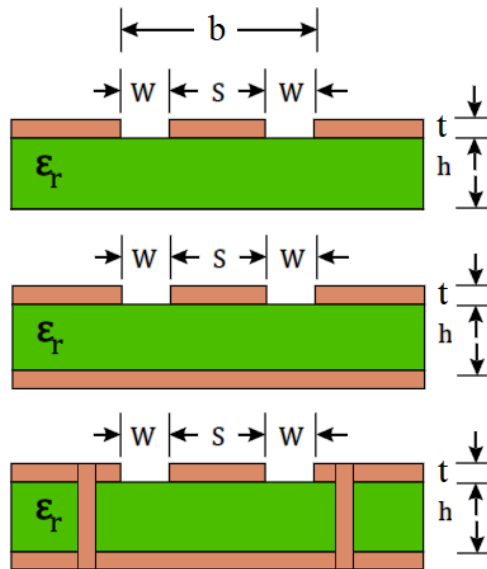

Figure J2: (a) Coplanar waveguide configuration (b) Conductor-backed CPW (c) Grounded CPW.

A CBCPW PCB was demonstrated to provide a 0.02 dB/mm less loss compared to a CPW [215]. If a CBCPW is not properly designed, it can exhibit behaviour microstrip. This can be prevented by ensuring that the width between the centre conductor and the ground *(w)* << to the height of the substrate *(h)* [214]. Designing a CPW with ground can be calculated by initially calculating Z_0 which requires K(k) [214] as shown below

$$Z_0 = \frac{60\pi}{\sqrt{\varepsilon_{eff}}} \frac{1}{\frac{K(k)}{K(k')} + \frac{K(k_1)}{K(k_1')}} , where\ k = \frac{s}{b} \qquad\qquad \text{G1.5}$$

here

$$k' = \sqrt{1.0 - k^2}\ and\ k_1' = \sqrt{1.0 - k_1{}^2} \qquad\qquad \text{G1.6}$$

and

$$k_1 = 1 + \frac{\tanh\left(\frac{\pi s}{4h}\right)}{\tanh\left(\frac{\pi b}{4h}\right)} \qquad\qquad \text{G1.7}$$

$$\varepsilon_{eff} = \frac{1 + \varepsilon_r \frac{K(k')}{K(k)} \frac{K(k_1)}{K(k_1')}}{1 + \frac{K(k')}{K(k)} \frac{K(k_1')}{K(k_1')}} \qquad\qquad \text{G1.8}$$

For even higher isolation it is recommended to have a via fence alongside the ground of the CBCPW to tie the ground pour of the top-layer to the ground plane. This configuration is known as grounded coplanar waveguide routing and provides top-layer induced return currents with a connection to ground [216].

Appendix K Stripline Simulation and Fabrication

A degradation in performance was observed, which was mainly believed to be due to the poor performance of the FR4 boards used for the radar fabrication. The FR4 boards used were claimed to be impedance-controlled boards purchased from JLCPCB.com. A means of resolving the issue was to simulate the PCB, enhance the performance and fabricate different transmission lines to study their S11 and S21 properties. The PCBs that were eventually designed, populated five different transmission lines to evaluate the performance of the FR4 boards. This was briefly mentioned at the end of section 3.10.1, whereas a detailed description is shown below.

The SMA used [222] was designed and simulated in CST, obtaining an impedance of 50.51Ω as shown in Figure K1. The four-layer JLC PCB stack-up used in the radar boards was also simulated in CST (shown in Figure K2) with a dielectric constant of 4.6. The top and ground layers were filled as copper (similar to the PCB), vias were added in the PCB and a thin layer of solder was placed under the SMA pins to emulate the real PCB design.
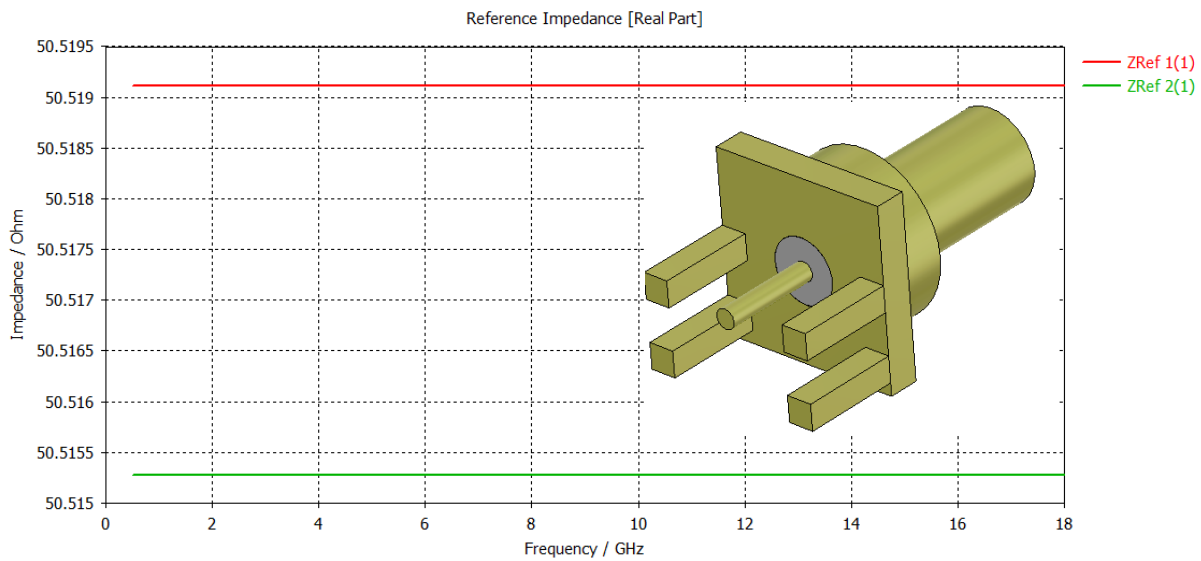

Figure K1: CST simulation of used SMA indicating an impedance of 50.51Ω. Inset shows the designed SMA.

The simulation results indicated a decrease in S21 with the increase of frequency. This was an immediate indicator of an FR4 board performance. Initial performance of the PCB showed (in Figure K2) an S21 of -2.74 dB and an S11 of -3.60, which meant that $\sim47\%$ of the power was reflected back. The simulations indicated that the transition from SMA (centre) conductor pin to PCB trace was wide. A wide trace results in a high shunt capacitance, which causes an impedance mismatch [193]. The shunt capacitance can be

reduced by cutting the 2nd ground layer under the trace, which results in an increase between the trace and ground layer [193], [194].
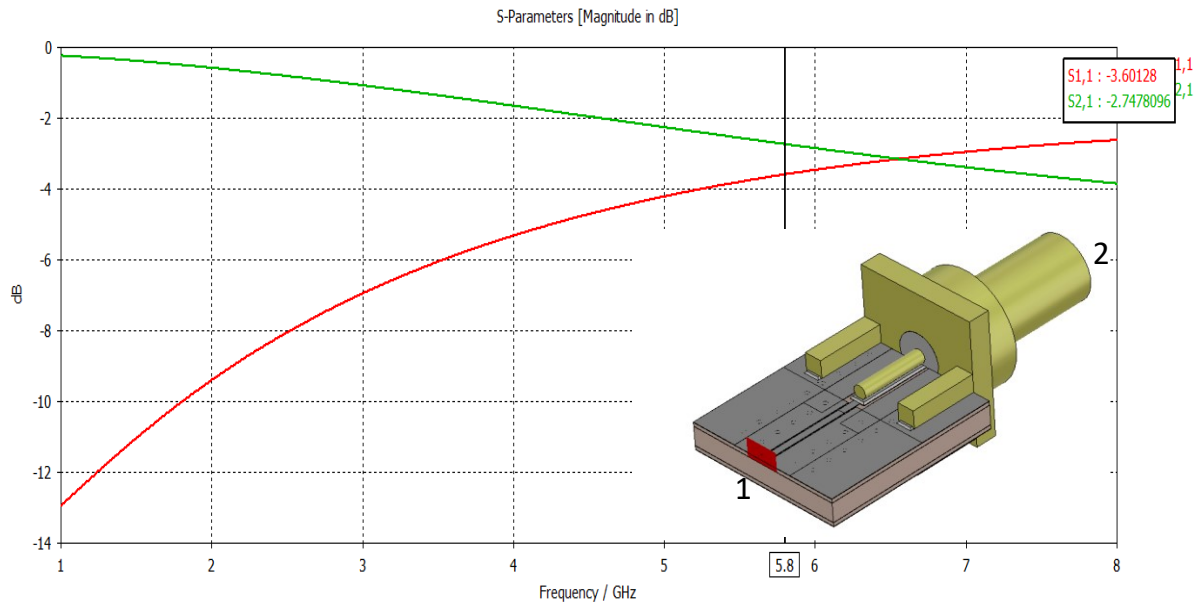
Figure K2: SMA and four-layer FR4 board simulation indicating a S11 and S21 parameters of −3.60 dB and −2.74 dB respectively.

A 2nd layer ground cut of 5.51 mm in length and 3.75 mm in width, a trace to pour gap of 0.07 mm and a trace width of 0.38 mm instead of 0.29 mm, lowered the S11 to −32.89 dB, which results in a reflection of 0.0514%. This is shown in Figure K3.
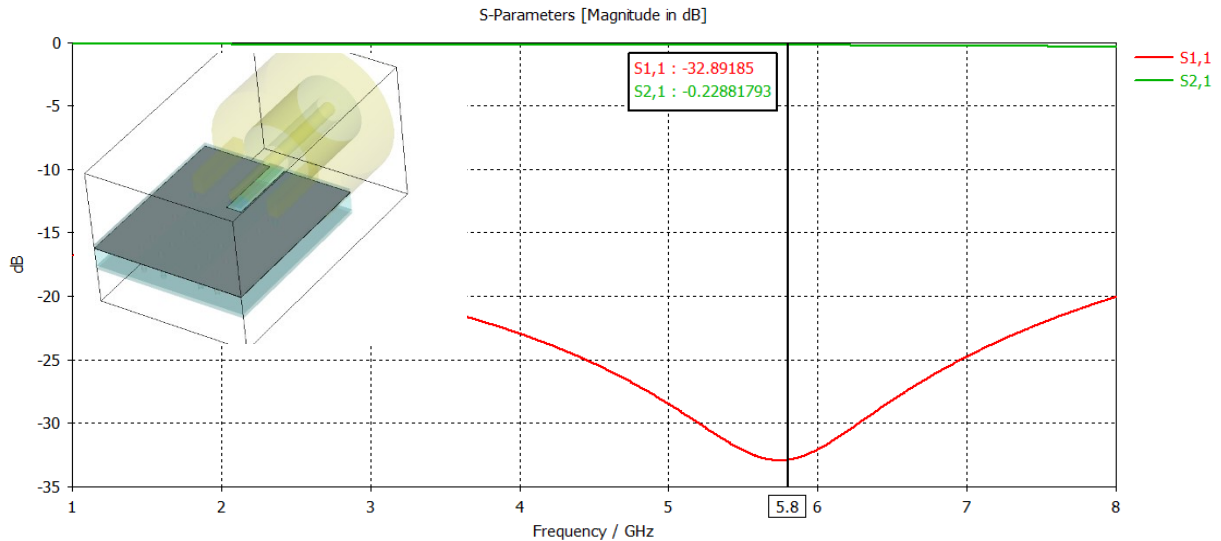

Figure K3: SMA and four-layer FR4 board simulation with 2nd layer ground cut, indicating a S11 and S21 parameters of −32.89 dB and −0.22 dB respectively.

The PCB was changed from FR4 to a Rogers RO4350B substrate without a cut in the 2nd layer ground plane. Roger substrates are known for being suitable substrates for high speed design, as opposed to FR4 substrates. The Rogers substrate resulted in a S11 and S21 of -7.68 dB and -0.92 dB, which meant that it reflected 17% back when compared to the FR4 board (without 2nd layer cut). When considering the Rogers sheet with a 2nd layer cut in ground, the simulation resulted in the expected behaviour of indicating a lower S11 and higher S21 of -36.33 dB and -0.065 dB. This meant that the Rogers sheet (with 2nd layer cut) reflects 0.023% back, while the FR4 (with 2nd layer cut) reflects 0.0514%.

As a result of the simulations conducted, four PCBs were designed, where each PCB populated five different transmission lines. Two of the four PCB designs were one thick SMA centre conductor (1 mm) termination and one thin SMA (0.38 mm) termination, where both PCB designs had no 2nd layer ground cut under the SMA pins in any of their transmission lines. The two remaining designs (out of the four) were thick SMA terminations and a thin SMA termination, where both PCB designs had a 2nd layer ground cut (of 5.75 mm × 3.75 mm) under SMA pins. As mentioned out of these four PCB design, each PCB had five transmission line, which resulted in a total of 20 transmission lines. Thick SMA terminations are shown in Figure K4 as an example where Figure K4(a) and (b) had no 2nd ground cut while Figure K4(c) and (d) had a 2nd layer ground cut.
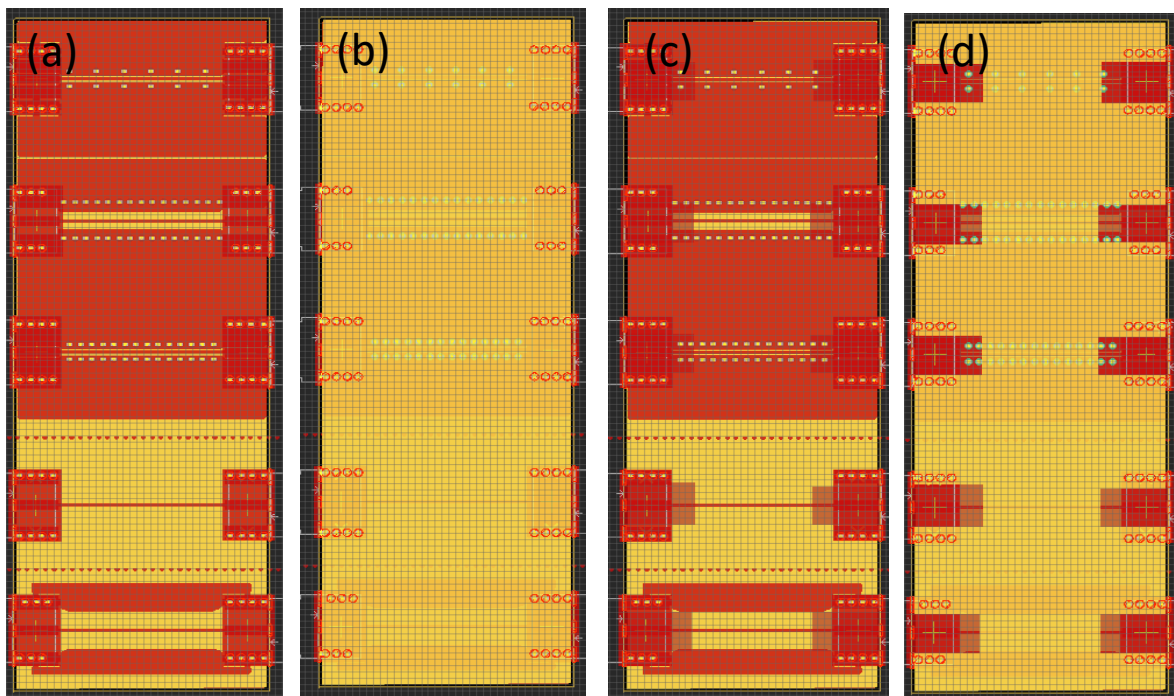

Figure K4:(a) Thick (1 mm trace) SMA top layer (b)Thick SMA 2nd layer showing no cuts under SMA pins(c) Thin (0.38 mm) SMA top layer (d) Thin SMA 2nd layer shown cuts under SMA pins.

The different transmission lines were tested using a VNA to identify their S11 and S21 parameters. Figure K5 combines VNA tests that were performed on thick and thin terminations with 2nd layer ground cuts of 5.75 mm × 3.75 mm, while showing the five different transmission lines in Figure K5(c). The highest S21 of −1.29 dB was observed in transmission line 1.1 for a thin SMA termination with a 2nd layer cut in ground, a spacing between trace and ground pour of 0.1 mm and via fencing spaced at λ/20 (2.58 mm). This was found to deliver a higher S21 (−1.29 dB) in comparison to a PCB with no 2nd layer ground cut-off, which showed an S21 of −2.15 dB.

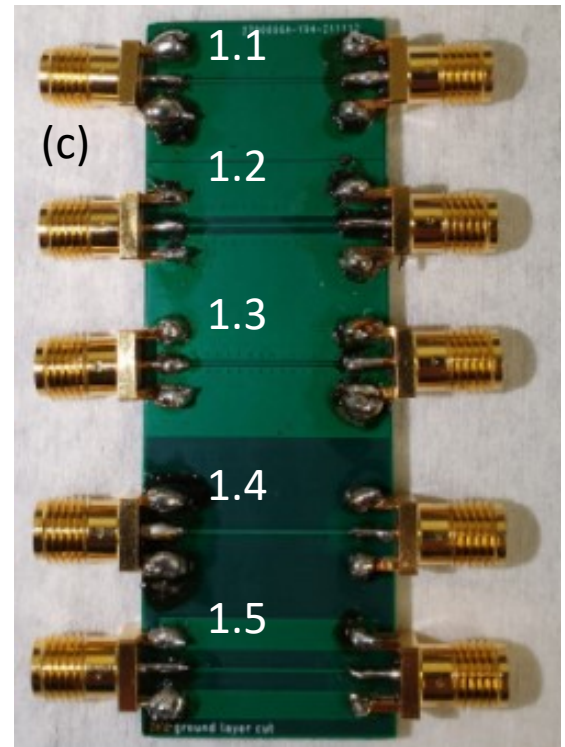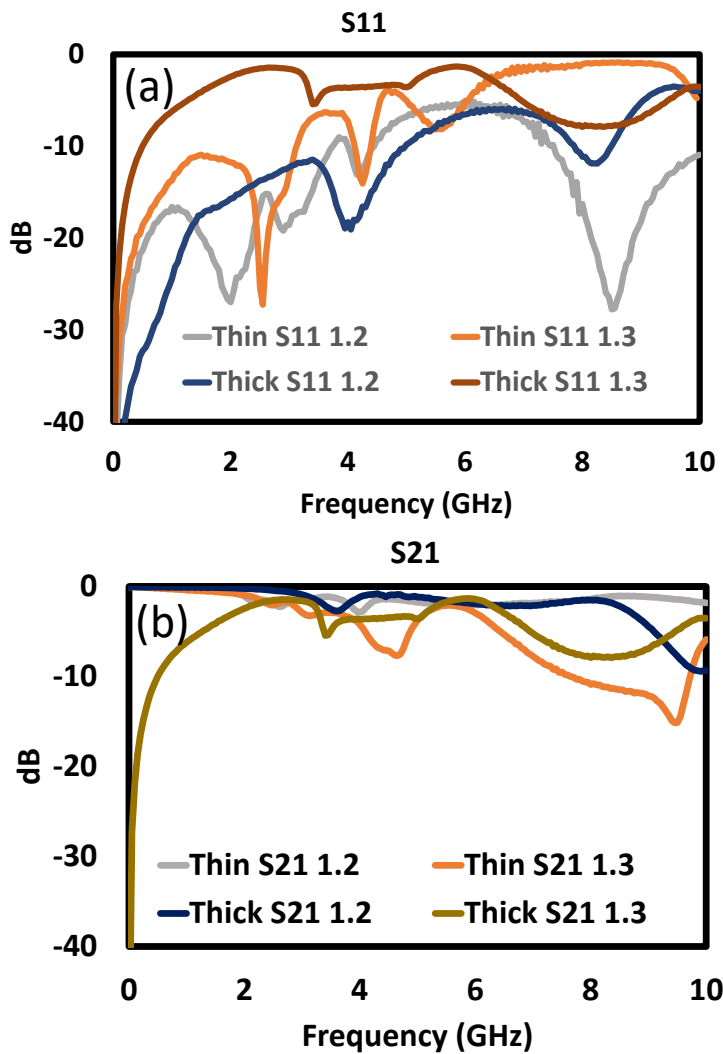Figure K5: VNA results of thin and thick SMAs with 2nd layer cut grounds (a)S11 (b) S21 (c) illustrates the five transmission lines with the numbering convention used in the S parameter plots.

Appendix L   MATLAB Codes

The MATLAB codes used in this project are compiled in are accessible using the following link.

https://drive.google.com/drive/folders/1NCzWHnbNQvslohOvPdCMhg124pw YXyRG?usp=share_link

Appendix M 5.8 GHz V2 Radar Connection and Setup

This section illustrates the connections of the 5.8 GHz V2 radar. The connections are shown in Figure M1. A voltage of 3.3 V is required to power the radar's VCO, while 5 V is for the rest of the components on the board. The IF output has a dedicated pin, which must be connected to the on-board amplification, by connecting a wire to loop the output from the IF to the amplifier. This is shown in a red drawn wire in Figure M1. As mentioned in chapter three, the amplifier has two output stages, where output one was 30 dB and output two was 60 dB. This provides the user a choice of amplification power, where one of these low pass filtered outputs can be chosen.

The chosen output is connected to the spliced end of the audio cable, where the audio jack is connected into the ADC USB's Line-in port, while ensuring the USB data cable is connected to the ADC USB and to the computer. Upon powering the radar, executing audacity on the computer and initiating the recording, the radar recorded signals are then displayed in audacity.
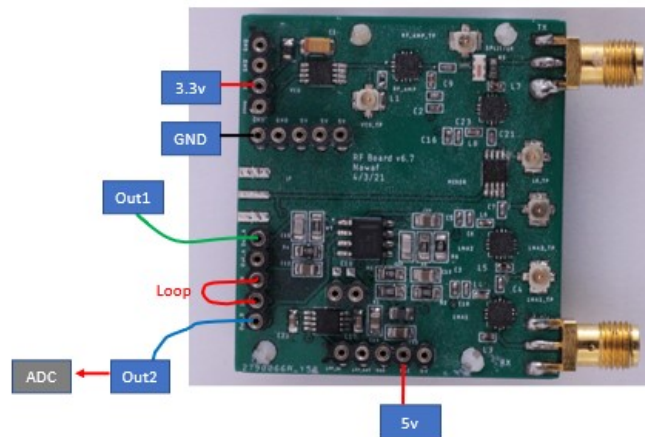
Figure M1: Illustration demonstrating how to connect the V2 radar.

Appendix N I/Q V3 Radar Connection and Setup

The V3 radar requires a Micro USB cable connected at the USB in, an AUX cable for the ADC and a power source (preferably a LiPo battery). The connections are indicated in Figure N1. The sequence of connecting the cables starts with connecting the USB, then the audio jack and turning the power on afterwards. The power regulator LED should turn on indicating that the power regulation is active and the USB LED should turn on to indicate an active USB connection.

A new audio device should automatically be detected, which is visible when entering the audio settings on the computer. This needs to be set at the sample rate of choice (44.1 KHz) and should be set to operate using two channels (allowing I/Q operation).
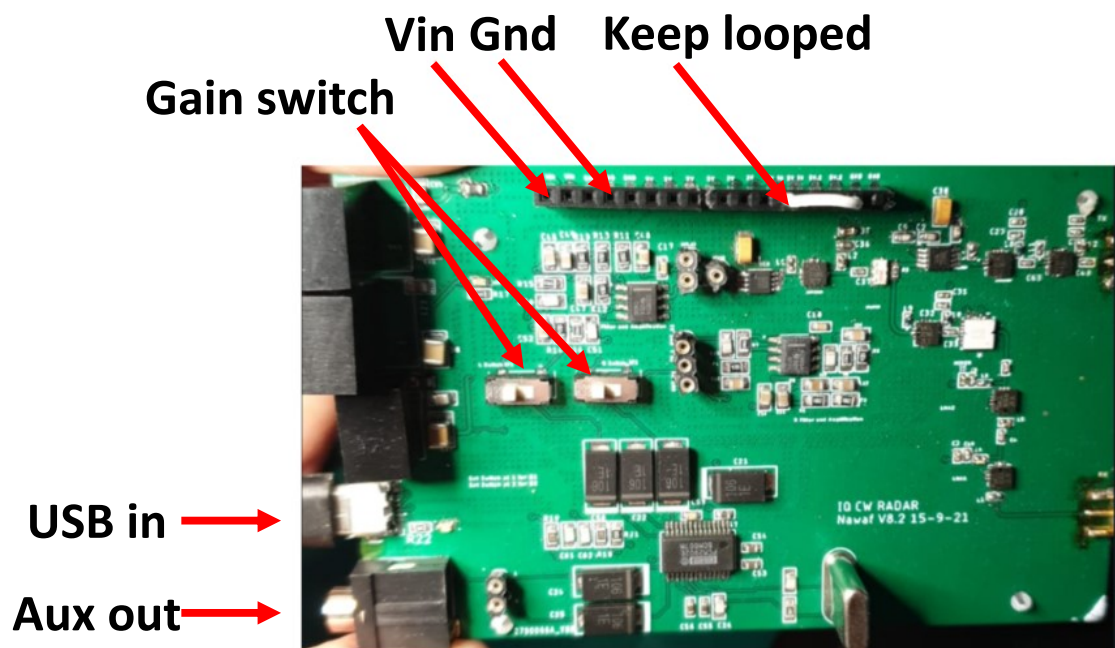
Figure N1: I/Q V3 radar set up.

Appendix O Radar Testing Footage
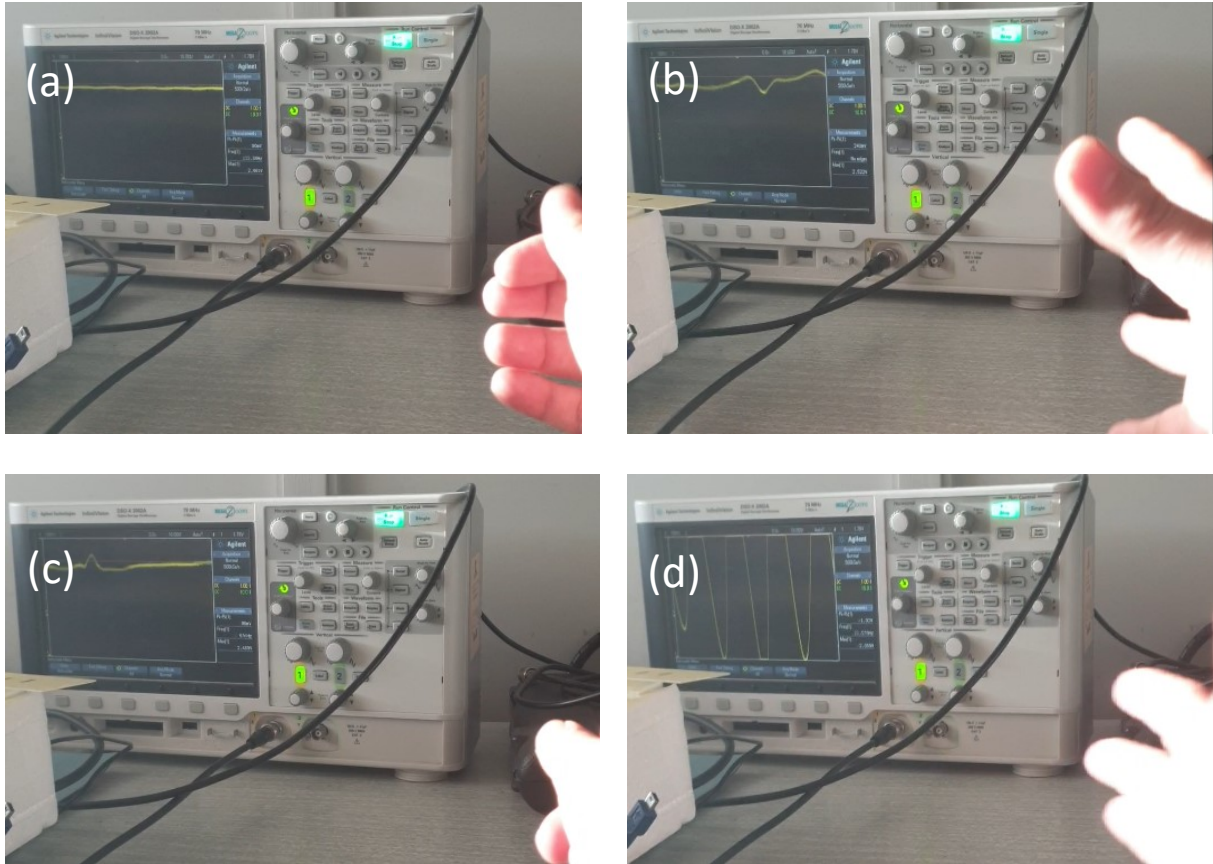
Figure O1: Oscilloscope measurements of the system's IF signal with different hand gestures and interactions (a) Oscilloscope response when no movements were made (b) Response when fingers were moved randomly (c) response when snapping a finger (d) Moving hand towards the radar.
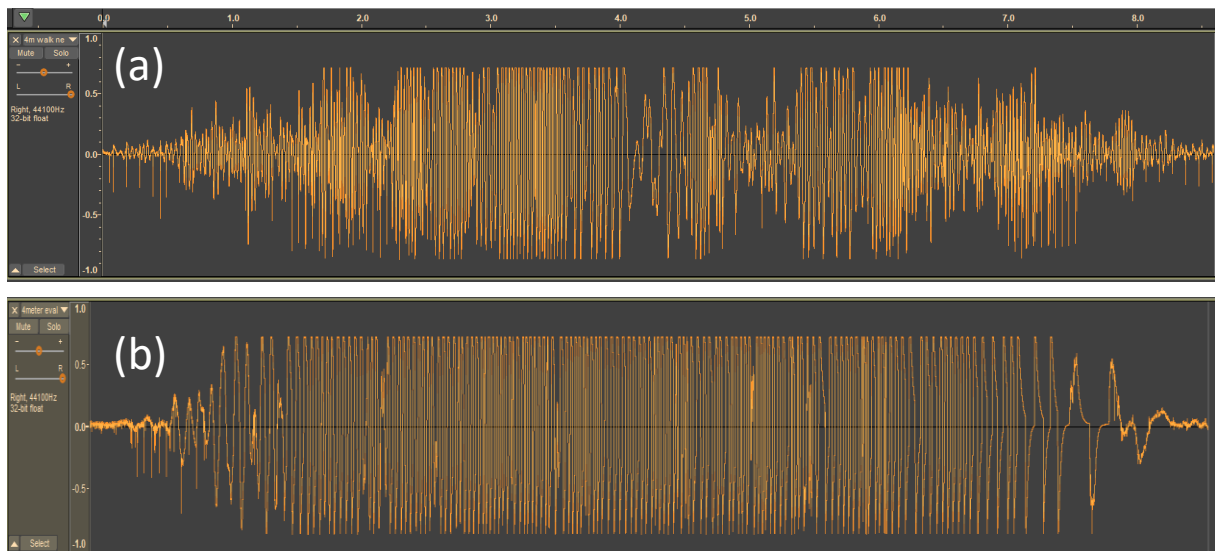
Figure O2: Walking away and towards the 5.8 GHz V2 radar, demonstrating a cleaner and more distinctive signal (b) Walking away and towards the V1 radar.
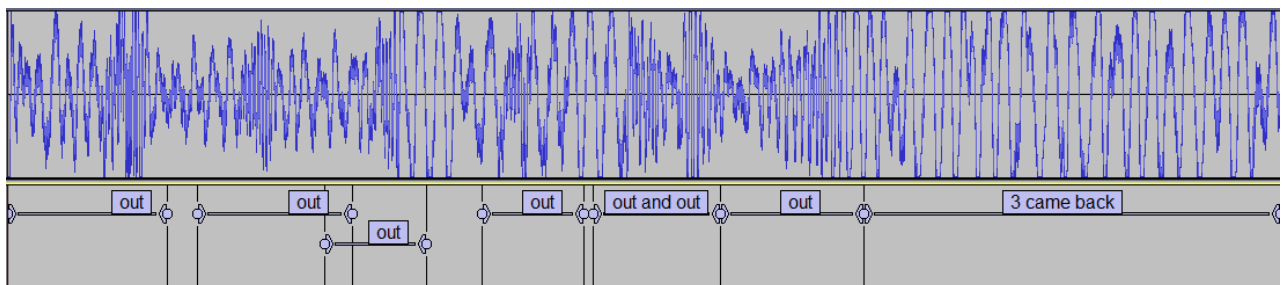
Figure O3: Example of labelled honeybee data

Figure O4: Example of a bee flying out. Arrows pointing at the bee and at the signature recorded.

Figure O5: Example of a bee flying in. Arrows pointing at the bee and at the signature recorded.

Appendix P   Hydrogel spheres as radar targets

It was mentioned in section 2.4.4.2 that hydrogel spheres were used as an early approach to test radar's capability to observe small targets. This assumption was based on the size of hydrogel spheres (10 mm diameter ≈ small honeybee) and their ability to absorb water, which —though not accurately— emulated the water content in a bee's body. Placing a hydrogel sphere in water for approximately 15 minutes allows it to double in diameter reaching 20 mm, due to its rapid absorption of water.
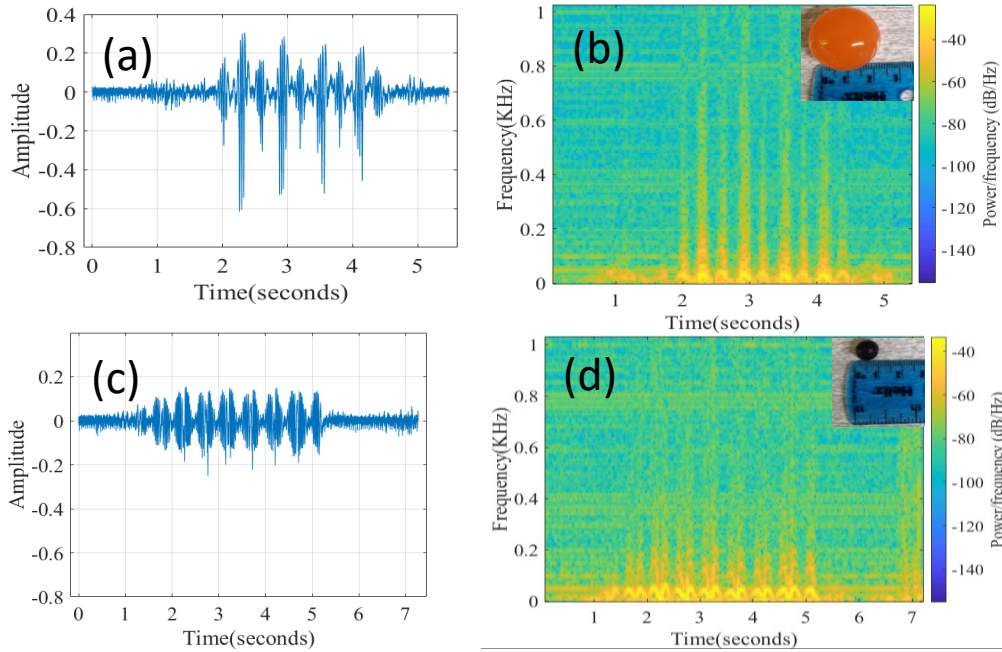

Figure P1:(a) Oscillogram of large hydrogel sphere (b) Spectrogram of large hydrogel sphere (c) Oscillogram of small hydrogel sphere (d) Spectrogram of small hydrogel sphere.

Figure P1 demonstrates the use of a spectrogram and oscillogram plotted in MATLAB to illustrate the signatures obtained from a 30 mm hydrogel sphere in Figure P1(a-b) and a 10 mm hydrogel sphere in Figure P1(c-d) respectively. Though observing single hydrogel radar signatures was promising, their smallest diameter was 10 mm. Referring to the simulation in chapter 2, Figure 2.13, a 10 mm hydrogel sphere resulted in a simulated RCS value of approximately −41 dBsm. This was much larger compared to the RCS values of honeybees (for higher frequencies) found in literature and to the RCS values obtained from simulation (−55 dBsm and −71 dBsm respectively). Additionally, hydrogel sphere's simulated RCS plot remained similar to water spheres up until 5 mm, and deviated afterwards. Further the spheres deflated over time due to water content loss. These factors ruled out the use of hydrogel gel spheres for calibration purposes.

Appendix Q Simulation and analysis of human micro-Doppler shifts

The signature of a human walking is a suitable example of a micro-Doppler signature addressed frequently in literature. As a human target walks, other body parts such as the head, knees, arms and legs move alongside the body to generate micro-Doppler shifts, which simultaneously contribute towards the overall Doppler signal. A simulation of a walking human model is shown in Figure Q1(a), which demonstrates the micro-Doppler signal achieved from a walking human. The simulation shows sinusoidal like features representing micro-Doppler signatures of the arms and legs of the walking model, where the leg has the highest speed and thus stands out [196].
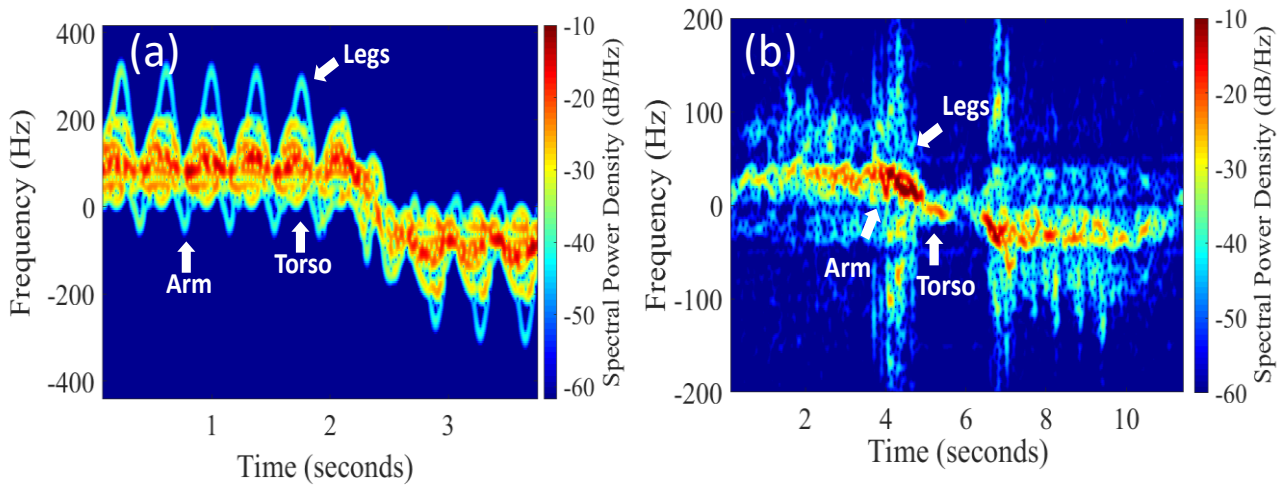
Figure Q1: (a) Simulation of walking human demonstrating micro-Doppler signatures (b) Walking human towards and away the I/Q radar v3 demonstrating a positive shift and negative shift respectively with micro-Doppler signatures.

The simulation model in [196] was adjusted in MATLAB [190] to represent the same height (1.5 metre) of the target walking in Figure Q1(b), while adjusting the simulation's radar frequency from 9.8 GHz to 5.8 GHz. The location of the radar was also changed from its initial diagonal placement with respect to the target, to being placed in front of the target, reflecting the location of the practical experiment that took place. The positioning of the radar is shown in Figure Q2, where the model walks towards the radar and continuous walking away, allowing the simulation to record the corresponding micro-Doppler features of the model.

Figure Q2: Radar positioning in simulation model. The human model walks towards the radar and away along the blue dashed arrow to provide micro-Doppler signatures with respect to the motion of the target.

Due to the reduction of the centre frequency, a slight decrease in the micro-Doppler features was observed. This reduction was additionally observed when the target's height was decreased, as the body's limbs' height reduced accordingly.

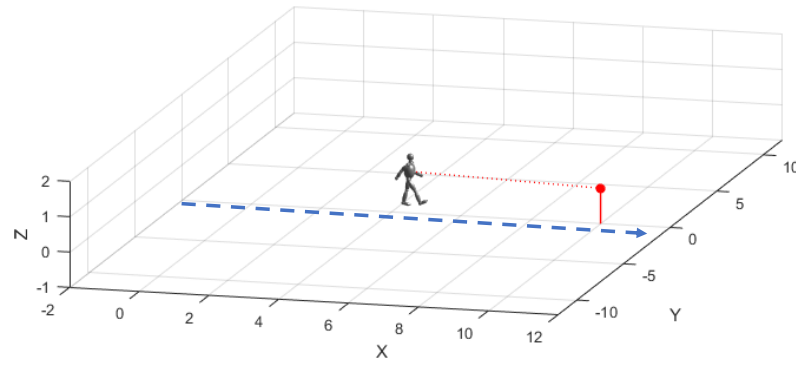Upon comparing the simulation to the practical experiment, a resemblance between the positive and negative Doppler shift can be observed in both. This is evident from the positive signal during the first half of both signals in Figure Q1(a) and (b). This can then be seen to transition towards the negative frequency spectrum as the walking target walks away from the radar in both (a) and (b). The target's torso is clearly observed in both figures, while the legs can be seen in both. The arms of the target can be faintly observed in the practical experiment. Due to the simulation model being an ideal model with no external interference and minimal losses, the micro-Doppler features are inherently more visible in Figure Q1(a) compared to (b). However, this was still deemed suitable for the demonstration and correlation of a micro-Doppler simulation and experiment. A collection of human micro-Doppler signatures extracted using the V3 I/Q radar are shown to demonstrate the additional information extracted from micro-Doppler feature extraction. Figure Q2(a) and (b) show the difference between fingers and the movement of a whole hand moving back and forth with respect to the radar. Figure Q2(c) and (d) illustrate a movement that may seem similar to one another, where the target was jumping away the radar with arms and legs fixed in position in (c) and performed jumping jacks in (d). When taking into account the micro-Doppler details a difference between the two can be observed. Figure Q3(c) shows the body's signature oscillating as the body jumps and lands repetitively away and back towards the radar. In Figure Q3(d), additional features that were fixed in (c) were in motion — while performing jumping jacks —which can be seen in the plot.
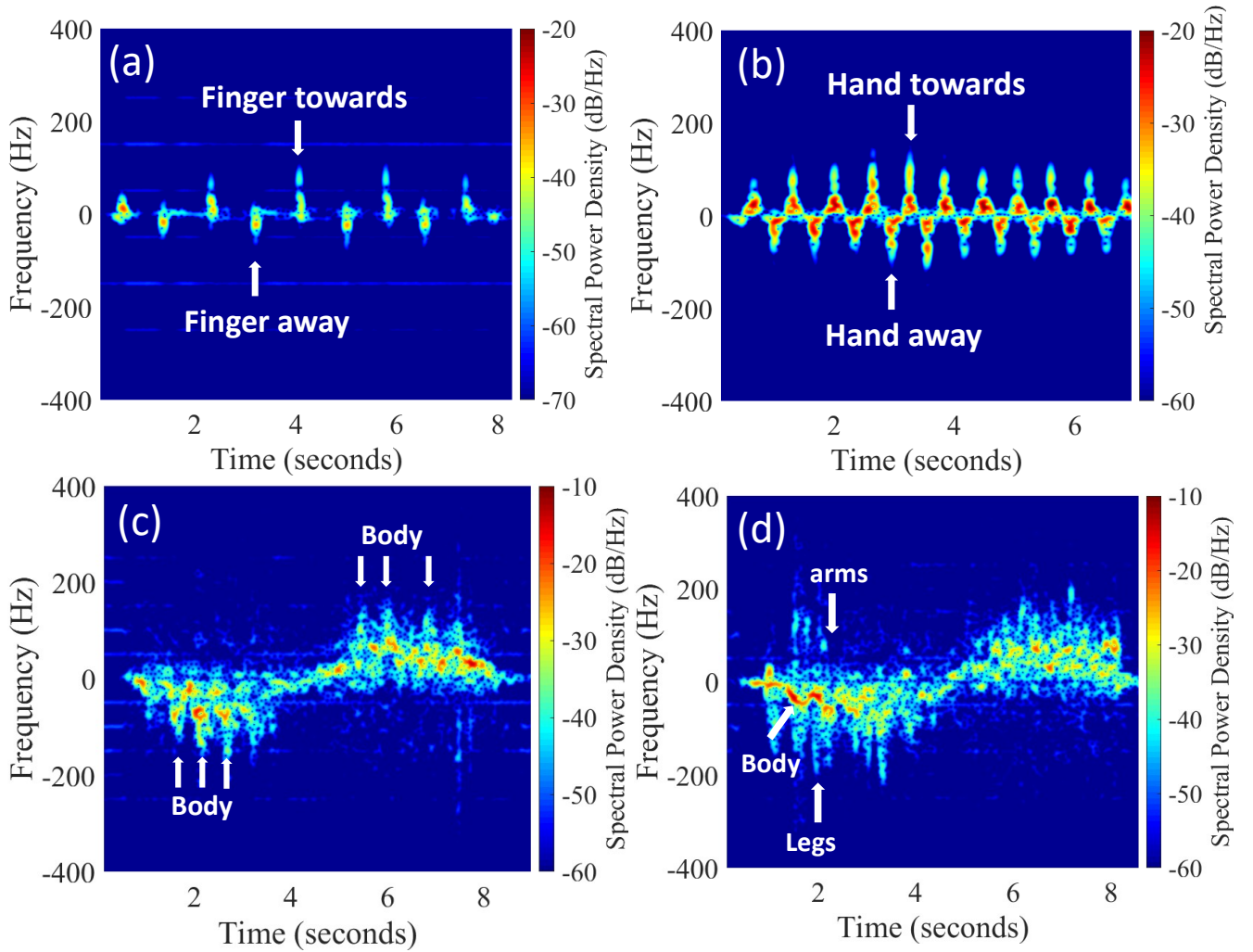
Figure Q3: Micro-Doppler signatures towards/away from radar (a) fingers (b) hand (c) jumping body with fixed arms and legs (d) jumping jacks with arms and legs swinging.

Pendulum equation derivation

Newton's second law of motion, mentions that the net torque is $I(d^2\theta/dt^2)$, where $d^2\theta/dt^2$ is the angular acceleration and I is the moment of inertia. Upon torque τ acting on the system, then $\tau = d^2\theta/dt^2$. If the length of the string is L and mass of the pendulum is m, the pivot's moment of inertia is then,

$$I = mL^2 \hspace{4cm} \text{Q1.1}$$

The vector torque τ, is the cross-product of the position vector L and the gravitational force vector *mg.* The torque's magnitude is,

$$\tau = L\,mg\,sin\theta \hspace{4cm} \text{Q1.2}$$

The pendulum's net torque is

$$-Lmg sin\theta = I\,\frac{d^2\theta}{dt^2} = mL^2\,\frac{d^2\theta}{dt^2} \qquad\qquad \text{Q1.3}$$

This finally becomes the equation mentioned as equation 4.1, which defines a relationship between pendulum's swinging angle and its second time derivatives, as shown below,

$$mL\,\frac{d^2\theta}{dt^2} = -mg\,sin\theta \qquad\qquad \text{Q1.4}$$

Appendix R Digital Signal Processing and Machine Learning

Fourier Transform

All monitored radar signals are recorded, digitised and saved as .wav files, allowing the signals to undergo digital signal processing. The Fourier transform is a mathematical technique, used to map signals in the time domain to their respective spectrum in the frequency domain. It is a mathematical relationship between the time domain and the frequency domain. The Fourier transform of $s(t)$ is the function of $S(\omega)$ where [197],

$$S(\omega) = \int_{-\infty}^{\infty} s(t) \, exp\{-i\omega t\} dt \qquad \text{R1.1}$$

Where $\omega = 2\pi f$ is the angular frequency and $S(\omega)$ can be interpreted as the projection of signal $s(t)$ onto a complex exponential function $exp\{-i\omega t\}$ at ω. The original function can be re-constructed from the projected values by using the inverse Fourier transform of $S(\omega)$ as [197],

$$s(t) = \frac{1}{2\pi} \int_{-\infty}^{\infty} S(\omega) \, exp\{-j\omega t\} d\omega \qquad \text{R1.2}$$

A Fourier transform uses complex exponentials of different frequencies as its basis function. Other transforms (e.g., Laplace, wavelet and Z) utilise other basis functions. Where $F(\omega)$ is also referred to as the spectral density of $f(x)$ or as the spectrum of $f(x)$.

Discrete Fourier Transform

The Discrete Fourier Transform (DFT) is a Fourier transform, which handles both signal representations, whether in time domain or in frequency domain as discrete/periodical signals. The DFT is a mathematical operator used for transforming a sequence of discrete signals, which can be the conversion of a series of time domain signals to frequency domain signals for instance. This allows the determination of the spectral content of the signal. This is practically useful when multiple targets are present in the doppler spectrum, which would first need to be digitised by an ADC. A DFT would then be able to convert the digital (sampled) time domain signal to a frequency spectrum.

An additional benefit of using a DFT is that it reduces the radar's effective noise bandwidth by the applied duration of the DFT as [177],

$$B_n = \frac{1}{\tau}$$

R1.3

Where τ is the duration of time to which the DFT is applied. The application of the DFT for a discretely sampled signal s_n recorded by the Doppler radar to obtain its frequency domain representation S_ω with N total number of samples is calculated as [223], [224].

$$S_\omega = \sum_{n=0}^{N} s_n e^{-j\omega n}$$

R1.4

Where $j = \sqrt{-1}$, $\omega = 2\pi f$, while f is the relative frequency and n is the discrete sample number of the analysed signal. The DFT total of samples are finite and are periodic. The signal can be either a real signal (Doppler radar V1 and V2) or a complex signal (I/Q V3 radar). A DFT implementation will only provide the N number of digitised data-points that were digitised by the ADC. Knowing the total sample size allows the identification of the resulting frequencies as,

$$t_{sample} = N/f_s$$

R1.5

Where t_{sample} is the total sample time from beginning to the end, and f_s is the digitiser's sample rate. Hence, considering the frequency steps for S_ω between each data point for a complex value s_n and for real-valued s_n is $\Delta f = 1/t_{sample}$ and $\Delta f = 2/t_{sample}$ respectively [223].

Fast Fourier Transform

Though the DFT is not used directly, a computationally efficient implementation of the DFT the Fast Fourier Transform (FFT) is commonly used instead [223]. This faster and more efficient implementation is automatically selected by software packages, when the number of samples N in S_ω is equal to a power of 2. The DFT has a computational cost of cost of N^2, while an FFT has a computational cost of $N \cdot log_2 \cdot N$. To put this in perspective, an N size of 4096 data points would require a FFT and an DFT to perform 49,152 and 16,777,216 complex multiplies and additions respectively, which is a computational effort of 0.29% when comparing the FFT to the DFT [225].

Frequency resolution

This determines the minimum discriminated frequency difference. It is a relation between the number of samples and the sampling frequency f_s as

$$Frequency\ Resolution = \frac{f_s}{N_{samples}} \qquad \text{R1.6}$$

Different monitored targets, require a different frequency resolution. Since honeybees expected frequencies are within the 100 to 250 Hz range, a moderate frequency resolution is required. However, when operating with heartbeats or wingbeats a finer resolution is necessary.

Scalograms

Since spectrograms generated using STFTs are limited by their window function and always experience a trade-off in a better time resolution or frequency resolution. The continuous wavelet transform (CWT), is a time-frequency representation capable of achieving variable resolution in one domain, while achieving a multi-resolution in the other domain [226]–[229].The definition of the CWT of a signal *s(t)* is [197],

$$CWT(t, \omega) = \left(\frac{\omega}{\omega_0}\right)^{1/2} \int s(t')\, \psi \cdot \left(\left(\frac{\omega}{\omega_0}\right)(t' - t)\right) dt' \qquad \text{R1.7}$$

Where $\frac{\omega}{\omega_0}$ is the scale parameter and $\psi(\cdot)$ is referred to as the "mother wavelet" in wavelet theory. The resulting two-dimensional magnitude display of the expression is known as the scalogram [197]. Assuming the mother wavelet oscillates at frequency ω_0 and is centred at time zero. The equation above can be interpreted as the decomposition of signal $s(t')$ into a series of dilated and shifted wavelets $\psi \cdot [\frac{\omega}{\omega_0}(t' - t)]$. The basis function $\psi \cdot [\frac{\omega}{\omega_0}(t' - t)]$ of the wavelet has a variable width which depends on ω at each time t. By shifting the $\psi(t')$ at a fixed ω or alternatively by dilating $\psi(t')$ at a fixed t the scale mechanism in the time response and the multiscale events can be analysed respectively [197] . This provides the scalogram with the multiresolution property that is an advantage over the STFT.

Neural Networks: Random Forest

Random forest is a classification algorithm, that is formed by a multitude of tree-structured classifiers $\{h(X, \Theta_k), k = 1, \dots\}$ where the $\{\Theta_k\}$ are random vectors that are independently created but with identical distribution [230]. Trees are grown using the training and vector Θ_k, which results in a classifier $h(X, \Theta_k)$, where x is the input vector. After a large set of trees are generated, the most popular class is voted for [230].

Line Spectral Pairs

Linear prediction is a known technique in speech applications [231]. This representation is used to estimate a signal as a linear combination of values that were previously observed and is defined as [231],

$$\hat{x}_k = \sum_{i=1}^{p} a_i x_k - i \qquad \text{R1.8}$$

Where p is the LP's order (i.e., the number of employed coefficients) and k is the time index. The prediction error is minimised through the calculation of a_i coefficients. The above equation can be rewritten in the frequency domain using a z-transform [232]. Using this equation, a short audio signal is assumed to be generated as an all-pole filter's output H(z) = 1/A(z), where A(z) is the inverse filter as,

$$H(z) = \frac{1}{A(z)} = \frac{1}{1 - \sum_{i=1}^{p} a_i z^{-i}} \qquad \text{R1.9}$$

Line Spectral Frequencies (LSFs) also known as Line Spectral Pairs (LSPs) [233], are an alternative representation of LP coefficients. The calculation of an LSP coefficient, requires the decomposition of the inverse polynomial filter into *P(z)* and *Q(z)*, as [231]

$$P(z) = A(z) + z^{p+1} A(z^{-1}) \; and \; Q(z) = A(z) - z^{p+1} A(z^{-1}) \qquad \text{R1.10}$$

Where *P(z)* and *Q(z)* are a symmetric and antisymmetric polynomial respectively and the LSP coefficients are determined by their roots [231]. LSPs are suitable for interpolation, quantisation and map large signals to small numbers of coefficients more effectively than other LP technique [231].

Temporal Signatures

Different methods were investigated that would simultaneously result in a high classification accuracy and low computational expenses. This involved using temporal signal features for ML. Such features include Root Mean Square (RMS), short-time energy, kurtosis, standard deviation, skew, mean, zero-crossing rate, spectral variance and energy.

Temporal features can provide a better understanding of the signal, where it aims to approximate primitive features that describe the waveform, such as the period and amplitude. The amplitude of a signal can be evaluated by its RMS. The RMS is defined by [233].

$$RMS = \frac{1}{n}\sqrt{\sum_{i=1}^{n} x_i^2} \qquad\qquad \text{R1.11}$$

In equation R1.11, x is a vector with length n used to represent the time series, x_i is used to define each observation, where $1 \leq i \leq n$. An alternative way to estimate RMS without the use of a square root, is known as short-term energy (STE),

$$ZCR = \frac{1}{n-1}\sum_{i=2}^{n} |S(x_i) - S(x_i - 1)| \qquad\qquad \text{R1.12}$$

Descriptive statistics are also used in temporal representation of data, such as standard deviation and variance. Higher order measures such as kurtosis and skewness are similarly utilised for the characterisation of waveform values distribution in a signal [233]. Kurtosis is applied to measure the flatness of amplitude distributions relative to the normal distribution, where a flat distribution is represented by a low kurtosis value and vice versa. Symmetry of a signal is characterised using skewness, where the symmetry in a signal increases as the skewness value approaches zero [233].

The zero-crossing rate (ZCR) can also be used for the estimation of the noise level in the signal, where low values of ZCR reflect low level noise and vice versa. A common interpretation of the ZCR is an estimation of the signal's complexity [233].

Appendix S   Electric field and SAR exposure to bees

The electric field magnitude *(E0),* can be estimated by calculating the main beam power flux *(S),* at the insect. This is estimated using equation S1.1[234],

$$S = \frac{G_t \times P_t}{4\pi \times r^2}$$
S1.1

Where G_t, is the gain of the transmitting antenna, P_t is the power transmitted and r is the range. Assuming $G_t = 17\ dBi$, $P_t = 30\ dBm$ and r is 2 metres. The main beam power flux can be calculated as,

$$S = \frac{50 \times 1}{4\pi \times 2^2} = 0.0998\ mW/cm^2$$

A main beam power flux of $0.0998\ mW/cm^2$. This can then be used to calculate the electric field magnitude by considering a Z0 of 377, using $E0 = \sqrt{2 \times S \times Z0}$, where $Z0 = 377\Omega$. The electric field *(E0)* is 27.43 V/m, which is not considered harmful to humans. The maximum Specific Absorption Rate (SAR) level for humans is known to be 1.6 W/kg [235]. To calculate the SAR for honeybees, the *E0*, conductivity *(σ)* and density of a honeybee needs to be known. Since *E0* was calculated earlier as 27.43 V/m and the conductivity of the bee can be extracted from reference [132] as 5.05 S/m at 6 GHz, the density still remains to be found. The density can be calculated by knowing the mass and volume of the object. The mass of a bee is approximately between 0.1 to 0.2 grams; hence it is safe to assume an average mass of 0.15 grams. The volume of an averaged sized bee can be approximated as the volume of an ellipsoid (similar to the one used in the study) with a length, width and height of 12.5 mm, 3 mm and 2 mm respectively. The volume can thus be calculated as $\frac{4}{3} \times \pi \times width \times length \times height = 3.1416\ cm^3$. The density can then be calculated as mass/volume = 0.0477 g/ cm^3. The variables are *E0*=27.43 V/m, hence E_{RMS}=19.3959 V, σ =5.05 S/m at 6 GHz, density=0.0477 g/ cm^3= 47.4 kg/ m^3. The SAR formula is [236],

$$SAR_{bee} = \frac{\sigma \times E_{RMS}^{\ 2}}{density}$$
S1.2

This is equal to 39.82 W/kg. Hence, the SAR for honeybees using the radar is ~40 W/Kg. Upon comparing this with a human exposed to a mobile phone, the density of a human is significantly different to that of a bee, which in addition to the conductivity is the primary variable that differs between the two.